THE EFFECT OF ENDWALL CONTOURING ON BOUNDARY LAYER DEVELOPMENT IN A TURBINE BLADE PASSAGE

Stephen P. Lynch

Dissertation submitted to the Faculty of
Virginia Polytechnic Institute and State University
in partial fulfillment of the requirements for the degree of

Doctor of Philosophy
in
Mechanical Engineering

Karen A. Thole, Chair
Wing Fai Ng
Walter F. O'Brien
Pavlos P. Vlachos
Roger L. Simpson

August 31, 2011
Blacksburg, Virginia

Keywords: Three-Dimensional Boundary Layers, Turbine Blade Endwalls, Film Cooling

The Effect of Endwall Contouring on Boundary Layer Development in a Turbine Blade Passage

Stephen P. Lynch

Abstract

Increased efficiency and durability of gas turbine components is driven by demands for reduced fuel consumption and increased reliability in aircraft and power generation applications. The complex flow near the endwall of an axial gas turbine has been identified as a significant contributing factor to aerodynamic loss and increased part temperatures. Three-dimensional (non-axisymmetric) contouring of the endwall surface has been shown to reduce aerodynamic losses, but the effect of the contouring on endwall heat transfer is not well understood.

This research focused on understanding the general flow physics of contouring and the sensitivity of the contouring to perturbations arising from leakage features present in an engine. Two scaled low-speed cascades were designed for spatially-resolved measurements of endwall heat transfer and film cooling. One cascade was intended for flat and contoured endwall studies without considering typical engine leakage features. The other cascade modeled the gaps present between a stator and rotor and between adjacent blades on a wheel, in addition to the non-axisymmetric endwall contouring.

Comparisons between a flat and contoured endwall showed that the contour increased endwall heat transfer and increased turbulence in the forward portion of the passage due to displacement of the horseshoe vortex. However, the contour decreased heat transfer further into the passage, particularly in regions of high heat transfer, due to delayed development of the passage vortex and reduced boundary layer skew. Realistic leakage features such as the stator-rotor rim seal had a significant effect on the endwall heat transfer, although leakage flow from the rim seal only affected the horseshoe vortex. The contours studied were not effective at reducing the impact of secondary flows on endwall heat transfer and loss when realistic leakage features were also considered. The most significant factor in loss generation and high levels of endwall heat transfer was the presence of a platform gap between adjacent airfoils.

Acknowledgments

This milestone in my life would not have been possible without the help of many, many people. First and foremost, I must acknowledge my Lord and savior Jesus Christ, who gave me the strength and fortitude to endure difficult times and shared in my peace and joy in the many good times. May your will be done in all I do.

I would also like to thank my advisor, Karen Thole. I don't think I have the faintest idea of how much you've really done for me, and I appreciate your guidance and support. There is no doubt that I am a better researcher and engineer because of your tutelage, and I hope you realize that your example has changed my life. You are an inspiration to me and I hope someday to be the same for the next generation of graduate students.

My PhD committee (Dr. Wing Ng, Dr. Walter O'Brien, Dr. Pavlos Vlachos, and Dr. Roger Simpson) also deserves many thanks. I have enjoyed interacting with you in the classroom, or during projects we worked together on. Thank you very much for taking time to review my preliminary prospectus and my dissertation, as well as your time in attending my defenses, and I appreciate your support during my many years as a PhD candidate.

I would like to thank the people at Virginia Tech and Penn State who have helped me in many little ways. Cathy Hill, you have always gone the extra mile for me and I truly believe my degree would not have been completed without your help. Thanks also to Jamie Archual, Ben Poe, and Melissa Williams for your help and friendship. Many thanks to Phil Irwin at Penn State for making my experiments possible. Also, thanks are due to Dr. Eric Marsh, Steve, Ashis, and Ryan for a great teaching experience.

To all of my many labmates who have come and gone over the years, thank you very much for your help, your support, your time, and your friendship. For the folks in my first years as a newbie: Paul, Scott W., Nick, Will, Sundar, Scott B., Eric, Erin, and Joe: thank you for the Lab Olympics, Hokie football, white t-shirt day, and of course all of the lab lessons. For the folks in my time at PSU: Mike, Alan, Seth, Jason, Grant, Gaelyn, Robert, Duane, Gina, Steve: thanks for intramural basketball, Frisbee in the IM fields, and putting up with an old married man with a kid. I have enjoyed interacting with you all and I wish you all the best.

To my parents Pat and Cathy, thank you for your love, support, encouragement, and belief in me. Every day I realize more and more how much you sacrificed and worked to help me

get to this point in my life, and I will be forever grateful. I hope my children can say the same thing about me someday. To my siblings Liz, Kevin, Michelle, and Brian, thank you for your love and support (and teasing!), which helped me realize what is important in my life. I love you all very much and may God bless everything you do.

Last but most definitely not least is my little family. There are no words to truly describe how much you mean to me, but I'll try. Becca, you are the best thing that has ever happened to me. I know this has been a long time coming, and you will probably celebrate more than I will. You have sacrificed so much and have been so supportive that I will never be able to repay you. I love you more than I can ever say in words or actions, and I will love you always. Thank you for being my rock. To my children Jack and Colleen, thank you for being the light of my life and my daily reminder of God's blessings. I love you very much and I am looking forward to many more adventures.

This dissertation is dedicated to my family: Becca, Jack, and Colleen Lynch

Attribution

The co-authors for Paper 1, entitled, "Heat Transfer for a Turbine Blade with Non-Axisymmetric Endwall Contouring", are Karen Thole, Narayan Sundaram, Atul Kohli, and Christopher Lehane. Karen Thole is affiliated with the Mechanical and Nuclear Engineering Department at The Pennsylvania State University in University Park, PA. Her contribution to Paper 1 included general advising on the experimental setup and data analysis, as well as editing of the manuscript. Narayan Sundaram was also affiliated with Penn State. His contribution included initial design and some construction for the test section and wind tunnel modifications, as well as some manuscript editing. Atul Kohli and Christopher Lehane are both affiliated with United Techologies—Pratt & Whitney in East Hartford, CT. Their contributions included procuring funding for the work, advice on the experimental results and manuscript editing.

The co-authors for Paper 2, entitled, "Computational Predictions of Heat Transfer and Film Cooling for a Turbine Blade with Non-Axisymmetric Endwall Contouring", are Karen Thole, Atul Kohli, and Christopher Lehane. Karen Thole's contribution included general advice on the experimental and computational setup and data analysis, as well as editing of the manuscript. Atul Kohli and Christopher Lehane provided funding for the work, advice on the experimental and computational results, and some editing of the manuscript.

The co-author for Paper 3, entitled, "Investigation of the Three-Dimensional Boundary Layer on a Turbine Endwall with Non-axisymmetric Contouring", is Karen Thole. Karen Thole's contribution included general advice on the experimental setup and data analysis, as well as editing of the manuscript.

The co-authors for Paper 4, entitled, "Endwall Heat Transfer for a Turbine Blade with an Upstream Cavity and Rim Seal Leakage", are Karen Thole, Atul Kohli, and Christopher Lehane. Karen Thole's contribution included general advice on the experimental setup and data analysis, as well as editing of the manuscript. Atul Kohli and Christopher Lehane provided funding for the work and advice on the experimental results.

The co-authors for Paper 5, entitled, "Measurements of Aerodynamic Loss for a Turbine Blade with Endwall Leakage Features and Contouring", are Karen Thole, Atul Kohli, and Christopher Lehane. Karen Thole's contribution included general advice on the experimental

setup and data analysis, as well as editing of the manuscript. Atul Kohli and Christopher Lehane provided funding for the work and advice on the experimental results.

The co-authors for Paper 6, entitled, “Heat Transfer and Film-Cooling for a Turbine Blade with Endwall Leakage Features and Contouring”, are Karen Thole, Atul Kohli, and Christopher Lehane. Karen Thole’s contribution included general advice on the experimental setup and data analysis, as well as editing of the manuscript. Atul Kohli and Christopher Lehane provided funding for the work and advice on the experimental results.

Table of Contents

List of Tables

Paper 6: Heat Transfer and Film-Cooling for a Turbine Blade with Endwall Leakage Features and Contouring

Appendix A: Velocity Transformations for Laser Doppler Velocimeter Measurements

Appendix B: Uncertainty Estimates for Reported Variables

List of Figures

Introduction

Paper 1: Heat Transfer for a Turbine Blade with Non-Axisymmetric Endwall Contouring

Paper 2: Computational Predictions of Heat Transfer and Film Cooling for a Turbine Blade with Non-Axisymmetric Endwall Contouring

Paper 3: Investigation of the Three-Dimensional Boundary Layer on a Turbine Endwall with Non-axisymmetric Contouring

Paper 4: Endwall Heat Transfer for a Turbine Blade with an Upstream Cavity and Rim Seal Leakage

Paper 5: Measurements of Aerodynamic Loss for a Turbine Blade with Endwall Leakage Features and Contouring

Paper 6: Heat Transfer and Film-Cooling for a Turbine Blade with Endwall Leakage Features and Contouring

Appendix A: Velocity Transformations for Laser Doppler Velocimeter Measurements

Appendix C: Design and Construction of Endwalls

Appendix D: Comparison of CFD to Measurements

Introduction

Motivation

Gas turbine engines are attractive sources for aircraft motive power due to their high power-to-weight ratios, and also for electrical generation shaft power due to high thermal efficiencies and relatively rapid response times. Like all energy conversion devices, however, there is significant motivation to improve performance and efficiency further, particularly given that most gas turbines operate on increasingly costly fossil fuels. While gains can in part be accomplished by increasing the temperature of the combustion gases, durability considerations for components downstream of the combustor result in limitations to the maximum allowable temperature. Advanced cooling designs are making higher combustion temperatures realizable, but those designs increasingly require a thorough understanding of the turbine environment.

Incremental gains in individual component efficiencies can add up to significant savings over the whole engine, especially when considering the large number of airfoils typically found in modern turbine engines (the GP7000 engine for the Airbus A380 superjumbo airliner has 14 compressor stages and 8 turbine stages, where each stage can contain around 200 airfoils). In an axial-flow turbomachine, one area identified by designers as a source of efficiency improvement is the complex flow present at the inner and outer casings, which are termed endwalls. Three-dimensional boundary layers, large streamwise vortices, and separated and reattaching flows present at the endwall are collectively referred to as secondary flows. Secondary flows are termed as such since they do not follow the primary inviscid flow through the passage, and it is well-known that secondary flows have a significant impact on the aerodynamic efficiency and durability of turbine components. In modern low-aspect ratio turbines, secondary flows are responsible for up to 30 percent of the total pressure loss in a passage (Denton [2]). Secondary flows also increase convective heat transfer coefficients and displace coolant injected near part surfaces, which has a significant effect on part temperature. A 25°C temperature increase for a part operating in a 1500°C environment (typical of modern turbine inlet temperatures) can reduce part life by half (Han, et al. [3]).

It is clear that reducing or eliminating secondary flows can benefit turbine performance and durability, but the most appropriate and efficient mechanisms by which this can be

accomplished are not well understood. The work presented in this dissertation examines one method of mitigating secondary flows and considers the implications of realistic endwall design features that are necessarily present in an engine. The overall goal of the research is to understand the fundamental physics behind secondary flow mitigation and determine how those physics might be altered by engine-representative features.

Background

Many studies have been devoted to understanding the physics of secondary flows, such that the general features are now fairly well understood. Models such as the one by Langston [1], depicted in Figure 1, describe the major flow features. The incoming endwall boundary layer separates upstream of the airfoil due to the adverse pressure gradient imposed by the blockage and rolls up into a horseshoe vortex. The vortex splits into legs that wrap around the pressure and suction sides of the airfoil, where the pressure side leg merges with streamwise vorticity generated by flow turning in the passage to create a large vortex known as the passage vortex. The suction side leg initially remains close to the airfoil suction side but eventually begins to orbit the passage vortex. A corner vortex is formed where the crossflow impinges on the blade suction side-endwall corner. These vortices entrain boundary layer fluid and promote mixing, which generates total pressure losses. Kang and Thole [4] noted that local heat transfer

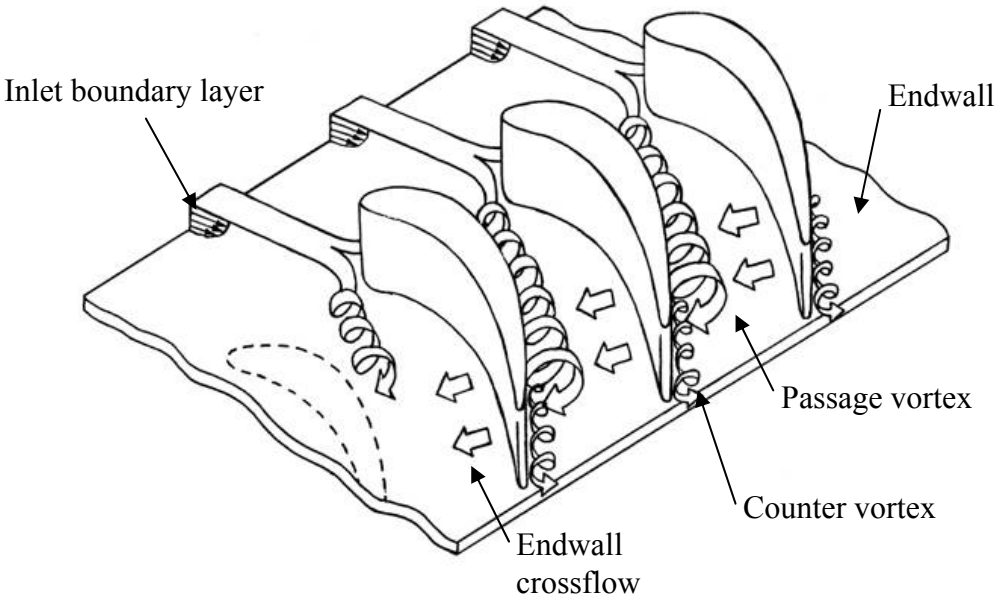

Figure 1. Depiction of endwall secondary flow by Langston [1].

coefficients are high where the vortices induce velocity toward the wall. Coolant ejected onto the endwall can be swept up into the mainstream flow, as demonstrated by Blair [5], Knost and Thole [6], and others. A few studies, such as those by Devenport, et al. [7], Praisner and Smith [8], Radomsky and Thole [9], and Thrift, et al. [10], have also shown that the horseshoe vortex is unsteady and is associated with high turbulence intensity, which further contributes to high heat transfer.

Besides the large vortices, endwall secondary flows are also characterized by three-dimensional (skewed) boundary layers. The flow passing through an airfoil passage is turned by the cross-passage pressure gradient between adjacent airfoils. Fluid near the endwall will turn more sharply than fluid near the freestream, since the lower velocity near the wall relative to the freestream results in a smaller radius of curvature for a given cross-stream pressure gradient. A component of velocity in the cross-stream direction develops in the endwall boundary layer, resulting in mean streamwise vorticity that develops into the passage vortex. The structure of the turbulence in a three-dimensional boundary layer is distorted compared to a two-dimensional boundary layer; Anderson and Eaton [11] reported anisotropic eddy viscosity and reduced effectiveness of the boundary layer at generating Reynolds shear stresses, and Olcmen and Simpson [12] indicated reduced correlation of streamwise and wall-normal velocity fluctuations. A few studies with moderate skewness (Abrahamson and Eaton [13] and Lewis and Simpson [14]) have also indicated that heat transfer is lower for a three-dimensional turbulent boundary layer relative to a two-dimensional boundary layer. Some investigators (Langston, et al. [15], Harrison [16], and Vera, et al. [17]) have noted that the endwall boundary layer may be laminar in the region downstream of the horseshoe vortex separation line. There are very few studies, however, that have presented measurements of the highly skewed boundary layer in a turbine passage.

Although secondary flows and their effects on aerodynamic loss and heat transfer have been extensively studied, it is less clear how best to eliminate them or reduce their impact. Some of the more practical suggestions in the harsh environment of a turbine involve alteration of the endwall or airfoil geometry. Bulbs or large fillets at the leading edge of the airfoil-endwall junction, or contouring of the endwall surface in the passage, have shown promise in both cascade and engine-representative environments.

Leading-edge features are designed to prevent the development of the horseshoe vortex by accelerating the incoming boundary layer. Zess and Thole [18] demonstrated the elimination of the horseshoe vortex and an order of magnitude reduction in local turbulent kinetic energy for a fillet upstream of a vane, and Becz, et al. [19] measured 7% reduction in cascade aerodynamic loss for a blade with a fillet. A bulb on a blade leading edge reduced losses by 47% in a study by Sauer, et al. [20]. While these results are certainly encouraging, Sieverding [21] points out that elimination of the horseshoe vortex will not eliminate the passage vortex since its evolution is fundamentally dictated by flow turning through the passage. Thus, shaping (contouring) of the entire endwall has emerged as a popular tool to suppress the development of the passage vortex throughout the passage.

Endwall contouring can generally be classified into two types: axisymmetric or non-axisymmetric. In the former type, the endwall height varies with axial location along the turbine passage, but remains consistent in the circumferential direction at a given axial location. Axisymmetric contouring is typically applied to the first stage nozzle, where the flow area reduces from the combustor to the turbine. Flow acceleration due to the contouring helps to suppress secondary flows and reduce losses, as found by Boletis [22] and Morris and Hoare [23].

Non-axisymmetric contouring is fully three-dimensional, and is the focus of this work. Peaks and valleys in the endwall locally decrease or increase the static pressure, respectively, which can reduce the pressure gradient between adjacent airfoils that strengthens secondary flows. Generally the freestream flow is unaffected by non-axisymmetric endwall contouring, and only the secondary flows are influenced. Knezevici, et al. [24] documented a weaker passage vortex and lower secondary flow aerodynamic losses with endwall contouring but no change in the midspan flow angle or airfoil profile loss. However, few studies have considered the effect of non-axisymmetric contouring on endwall heat transfer and film cooling effectiveness, and no studies have examined the interaction of contouring with realistic turbine features that are present in an engine.

The design of the three-dimensional endwall surface has generally been performed through the use of an optimization routine coupled to three-dimensional Reynolds-Averaged Navier Stokes (RANS) simulations. Experimental validations of the resulting shapes have demonstrated reductions in the strength of secondary flows, but the predictions rarely capture all of the improvements demonstrated by experiments. An example of this is the measured

improvement of 30% in net secondary losses in the study of Hartland, et al. [25], which was significantly underpredicted by Harvey, et al. [26]. Although it is unclear exactly which modeling assumptions are responsible for the mispredictions, it is certainly true that the effect of secondary flows on loss generation and endwall boundary layer distortion are not fully understood. Further advances in secondary loss mitigation will require improved models based on high-fidelity measurements near the endwall.

A significant gap in the current understanding of non-axisymmetric contouring is its sensitivity to other endwall features that can be present in an engine. Manufacturing, assembly, and stationary-rotating clearance constraints result in leakage interfaces between turbine components. The geometric configuration of the leakage interface can influence the separation of the endwall boundary layer and the development of the passage vortex. Furthermore, coolant that is ejected from the interface can interact with the secondary flows in a positive or negative manner, depending on the location and manner of injection.

One necessary leakage interface is between the stationary and rotating components of the engine. A common method of limiting hot gas ingestion into the gap between the stator and rotor is to design a backward-facing overlap in the endwalls, known as a rim seal. High-pressure compressor discharge flow is designed to exhaust through the rim seal as an additional guard against hot gas ingestion. The leakage air can develop a significant circumferential (swirl) velocity due to viscous drag on the rotor wheel, or due to the manner of its injection below the rim seal. Reid, et al. [27] found that turbine stage efficiency decreased as the circumferential velocity of upstream leakage flow was increased, and Popovic and Hodson [28] showed leakage coolant pushed toward the suction side of the passage at high leakage swirl velocities. Flow separation and reattachment around the overlap can influence the development of the passage vortex. de la Rosa Blanco, et al. [29] determined that the passage vortex was shifted upstream for flow over a backward-facing step located upstream of a turbine cascade, which reduced the interaction of the secondary flows with a pressure-side separation bubble and resulted in lower losses than a flat endwall. In contrast, Abo El Ella, et al. [30] found that losses increased for an endwall with an upstream backward-facing cavity due to a separation bubble in the cavity that strengthened the passage vortex. While the effects of an upstream overlap and leakage flow might not be completely understood, it is clear that they can significantly affect the passage

vortex. However, no studies have been performed to assess the interaction with non-axisymmetric endwall contouring.

A gap in the rotor endwall is present between airfoils that are assembled individually on the wheel of a turbine blade section, which is commonly referred to as a platform gap. The platform gap extends through the passage and thus is subject to a large pressure differential between its upstream and downstream sections. The pressure difference influences the uniformity of the leakage flow exiting the gap, whereby most of the flow exits at the low-pressure region around the minimum flow area (throat) of the rotor passage. This flow can disturb the progression of the passage vortex, and the discontinuity in the endwall resulting from the gap can act as a trip to locally enhance endwall heat transfer. Both Piggush and Simon [31] and Lynch and Thole [32] showed high heat transfer coefficients near the throat of the passage where the gap leakage flow is ejected, and Cardwell, et al. [33] reported significant reductions in adiabatic film effectiveness due to ingestion of coolant into the gap in the forward portion of the passage. Hada and Thole [34] indicated disruption of the passage vortex for an endwall with a platform gap due to ejected flow from the gap, and Reid, et al. [35] reported reduced stage efficiency when the gap was considered. Again, this leakage feature is known to have an impact on secondary flow but no studies have yet considered how an endwall contour design might behave when combined with a platform gap.

Methodology

Several areas noted above have not received adequate research to address the unknowns including the details of the highly-skewed endwall boundary layer in a turbine passage, the effects of contouring on the boundary layer and the associated heat transfer, and the sensitivity of contouring to leakage features. The intent of this dissertation was to use those research avenues to advance the understanding of endwall secondary flows. In particular, the following questions were addressed:

1. What is the effect of non-axisymmetric endwall contouring on the mean and turbulent flowfield in an airfoil passage, and what are the mechanisms by which it increases or reduces endwall heat transfer?

2. How effective is non-axisymmetric contouring when combined with endwall leakage features, and how is the secondary flow physics altered?

These questions were addressed through a variety of studies for an endwall with and without non-axisymmetric endwall contouring. The contouring provides a means of perturbing the endwall secondary flow without influencing the primary inviscid flow. Several studies (Hartland, et al. [25], Knezevici, et al. [24], Torre, et al. [36]) have shown that contouring reduces secondary kinetic energy and total pressure loss associated with secondary flows, but how contouring alters endwall heat transfer coefficients is not clear. Saha and Acharya [37] predicted significant reductions primarily at the throat, but Mahmood and Acharya [38] measured small reductions around the suction side horseshoe vortex and passage vortex. Furthermore, no studies have measured mean and turbulent statistics for the three-dimensional endwall boundary layer in a turbine cascade, which would provide insight into the mechanisms of heat transfer augmentation or reduction. In order to provide those measurements, a cascade was designed for non-intrusive measurements of heat transfer and endwall boundary layers with and without contouring. For initial studies, no leakage features were considered in order to more clearly identify flow physics associated with non-axisymmetric contouring.

A low-pressure turbine airfoil geometry supplied by an industrial sponsor, and studied in detail by Knezevici, et al. [24], was selected for the cascade. Although the thermal environment of a low-pressure turbine is not as critical as for a high-pressure turbine, the fundamental secondary flow physics are similar. Advantages of the airfoil selected were the availability of measurements to compare against, and the thin profile of the blade which allowed for a high level of optical access in the passage. Infrared thermography was used to acquire endwall heat transfer and film effectiveness measurements, and a three-component laser Doppler velocimeter was used to acquire endwall mean and turbulent flowfields. Complementary measurements of endwall shear stress at selected locations were obtained by the oil film interferometry technique in order to more fully characterize the endwall boundary layer.

A supplemental computational study was performed due to the importance of computational fluid dynamics simulations in the design of endwall contours, and also to help guide the selection of experimental measurement locations toward interesting regions of the endwall. The focus of the computational study was to assess the capability of steady RANS to

accurately predict the endwall heat transfer measurements acquired earlier, as well as aerodynamic loss measured by Knezevici, et al. [24]. Both metrics are important design parameters for engine components but are generally the most difficult to accurately capture. The variation in solution accuracy for two popular turbulence closure models was also investigated to provide some insight into the strengths and weaknesses of the models.

The effect of leakage features and their interaction with endwall contouring was considered in a separate cascade containing a high-pressure turbine airfoil geometry. Cooling provided by flow from leakage features is more critical in the high-temperature environment of a high-pressure turbine blade, and blade loading is high which results in strong secondary flows. This was desirable so that the secondary flows would strongly interact with the leakage features. The representative features modeled in the cascade included a rim seal overlap geometry upstream, and a platform gap through the passage.

The rim seal had an overlapping configuration that formed a backward-facing step upstream of the cascade. The endwall downstream of the step smoothly merged back to the upstream endwall level, such that a cavity was present at the backward-facing step. The cavity provided a means of perturbing the horseshoe vortex by promoting boundary layer separation. The introduction of swirled or unswirled leakage flow through the rim seal was also employed to perturb the horseshoe vortex. Although the aerodynamics of the rim seal and swirled leakage flow have been studied, very little is known about the associated heat transfer, so measurements of endwall heat transfer, film effectiveness, and aerodynamic loss were obtained for a variety of leakage flow conditions. The goal of those studies was to first understand the significance of the rim seal geometry and swirled leakage flow on endwall secondary flow, and then assess whether a non-axisymmetric contour would have an influence above and beyond that of the rim seal alone.

The other endwall leakage feature considered was a platform gap through the passage. The aforementioned studies by Lynch and Thole [32], Reid, et al. [35], and others have indicated that the platform gap dramatically increases heat transfer and aerodynamic loss relative to a continuous endwall due to the ejection mechanism of the gap flow, and it is unclear if a non-axisymmetric contour can provide a significant benefit. Measurements of loss, heat transfer, and film effectiveness were obtained in the high-pressure turbine cascade for various leakage flowrates. Also, the configuration of the gap allowed the ability to vertically misalign the

endwalls of adjacent blades, as might occur in an engine due to differential thermal expansion or installation tolerances. The creation of forward- or backward-facing steps due to the misalignment could act to locally trip the flow and further augment endwall heat transfer, as indicated by Piggush and Simon [39]. How this effect ranks relative to other effects was considered through measurements of endwall heat transfer and film cooling.

The work presented in this dissertation is unique in several aspects: 1) it presents some of the first detailed measurements of heat transfer with endwall contouring; 2) it provides some of the first global flowfield data in the forward portion of the cascade where the passage vortex develops; 3) it presents the only known three-component measurements of the mean and fluctuating velocities in the endwall boundary layer in a turbine cascade; and 4) it presents one of the first studies to consider turbine leakage features in combination with non-axisymmetric endwall contouring.

Summary of Findings

The initial thrust of the work was to characterize the secondary flow physics for an endwall without leakage features. A flat endwall was studied to provide a baseline for determining the effects of non-axisymmetric contouring, but also to advance the understanding of the three-dimensional boundary layer in a turbine passage. Measurements of the turbulent boundary layer entering the cascade showed acceleration and development of significant skew as the flow was turned toward the suction side of the passage, which correlated with reduced endwall heat transfer compared to a two-dimensional zero-pressure-gradient boundary layer. Further into the passage, however, the development of the passage vortex promoted downwash of fluid near the blade pressure side and high turbulence levels, which resulted in high heat transfer there. The passage vortex also caused high levels of skew in the endwall boundary layer, where in some locations the wall shear direction was turned by more than 70 degrees relative to the local freestream direction.

Given the significance of the passage vortex on the endwall boundary layer, it was appropriate to apply non-axisymmetric endwall contouring to perturb it. Oil flow visualization of the endwall flow pattern indicated displacement of the horseshoe vortex upstream of the cascade compared to the flat endwall but elimination of the strong sweeping effect of the passage vortex in the passage. The displacement of the horseshoe vortex by the contour caused the turbulent

boundary layer approaching the forward suction side of the passage to be further accelerated and skewed, and heat transfer further reduced, compared to the flat endwall. However, the displacement also increased heat transfer near the saddle point since the roll-up of the horseshoe vortex occurred further upstream.

The most significant benefit of the contour occurred in the passage, where the oil flow visualization indicated reduced passage vortex influence on the endwall. Near the origin of the passage vortex in the forward portion of the passage, near-wall turbulence levels and endwall heat transfer were slightly higher with contouring but the size of the vortex was reduced, compared to a flat endwall. As the passage vortex was convected downstream, its development was further suppressed and endwall heat transfer levels were significantly reduced, compared to the flat endwall. Secondary kinetic energy and turbulent kinetic energy, both of which contribute to aerodynamic loss generation, were reduced at the exit of the cascade with the application of contouring.

Overall, non-axisymmetric contouring acted to shift the horseshoe vortex away from the passage vortex and delay the development of the passage vortex. The resulting smaller passage vortex had a reduced influence on the endwall boundary layer and lower levels of heat transfer, compared to a flat endwall.

It was uncertain, however, if the same physics would occur in the presence of realistic turbine leakage features. To address this, a rim seal with an upstream cavity and swirled leakage flow was studied to understand its effect on the development of the horseshoe vortex, and to probe the sensitivity of endwall contouring to horseshoe vortex development. The upstream cavity promoted early separation of the incoming boundary layer and low heat transfer levels upstream of the cascade. The horseshoe vortex saddle point was positioned quite far away from the blade leading edge, toward the adjacent blade suction side. This reduced the distance that the passage vortex was convected through the passage before encountering the adjacent airfoil suction side. The large amount of separated flow from the upstream cavity resulted in a strong passage vortex, which when coupled with the short distance to the adjacent blade, limited the impact that endwall contouring could provide. Aerodynamic loss measurements indicated no significant improvement for the contour studied.

Swirled leakage from the rim seal was also employed to perturb the horseshoe vortex. The saddle point was shifted in the direction of the swirl, which increased both the endwall heat

transfer on the upstream platform and the aerodynamic loss across the cascade, relative to unswirled leakage. The contour exhibited a negative sensitivity to leakage swirl condition, whereby the off-design condition of no upstream swirl resulted in slightly higher aerodynamic loss relative to a flat endwall with the same upstream conditions.

The other realistic feature studied was the platform gap, which was a means of perturbing the passage vortex. Endwall heat transfer and aerodynamic loss were both significantly increased by leakage from the platform gap, although high levels of coolant effectiveness resulted in reduced net heat flux to the endwall. Misalignment of adjacent gaps was not as significant as net leakage flowrate from the gap. Given the lack of improvement in aerodynamic loss over a flat endwall, and the fact that it was not designed around a platform gap, it is unlikely that the contour studied would reduce the detrimental effects of the platform gap on the endwall heat transfer.

Of the two types of realistic leakage features examined, the platform gap had the most significant effect on endwall heat transfer and aerodynamic loss. The contour studied was less effective when used in combination with realistic leakage interfaces, which emphasizes that careful consideration of the total environment of a turbine blade is critically important for improved efficiency and durability goals. Future improvements in part performance will depend on methodologies that incorporate what used to be considered secondary effects.

Outline of Document

The following document has been prepared in manuscript format, whereby several papers are used to report the overall results of the dissertation. Papers 1-3 present the methodology and results of the initial studies of non-axisymmetric endwall contouring without the effects of leakage interfaces. In Paper 1, extensive benchmarking is described for the low-pressure turbine cascade, and the effect of non-axisymmetric contouring on endwall heat transfer is examined. Paper 1 was presented at the 2009 IGTI Turbo Expo, and has been published in the *Journal of Turbomachinery*. Paper 2 includes measurements of endwall film effectiveness with and without contouring, and examines the current capability of RANS-based predictions (similar to those used to design the contour) to capture the flow physics through comparison to the measured endwall heat transfer. Paper 2 was presented at the 2010 IGTI Turbo Expo and was also published in the *Journal of Turbomachinery*. Paper 3 documents three-component measurements

of the flowfield and endwall boundary layer obtained at selected locations in the cascade with a laser Doppler velocimeter. The results of that study provide information on the mean and turbulent flow features that affect momentum and heat transport in the three-dimensional endwall boundary layer. Paper 3 will be submitted to the *International Journal of Heat and Mass Transfer*. Overall conclusions from Papers 1-3 are that the contour increases heat transfer in the forward portion of the passage relative to a flat endwall due to increased streamwise flow acceleration and displacement of the horseshoe vortex system, but decreases heat transfer in the more critical region of high heat transfer in the aft portion of the passage due to reduced passage vortex strength.

The last three papers report the effects of leakage interfaces on the endwall secondary flow. A preliminary study of the stator-rotor leakage feature was performed to understand its effect without the influence of non-axisymmetric contouring. In Paper 4, the rim seal with a flat endwall is modeled in the high-pressure turbine cascade. The effect of the endwall overlap geometry and swirled leakage flow is examined through oil flow visualization and measurements of endwall heat transfer. Paper 5 discusses the effect of non-axisymmetric endwall contouring in combination with the rim seal by comparing total pressure loss measurements obtained downstream of the cascade for the flat versus contoured endwalls. In addition, the effect of a platform gap with leakage flow is considered for the contoured endwall. Paper 6 focuses on the effect of the platform gap flow with regards to endwall heat transfer and film cooling for the contoured endwall. Papers 4-6 will be submitted to the *Journal of Turbomachinery*. Major conclusions from the leakage feature-endwall contouring interaction work were that the overlap geometry and swirled leakage from the rim seal strengthen and reposition the horseshoe vortex, which can decrease the effectiveness of the endwall contouring. Also, leakage from the platform gap had the most significant role in increasing endwall heat transfer and aerodynamic loss due to its interaction with the secondary flow.

An overview of the major results and conclusions of the study, as well as recommendations for future work, are presented at the end of this document. Also included are appendices documenting the three-component velocity transformations, measurement uncertainty analysis, the design and construction of the flat and contoured endwalls, and comparisons of computational predictions using the SST k-ω model to the measurements in Paper 3.

References

[1] Langston, L. S., 1980, "Crossflows in a Turbine Cascade Passage," *J. Eng. Power*, **102**, pp. 866-874.

[2] Denton, J. D., 1993, "The 1993 IGTI Scholar Lecture: Loss Mechanisms in Turbomachines," *J. Turbomach.*, **115**(4), pp. 621-656.

[3] Han, J. C., Dutta, S., and Ekkad, S., 2000, "Gas Turbine Heat Transfer and Cooling Technology," Taylor & Francis, New York, NY, USA.

[4] Kang, M. B., and Thole, K. A., 2000, "Flowfield Measurements in the Endwall Region of a Stator Vane," *J. Turbomach.*, **122**(3), pp. 458-466.

[5] Blair, M. F., 1974, "An Experimental Study of Heat Transfer and Film Cooling on Large-Scale Turbine Endwalls," *J. Heat Transfer*, **November 1974**, pp. 524-529.

[6] Knost, D. G., and Thole, K. A., 2005, "Adiabatic Effectiveness Measurements of Endwall Film-Cooling for a First Stage Vane," *J. Turbomach.*, **127**(2), pp. 297-305.

[7] Devenport, W. J., Agarwal, N. K., Dewitz, M. B., Simpson, R. L., and Poddar, K., 1990, "Effects of a Fillet on the Flow Past a Wing-Body Junction," *AIAA J.*, **28**(12), pp. 2017-2024.

[8] Praisner, T. J., and Smith, C. R., 2006, "The Dynamics of the Horseshoe Vortex and Associated Endwall Heat Transfer---Part I: Temporal Behavior," *J. Turbomach.*, **128**(4), pp. 747-754.

[9] Radomsky, R. W., and Thole, K. A., 2000, "High Free-Steam Turbulence Effects on Endwall Heat Transfer for a Gas Turbine Stator Vane," *J. Turbomach.*, **122**(4), pp. 699-708.

[10] Thrift, A. A., Thole, K. A., and Hada, S., 2011, "Effects of an Axisymmetric Contoured Endwall on a Nozzle Guide Vane: Convective Heat Transfer Measurements," *J. Turbomach.*, **133**(4), pp. 041008-041010.

[11] Anderson, S. D., and Eaton, J. K., 1989, "Reynolds Stress Development in Pressure-Driven Three-Dimensional Turbulent Boundary Layers," *J. Fluid Mech.*, **202**, pp. 263-294.

[12] Olcmen, M. S., and Simpson, R. L., 1995, "An Experimental Study of a Three-Dimensional Pressure-Driven Turbulent Boundary Layer," *J. Fluid Mech.*, **290**, pp. 225-262.

[13] Abrahamson, S. D., and Eaton, J. K., 1991, "Heat Transfer through a Pressure-Driven Three-Dimensional Boundary Layer," *J. Heat Transfer*, **113**(2), pp. 355-362.

[14] Lewis, D. J., and Simpson, R. L., 1998, "Turbulence Structure of Heat Transfer through a Three-Dimensional Turbulent Boundary Layer," *J. Thermophys. Heat Transfer*, **12**(2), pp. 248-255.

[15] Langston, L. S., Nice, M. L., and Hooper, R. M., 1977, "Three-Dimensional Flow within a Turbine Cascade Passage," *J. Eng. Power*, **99**, pp. 21-28.

[16] Harrison, S., 1990, "Secondary Loss Generation in a Linear Cascade of High-Turning Turbine Blades," *J. Turbomach.*, **112**(4), pp. 618-624.

[17] Vera, M., Blanco, E. d. l. R., Hodson, H., and Vazquez, R., 2009, "Endwall Boundary Layer Development in an Engine Representative Four-Stage Low Pressure Turbine Rig," *J. Turbomach.*, **131**(1), p. 011017.

[18] Zess, G. A., and Thole, K. A., 2002, "Computational Design and Experimental Evaluation of Using a Leading Edge Fillet on a Gas Turbine Vane," *J. Turbomach.*, **124**(2), pp. 167-175.

[19] Becz, S., Majewski, M. S., and Langston, L. S., "An Experimental Investigation of Contoured Leading Edges for Secondary Flow Loss Reduction," Proc. ASME Turbo Expo 2004, Paper No. GT2004-53964.

[20] Sauer, H., Muller, R., and Vogeler, K., 2001, "Reduction of Secondary Flow Losses in Turbine Cascades by Leading Edge Modifications at the Endwall," *J. Turbomach.*, **123**(2), pp. 207-213.

[21] Sieverding, C. H., 1985, "Recent Progress in the Understanding of Basic Aspects of Secondary Flows in Turbine Blade Passages," *J. Eng. Gas Turbines Power*, **107**(2), pp. 248-257.

[22] Boletis, E., 1985, "Effects of Tip Endwall Contouring on the Three-Dimensional Flow Field in an Annular Turbine Nozzle Guide Vane: Part 1---Experimental Investigation," *J. Eng. Gas Turbines Power*, **107**(4), pp. 983-990.

[23] Morris, A. W. H., and Hoare, R. G., "Secondary Loss Measurements in a Cascade of Turbine Blades with Meridional Wall Profiling," Proc. ASME Winter Annual Meeting 1975, Paper No. 75-WA/GT-13.

[24] Knezevici, D. C., Sjolander, S. A., Praisner, T. J., Allen-Bradley, E., and Grover, E. A., 2010, "Measurements of Secondary Losses in a Turbine Cascade with the Implementation of Nonaxisymmetric Endwall Contouring," *J. Turbomach.*, **132**(1), p. 011013.

[25] Hartland, J. C., Gregory-Smith, D. G., Harvey, N. W., and Rose, M. G., 2000, "Nonaxisymmetric Turbine End Wall Design: Part Ii---Experimental Validation," *J. Turbomach.*, **122**(2), pp. 286-293.

[26] Harvey, N. W., Rose, M. G., Taylor, M. D., Shahpar, S., Hartland, J., and Gregory-Smith, D. G., 2000, "Nonaxisymmetric Turbine End Wall Design: Part I--- Three-Dimensional Linear Design System," *J. Turbomach.*, **122**(2), pp. 278-285.

[27] Reid, K., Denton, J. D., Pullan, G., Curtis, E., and Longley, J., "The Effect of Stator-Rotor Hub Sealing Flow on the Mainstream Aerodynamics of a Turbine," Proc. ASME Turbo Expo 2006, Paper No. GT2006-90838.

[28] Popovic, I., and Hodson, H. P., "Aerothermal Impact of the Interaction between Hub Leakage and Mainstream Flows in Highly-Loaded Hp Turbine Blades," Proc. ASME Turbo Expo 2010, Paper No. GT2010-22311.

[29] de la Rosa Blanco, E., Hodson, H. P., and Vazquez, R., "Effect of Upstream Platform Geometry on the Endwall Flows of a Turbine Cascade," Proc. ASME Turbo Expo 2005, Paper No. GT2005-68938.

[30] Abo El Ella, H. M., Sjolander, S. A., and Praisner, T. J., "Effects of an Upstream Cavity on the Secondary Flow in a Transonic Turbine Cascade," Proc. ASME Turbo Expo 2010, Paper No. GT2010-22843.

[31] Piggush, J., and Simon, T. W., "Flow Measurements in a First Stage Nozzle Cascade Having Leakage and Assembly Features: Effects of Endwall Steps and Leakage on Aerodynamic Losses," Proc. ASME International Mechanical Engineering Congress and Expo, Paper No. IMECE2005-83032.

[32] Lynch, S. P., and Thole, K. A., 2011, "The Effect of the Combustor-Turbine Slot and Midpassage Gap on Vane Endwall Heat Transfer," *J. Turbomach.*, **133**(4), pp. 041002-041009.

[33] Cardwell, N. D., Sundaram, N., and Thole, K. A., 2006, "Effect of Midpassage Gap, Endwall Misalignment, and Roughness on Endwall Film-Cooling," *J. Turbomach.*, **128**(1), pp. 62-70.

[34] Hada, S., and Thole, K. A., 2011, "Computational Study of a Midpassage Gap and Upstream Slot on Vane Endwall Film-Cooling," *J. Turbomach.*, **133**(1), pp. 011024-011029.

[35] Reid, K., Denton, J., Pullan, G., Curtis, E., and Longley, J., 2007, "The Interaction of Turbine Inter-Platform Leakage Flow with the Mainstream Flow," *J. Turbomach.*, **129**(2), pp. 303-310.

[36] Torre, D., Vazquez, R., Blanco, E. d. l. R., and Hodson, H. P., 2011, "A New Alternative for Reduction in Secondary Flows in Low Pressure Turbines," *J. Turbomach.*, **133**(1), pp. 011029-011010.

[37] Saha, A. K., and Acharya, S., 2008, "Computations of Turbulent Flow and Heat Transfer through a Three-Dimensional Nonaxisymmetric Blade Passage," *J. Turbomach.*, **130**(3), p. 031008.

[38] Mahmood, G. I., and Acharya, S., "Measured Endwall Flow and Passage Heat Transfer in a Linear Blade Passage with Endwall and Leading Edge Modifications," Proc. ASME Turbo Expo 2007, Paper No. GT2007-28179.

[39] Piggush, J. D., and Simon, T. W., 2007, "Heat Transfer Measurements in a First-Stage Nozzle Cascade Having Endwall Contouring: Misalignment and Leakage Studies," *J. Turbomach.*, **129**(4), pp. 782-790.

Paper 1: Heat Transfer for a Turbine Blade with Non-Axisymmetric Endwall Contouring

Published in the *Journal of Turbomachinery**:

Lynch, S. P., Sundaram, N., Thole, K. A., Kohli, A. and Lehane, C., 2011, "Heat Transfer for a Turbine Blade with Non-Axisymmetric Endwall Contouring," *J. of Turbomachinery*, Vol. 133, pp. 011019-1-9. Used with permission of ASME, 2011.

Abstract

Complex vortical secondary flows that are present near the endwall of an axial gas turbine blade are responsible for high heat transfer rates and high aerodynamic losses. The application of non-axisymmetric, three-dimensional contouring to the endwall surface has been shown to reduce the strength of the vortical flows and decrease total pressure losses when compared to a flat endwall. The reduction of secondary flow strength with non-axisymmetric contouring might also be expected to reduce endwall heat transfer.

In this study, measurements of endwall heat transfer were taken for a low-pressure turbine blade geometry with both flat and three-dimensional contoured endwalls. Endwall oil flow visualization indicated a reduction in the passage vortex strength for the contoured endwall geometry. Heat transfer levels were reduced by 20 percent in regions of high heat transfer with the contoured endwall, as compared to the flat endwall. The heat transfer benefit of the endwall contour was not affected by changes in the cascade Reynolds number.

*Co-authors: Dr. Karen A. Thole, Mechanical & Nuclear Engineering Department, Penn State
Dr. Narayan Sundaram, Mechanical & Nuclear Engineering Department, Penn State
Dr. Atul Kohli, United Technologies--Pratt & Whitney
Dr. Christopher Lehane, United Technologies--Pratt & Whitney

Introduction

A fundamental issue in the design of gas turbine engines is the detrimental effects of vortical flows that are present near the junction of the airfoil and its endwall. These flows, generally termed secondary flows, increase aerodynamic losses through the turbine, leading to lower overall engine efficiency. Furthermore, the vortical flows result in high heat transfer rates due to mean flow distortion and high turbulence levels. For highly loaded parts such as the low-pressure turbine blade in this study, part durability can be significantly impacted by high heat transfer. It is obvious that reducing or eliminating the effects of the secondary flows would result in appreciable benefits in an engine, and thus much research has been conducted to understand these flows and control them.

Past research has shown that three-dimensional modifications to the endwall surface, generally referred to as non-axisymmetric contouring, are an effective method of reducing or eliminating secondary flows. Peaks and valleys in the endwall locally decrease or increase the static pressure, respectively, which can reduce the pressure gradient between adjacent airfoils that strengthens secondary flows. Weaker secondary flows result in lower aerodynamic losses, as has been documented by many researchers. However, few studies have considered the effect of non-axisymmetric contouring on endwall heat transfer, and thus the overall benefit of contouring in an engine is not completely understood as of yet.

This paper discusses the effect of non-axisymmetric contouring on the endwall heat transfer for a low-pressure turbine blade. The effect of varying the cascade Reynolds number for both the flat and contoured endwalls is also considered.

Relevant Past Studies

Given our current understanding of secondary flow (e.g., the endwall flow models of Langston [1], Sharma and Butler [2], and Goldstein and Spores [3]), attempts to eliminate such flow have focused on influencing the horseshoe vortex and/or the passage vortex development. Manipulation of the endwall-airfoil geometry has shown the most promise in this area, and can be loosely categorized into modifications of the airfoil leading edge (not addressed here), and modifications to the entire passage endwall.

Endwall-airfoil geometry can be altered to reduce secondary flows through the use of a contour. This category might be further subdivided into axisymmetric contouring (contour shape is only a function of axial coordinate), and non-axisymmetric contouring (contour shape is three-dimensional). Although axisymmetric contouring has been successful at reducing exit losses and surface heat transfer (e.g., see Boletis [4], Morris and Hoare [5], and Lin and Shih [6]), it has generally only been applied to stator vanes and is not considered further here.

Non-axisymmetric contouring has also demonstrated significant improvements in turbine performance, and is the focus of this study. A computational optimization study by Harvey, et al. [7] produced a three-dimensional blade endwall contour intended to minimize exit flow angle deviations and pitchwise static pressure gradients. The optimum design had convex endwall curvature near the pressure side and concave curvature at the suction side in the front of the passage to reduce cross-passage pressure gradients, while convex curvature near the trailing edge suction side reduced exit flow angle deviation. Unfortunately, it was also noted that a strong corner vortex developed near the suction side trailing edge. Experimental validation by Hartland, et al. [8] confirmed the general conclusions of Harvey, et al. [7], and found that net secondary losses decreased by 30% for the contoured wall relative to a flat wall. Brennan, et al. [9] and Rose, et al. [10] used the design method of Harvey, et al. [7] on a Trent 500 high-pressure turbine stage and demonstrated 0.59% stage efficiency improvement. Recently, Germain, et al. [11] and Schuepbach, et al. [12] examined the effect of non-axisymmetric contouring of the stator and rotor endwalls in a 1-1/2 stage turbine. Overall stage efficiency was improved by 1.0%±0.4%, which was largely attributed to reductions in the stator time-averaged and unsteady losses.

Saha and Acharya [13] presented the first known study to consider the effect of non-axisymmetric contouring on the endwall heat transfer for a high-pressure turbine blade. They computationally evaluated nine endwall shapes and found that the best design reduced overall heat transfer by 8%, with significant reductions of over 300% near the suction side leading edge and approximately 20% in the throat compared to a flat endwall. Gustafson, et al. [14] reported aerodynamic measurements for the same airfoil and contoured endwall. They found a stronger suction side horseshoe vortex and a weaker passage vortex, which resulted in a measured overall loss reduction of 50% relative to a flat endwall. However, their smoke flow visualization (at a lower cascade Reynolds number) indicated that the saddle point moved farther from the blade leading edge for the contour, in contradiction to the conclusions of Saha and Acharya [13].

Furthermore, Saha and Acharya's results did not indicate a stronger suction side horseshoe vortex.

Praisner, et al. [15] and Knezevici, et al. [16] examined non-axisymmetric contouring for the same low-pressure turbine blade as in this study. Praisner, et al. [15] used computational optimization based on secondary loss reduction to design non-axisymmetric endwall contours for the Pack-B airfoil, as well as for a related family of high-lift airfoils (Pack-D fore- and aft-loaded). The Pack-B endwall contour reduced losses (4% predicted, 10% measured) and turbulent kinetic energy levels associated with the secondary flow, when compared to the flat endwall. Knezevici, et al. [16] presented oil flow visualization and seven-hole probe measurements that showed a reduction in passage vortex strength with the contour, although the corner vortex and near-wall passage crossflow were intensified near the trailing edge where the contour merged back to the flat endwall level.

The study reported in this paper expands on the work of Praisner, et al. [15] and Knezevici, et al. [16] by considering the effect of non-axisymmetric contouring on endwall heat transfer for the same low-pressure turbine blade. Although the heat loads for low-pressure turbine blades are not as critical as for high-pressure turbine blades, part durability is still a design consideration, especially given the trend of highly loading the low-pressure turbine to lower airfoil count (Praisner, et al. [17]). Also considered in this study is the effect of cascade Reynolds number on the endwall heat transfer for the flat and contoured geometries.

Experimental Methodology

Endwall heat transfer measurements, with and without a three-dimensional contoured endwall, were obtained in a newly constructed test section containing seven scaled-up turbine blades based on the low-pressure turbine Pack-B airfoil geometry. Flow through the test section was supplied by a large-scale low-speed wind tunnel, depicted in Figure 1.1a. For this tunnel, the large scale allows engine Reynolds numbers to be matched, and provides for high resolution measurements. Flow through the tunnel's closed loop was powered by an axial fan, was cooled by a heat exchanger, and then passed through a series of flow conditioning screens before entering the convergence section.

The convergence, shown in Figure 1.1b, was designed to reduce the flow area from 1.11 m^2 to 0.62 m^2 by symmetric quarter-round sections on the top and bottom walls, and was located

nearly 11 axial chords upstream of the center blade. An analysis of the variation in boundary layer thickness in the pitch direction across the blade cascade, which was angled to match the blade inlet flow angle, indicated that δ/S would vary ±11% relative to the boundary layer approaching the center blade. Details of the measured boundary layer are presented later.

Immediately downstream of the convergence, a passive bar grid was mounted in the flowpath. The grid consisted of 2.54 cm square bars, separated by 10.2 cm from center to center. The grid bar width, spacing, and location upstream of the cascade were designed using the results of Baines and Peterson [18] to achieve a freestream turbulence level of approximately 4% at the inlet plane of the blade cascade. A prediction of the turbulence intensity across the blade inlet plane in the pitch direction indicated that the turbulence intensity would range from 3.9% at the blade farthest downstream of the grid, to 4.8% at the blade closest to the grid. Measurements of the turbulence decay downstream of the grid are presented later.

As mentioned previously, a new test section was constructed to house seven blades, based on the Pack-B airfoil geometry and scaled to 8.6 times engine scale. The blade geometry and nominal flow conditions are given in Table 1.1. The Pack-B blade was designed for studies of low-pressure turbine aerodynamics in low-speed cascades. It is a highly-loaded blade (Zweifel coefficient of 1.13), and its aerodynamic characteristics have been reported extensively in the literature (Praisner, et al. [15], Knezevici, et al. [16], Praisner, et al. [17], Lake, et al. [19], Murawski and Vafai [20], Mahallati, et al. [21], Zoric, et al. [22], Popovic, et al. [23]). Figure 1.2a shows a top view of the cascade, which had adjustable bleed flaps on the sides of the lower blade (blade 1) and upper blade (blade 7) to control the uniformity of the velocity entering the cascade. Tailboards attached to the trailing edges of blades 1 and 7 also controlled the flow through the cascade to achieve periodicity. The blades were constructed by stereolithography with static pressure taps at the blade midspan incorporated into the stereolithography design.

Two types of endwalls were applied to the bottom wall of the blade cascade: a baseline flat endwall, and a three-dimensional non-axisymmetric contour. The top endwall remained flat for all studies. The design of the contour shape, depicted in Figure 1.2b, is described in further detail in Praisner, et al. [15] and Knezevici, et al. [16]. The contour generally consisted of a depression near the suction side and a peak near the pressure side in the forward portion of the passage, as well as a ridge running from the pressure side to the suction side through the aft portion of the passage. The highest point on the contour was approximately $0.06C_{ax}$ above the

flat endwall height, while the lowest point on the contour was approximately $0.04C_{ax}$ below the flat endwall. The contouring was contained between the inlet and exit planes of the blade cascade, and merged smoothly to the level of the flat endwall in the regions outside of the blade passage.

Endwall Heat Transfer Measurements

Heat transfer coefficients were measured on both the flat and contoured endwalls by imaging surface temperatures on uniform heat flux plates. The heat flux plates, depicted in Figure 1.2a, were manufactured in three sections, where the center section around the blades could be removed to install the flat or the contoured endwalls. For both endwall types, the heat flux plates consisted of serpentine inconel circuits encapsulated in kapton for a total thickness of 75 μm, with a 37 μm copper layer adhered to the top surface to increase heat flux uniformity (Kang, et al. [24]). The copper was painted with flat black paint to increase emissivity for infrared camera measurements. Type-E thermocouples were adhered to the bottom side of the kapton heater with thermal cement. A conduction bias of 0.8°C between the bottom and top heater surface temperature measurements was accounted for by a one-dimensional calculation of the heater thermal resistance.

For the flat endwall, the kapton heater was attached to a 3.2 mm thick lexan sheet ($k\approx0.2$ W/m^2-K), below which was a 12.7 mm thick closed-cell polyurethane foam ($k\approx0.032$ W/m^2-K) and a 12.7 mm thick medium density fiberboard support ($k\approx0.12$ W/m^2-K). The conductive thermal resistance of the contoured endwall assembly was matched to that of the flat endwall.

Due to the non-developable nature of the contoured endwall surface, the heat flux plate design was non-trivial. The kapton heater was adhered uniformly by a vacuum bag process to a 3.2 mm thick stereolithography surface ($k\approx0.17$ W/m^2-K) in the shape of the contour, as shown in Figure 1.2c. A mold was used to create a polyurethane foam body attached to the underside of the heat flux plate, where the top surface of the foam had the same shape as the contour and the bottom surface was flat.

The input heat flux of 1000 W/m^2 was calculated by measuring the input power to the inconel circuit and dividing by the heater area. The convective heat flux was then determined by subtracting conduction and radiation losses. Conduction losses through the bottom wall were estimated by a one-dimensional calculation, and subsequently verified by thermocouple measurements, to be less than 2% of the input heat flux for both types of endwalls. Radiation

losses from the high-emissivity endwalls were estimated to be less than 18% of the input heat flux, assuming blackbody radiation exchange with isothermal surroundings at the freestream temperature. Both conduction and radiation loss corrections varied locally, with the highest corrections at the highest surface temperatures (nominally 44°C).

Surface temperatures on the bottom endwall were measured with an infrared camera by imaging the endwall from holes in the top endwall. These holes were covered during the test, and only opened to allow direct optical access when IR images were being acquired. Since the pressure differences between the inside and outside of the tunnel were very small, opening a hole in the top endwall did not affect the bottom endwall measurements, as determined by monitoring the endwall temperature before, during, and after image acquisition. The camera had a resolution of 1.4 pixels/mm, and a field of view of 320x240 pixels. Images were taken throughout the blade cascade to map the entire endwall, and assembled via an in-house computer code. At each image location, five images were taken and averaged, where each image was an average of 16 frames. Calibration of the images for emissivity and reflected temperature was performed by matching the image temperatures to the thermocouple readings. Typical values for emissivity and reflected temperature were ε=0.96 and T_{reflc}=10°C, which agreed well with the published value for flat black paint (ε=0.96), as well as the average measured freestream temperature ($T_{\infty,in}$=13°C). Calibrated infrared images generally agreed with the thermocouple measurements to within 0.3°C. No correction was performed for perspective distortion with the contoured endwall, since the moderate amount of three-dimensionality did not affect the camera focus.

Uncertainty in heat transfer measurements was estimated by the partial derivative method described by Moffat [25]. The largest source of uncertainty in the heat transfer was the measurement of surface temperature. The bias error was estimated to be 0.7°C and was driven by infrared camera bias and thermocouple bias. The precision error of 0.3°C was determined by taking the standard deviation of six sets of infrared images, where each set contained five images. With a confidence interval of 95%, the total error in heat transfer was estimated to be ∂Nu=4.0% at a low value of Nu=220, and ∂Nu=5.6% at a high value of Nu=358.

Cascade Inlet Conditions

The velocity boundary layer upstream of the cascade and the turbulence level produced by the grid were measured to benchmark the inlet conditions. The streamwise component of velocity was measured with a single-component backscatter laser Doppler velocimeter, with

velocity bias correction by residence time weighting. The red cross mark in Figure 1.2a indicates the location where the inlet boundary layer was measured, which was $2.85C_{ax}$ upstream of the center blade in the cascade. Boundary layer measurements were obtained with and without the turbulence grid installed, to ensure that the grid did not alter the flow unexpectedly. Figure 1.3 shows the streamwise component of velocity plotted in wall coordinates, which resembles a flat plate turbulent boundary layer. Note that the figure legend indicates the measured boundary layer thickness and freestream turbulence level. As expected, the addition of the turbulence grid results in a depressed wake region due to the higher freestream turbulence. Based on the measured boundary layer, a prediction of the boundary layer thickness at the blade inlet plane indicated that δ/S would be approximately 0.071. Refer to Table 1.2 for a summary of the measured inlet boundary layer parameters.

As shown in Figure 1.2a, the endwall heaters extended $3.32C_{ax}$ upstream of the blade cascade. This length was designed to minimize the unheated starting length effect on the measured endwall heat transfer. Figure 1.4 shows the development of the heat transfer coefficient along a line extending from the start of the heater to the leading edge of the center blade (see blue dashed line in Figure 1.2a). Underside-mounted thermocouples were used to determine the surface temperature near the start of the heater where optical access was not available, and IR thermography was used near the blade leading edge, along with the underside-mounted thermocouples. Both measurement methods agree well with each other where they overlap.

The measured Stanton numbers presented in Figure 1.4 were obtained with the turbulence grid installed. St values are slightly higher than the turbulent flat plate correlation of Kays and Crawford [26] with an unheated starting length. This is due to heat transfer augmentation by the high freestream turbulence, as noted by Thole and Bogard [27]. The increase in St for the IR thermography measurements at $Re_s>9x10^5$ is due to the effect of the horseshoe vortex augmenting endwall heat transfer in front of the blade leading edge.

To verify the turbulence grid design, the freestream turbulence level was measured along the centerline of the tunnel with a laser Doppler velocimeter, from 30 to 70 bar widths downstream of the grid ($7.10C_{ax}$ to $2.74C_{ax}$ upstream of the center blade). These measurements are shown in Figure 1.5, where the abscissa is the distance downstream of the grid normalized by the bar width. The measured turbulence decay followed the trend indicated by Baines and Peterson [18], and indicated a freestream turbulence level of 4% at the cascade inlet plane.

Results and Discussion

The uniformity and periodicity of the flow around the blades was benchmarked by comparing the measured static pressure on the blade surfaces at midspan to a computational prediction. Figure 1.6 shows the midspan blade static pressure, normalized as a pressure coefficient, for blades 2-7 in the cascade. Excellent agreement with the prediction, and good periodicity across the cascade, is seen from examination of the flat endwall results. The midspan pressure distribution with a contoured endwall is also plotted for the center blade (blade 4) in Figure 1.6. The large blade aspect ratio and the relatively modest contouring result in a similar blade midspan static pressure distribution when compared to the flat endwall.

Oil Flow Visualization

Oil flow visualization with a mixture of oil and black paint was performed for both endwalls to provide a qualitative understanding of the effects of the three-dimensional contouring on the endwall flow pattern. Visual interpretation of the paint streaks was used to draw streaklines to emphasize endwall flow patterns. In Figure 1.7a, the classic features of secondary flow are visible for the flat endwall. The saddle point region has an accumulation of paint and oil due to the separation of the inlet boundary layer as it rolls up into the horseshoe vortex in front of the leading edge of the blade. In the passage, a scoured region is seen where the passage vortex sweeps flow over the endwall from the pressure side to the suction side. Another scoured region attributed to a corner vortex is seen near the impingement location of the passage vortex on the blade suction side. The endwall streaklines near the pressure side-endwall corner tend to overturn toward the suction side, with respect to inviscid streamlines that would tend to follow the airfoil. This overturning is a result of the cross-passage pressure gradient acting on the new endwall boundary layer starting downstream of the inlet boundary layer separation.

The contoured endwall oil flow pattern in Figure 1.7b shows a remarkable difference in the passage when compared to the flat endwall (Figure 1.7a). The scoured region of the passage vortex is no longer apparent. Although it is less obvious, the saddle point region appears to have shifted slightly farther upstream, and the scoured region of the suction side corner vortex is closer to the leading edge of the blade, when compared to the flat endwall. In the passage, the overturning of the endwall streaklines near the pressure side appears to be reduced for the contoured endwall. However, further downstream the overturning is seen to increase, where the

endwall contour merges back to the flat endwall level. This trend was also noted by Knezevici, et al. [16], who attributed it to re-acceleration of the exit flow due to the lack of contouring downstream of the blade passage. Overall, the three-dimensional endwall contour has reduced the strength of the passage vortex and overturning of the near-wall flow in a large part of the passage, compared to a baseline flat endwall.

Endwall Heat Transfer

Flat endwall heat transfer results are presented in Figure 1.8 for the nominal cascade Reynolds number (Re_{exit}=200,000), where the heat transfer coefficients are non-dimensionalized as Nusselt numbers based on the blade axial chord. Good periodicity in the heat transfer measurements is seen by comparing the heat transfer patterns in each of the blade passages. The heat transfer contours in Figure 1.8 demonstrate the well-documented influence of secondary flows on endwall heat transfer. As the inlet boundary layer separates in front of the blade and is rolled up into the horseshoe vortex, the sweeping action of the vortex results in high heat transfer levels near the blade leading edge. The inlet boundary layer penetrates farther into the center of the passage, but is swept toward the suction side by the cross-passage pressure gradient. High heat transfer is seen near the junction of the blade pressure side and the endwall, where a new boundary layer starts downstream of the separation of the inlet boundary layer. The effect of the passage vortex impinging on the blade suction side-endwall corner, and the presence of the corner vortex indicated by the flow visualization results (Figure 1.7a), both result in high Nusselt numbers near the trailing edge suction side of the blade. The effect of the blade wake is visible as a spike of high heat transfer that persists far downstream of the blade trailing edge.

Quantitative evaluations of endwall heat transfer results were obtained by extracting Nu values along streamwise and pitchwise lines in the cascade. For the streamwise line plots, inviscid streamline paths were obtained from a FLUENT [28] prediction of the blade midspan flowfield. Streamlines were released $0.46C_{ax}$ upstream of the cascade from three pitchwise locations, so that the streamlines would pass through Y/P=0.25, 0.50 and 0.75 at the inlet plane of the cascade. These streamlines are denoted as 0.25P, 0.50P, and 0.75P, respectively. See the inset in Figure 1.9 for the paths of the streamlines superimposed on the flat endwall heat transfer contours. Extracted endwall results are presented as a function of the axial (X) coordinate of the streamline, normalized by the blade axial chord, so that X/C_{ax}=0 corresponds to the inlet plane of the cascade and X/C_{ax}=1 corresponds to the exit plane.

Nusselt numbers extracted from the contour plot of Figure 1.8 are plotted along the inviscid streamline paths in Figure 1.9. Data is extracted from two passages, where each passage is described by the blades surrounding it (i.e., passage 4-5 is between blades 4 and 5). Good periodicity is seen for the flat endwall results. Note that heat transfer coefficients are higher along the 0.25P streamline in Figure 1.9, as compared to the other streamlines through the passage. In general, Nu values increase through the passage and then begin to decay downstream of the trailing edge plane ($X/C_{ax}>1$).

The data presented in Figure 1.10 was extracted from Figure 1.8 along pitchwise lines, as shown in the inset in Figure 1.10. Note that the pitchwise coordinate (Y) is normalized by the blade pitch and is referenced from the camber line of the blade (i.e., Y/P=0 starts at the camber line and Y/P=1 ends at the camber line of the adjacent blade above). When comparing the different axial locations plotted in Figure 1.10, it was noted that the highest pitchwise gradients in Nu are near the forward part of the passage ($0.25C_{ax}$), as compared to the other pitchwise locations. Note from Figure 1.2 that the endwall contouring is also strongest around this location.

Contoured endwall heat transfer was compared to the flat endwall heat transfer through an augmentation parameter. Figure 1.11 was generated by taking the local differences in heat transfer coefficients between the contoured and flat endwalls, and then normalizing by the flat endwall heat transfer. Values less than 0 indicate that the contoured endwall produces lower heat transfer levels than the flat endwall. Figure 1.11 shows a negative augmentation along most of the pressure surface of the blade. This is especially significant since it occurs in a region of nominally high heat transfer coefficients. The reduced crossflow seen in Figure 1.7b as compared to Figure 1.7a would likely result in lower heat transfer levels for the new boundary layer downstream of the horseshoe vortex separation. Negative augmentation also occurs along the downstream portion of the suction side of the blade. A weakening of the horseshoe and passage vortices due to non-axisymmetric endwall contouring reduces the strength of the corner vortex and thus the associated heat transfer. Sieverding [29] indicates that the corner vortex develops from the impingement of the pressure side leg of the horseshoe vortex on the blade suction side.

In Figure 1.11, positive augmentations are seen near the leading edge in the corner between the endwall and blade suction side, possibly indicating a stronger suction side horseshoe vortex as found by Gustafson, et al. [14]. Near the saddle point region, augmentation levels are also high. However, the magnitudes of Nu in Figure 1.8 are relatively low at this location,

thereby indicating that the contoured endwall is not severely impacting the endwall. Slightly downstream of the exit plane of the passage, augmentation levels tend to increase, which could be attributed to the stronger crossflow that develops there for the contoured endwall relative to the flat endwall.

Data extracted from the augmentation contour is plotted along the inviscid streamline paths in Figure 1.12. Note that the highest level of augmentation occurs along the 0.25P streamline where it passes through the saddle point region. The lowest level of augmentation occurs near the pressure side of the passage (0.25P streamline), with low augmentation also present along the suction side of the passage (0.75P streamline) toward the trailing edge.

Heat transfer augmentation is plotted along the pitchwise lines through the passage in Figure 1.13. At $0.25C_{ax}$, the contoured endwall shows decreased heat transfer (negative augmentation) relative to the flat endwall near the pressure side from Y/P=0.1 to Y/P=0.25, but increased heat transfer in the saddle point region around Y/P=0.35. Recall, however, that the magnitude of Nu is low around Y/P=0.35 (refer to Figure 1.10), so that high augmentation is not as meaningful. Further into the passage ($0.75C_{ax}$ in Figure 1.13), the contoured endwall has overall lower heat transfer than the flat endwall. Downstream of the cascade at $1.25C_{ax}$, augmentation values indicate nearly the same heat transfer coefficients for the flat and contoured endwalls, which would be expected since the contouring does not continue past the trailing edge plane ($X/C_{ax}=1.0$).

When averaging over all passages, from the leading edge plane ($X/C_{ax}=0$) to the trailing edge plane ($X/C_{ax}=1.0$), the contoured endwall results in a 3.1% reduction in area-averaged heat transfer. Peaks and valleys in the contoured endwall shape cause it to have a slightly larger surface area than the flat endwall (1.3% larger). The combination of the heat transfer reduction and the larger surface area indicate that the contoured endwall will have a slightly lower overall heat load (average heat transfer coefficient multiplied by surface area) than a flat endwall:

$$\frac{\overline{\overline{h}}_{contour}}{\overline{\overline{h}}_{flat}} \frac{A_{contour}}{A_{flat}} = 0.969 * 1.013 = 0.98 \tag{1.1}$$

More importantly, the reduced local heat load in high heat transfer regions for the contoured endwall (refer to Figure 1.11) may improve the overall turbine part durability.

Cascade Reynolds Number Effect

To test the robustness of the contoured endwall to off-design conditions, heat transfer coefficients were obtained for the flat and contoured endwalls at cascade Reynolds numbers lower and higher than the nominal condition of Re_{exit}=200,000. Figure 1.14 shows contour plots of flat endwall Nusselt numbers for three Reynolds numbers. As expected, Nu increases with increasing Re_{exit} for the flat endwall. At a location approximately $0.5C_{ax}$ upstream of the cascade, the measured change in Nu as the Reynolds number increased from Re_{exit}=118,000 to 307,000 was within 7% of the expected change based on flat plate turbulent boundary layer correlations. For the range of Re_{exit} tested, the endwall heat transfer features described earlier for the flat endwall do not appear to be significantly different between the various cascade Reynolds number cases.

The heat transfer augmentation of the contoured versus flat endwalls for various cascade Reynolds numbers is shown in Figure 1.15. Note that for most of the passage the augmentation does not appear to change for the range of Reynolds numbers tested, which suggests that the effect of the contour on endwall heat transfer would not be strongly dependent on the turbine operating condition. Figure 1.16 shows the augmentation extracted along the streamwise paths. Again, the augmentation of the contoured endwall appears to be fairly consistent for a range of cascade Reynolds numbers.

Conclusions

A low-pressure turbine blade cascade based on the Pack-B airfoil geometry was developed for the purpose of testing the effects of three-dimensional endwall contouring on endwall heat transfer. Heat transfer measurements were obtained for a baseline flat endwall, as well as for a contoured endwall geometry, for three cascade exit Reynolds numbers. Oil flow visualization was used to determine the effects of the contouring on the near-wall flow.

The oil flow visualization for the flat endwall showed the classic features of secondary flow, including a scoured region describing the path of the passage vortex from pressure to suction side, and overturning of endwall streamlines near the blade pressure side-endwall corner. When the contour was present, the scoured region was not visible, indicating reduced passage vortex strength. Also, the overturning of endwall streamlines near the pressure side was reduced, as compared to the flat endwall, suggesting a reduced effect of the cross-passage pressure gradient on the endwall boundary layer.

The features of the flat endwall heat transfer measurements agreed with the well-documented effects of the leading edge horseshoe vortex, the cross-passage flow, the new endwall boundary layer downstream of the separation line, and the blade wake on endwall heat transfer.

The contoured endwall heat transfer results were compared to the flat endwall through an augmentation parameter. Augmentation levels were high near the saddle point, but were as low as -20% near the blade pressure side-endwall corner. Low augmentation levels were also seen near the suction side of the blade, around the region where the passage vortex impinges on the blade. This reduction was likely due to the decreased effect of the passage vortex on the endwall with contouring, as seen in the oil flow visualization results. Area-averaged heat transfer was reduced by 3.1% for the contoured endwall versus a flat endwall.

The effect of contouring on the endwall heat transfer was tested for off-design performance by measuring heat transfer coefficients at cascade exit Reynolds numbers lower and higher than the nominal value. No major change in the endwall heat transfer pattern was noted for the flat endwall over the range of Reynolds numbers tested. Also, the effect of the contour on endwall heat transfer was not dependent on cascade exit Reynolds number.

Acknowledgments

The authors gratefully acknowledge United Technologies—Pratt & Whitney for their support of this work, and Eunice Allen-Bradley for performing the endwall contour design. The authors would also like to thank Steven Walker for his help with test section construction.

Nomenclature

b	turbulence grid bar width
BL	boundary layer
C	true chord of blade
C_{ax}	axial chord of blade
C_p	specific heat at constant pressure, or static pressure coefficient, $C_p = \left(P_s - P_{s,in}\right) / 0.5\rho U_{\infty,in}$
h	heat transfer coefficient, $h = q''_w / \left(T_w - T_{\infty,in}\right)$
H	boundary layer shape factor

k	thermal conductivity
Nu	Nusselt number, $Nu = hC_{ax} / k_{air}$
P	blade pitch
P_s	static pressure
q''_w	wall heat flux
Re_{exit}	cascade exit Reynolds number, $Re_{exit} = C_{ax} U_{\infty,exit} / \nu$
Re_s	boundary layer Reynolds number, $Re_s = sU_\infty / \nu$
s	distance from start of velocity boundary layer, or surface distance along airfoil
S	blade span
St	Stanton number, $St = h / \rho C_p U_\infty$
T	temperature
T_{reflc}	average temperature associated with radiation reflected off the endwall from the surroundings
x	streamwise distance downstream of the turbulence grid
X, Y, Z	global coordinates, where X is blade axial direction
U	streamwise velocity

Greek

δ	boundary layer thickness
δ*	displacement thickness
ε	emissivity
θ	momentum thickness
ν	kinematic viscosity
ρ	density

Subscripts

exit	exit conditions
in	inlet conditions
w	wall conditions
∞	local freestream conditions

Superscripts

+	boundary layer inner coordinates
'	rms of fluctuating parameter

References

[1] Langston, L. S., 1980, "Crossflows in a Turbine Cascade Passage," *Journal of Engineering for Power*, **102**, pp. 866-874.

[2] Sharma, O. P., and Butler, T. L., 1987, "Predictions of Endwall Losses and Secondary Flows in Axial Flow Turbine Cascades," *Journal of Turbomachinery*, **109**(2), pp. 229-236.

[3] Goldstein, R. J., and Spores, R. A., 1988, "Turbulent Transport on the Endwall in the Region between Adjacent Turbine Blades," *Journal of Heat Transfer*, **110**(4a), pp. 862-869.

[4] Boletis, E., 1985, "Effects of Tip Endwall Contouring on the Three-Dimensional Flow Field in an Annular Turbine Nozzle Guide Vane: Part 1---Experimental Investigation," *Journal of Engineering for Gas Turbines and Power*, **107**(4), pp. 983-990.

[5] Morris, A. W. H., and Hoare, R. G., 1975, "Secondary Loss Measurements in a Cascade of Turbine Blades with Meridional Wall Profiling," Proc. ASME Winter Annual Meeting 1975, Paper No. 75-WA/GT-13.

[6] Lin, Y. L., and Shih, T. I.-P., 2000, "Flow and Heat Transfer in a Turbine Nozzle Guide Vane with Endwall Contouring," Proc. 35th Intersociety Energy Conversion Engineering Conference, Paper No. AIAA2000-3002.

[7] Harvey, N. W., Rose, M. G., Taylor, M. D., Shahpar, S., Hartland, J., and Gregory-Smith, D. G., 2000, "Nonaxisymmetric Turbine End Wall Design: Part I--- Three-Dimensional Linear Design System," *Journal of Turbomachinery*, **122**(2), pp. 278-285.

[8] Hartland, J. C., Gregory-Smith, D. G., Harvey, N. W., and Rose, M. G., 2000, "Nonaxisymmetric Turbine End Wall Design: Part II---Experimental Validation," *Journal of Turbomachinery*, **122**(2), pp. 286-293.

[9] Brennan, G., Harvey, N. W., Rose, M. G., Fomison, N., and Taylor, M. D., 2003, "Improving the Efficiency of the Trent 500-HP Turbine Using Nonaxisymmetric End Walls---Part I: Turbine Design," *Journal of Turbomachinery*, **125**(3), pp. 497-504.

[10] Rose, M., Harvey, N. W., Seaman, P., Newman, D. A., and Mcmanus, D., 2001, "Improving the Efficiency of the Trent 500 HP Turbine Using Non-Axisymmetric End Walls. Part II: Experimental Validation," Proc. ASME Turbo Expo 2001, Paper No. 2001-GT-0505.

[11] Germain, T., Nagel, M., Raab, I., Schupbach, P., Abhari, R. S., and Rose, M., 2010, "Improving Efficiency of a High Work Turbine Using Nonaxisymmetric Endwalls--- Part I: Endwall Design and Performance," *Journal of Turbomachinery*, **132**(2), pp. 021007.

[12] Schuepbach, P., Abhari, R. S., Rose, M. G., Germain, T., Raab, I., and Gier, J., 2010, "Improving Efficiency of a High Work Turbine Using Nonaxisymmetric Endwalls---Part II: Time-Resolved Flow Physics," *Journal of Turbomachinery*, **132**(2), pp. 021008.

[13] Saha, A. K., and Acharya, S., 2008, "Computations of Turbulent Flow and Heat Transfer through a Three-Dimensional Nonaxisymmetric Blade Passage," *Journal of Turbomachinery*, **130**(3), pp. 031008.

[14] Gustafson, R., Mahmood, G. I., and Acharya, S., 2007, "Aerodynamic Measurements in a Linear Turbine Blade Passage with Three-Dimensional Endwall Contouring," Proc. ASME Turbo Expo 2007, Paper No. GT2007-28073.

[15] Praisner, T. J., Allen-Bradley, E., Grover, E. A., Knezevici, D. C., and Sjolander, S. A., 2007, "Application of Non-Axisymmetric Endwall Contouring to Conventional and High-Lift Turbine Airfoils," Proc. ASME Turbo Expo 2007, Paper No. GT2007-27579.

[16] Knezevici, D. C., Sjolander, S. A., Praisner, T. J., Allen-Bradley, E., and Grover, E. A., 2010, "Measurements of Secondary Losses in a Turbine Cascade with the Implementation of Nonaxisymmetric Endwall Contouring," *Journal of Turbomachinery*, **132**(1), pp. 011013.

[17] Praisner, T. J., Grover, E. A., Knezevici, D. C., Popovic, I., Sjolander, S. A., Clark, J. P., and Sondergaard, R., 2008, "Toward the Expansion of Low-Pressure-Turbine Airfoil Design Space," Proc. ASME Turbo Expo 2008, Paper No. GT2008-50898.

[18] Baines, W. D., and Peterson, E. G., 1951, "An Investigation of Flow through Screens," *Transactions of the ASME*, **July 1951**, pp. 467-478.

[19] Lake, J. P., King, P. I., and Rivir, R. B., 1999, "Reduction of Separation Losses on a Turbine Blade with Low Reynolds Numbers," Proc. 37th AIAA Aerospace Sciences Meeting and Exhibit, Paper No. AIAA-1999-242.

[20] Murawski, C. G., and Vafai, K., 2000, "An Experimental Investigation of the Effect of Freestream Turbulence on the Wake of a Separated Low-Pressure Turbine Blade at Low Reynolds Numbers," *Journal of Fluids Engineering*, **122**(2), pp. 431-433.

[21] Mahallati, A., Mcauliffe, B., Sjolander, S. A., and Praisner, T. J., 2007, "Aerodynamics of a Low-Pressure Turbine Airfoil at Low Reynolds Numbers Part 1: Steady Flow Measurements," Proc. ASME Turbo Expo 2007, Paper No. GT2007-27347.

[22] Zoric, T., Popovic, I., Sjolander, S. A., Praisner, T. J., and Grover, E. A., 2007, "Comparative Investigation of Three Highly Loaded LP Turbine Airfoils: Part I: Measured Profile and Secondary Losses at Design Incidence," Proc. ASME Turbo Expo 2007, Paper No. GT2007-27537.

[23] Popovic, I., Zhu, J., Dai, W., Sjolander, S. A., Praisner, T. J., and Grover, E. A., 2006, "Aerodynamics of a Family of Three Highly Loaded Low-Pressure Turbine Airfoils: Measured Effects of Reynolds Number and Turbulence Intensity in Steady Flow," Proc. ASME Turbo Expo 2006, Paper No. GT2006-91271.

[24] Kang, M. B., Kohli, A., and Thole, K. A., 1999, "Heat Transfer and Flowfield Measurements in the Leading Edge Region of a Stator Vane Endwall," *Journal of Turbomachinery*, **121**(3), pp. 558-568.

[25] Moffat, R. J., 1988, "Describing the Uncertainties in Experimental Results," *Experimental Thermal and Fluid Science*, **1**, pp. 3-17.

[26] Kays, W. M., and Crawford, M. E., 1980, *Convective Heat and Mass Transfer*, McGraw-Hill, Inc., New York.

[27] Thole, K. A., and Bogard, D. G., 1995, "Enhanced Heat Transfer and Shear Stress Due to High Free-Stream Turbulence," *Journal of Turbomachinery*, **117**(3), pp. 418-424.

[28] "FLUENT" (version 6.3.26), Fluent, Inc., Lebanon, NH.

[29] Sieverding, C. H., 1985, "Recent Progress in the Understanding of Basic Aspects of Secondary Flows in Turbine Blade Passages," *Journal of Engineering for Gas Turbines and Power*, **107**(2), pp. 248-257.

Table 1.1 Blade Geometry and Flow Conditions

Number of blades	7
Scale factor	8.6
Axial chord (C_{ax})	0.218 m
Pitch/chord (P/C_{ax})	0.826
Span/chord (S/C_{ax})	2.50
Inlet Re $\left(Re_{in} = C_{ax} U_{\infty,in} / \nu\right)$	1.25×10^5
Exit Re $\left(Re_{exit} = C_{ax} U_{\infty,exit} / \nu\right)$	2.00×10^5
Inlet velocity ($U_{\infty,in}$)	8.7 m/s
Inlet, exit flow angles	35°, 60°
Inlet, exit Mach	0.026, 0.042

Table 1.2 Turbulent Boundary Layer Parameters at $2.85C_{ax}$ Upstream of Center Blade

Boundary layer thickness/span (δ/S)	0.074
Displacement thickness/span (δ^*/S)	0.012
Momentum thickness/span (θ/S)	0.011
Shape factor (H)	1.14
Momentum thickness Reynolds number (Re_θ)	3109
Freestream turbulence level (u'/U)	0.056

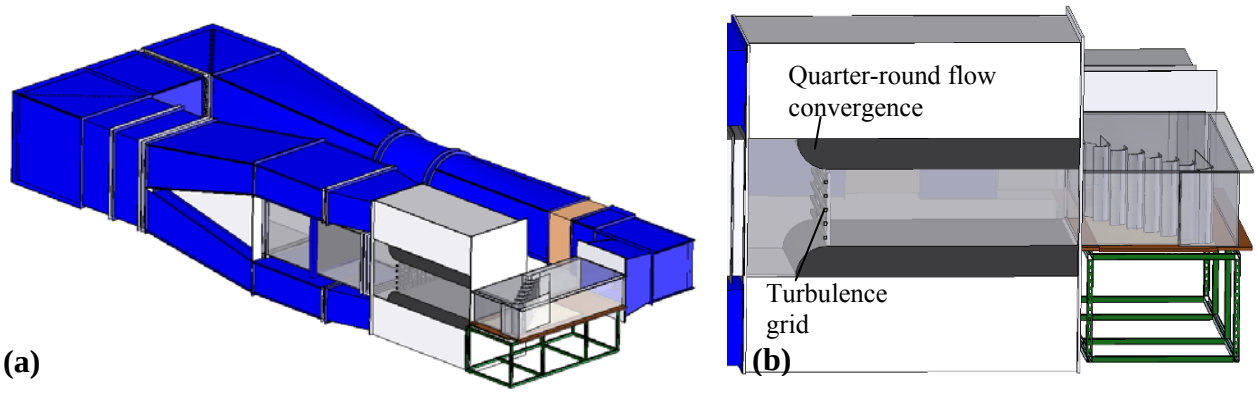

Figure 1.1. Depiction of the (a) large-scale low-speed wind tunnel, with a corner test section housing the Pack-B cascade, and (b) the inlet flow development section.

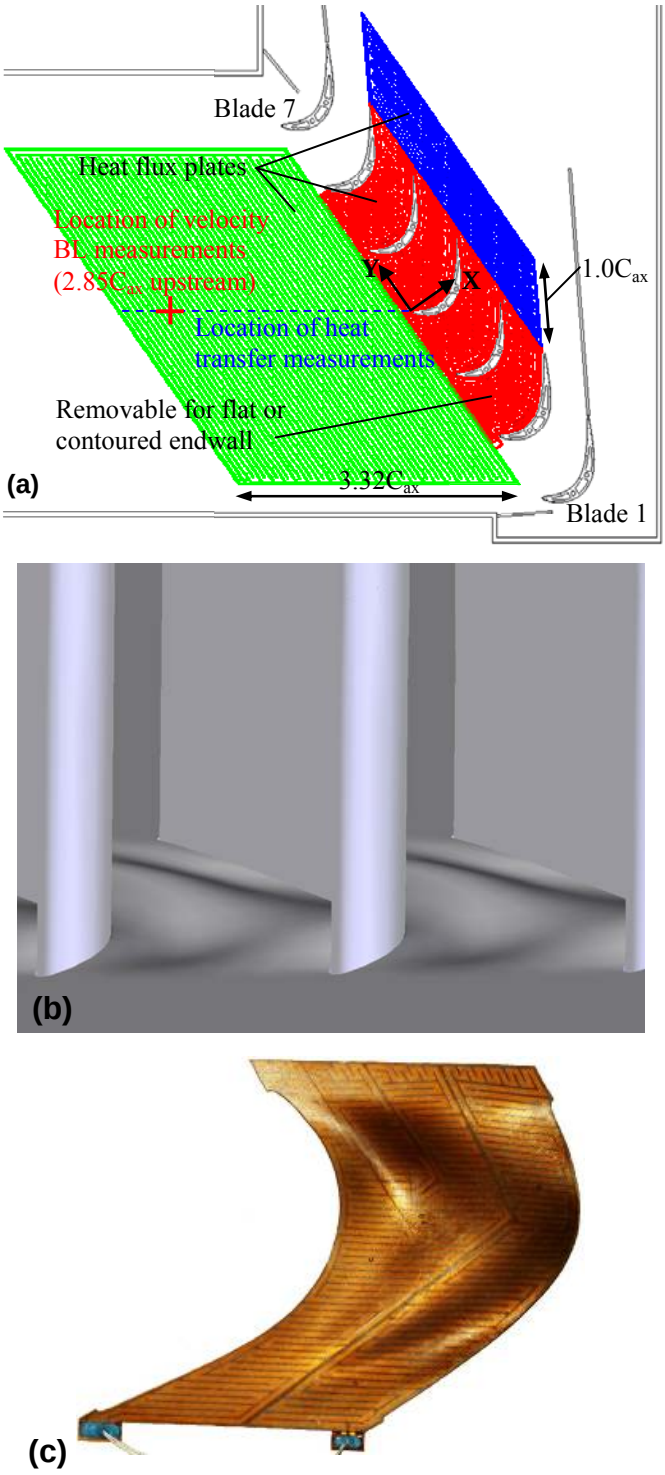

Figure 1.2. Schematic of the blade cascade with heat flux plates on the endwall (a); isometric view of the contoured endwall (b); and the contoured endwall heater mounted on a thin stereolithography plate (c).

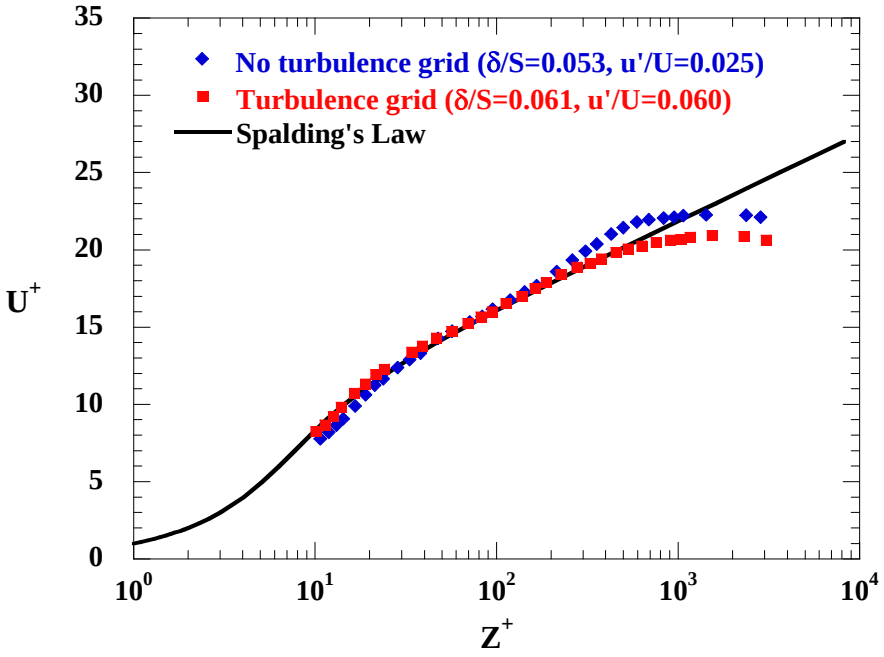

Figure 1.3. Inlet turbulent boundary layer measured $2.85C_{ax}$ upstream of blade 4 (see Figure 1.2a), with and without the turbulence grid installed.

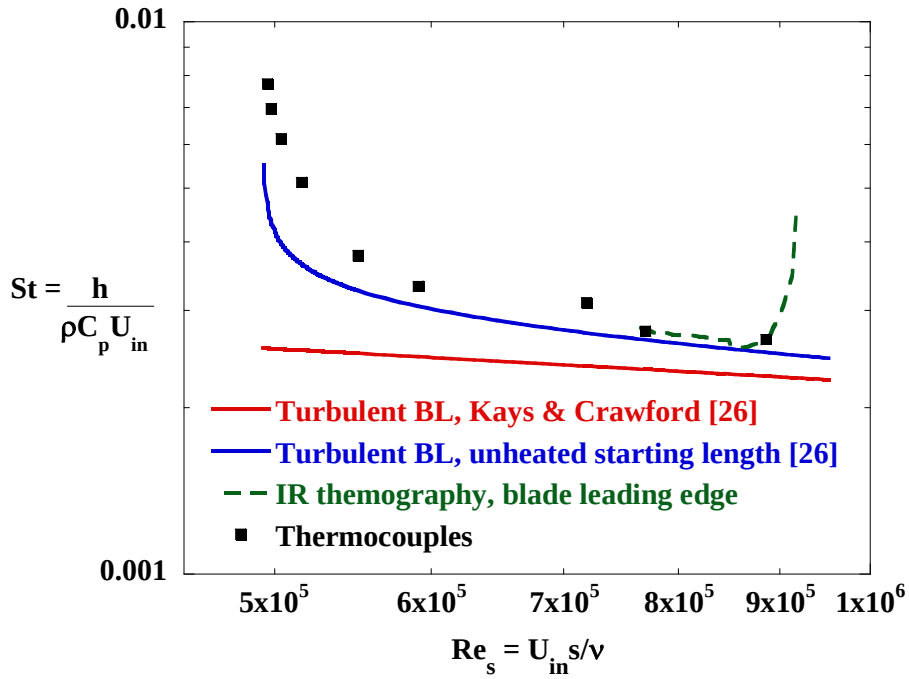

Figure 1.4. Heat transfer coefficient development along a line approaching blade 4 (see Figure 1.2a), with the turbulence grid installed.

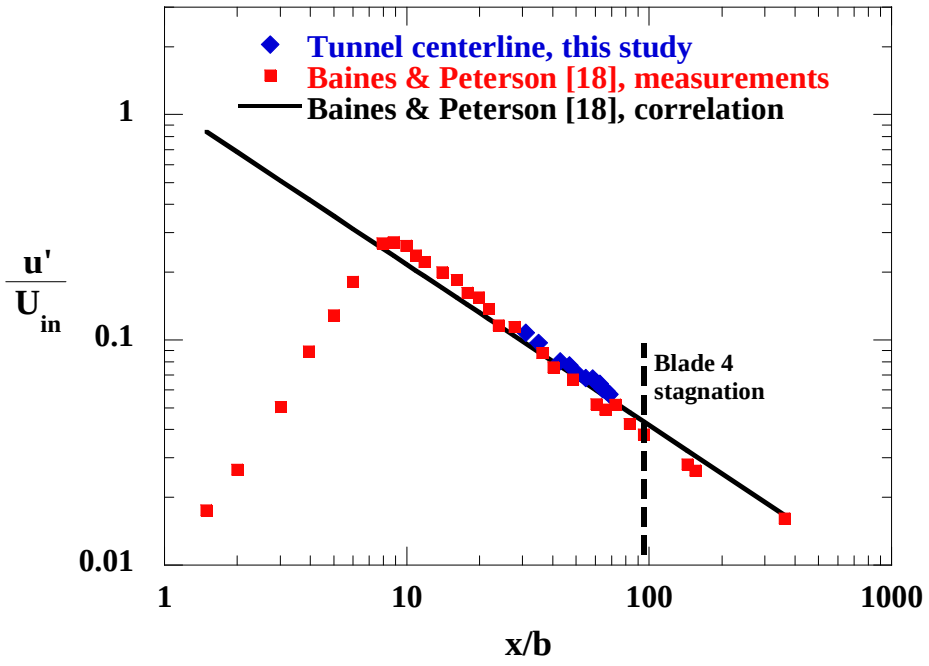

Figure 1.5. Freestream turbulence decay downstream of the turbulence grid, measured along the midspan centerline of the tunnel.

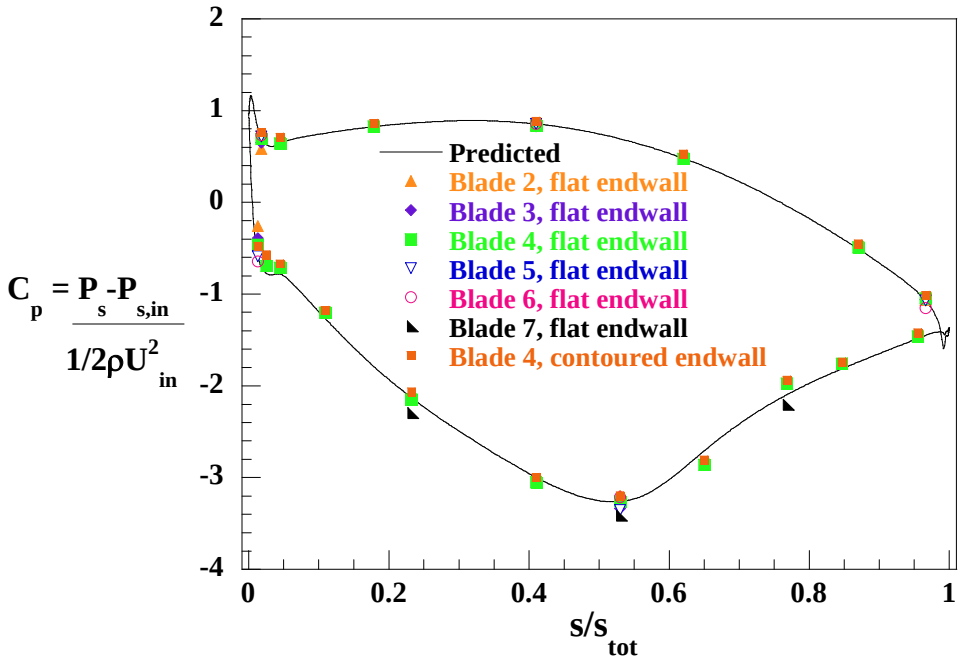

Figure 1.6. Blade static pressure distribution at the midspan plane for the flat and contoured endwalls.

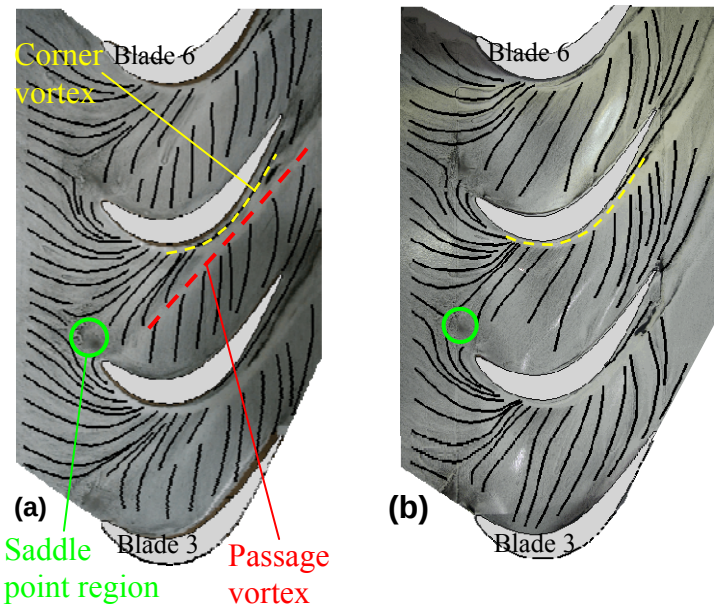

Figure 1.7. Qualitative interpretation of endwall streaklines from oil flow visualization on the (a) flat endwall and (b) contoured endwall.

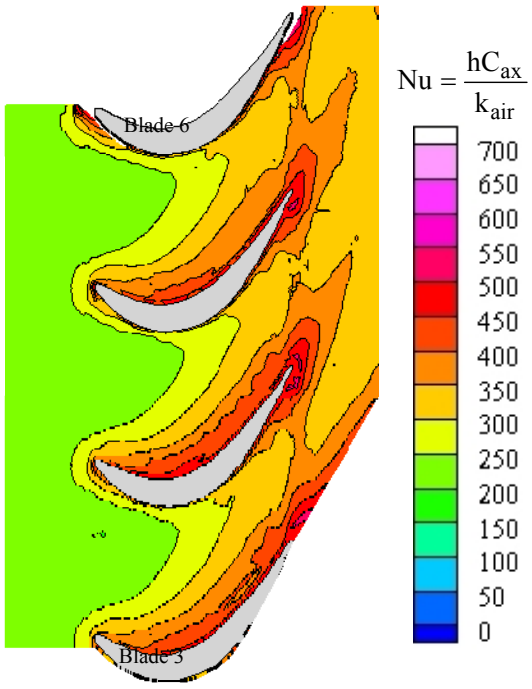

Figure 1.8. Contours of endwall Nusselt number for the flat endwall.

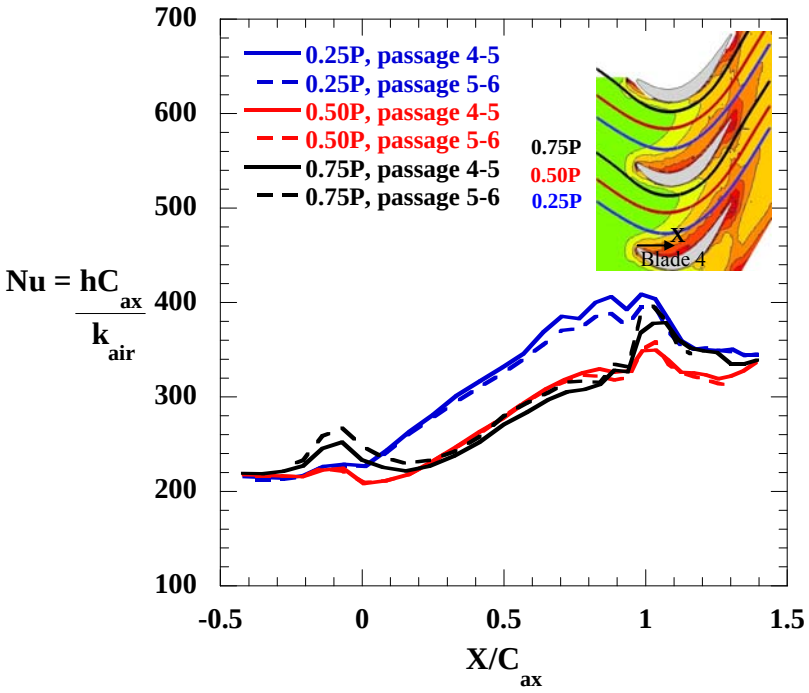

Figure 1.9. Nusselt numbers for the flat endwall, plotted along inviscid streamlines passing through 0.25P, 0.50P, and 0.75P (see inset).

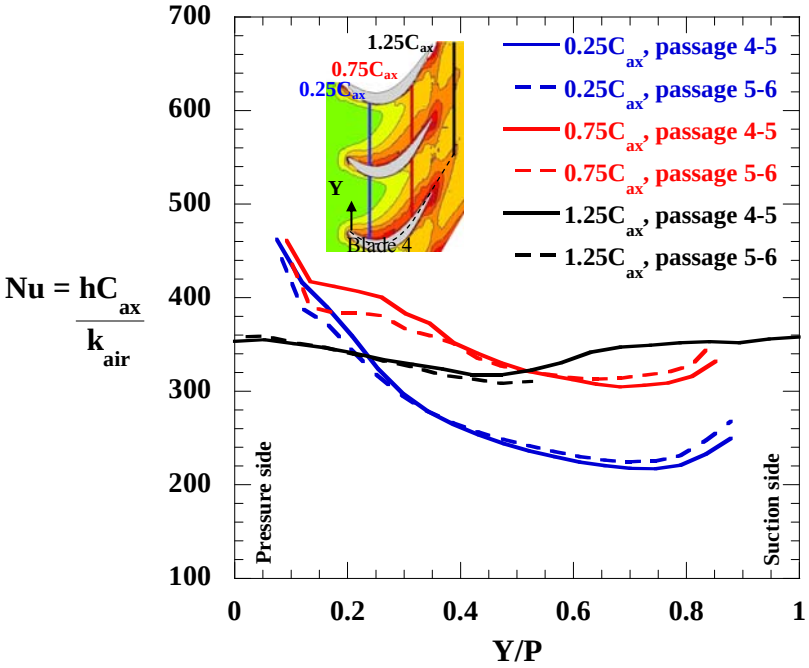

Figure 1.10. Nusselt numbers for the flat endwall, plotted along pitchwise lines at $0.25C_{ax}$, $0.75C_{ax}$, and $1.25C_{ax}$ from the leading edge (see inset).

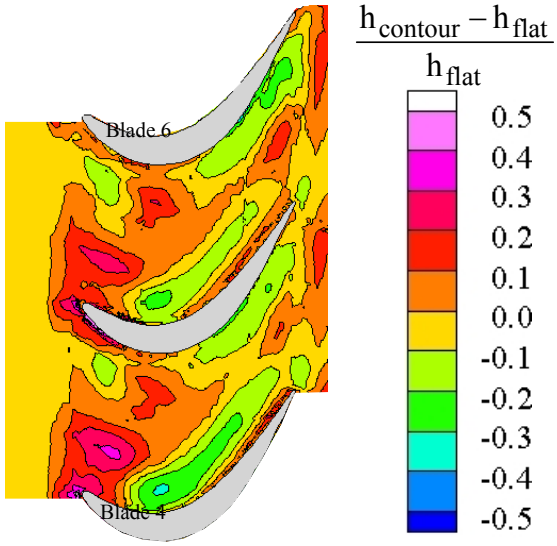

Figure 1.11. Contours of heat transfer coefficient augmentation for the flat versus contoured endwalls.

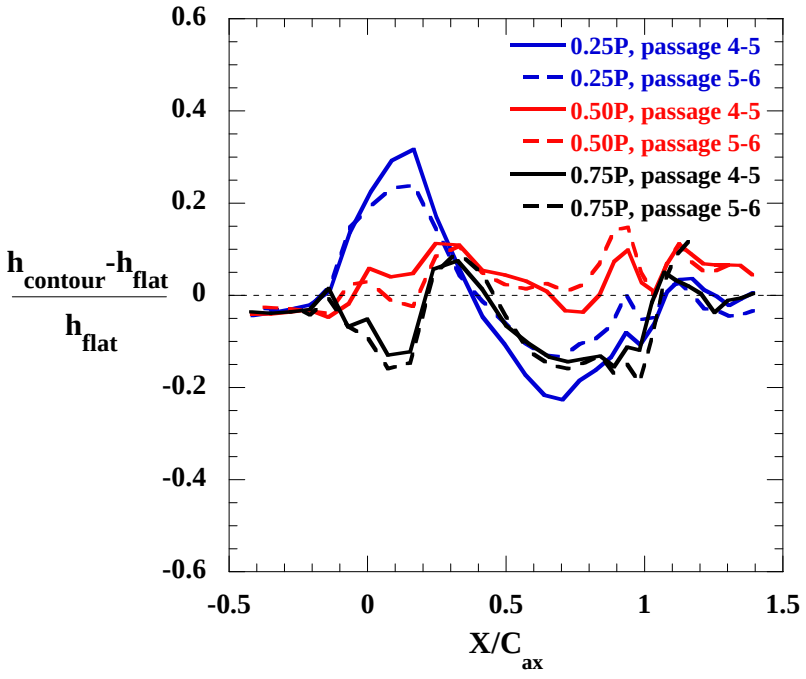

Figure 1.12. Heat transfer coefficient augmentation along inviscid streamline paths (see Figure 1.9).

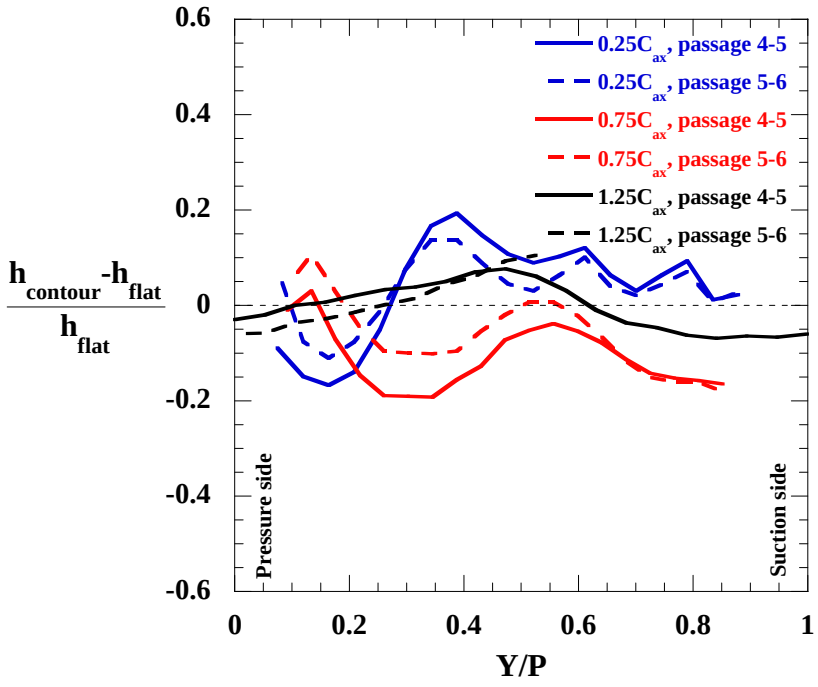

Figure 1.13. Heat transfer coefficient augmentation along pitchwise lines (see Figure 1.10).

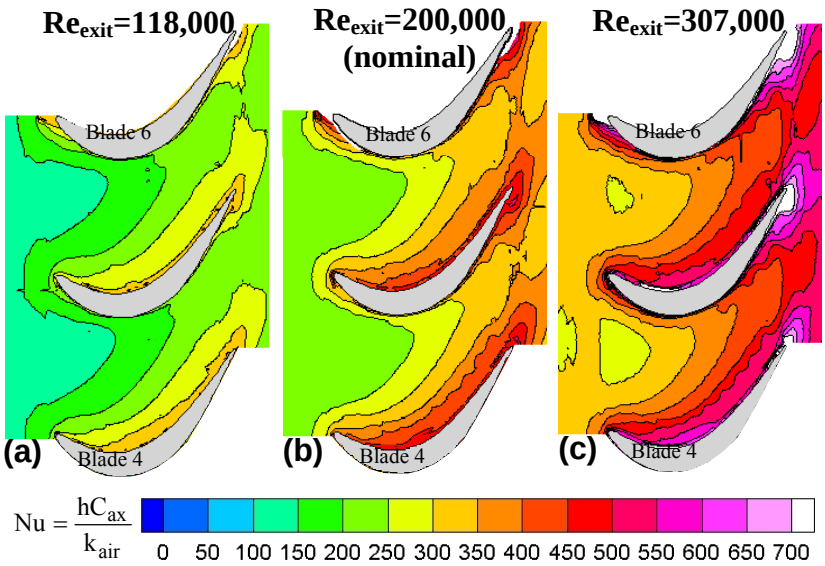

Figure 1.14. Contours of Nusselt number for the flat endwall at (a) Re_{exit}=118,000, (b) Re_{exit}=200,000 (nominal), and (c) Re_{exit}=307,000.

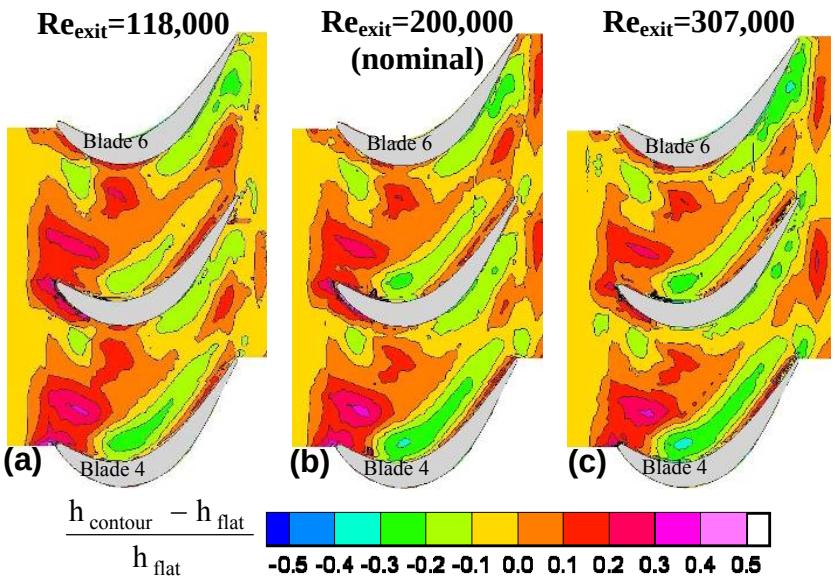

Figure 1.15. Contours of heat transfer augmentation for (a) Re_{exit}=118,000, (b) Re_{exit}=200,000 (nominal), and (c) Re_{exit}=307,000.

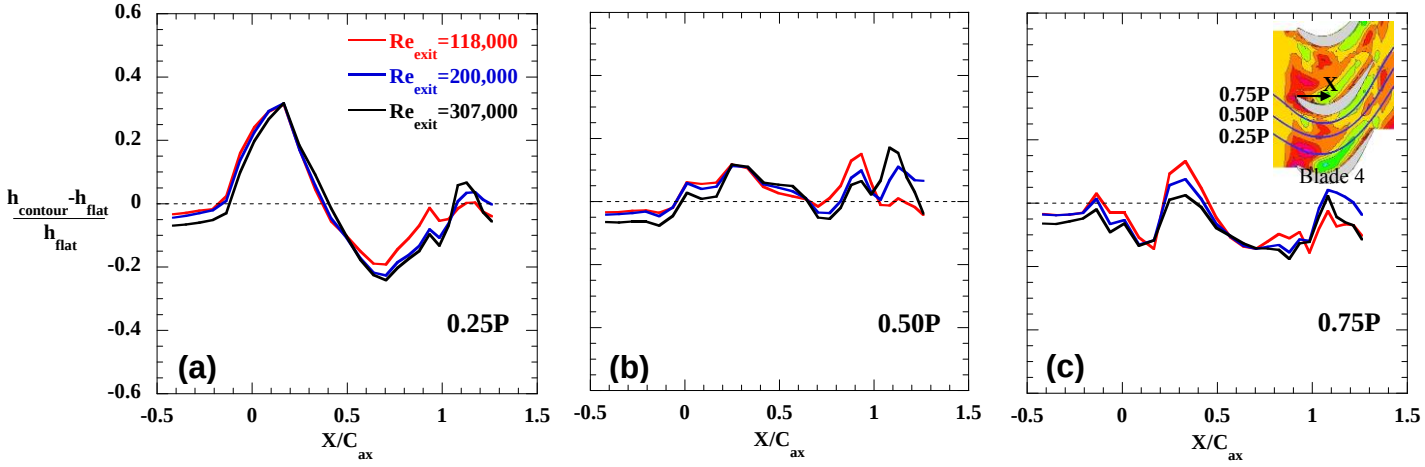

Figure 1.16. Contoured versus flat endwall heat transfer augmentation at various cascade exit Reynolds numbers, plotted along the inviscid streamlines passing through (a) 0.25P, (b) 0.50P, and (c) 0.75P (see inset).

Paper 2: Computational Predictions of Heat Transfer and Film Cooling for a Turbine Blade with Non-Axisymmetric Endwall Contouring

Published in the *Journal of Turbomachinery**:

Lynch, S. P., Thole, K. A., Kohli, A. and Lehane, C., 2011, "Computational Predictions of Heat Transfer and Film Cooling for a Turbine Blade with Non-Axisymmetric Endwall Contouring," *J. of Turbomachinery*, Vol. 133, pp. 041003-1-10. Used with permission of ASME, 2011.

Abstract

Three-dimensional contouring of the compressor and turbine endwalls in a gas turbine engine has been shown to be an effective method of reducing aerodynamic losses by mitigating the strength of the complex vortical structures generated at the endwall. Reductions in endwall heat transfer in the turbine have been also previously measured and reported in the literature. In this study, computational fluid dynamics simulations of a turbine blade with and without non-axisymmetric endwall contouring were compared to experimental measurements of the exit flowfield, endwall heat transfer and endwall film-cooling. Secondary kinetic energy at the cascade exit was closely predicted with a simulation using the SST k-ω turbulence model. Endwall heat transfer was overpredicted in the passage for both the SST k-ω and realizable k-ε turbulence models, but heat transfer augmentation for a non-axisymmetric contour relative to a flat endwall showed fair agreement to the experiment. Measured and predicted film-cooling results indicated that the non-axisymmetric contouring limits the spread of film-cooling flow over the endwall depending upon the interaction of the film with the contour geometry.

*Co-authors: Dr. Karen A. Thole, Mechanical & Nuclear Engineering Department, Penn State
Dr. Atul Kohli, United Technologies--Pratt & Whitney
Dr. Christopher Lehane, United Technologies--Pratt & Whitney

Introduction

Vortical secondary flows near the airfoil-endwall junction in an axial turbine are responsible for reduced aerodynamic efficiency and high heat transfer rates. Furthermore, the sweeping action of the flows can displace coolant ejected through holes in the part, which normally provides a film of cool air to shield the part from hot gas temperatures. This complex flowfield near the endwall is difficult to accurately model with current computational methods, and improvement in modeling fidelity is important to achieve further gains in turbine efficiency and durability.

The potential for efficiency and durability improvement using computational fluid dynamics (CFD) simulations is illustrated by the development of non-axisymmetric (three-dimensional) contouring designs for turbine endwalls. Three-dimensional variation of the endwall surface has been generally determined through an optimization routine coupled to three-dimensional Reynolds-Averaged Navier Stokes (RANS) simulations. Experimental validations of the resulting shapes have demonstrated reductions in the strength of vortical secondary flows and improvements in turbine efficiency.

Although current computational methods are adequate to produce optimized endwall designs, predictions rarely capture all of the improvements demonstrated by experiments. A complete turbine design also must consider the full aerodynamic and thermal environment. The motivation for this paper is to examine the validity of RANS-based modeling for non-axisymmetric contour design through comparison to measured flowfields, endwall heat transfer, and film cooling effectiveness.

Relevant Past Studies

The complex shape of a non-axisymmetric contoured endwall is typically generated through a geometric optimization coupled to a three-dimensional CFD code. An example of the power of this method was presented by Harvey, et al. [1]. Their optimal design was based on reducing the cross-passage pressure gradient and exit flow angle deviation. Significant reductions in secondary kinetic energy and flow angle deviation with contouring were predicted relative to the baseline flat endwall. Experimental validation by Hartland, et al. [2] demonstrated the reduction in secondary kinetic energy, but also found an improvement in loss not predicted

by Harvey, et al. [1]. Nagel and Baier [3] optimized the endwall and airfoil of a low-pressure turbine blade, and demonstrated reasonably close predictions of loss for the optimized shape.

Germain, et al. [4] used a 3D RANS code to design endwall contours for the stator and rotor of a 1 ½ stage rotating turbine. Although secondary kinetic energy agreed well with experiments of Schuepbach, et al. [5], overall turbine efficiency improvement with contouring was underpredicted.

A series of studies have been performed to analyze the usefulness of endwall contouring in a family of highly loaded low pressure turbine blades. Praisner, et al. [6] presented a computational optimization methodology for a baseline Pack-B low pressure airfoil and two related highly-loaded designs. Loss reduction was a primary metric in the optimization. Flowfield measurements of the resulting geometries by Knezevici, et al. [7] and Knezevici, et al. [8] demonstrated reduced loss and secondary kinetic energy compared to a flat endwall.

Saha and Acharya [9] used endwall heat transfer as the optimization metric for a contour design. Significant reductions in heat transfer were predicted near the suction side leading edge and in the throat, relative to a flat endwall. Measurements of the contour by Mahmood and Acharya [10] did not reproduce the same magnitude of heat transfer reduction, but heat transfer augmentation due to the passage vortex and the suction side leg of the horseshoe vortex were reduced. Lynch, et al. [11] measured endwall heat transfer for the contour design studied by Praisner, et al. [6] and Knezevici, et al. [7]. Relative to a flat endwall, the contour increased heat transfer near the saddle point but reduced heat transfer near the pressure side-endwall junction, which was considered more significant since flat endwall heat transfer levels were high in that region.

Film-cooling for non-axisymmetric endwall contours was considered in a computational study by Okita and Nakamata [12]. A reduction in passage vortex strength with contouring allowed the coolant to remain closer to the endwall in the downstream portion of the passage. Flowfield measurements were performed by Gustafson, et al. [13] for full-coverage film cooling on the contour of Saha and Acharya [9]. Gustafson, et al. [13] concluded that coolant jets stay close to the surface, although overall cascade loss (including losses through the holes) increased with blowing ratio. Increases in blowing ratio for the same film-cooled contour resulted in higher film effectiveness and reduced near-wall overturning, in the study ofMahmood, et al. [14].

The computational predictions reported here simulated the flat and non-axisymmetric geometries studied by Knezevici, et al. [7] and Lynch, et al. [11]. Also included in this paper are experimental measurements and computational predictions of film-cooling for the flat and contoured endwalls.

Computational Methodology

Simulations of the flat and contoured endwall geometries studied by Knezevici, et al. [7] and Lynch, et al. [11] were performed using the commercial computational fluid dynamics software FLUENT [15]. The pressure-based formulation of the steady Reynolds-Averaged Navier-Stokes equations (RANS), the turbulence closure equations, and the energy equation were solved with second-order discretization of all variables. The SST k-ω turbulence model (Menter [16]) was chosen for closure of the RANS equations. This model has shown reasonable agreement with experimental results in turbomachinery applications (Schwaenen and Duggleby [17], Snedden, et al. [18]). The realizable k-ε turbulence model (Shih, et al. [19]) has also shown reasonable agreement with experimental heat transfer data (Harrison and Bogard [20], Yang, et al. [21], Hermanson, et al. [22]), and predictions with this model are also considered.

The experimental setup described in Lynch, et al. [11] included a heater on the endwall that extended $3.32C_{ax}$ upstream of the blade (along the streamwise direction). To capture the development of the endwall heat transfer upstream of the cascade, the computational grid extended $4.3C_{ax}$ upstream of the blade leading edge, as shown in Figure 2.1a. A velocity inlet with a boundary layer profile benchmarked to the experiment was set at this location; see benchmarking details in a later section. Periodic boundaries were employed on the sides of the domain, and an outflow boundary extended $1.5C_{ax}$ downstream of the blade trailing edge. A symmetry boundary condition was applied at midspan. For heat transfer studies, a uniform heat flux boundary condition was imposed on the endwall, starting at $3.32C_{ax}$ upstream of the blade and extending to the domain exit. All other surfaces were modeled as adiabatic, as per the experiment. For the film cooling cases, all surfaces were modeled as adiabatic.

The commercial grid generation program ICEM [23] was used to create multi-block structured grids for the flat and contoured endwall geometries. The initial grid size for the heat transfer studies was 1.2 million cells, with grid spacing refined near walls such that y^+ was less than 1 everywhere. Refer to Figure 2.1b-c for a depiction of the flat and contoured endwall grids

in the passage. For the film-cooling predictions, the same multi-block format was used, with O-grids created around each of the film-cooling holes. Figure 2.2 depicts the flat and contoured endwall grids. A plenum was added below the endwall to feed the cooling holes. The dimensions of the plenum relative to the hole diameter are also shown. A more detailed description of the hole geometry is presented later.

Convergence of a simulation was determined through the following three ways: normalized residuals had to reach values lower than 10^{-4} (10^{-6} for energy); area-averaged endwall Nusselt number (for heat transfer cases) or area-averaged endwall film effectiveness (for film-cooling cases) had to change by less than 0.1% over 500 iterations; and mass-averaged total pressure over a plane located $1.4C_{ax}$ downstream of the blade leading edge had to change by less than 0.1% over 500 iterations.

Grid independence for the heat transfer cases was determined by refining and coarsening the mesh relative to the nominal mesh size of 1.7 million cells. The difference in area-averaged Nu over the endwall varied by less than 1% for the coarse grid (0.68 million cells) and the refined grid (3.17 million cells), relative to the nominal grid. Mass-averaged total pressure over the plane located $1.4C_{ax}$ downstream of the blade leading edge also varied by less than 0.6% for the coarse and refined grids, relative to the nominal grid. Based on these results, the nominal grid size was considered to be sufficient for heat transfer and flowfield predictions.

The solution-based grid adaption capability in FLUENT was used to check grid independence for the film-cooling studies by refining the mesh based on gradients of temperature. For each film-cooling flowrate, the baseline converged mesh (2.8 million cells) was initially refined to reduce the gradient in temperature by 20%, which added nominally 250,000 cells. The case was then run again to convergence. A second refining adaption resulted in a final mesh size of approximately 3.5 million cells. Area-averaged effectiveness increased by about 1% for the first refinement relative to the baseline grid, and increased further by 0.2% for the second refinement relative to the first. Results from the largest grid are reported here.

Benchmarking of Inlet Conditions

Lynch, et al. [11] made measurements of the inlet boundary layer at a location $2.85C_{ax}$ upstream of the blade leading edge along the direction of the inlet velocity ($2.33C_{ax}$ in the axial direction). As noted earlier, the computational grid inlet was placed upstream of that location. The boundary layer code TEXSTAN (Crawford [24]) was used to generate profiles of velocity,

turbulent kinetic energy, and turbulent dissipation for the grid inlet, such that the measured boundary layer and endwall heat transfer development downstream of the start of the endwall heater were duplicated in the FLUENT simulations. The dissipation profile from TEXSTAN was converted to specific dissipation for the SST k-ω model using the relationship outlined in Menter [16].

Figure 2.3 compares the measured boundary layer to a prediction using TEXSTAN, and to results from the FLUENT simulations using inlet profiles generated by TEXSTAN. All of the predictions agree well with the measured boundary layer. See Table 2.1 for a comparison of the boundary layer parameters for the various predictions, and a comparison to the measured boundary layer parameters of Knezevici, et al. [7]. The boundary layer thickness in the simulation is slightly smaller than that of Knezevici, et al. [7], but was deemed reasonably close for comparison.

The development of the endwall heat transfer upstream of the blade cascade along the streamwise direction is shown in Figure 2.4. Note that Re_s for each data set is referenced to its respective virtual origin. Both the trend and the magnitude of measured endwall heat transfer are well-predicted by the FLUENT simulation, and both match the expected behavior from the unheated starting length correlation of Kays and Crawford [25].

Blade surface static pressures at midspan were compared to the measurements of Lynch, et al. [11] to confirm proper blade loading for the simulations. Figure 2.5 shows blade static pressure, non-dimensionalized as a pressure coefficient. Both turbulence model cases demonstrated good agreement to measurements. Note that the high aspect ratio of the blade and the relatively modest contouring resulted in the same loading at midspan for the flat and contoured endwall geometries.

Film Cooling Measurements

Measurements of film cooling effectiveness were obtained in a large-scale low-speed test section that could be fitted with a flat or a three-dimensionally contoured endwall. The geometry, benchmarking, and endwall heat transfer measurement method were presented previously by Lynch, et al. [11]; thus, only a brief overview of those topics is given here.

A large low-speed wind tunnel provided flow through a scaled low-pressure turbine blade cascade. The wind tunnel, depicted in Figure 2.6, has the capability to create a temperature

differential between the mainstream and the coolant air by heating the former with a 55 kW electric heater bank, and cooling the latter with a 40 kW chiller. For the film-cooling measurements presented here, a temperature differential of at least 20°C was maintained, with the coolant nominally at 23°C. This resulted in a coolant-to-mainstream density ratio of approximately 1.06. The benchmarking and heat transfer studies in Lynch, et al. [11] required no heating or cooling.

The rectilinear blade test section contained seven low-pressure turbine blades based on the Pack-B midspan airfoil geometry. This geometry has been presented in several studies in the literature, on topics ranging from active flow control (Bons, et al. [26], McAuliffe and Sjolander [27]), to benchmarking with higher-loaded designs (Popovic, et al. [28], Zoric, et al. [29]), to the optimization and measured performance of three-dimensional endwall contouring (Praisner, et al. [6], Knezevici, et al. [7]). See Table 2.2 for a summary of the test section geometry and flow parameters. The contour endwall shape consisted of a peak near the pressure side of the airfoil and a depression near the suction side in the forward part of the passage, and a ridge through the passage from the pressure to suction side (see Figure 2.1c).

Adiabatic film cooling effectiveness was measured for the flat and three-dimensionally contoured endwalls by capturing the steady-state endwall temperature with an infrared camera. Coolant was ejected onto the endwall through discrete holes located near the blade pressure side. The flat and contoured endwalls were constructed of low thermal conductivity foam ($k \approx 0.03$ W/m-K) for minimal conduction losses. The flat endwall foam was uniformly 12.7 mm thick. A two-part expanding foam cast in a mold was used to model the shape of the three-dimensional contour.

The endwall surfaces were painted flat black for high emissivity and resolution in IR measurements. An IR camera with 240x320 pixel resolution (spatial integration of 0.16d) was used to capture images at each of several locations over the entire endwall. The average of five images at a location was then calibrated for emissivity and background temperature by comparison to embedded thermocouples in the endwall. Typical values for emissivity and background temperature were $\varepsilon=0.92$ and $T_{back}=50°C$, which compared well to published emissivity for black paint ($\varepsilon=0.94$) and the measured freestream temperature ($T_\infty=46°C$). The resulting calibrated images were assembled into a temperature map of the endwall and converted to film effectiveness (η) using measured freestream and coolant plenum temperatures.

Five cylindrical holes (d/C_{ax}=0.020) were spaced evenly near the airfoil pressure side-endwall junction, in a region of high heat transfer seen in the flat endwall heat transfer measurements. Hole locations were kept consistent relative to the blade for both the flat and contoured endwall studies as shown in Figure 2.2. Injection angles for the flat endwall holes were aligned with the direction of flat endwall streaklines from the oil flow visualization reported in Lynch, et al. [11]. It was considered that since the holes were so close to the airfoil, the surface inclination angle in a manufactured part would be limited so that the film hole can be fed from below the blade platform. To accommodate this limitation, the surface inclination angle for the flat endwall holes was 40°, except for hole 1 which had a surface inclination angle of 45°. The L/d ratio of the flat endwall film holes was 4.1.

The same coolant feed limitation was considered for the contoured endwall due to the varying thickness and surface orientation of the three-dimensional endwall. Because of this, holes 1 and 2 near the peak of the endwall contour had surface inclination angles of 80° and 60°, respectively. Holes 3-5 had more modest surface inclination angles, ranging from 45° to 30°. In keeping with the methodology of the flat endwall, the injection directions for the contoured endwall were aligned with streaklines for that geometry. Lynch, et al. [11] noted that the endwall streaklines originating from the pressure side of the passage were less directed toward the suction side for the contoured endwall; thus, injection angles were slightly different than those of the flat endwall. L/d ratios for the contoured endwall holes ranged from 7 to 8.5.

Film-cooling flowrates were characterized by averaging the ideal blowing ratio (based on inviscid local velocities) for each hole to obtain a global average M_{ideal}. The ideal blowing ratio for each hole was determined through measurements of the plenum total pressure and the local endwall static pressure, where local endwall static pressure was measured in an adjacent passage without film cooling. The calculation of an individual hole's ideal blowing ratio was:

$$M_{ideal} = \frac{(\rho U)_c}{(\rho U)_{\infty,local}} = \sqrt{\frac{\rho_c}{\rho_\infty}\left(\frac{P_{o,plen} - P_{s,endwall}}{P_{o,in} - P_{s,endwall}}\right)} \tag{2.1}$$

The average ideal blowing ratio of all five holes was then determined and used to characterize the leakage:

$$\overline{M_{ideal}} = \sum_{k=1}^{N} M_{ideal,k} \Big/ N \tag{2.2}$$

This method for calculating ideal blowing ratio was also used to set the mass flow inlet conditions for the coolant plenum in the computational studies. The predicted mass flow rates into the plenum (as a percent of mainstream mass flow) at each ideal average blowing ratio in this study are listed in Table 2.3.

Uncertainty in adiabatic film cooling measurements was estimated with the partial derivative method of Moffat [30]. The largest contribution to uncertainty was the surface temperature measurement with the IR camera, which had a bias error of 0.6°C and a precision error of 0.2°C. Total uncertainty in adiabatic film cooling effectiveness was estimated to be $\partial\eta=\pm 0.04$ at a value of $\eta=0.3$.

Results and Discussion

Steady 3D RANS predictions for a flat and a contoured endwall were compared to experimental results. Flowfield validation is followed by comparisons to endwall heat transfer. Finally, measured film-cooling effectiveness with and without a contour is discussed and the resulting predictions are analyzed.

Cascade Exit Flowfield Predictions

A comparison of planar measurements (Knezevici, et al. [7]) and computational predictions for the flat and contoured endwalls (from the grids without film-cooling) is shown in Figure 2.7. The measurement plane is located at $X/C_{ax}=1.4$ downstream of the blade leading edge (see Figure 2.1). In Figure 2.7, line contours of total pressure loss coefficient (C_{Ptot}) are overlaid on flood contours of secondary kinetic energy coefficient (C_{SKE}). Comparisons of Figure 2.7a to Figure 2.7b indicate good agreement between measured and predicted C_{SKE} with the SST k-ω turbulence model for the flat endwall. The only exception is an underprediction of the magnitude of C_{SKE} very close to the endwall ($Z/S<0.05$). The predicted total pressure loss coefficient contours in Figure 2.7b show similar trends to the measurements in Figure 2.7a, especially in capturing the two distinct loss cores between $0.1<Z/S<0.2$. The predicted magnitudes of C_{Ptot} are higher, however, particularly in the loss cores and in the blade wake. While the difference might be partially due to limited spatial resolution in the experiment, it has also been shown that eddy-viscosity turbulence models tend to overpredict both secondary and midspan blade wake losses (Cleak and Gregory-Smith [31]).

The flat endwall predictions using the realizable k-ε turbulence model (Figure 2.7c) show poor agreement for both C_{SKE} and C_{Ptot} when compared to the measurements in Figure 2.7a. The peak magnitude of secondary kinetic energy is underpredicted and shifted closer to the endwall. There is a gross overprediction of the blade wake near midspan (Z/S=0.5), compared to the measurement. Also, the two distinct loss cores seen in the measurements are not apparent in the prediction in Figure 2.7c, which shows only a single loss core.

Knezevici, et al. [7] attributed the reduction in C_{SKE} and C_{Ptot} for the contoured endwall (Figure 2.7d) versus the flat endwall (Figure 2.7a) to reduced pitchwise cross-flow in the passage. This in turn weakened the passage vortex and reduced associated losses. The blending of the contour back to a flat wall at the trailing edge plane of the cascade increased pitchwise cross-flow, however, which is indicated by the higher near-wall C_{SKE} in Figure 2.7d. The prediction for the contoured endwall using the SST k-ω model (Figure 2.7e) shows good agreement for C_{SKE} but, as was seen for the flat endwall, continues to overpredict C_{Ptot} in the loss cores and the blade profile loss. Overall, the measured trends between the flat and contoured endwalls appear to be well-replicated by the use of the SST k-ω model, even if C_{Ptot} magnitudes are not. The realizable k-ε model (Figure 2.7f) again results in poor predictions. Interestingly, a predicted 30 percent reduction in the peak C_{SKE} between Figure 2.7c and Figure 2.7f compares reasonably to the measured percent reduction of approximately 24%, suggesting that perhaps trends between the flat and contoured endwall are being correctly predicted.

Figure 2.8 and Figure 2.9 compare spanwise distributions of C_{SKE} and C_{Ptot} extracted from the measured and predicted flowfields. In Figure 2.8, C_{SKE} distributions are plotted at Y/P=0.3, which passes through the peak of secondary kinetic energy coefficient. The SST k-ω model prediction demonstrates very good agreement in peak C_{SKE} at Z/S=0.15 for the flat endwall, but underpredicts C_{SKE} below Z/S=0.08. The contoured endwall prediction with the SST k-ω model is not quite as good around the peak C_{SKE} as for the flat endwall, suggesting some physics of the contouring may not be as well captured. The realizable k-ε model does not reproduce the location or magnitude of the peak C_{SKE} for the flat or contoured endwall.

The spanwise distribution of C_{Ptot} in Figure 2.9 is taken at Y/P=0.2, which passes through the peak of the leftmost total pressure loss core in Figure 2.7a-f. As noted earlier, neither turbulence model correctly captured the magnitude of total pressure loss cores; however, the SST k-ω model predicts the peak C_{Ptot} to occur at the same location in the flowfield (Z/S=0.17) as

indicated by the measurements. In contrast, the realizable k-ε predicts the total pressure loss peak to occur at Z/S=0.14.

The difference in prediction accuracy between the two turbulence models examined here seems to have important implications for non-axisymmetric endwall design. As noted earlier, three-dimensional endwall contours in the published literature have generally been designed through computational optimization coupled to a RANS-based solver. It would appear from the results presented here that a RANS-based contour design methodology might be sensitive to not only the variable or variables being optimized (e.g., C_{SKE}, C_{Ptot}), but also to the turbulence model employed in the optimization routine. To the authors' knowledge, this is an area that has not received much attention as of yet.

Endwall Heat Transfer Predictions

Comparisons of flat endwall heat transfer predictions to the measurements of Lynch, et al. [11] are shown in Figure 2.10. The SST k-ω model results in a significant overprediction of Nu in the passage, particularly near and downstream of the trailing edge plane. There is a region of high Nu upstream of a small island of low Nu near the blade pressure side toward the leading edge in Figure 2.10b, which is not seen in the measurements (Figure 2.10a). Also, the prediction indicates low heat transfer very close to the blade suction side in the aft part of the passage. The realizable k-ε prediction of flat endwall heat transfer is shown in Figure 2.10c. This model results in better agreement to Figure 2.10a in the forward portion of the passage, and does not exhibit the unique low-Nu regions seen in Figure 2.10b. Toward the aft portion of the passage in Figure 2.10c, however, the realizable k-ε prediction also indicates higher Nu than was measured. The improvement of the realizable k-ε over the SST k-ω model prediction seems to be in opposition to the conclusions from the earlier flowfield comparisons, although neither turbulence model produces satisfactory heat transfer predictions over the entire endwall.

Figure 2.11presents contours of heat transfer augmentation, where positive augmentation values indicate an increase in heat transfer for the contour versus the flat endwall and negative values indicate a reduction. Lynch, et al. [11] noted that the contour tends to increase heat transfer near the saddle point where heat transfer is nominally low, but also reduce it near the pressure side-endwall junction where heat transfer is nominally high. These two effects are somewhat reproduced in the SST k-ω prediction in Figure 2.11b, although there are some notable differences. The magnitude of heat transfer augmentation around the saddle point is significantly

higher than the measured augmentation in Figure 2.11a. Also, the SST k-ω model predicts larger reductions in contoured endwall heat transfer (large negative augmentation values) near the pressure side than is indicated by the measurements in Figure 2.11a. The region of large negative augmentation values in Figure 2.11b does not persist near the pressure side in the aft portion of the passage, but instead crosses the passage toward the suction side.

Heat transfer augmentation with the realizable k-ε model in Figure 2.11c agrees fairly well with the measurements (Figure 2.11a), particularly regarding the magnitudes of augmentation in the saddle point region and in the region of heat transfer reduction near the pressure side. Like the SST k-ω prediction, however, the heat transfer reduction region near the pressure side is not as large or as close to the blade-endwall junction as is indicated in the measurements.

Line plots of heat transfer augmentation in Figure 2.12 were created by extracting data from Figure 2.11 along an inviscid streamline passing through a point located 25% of the pitch (0.25P) from the blade leading edge in the pitch direction. The extracted data and an inset showing the 0.25P streamline are shown in Figure 2.12. The 0.25P streamline passes through the region of high heat transfer augmentation near the saddle point, as well as through the region of heat transfer reduction near the pressure side. Note that the magnitude of augmentation around the saddle point ($X/C_{ax}\approx0.15$) is overpredicted by the SST k-ω model but underpredicted by the realizable k-ε model, although both models capture the axial location of the peak augmentation. Unfortunately, the location of the largest heat transfer reduction (large negative augmentation values) beyond $X/C_{ax}=0.4$ in Figure 2.12 is not as well-predicted, with the measurements indicating that this region is spread out nearly to the trailing edge plane. The discrepancy in the predictions downstream of $X/C_{ax}=0.4$ is not unexpected given the poor agreement between the predicted and measured flat endwall heat transfer in the aft portion of the passage in Figure 2.10. This mis-prediction of the augmentation, however, could conceivably affect the optimal shape for an endwall design that attempts to incorporate endwall heat transfer as an optimization variable.

Film-Cooling Measurements and Predictions

Measurements of flat endwall adiabatic film-cooling effectiveness for two average ideal blowing ratios ($\overline{M_{ideal}}$) are presented in Figure 2.13a-b. The influence of the cross-passage flow near the endwall is apparent in the sweeping of the coolant from the pressure to suction side,

which provides some coverage over the aft portion of the passage. In Figure 2.13a, holes 3-5 toward the trailing edge appear to be providing more endwall cooling than holes 1 and 2. The exits of holes 1 and 2 are located in a region of higher pressure relative to the exits of holes 3-5, and thus for a given plenum total pressure, more massflow is ejected through the downstream holes where the pressure differential is larger. In Figure 2.13b, nearly all of the jets lift off the endwall at the average ideal blowing ratio of 2.0.

Based on the close comparison of the SST k-ω turbulence model to the measured exit flowfield, it was selected in this study for predictions of endwall adiabatic effectiveness. The predictions for the flat endwall over a range of $\overline{M_{ideal}}$ are shown in Figure 2.13c-d. The trend of coolant sweeping from the pressure to suction side is visible in the predictions, and Figure 2.13d also indicates jet lift-off for $\overline{M_{ideal}}$=2.0. However, jet spreading appears to be underpredicted, while peak (centerline) effectiveness is overpredicted. This is a common problem for two-equation models (Walters and Leylek [32], Bogard and Thole [33]).

Film-cooling effectiveness values downstream of hole 3 were extracted from the contour plots in Figure 2.13 to provide quantitative comparisons in Figure 2.14and Figure 2.15. These figures contain plots of maximum and laterally-averaged effectiveness along the jet direction. Since the jet trajectory downstream of hole 3 curves slightly as it moves toward the suction side, the abscissa of Figure 2.14 and Figure 2.15 is streamwise distance downstream of the hole exit along the direction of maximum effectiveness, normalized by the hole diameter. The extent of lateral averaging in Figure 2.15was limited to half of the hole pitch (pitch≈4d) on either side of hole 3.

In Figure 2.14, maximum effectiveness is significantly overpredicted downstream of hole 3 for $\overline{M_{ideal}}$=1.0. For the highest blowing ratio, the prediction indicates better jet re-attachment than was seen in the experiment. Figure 2.15shows good agreement in laterally-averaged effectiveness, however, for the average ideal blowing ratio of 1.0. The laterally-averaged effectiveness of the detached jet at $\overline{M_{ideal}}$=2.0 is not accurately simulated, with the prediction indicating much higher average effectiveness downstream of s/d=5. The performance of the SST k-ω model for maximum and laterally-averaged effectiveness is consistent with simulations of film-cooling presented in the literature (Harrison and Bogard [20], Na, et al. [34]).

The contoured endwall film-cooling measurements are shown in Figure 2.16a-b. Recall that holes 1 and 2 were required to have surface inclination angles of 80° and 60° due to manufacturing considerations so jet blow-off is expected. As the average ideal blowing ratio increases to $\overline{M_{ideal}}$ =2.0, all of the jets have so much momentum that they detach from the surface.

Comparisons of the contoured endwall film coverage (Figure 2.16a-b) to the flat endwall measurements (Figure 2.13a-b) indicate that, in general, the cooling coverage is less spread out across an endwall with a three-dimensional contour. Furthermore, cooling jets from holes 1 and 2 in the contoured endwall are more aligned with the inviscid flow direction than the corresponding jets on the flat endwall. The effect of the contour ridge in reducing cross-passage flow has also resulted in a tendency to limit the spread of coolant across the passage. This is an important point for a designer to consider when developing a film-cooling pattern, since the development might be based off of previous experience with flat endwalls.

Contoured endwall film cooling predictions in Figure 2.16c-d reproduce the measured endwall coverage pattern indicated in Figure 2.16a-b. As was seen for the flat endwall, jet spreading and maximum effectiveness were under- and overpredicted, respectively. In Figure 2.17, laterally-averaged effectiveness downstream of hole 3 for $\overline{M_{ideal}}$ =1.0 is plotted for the flat and contoured endwall measurements, as well as for their respective predictions. Note that hole 3 has a surface inclination angle of 40° for the flat endwall and 45° for the contoured endwall. Figure 2.17 shows that the contour has reduced effectiveness compared to the flat endwall, although a direct comparison is somewhat complicated by the difference in surface inclination angles. The prediction of laterally-averaged effectiveness for the contour is higher than the experiment. This may be due to a mis-prediction of the near-wall flowfield with endwall contouring in this region; recall in Figure 2.11b that the heat transfer augmentation was also mis-predicted near the pressure side-endwall junction.

Conclusions

Computational simulations of a flat and non-axisymmetric contoured endwall were performed with a steady RANS code and compared to exit flowfield, endwall heat transfer, and endwall film cooling effectiveness measurements. The computations compared two turbulence models (SST k-ω and realizable k-ε) for predictions of the exit flowfield and endwall heat transfer. For the SST k-ω model, predicted secondary kinetic energy agreed well with flat

endwall measurements above 8% span but underpredicted C_{SKE} below that span. Predictions for the contoured endwall were not quite as good as for the flat endwall, suggesting that RANS models may not be fully capturing the physics of contouring. Total pressure loss predictions of the flat and contoured endwalls indicated similar loss structures but the magnitude of loss was overpredicted. The realizable k-ε model significantly underpredicted secondary kinetic energy and did not accurately capture either the structure or magnitude of total pressure loss.

The SST k-ω model and the realizable k-ε model significantly overpredicted flat endwall heat transfer in the passage. Measured heat transfer for a contoured versus flat endwall was augmented around the saddle point but reduced near the pressure side. These trends were reproduced in the SST k-ω and realizable k-ε simulations, although the level of augmentation was overpredicted by the SST k-ω model.

Film cooling holes were placed in the region of high heat transfer near the pressure side-endwall junction for both the flat and contoured endwall geometries. Measured effectiveness illustrated the effect of the cross-passage flow on the spreading of coolant over the flat endwall, and the tendency for jet lift-off at high blowing ratios. Predictions for the flat endwall using the SST k-ω model replicated these trends, with good agreement in laterally-averaged effectiveness. The application of endwall contouring was shown to reduce the spreading of coolant across the endwall, due to the reduction in cross-passage flow with a contour. Effectiveness simulations duplicated the measured trends, but overpredicted laterally-averaged effectiveness.

Overall, the steady RANS simulations demonstrated good predictions of secondary kinetic energy and endwall film-cooling effectiveness, but poor predictions of total pressure loss and endwall heat transfer. Improving the latter appears to be the next major hurdle in increasing axial turbine efficiency and durability through fully optimal aerodynamic and thermal designs.

Acknowledgments

The authors gratefully acknowledge United Technologies—Pratt & Whitney for their support of this work, and Eunice Allen-Bradley for performing the endwall contour design. We also would like to thank Daniel Knezevici and Dr. Steen Sjolander for providing us with a copy of the experimental dataset for the cascade exit flowfield.

Nomenclature

BL	boundary layer
C	true chord of blade
C_{ax}	axial chord of blade
C_p	specific heat at constant pressure, or static pressure coefficient, $C_p = \left(P_s - P_{s,in}\right) \Big/ 0.5\rho\overline{U}_{\infty,in}^2$
C_{Ptot}	total pressure loss coefficient, $C_{Ptot} = \left(P_{tot} - P_{tot,\infty,in}\right) \Big/ 0.5\rho\overline{U}_{\infty,in}^2$
C_{SKE}	secondary kinetic energy coefficient, $C_{SKE} = \left(V_n^2 + V_z^2\right) \Big/ \overline{U}_{\infty,in}^2$
d	film-cooling hole diameter
h	heat transfer coefficient, $h = q''_w \big/ \left(T_w - T_{\infty,in}\right)$
H	boundary layer shape factor
k	thermal conductivity, or turbulent kinetic energy
L	film-cooling hole length
$\dot{m}$	mass flow rate
M_{ideal}	ideal (lossless) blowing ratio, see Eq. 2.1
$\overline{M_{ideal}}$	average ideal blowing ratio, see Eq. 2.2
N	total number of film holes
Nu	Nusselt number, $Nu = hC_{ax} / k_{air}$
P	blade pitch
P_s	static pressure
P_{tot}	total pressure
q''_w	wall heat flux
Re_s	boundary layer Reynolds number, $Re_s = s\overline{U}_\infty / \nu$
Re_θ	momentum thickness Reynolds number, $Re_\theta = \theta\overline{U}_\infty / \nu$
s	streamwise distance along maximum film effectiveness, or distance downstream of start of BL
S	blade span
SST	Shear Stress Transport

St	Stanton number, $St = h/\rho C_p \overline{U}_\infty$
T	temperature
T_{back}	average background temperature associated with radiation reflected off a surface from its surroundings
Tu	freestream turbulence intensity
X, Y, Z	global coordinates, where X is blade axial direction
U, V, W	velocity components aligned with global coordinates
$\overline{U}$	streamwise velocity
V_n	pitchwise component of mean velocity on a plane normal to the mass-averaged velocity vector, $V_n = -U\sin\left(\overline{\overline{\alpha}}\right) + V\cos\left(\overline{\overline{\alpha}}\right)$
V_z	spanwise component of mean velocity on a plane normal to the mass-averaged velocity vector, $V_z = W$

Greek

$\overline{\overline{\alpha}}$	mass-averaged yaw angle
δ_{99}	boundary layer thickness (99%)
ε	emissivity, or turbulent dissipation
η	adiabatic effectiveness, $\eta = (T_\infty - T_{aw})/(T_\infty - T_c)$
$\overline{\eta}$	laterally averaged adiabatic effectiveness
θ	momentum thickness
ν	kinematic viscosity
ρ	density
ω	specific dissipation, $\omega \propto \varepsilon/k$

Subscripts/Superscripts

aw	adiabatic wall conditions
exit	exit conditions
c	coolant conditions
in	inlet conditions
k	k-th film cooling hole

max	maximum value
w	wall conditions
∞	local freestream conditions

References

[1] Harvey, N. W., Rose, M. G., Taylor, M. D., Shahpar, S., Hartland, J., and Gregory-Smith, D. G., 2000, "Nonaxisymmetric Turbine End Wall Design: Part I--- Three-Dimensional Linear Design System," *Journal of Turbomachinery*, **122**(2), pp. 278-285.

[2] Hartland, J. C., Gregory-Smith, D. G., Harvey, N. W., and Rose, M. G., 2000, "Nonaxisymmetric Turbine End Wall Design: Part II---Experimental Validation," *Journal of Turbomachinery*, **122**(2), pp. 286-293.

[3] Nagel, M. G., and Baier, R.-D., 2005, "Experimentally Verified Numerical Optimization of a Three-Dimensional Parametrized Turbine Vane with Nonaxisymmetric End Walls," *Journal of Turbomachinery*, **127**(2), pp. 380-387.

[4] Germain, T., Nagel, M., Raab, I., Schupbach, P., Abhari, R. S., and Rose, M., 2010, "Improving Efficiency of a High Work Turbine Using Nonaxisymmetric Endwalls--- Part I: Endwall Design and Performance," *Journal of Turbomachinery*, **132**(2), pp. 021007.

[5] Schuepbach, P., Abhari, R. S., Rose, M. G., Germain, T., Raab, I., and Gier, J., 2010, "Improving Efficiency of a High Work Turbine Using Nonaxisymmetric Endwalls---Part II: Time-Resolved Flow Physics," *Journal of Turbomachinery*, **132**(2), pp. 021008.

[6] Praisner, T. J., Allen-Bradley, E., Grover, E. A., Knezevici, D. C., and Sjolander, S. A., 2007, "Application of Non-Axisymmetric Endwall Contouring to Conventional and High-Lift Turbine Airfoils," Proc. ASME Turbo Expo 2007, Paper No. GT2007-27579.

[7] Knezevici, D. C., Sjolander, S. A., Praisner, T. J., Allen-Bradley, E., and Grover, E. A., 2010, "Measurements of Secondary Losses in a Turbine Cascade with the Implementation of Nonaxisymmetric Endwall Contouring," *Journal of Turbomachinery*, **132**(1), pp. 011013.

[8] Knezevici, D. C., Sjolander, S. A., Praisner, T. J., Allen-Bradley, E., and Grover, E. A., 2009, "Measurements of Secondary Losses in a High-Lift Front-Loaded Turbine Cascade with the Implementation of Non-Axisymmetric Endwall Contouring," Proc. ASME Turbo Expo 2009, Paper No. GT2009-59677.

[9] Saha, A. K., and Acharya, S., 2008, "Computations of Turbulent Flow and Heat Transfer through a Three-Dimensional Nonaxisymmetric Blade Passage," *Journal of Turbomachinery*, **130**(3), pp. 031008.

[10] Mahmood, G. I., and Acharya, S., 2007, "Measured Endwall Flow and Passage Heat Transfer in a Linear Blade Passage with Endwall and Leading Edge Modifications," Proc. ASME Turbo Expo 2007, Paper No. GT2007-28179.

[11] Lynch, S. P., Sundaram, N., Thole, K. A., Kohli, A., and Lehane, C., 2009, "Heat Transfer for a Turbine Blade with Non-Axisymmetric Endwall Contouring," Proc. ASME Turbo Expo 2009, Paper No. GT2009-60185.

[12] Okita, Y., and Nakamata, C., 2008, "Computational Predictions of Endwall Film Cooling for a Turbine Nozzle Vane with an Asymmetric Contoured Passage," Proc. ASME Turbo Expo 2008, Paper No. GT2008-50878.

[13] Gustafson, R., Mahmood, G. I., and Acharya, S., 2007, "Flowfield in a Film-Cooled Three-Dimensional Contoured Endwall Passage: Aerodynamic Measurements," Proc. ASME Turbo Expo 2007, Paper No. GT2007-28154.

[14] Mahmood, G. I., Gustafson, R., and Acharya, S., 2009, "Flow Dynamics and Film Cooling Effectiveness on a Non-Axisymmetric Contour Endwall in a Two Dimensional Cascade Passage," Proc. ASME Turbo Expo 2009, Paper No. GT2009-60236.

[15] "FLUENT" (version 6.3.26), Fluent, Inc., Lebanon, NH.

[16] Menter, F. R., 1994, "Two-Equation Eddy-Viscosity Turbulence Models for Engineering Applications," *AIAA Journal*, **32**(8), pp. 1598-1605.

[17] Schwaenen, M., and Duggleby, A., 2009, "Identifying Inefficiencies in Unsteady Pin Fin Heat Transfer," Proc. ASME Turbo Expo 2009, Paper No. GT2009-60219.

[18] Snedden, G., Dunn, D., Ingram, G., and Gregory-Smith, D., 2009, "The Application of Non-Axisymmetric Endwall Contouring in a Single Stage, Rotating Turbine," Proc. ASME Turbo Expo 2009, Paper No. GT2009-59169.

[19] Shih, T.-H., Liou, W. W., Shabbir, A., Yang, Z., and Zhu, J., 1995, "A New K-[Epsilon] Eddy Viscosity Model for High Reynolds Number Turbulent Flows," *Computers & Fluids*, **24**(3), pp. 227-238.

[20] Harrison, K., and Bogard, D. G., 2008, "Comparison of RANS Turbulence Models for Prediction of Film Cooling Performance," Proc. ASME Turbo Expo 2008, Paper No. GT2008-51423.

[21] Yang, H., Acharya, S., Ekkad, S., Prakash, C., and Bunker, R. S., 2002, "Flow and Heat Transfer Predictions for a Flat-Tip Turbine Blade," Proc. ASME Turbo Expo, Paper No. GT2002-30190.

[22] Hermanson, K., Kern, S., Picker, G., and Parneix, S., 2003, "Predictions of External Heat Transfer for Turbine Vanes and Blades with Secondary Flowfields," *Journal of Turbomachinery*, **125**(1), pp. 107-113.

[23] 2009, "Ansys ICEM CFD" (version 11.0), ANSYS Inc., Canonsburg, PA.

[24] Crawford, M. E., 2009, "Texstan" (version academic), University of Texas, Austin, TX.

[25] Kays, W. M., and Crawford, M. E., 1980, *Convective Heat and Mass Transfer*, McGraw-Hill, Inc., New York.

[26] Bons, J. P., Sondergaard, R., and Rivir, R. B., 2001, "Turbine Separation Control Using Pulsed Vortex Generator Jets," *Journal of Turbomachinery*, **123**(2), pp. 198-206.

[27] Mcauliffe, B. R., and Sjolander, S. A., 2004, "Active Flow Control Using Steady Blowing for a Low-Pressure Turbine Cascade," *Journal of Turbomachinery-Transactions of the ASME*, **126**(4), pp. 560-569.

[28] Popovic, I., Zhu, J., Dai, W., Sjolander, S. A., Praisner, T. J., and Grover, E. A., 2006, "Aerodynamics of a Family of Three Highly Loaded Low-Pressure Turbine Airfoils: Measured Effects of Reynolds Number and Turbulence Intensity in Steady Flow," Proc. ASME Turbo Expo 2006, Paper No. GT2006-91271.

[29] Zoric, T., Popovic, I., Sjolander, S. A., Praisner, T. J., and Grover, E. A., 2007, "Comparative Investigation of Three Highly Loaded LP Turbine Airfoils: Part I: Measured Profile and Secondary Losses at Design Incidence," Proc. ASME Turbo Expo 2007, Paper No. GT2007-27537.

[30] Moffat, R. J., 1988, "Describing the Uncertainties in Experimental Results," *Experimental Thermal and Fluid Science*, **1**, pp. 3-17.

[31] Cleak, J. G. E., and Gregory-Smith, D. G., 1992, "Turbulence Modeling for Secondary Flow Prediction in a Turbine Cascade," *Journal of Turbomachinery*, **114**(3), pp. 590-598.

[32] Walters, D. K., and Leylek, J. H., 2000, "A Detailed Analysis of Film-Cooling Physics: Part I---Streamwise Injection with Cylindrical Holes," *Journal of Turbomachinery*, **122**(1), pp. 102-112.

[33] Bogard, D. G., and Thole, K. A., 2006, "Gas Turbine Film Cooling," *Journal of Propulsion and Power*, **22**(2), pp. 249-270.

[34] Na, S., Zhu, B., Bryden, M., and Shih, T. I.-P., 2006, "CFD Analysis of Film Cooling," Proc. 44th AIAA Aerospace Sciences Meeting and Exhibit, Paper No. AIAA-2006-0022.

Table 2.1 Comparison of Inlet Boundary Conditions

	Lynch, et al. [11]	TEXSTAN	FLUENT, SST k-ω	FLUENT, realizable k-ε	Knezevici, et al. [7]	FLUENT, SST k-ω
C_{ax} [mm]	218.4	218.4	218.4	218.4	75.4	218.4
S [mm]	546	546	546	546	203.2	546
Measurement location (axial)	$-2.33C_{ax}$	$-2.33C_{ax}$	$-2.33C_{ax}$	$-2.33C_{ax}$	$-1.2C_{ax}$	$-1.2C_{ax}$
δ/S	0.061	0.066	0.069	0.074	0.095	0.085
θ/S	0.0046	0.0046	0.0046	0.0047	0.0079	0.0058
Re_θ	1330	1330	1330	1340	2660	1670
H	1.3	1.3	1.3	1.3	1.2	1.3
Tu	6%	6%	6%	6%	4%	6%

Table 2.2 Blade Geometry and Flow Conditions

Number of blades	7
Scale factor	8.6
Axial chord (C_{ax})	0.218 m
True chord (C)	0.241 m
Pitch/chord (P/C_{ax})	0.826
Span/chord (S/C_{ax})	2.50
Inlet Re $\left(Re_{in} = C_{ax} U_{\infty,in} / \nu\right)$	1.25×10^5
Exit Re $\left(Re_{exit} = C_{ax} U_{\infty,exit} / \nu\right)$	2.00×10^5
Inlet velocity ($U_{\infty,in}$)	8.7 m/s
Inlet, exit flow angles	35°, 60°
Inlet, exit Mach	0.026, 0.042

Table 2.3 Ideal Blowing Ratios and Flowrates

	$\overline{M_{ideal}}$	$\dot{m}_c / \dot{m}_\infty$ (from CFD)
Flat	1.0	0.038%
Flat	2.0	0.088%
Contour	1.0	0.038%
Contour	2.0	0.088%

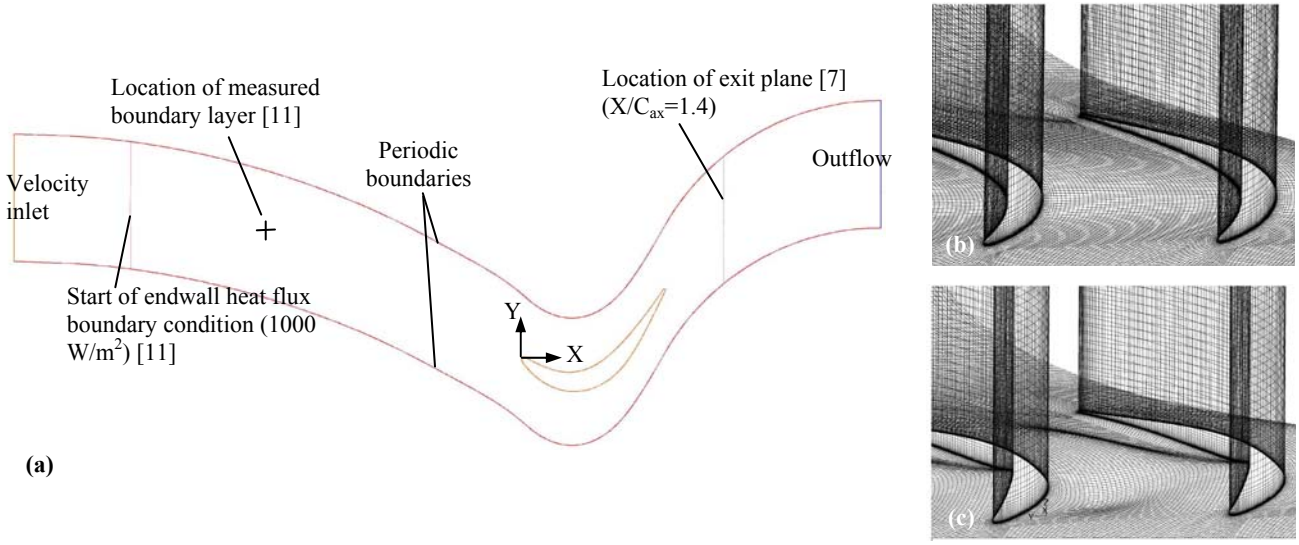

Figure 2.1. Depictions of (a) the computational domain and boundary conditions; (b) the flat endwall grid; and (c) the contoured endwall grid.

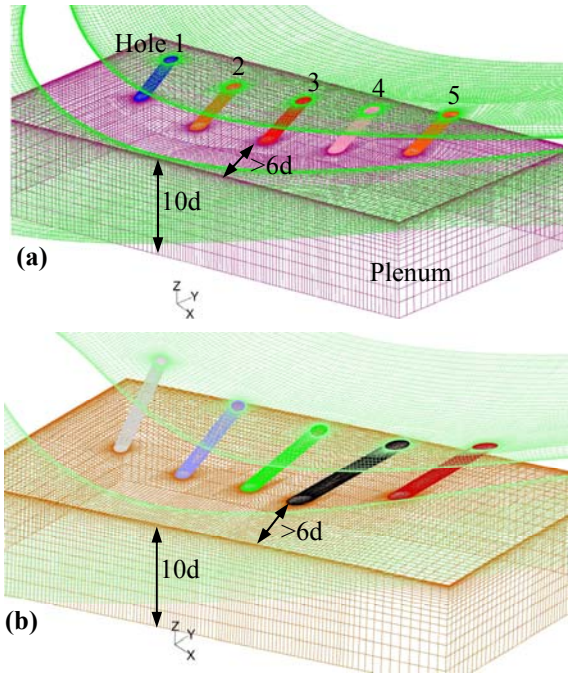

Figure 2.2. Depiction of (a) the flat endwall film-cooling grid and hole nomenclature; and (b) the contoured endwall film-cooling grid.

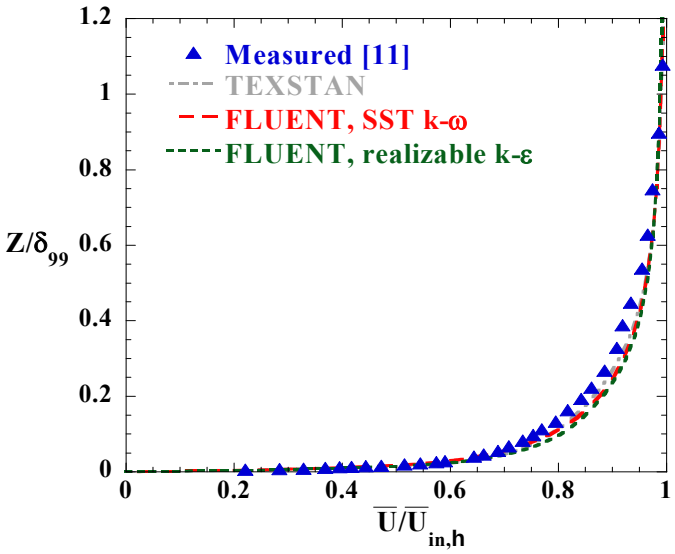

Figure 2.3. Measurement [11] and predictions of the boundary layer at X/C_{ax}=-2.33 upstream of the blade.

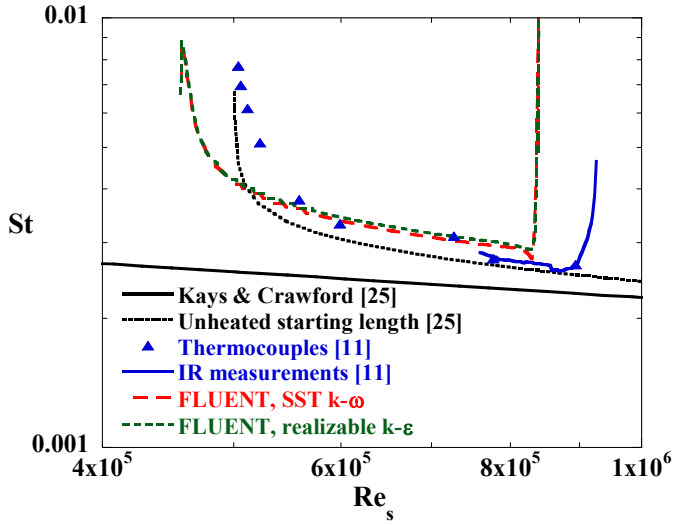

Figure 2.4. Measurements [11] and predictions of the endwall heat transfer upstream of the cascade.

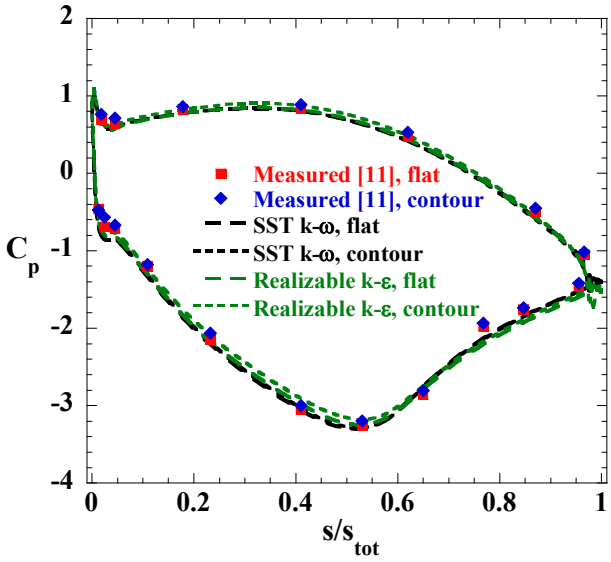

Figure 2.5. Measured [11] and predicted blade surface static pressure at midspan.

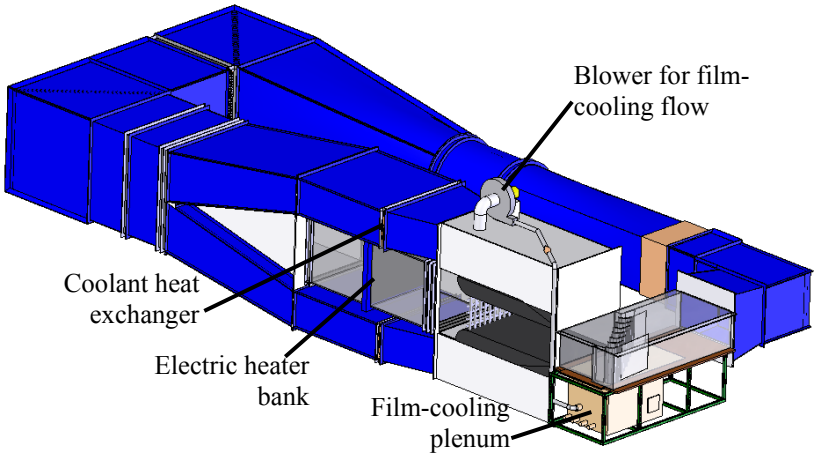

Figure 2.6. Depiction of the large-scale low-speed wind tunnel, with piping for the film-cooling studies.

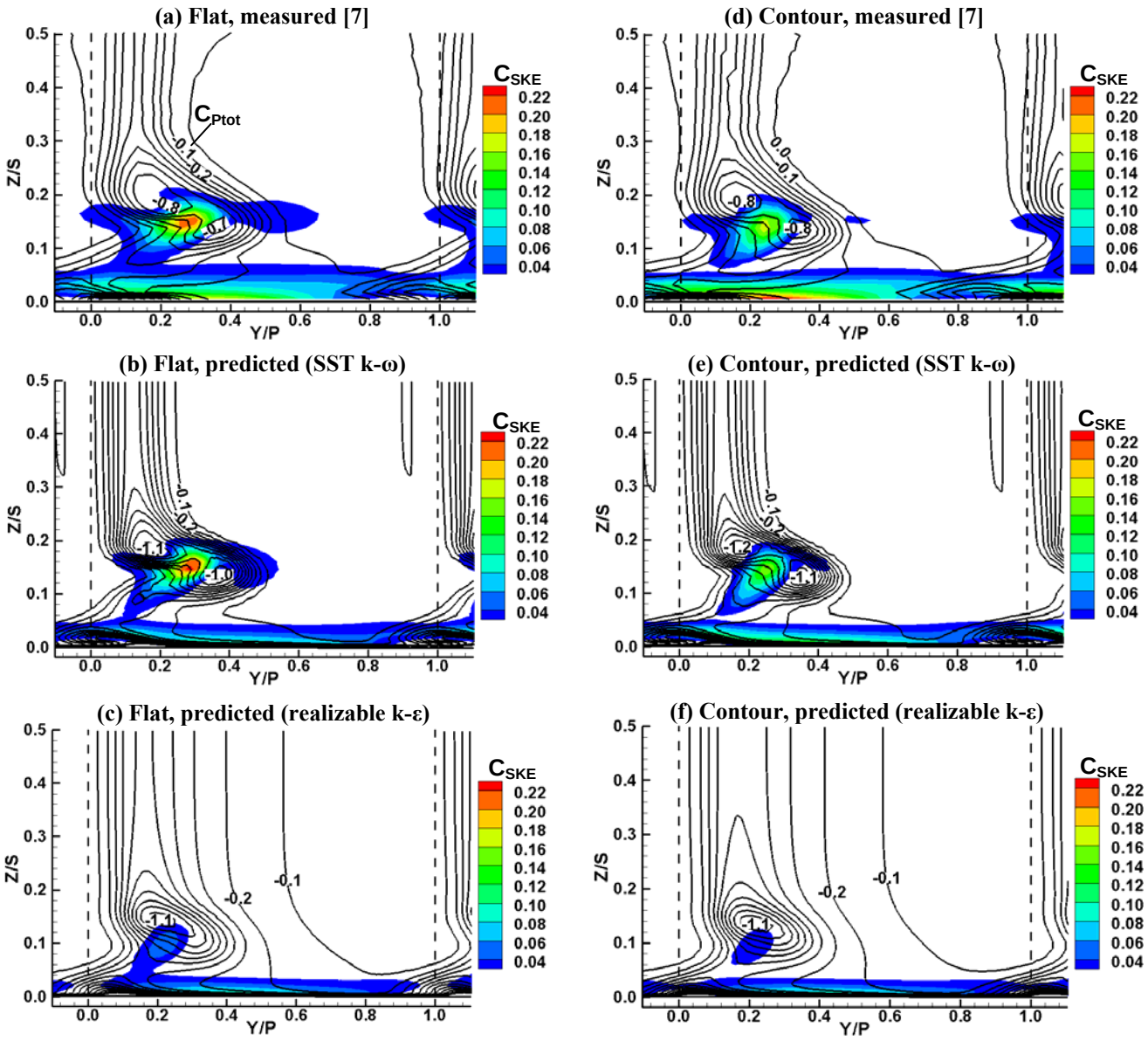

Figure 2.7. Line contours of C_{Ptot} overlaid with flood contours of C_{SKE} at X/C_{ax}=1.4, for the flat endwall (a-c) and the contoured endwall (d-f).

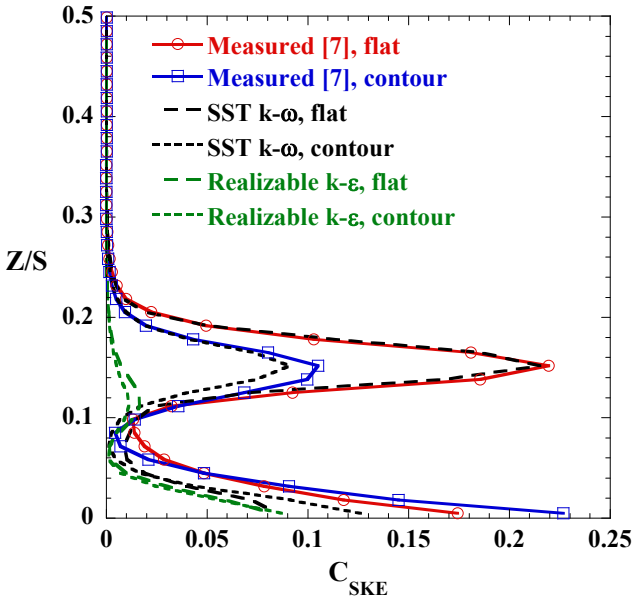

Figure 2.8. Comparison of measured [7] and predicted C_{SKE}, extracted from Figure 2.7 at Y/P=0.3.

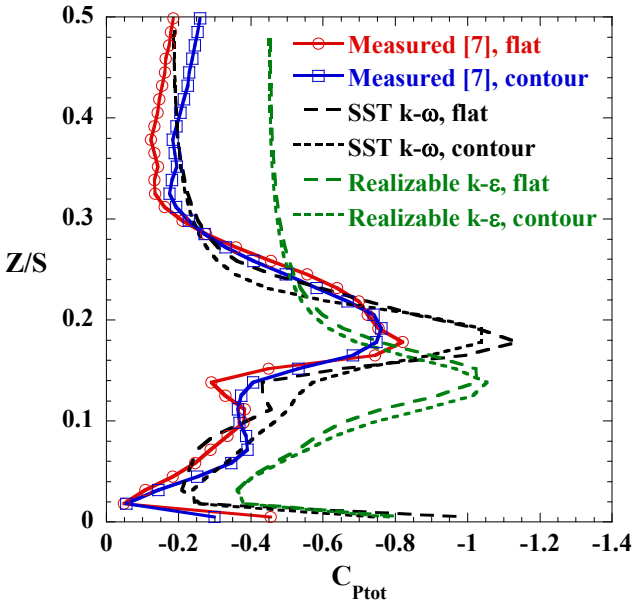

Figure 2.9. Comparison of measured [7] and predicted C_{Ptot}, extracted from Figure 2.7 at Y/P=0.2.

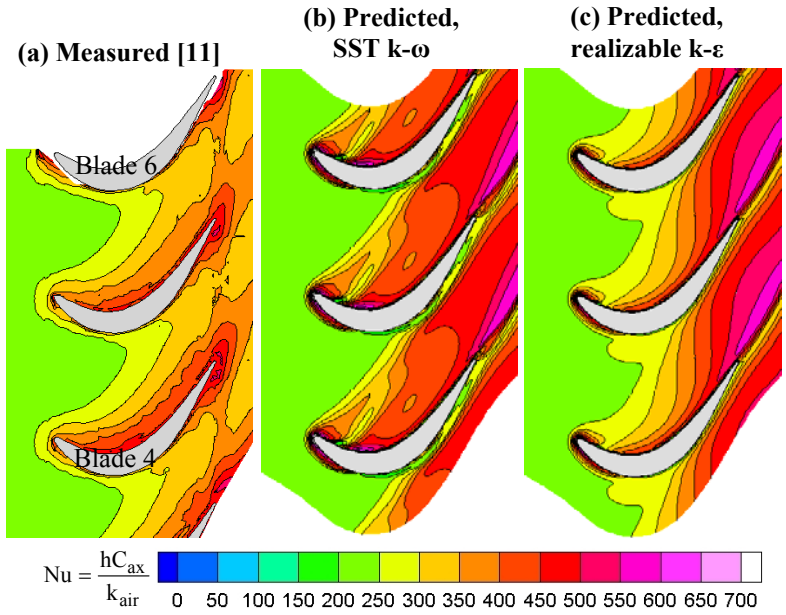

Figure 2.10. Flat endwall heat transfer; (a) measured [11], (b) predicted with SST k-ω, and (c) predicted with realizable k-ε.

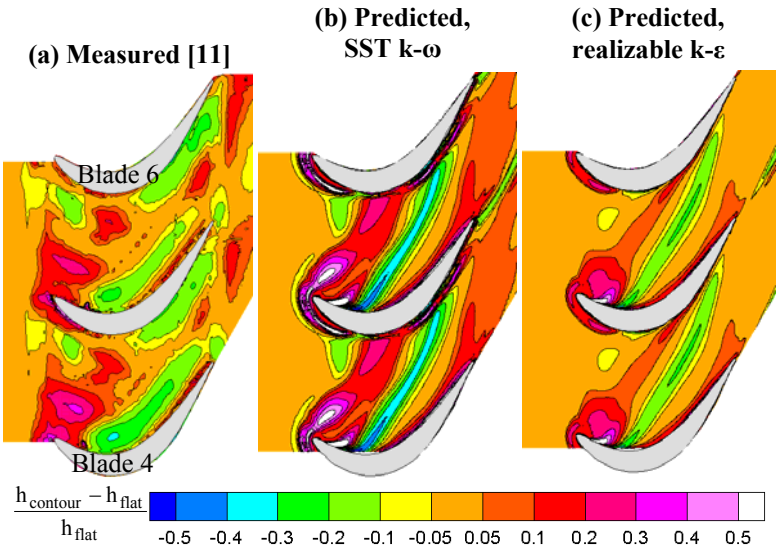

Figure 2.11. Endwall heat transfer augmentation; (a) measured [11], (b) predicted with SST k-ω, and (c) predicted with realizable k-ε.

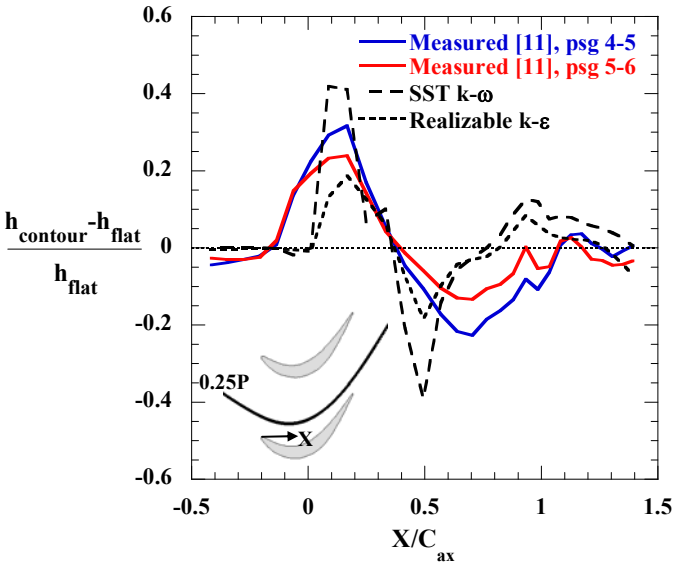

Figure 2.12. Heat transfer augmentation for the contoured versus flat endwall, extracted along an inviscid streamline passing through 0.25P.

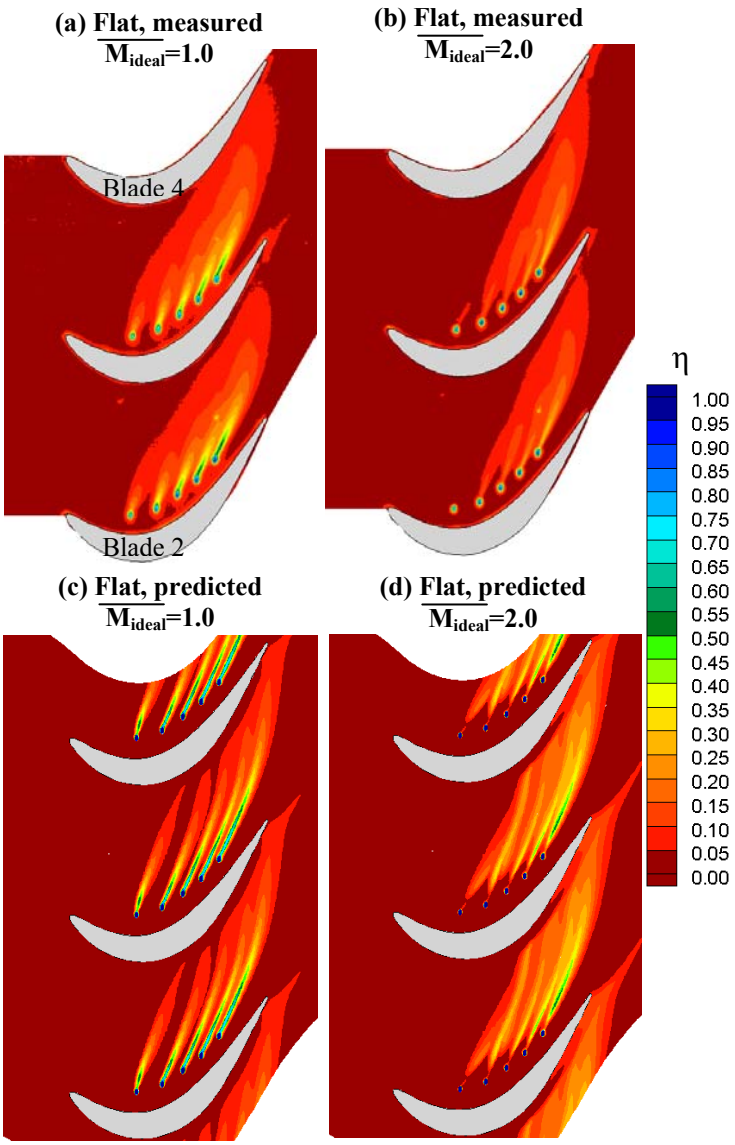

Figure 2.13. Flat endwall film-cooling effectiveness measurements (a-b), and predictions (c-d) using the SST k-ω model.

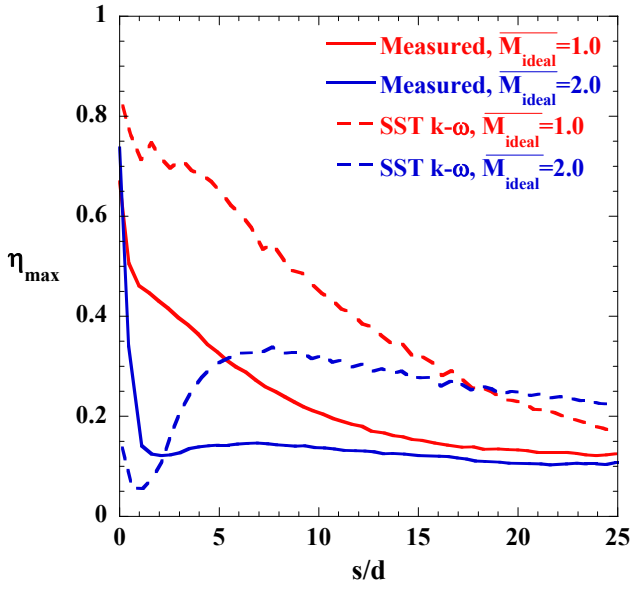

Figure 2.14. Maximum effectiveness downstream of hole 3, for the flat endwall.

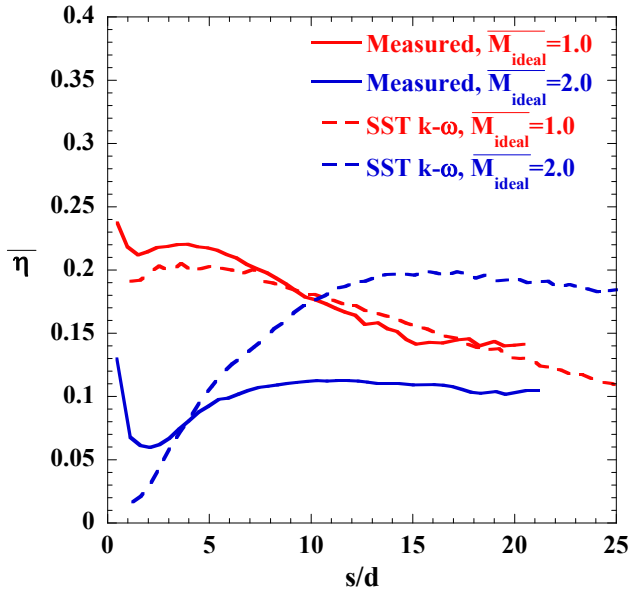

Figure 2.15. Laterally-averaged effectiveness down-stream of hole 3, for the flat endwall.

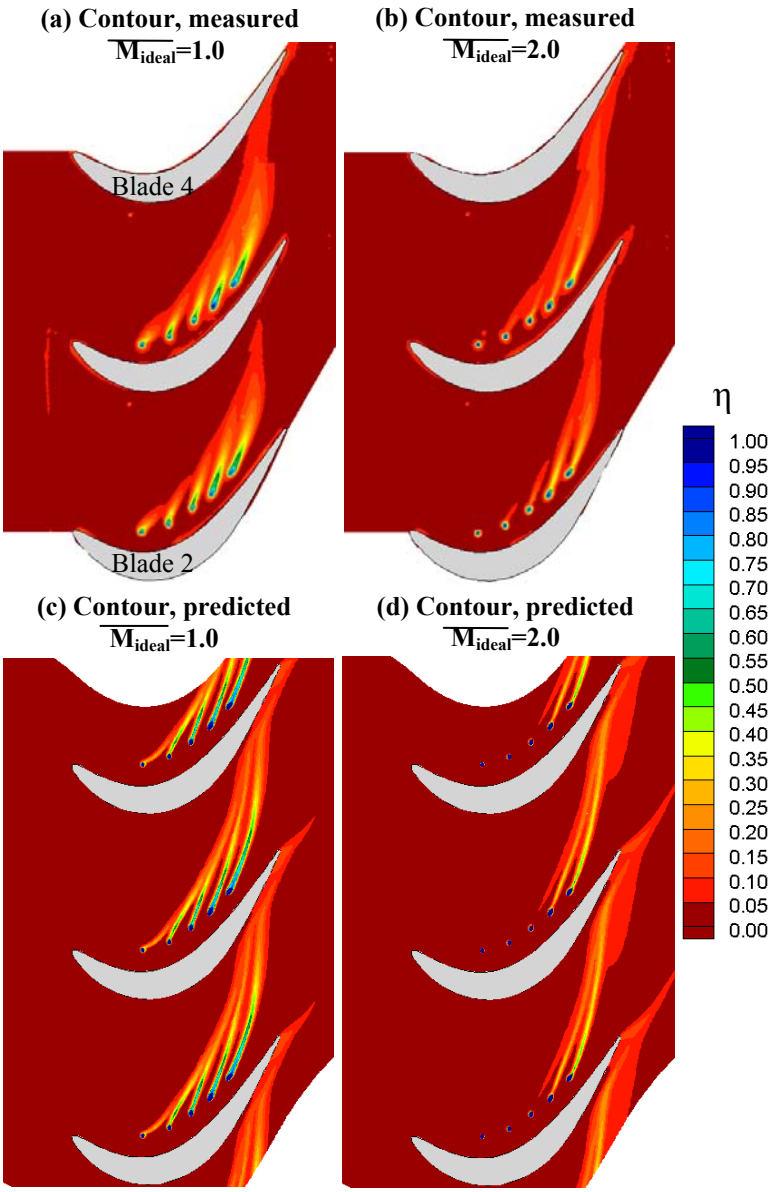

Figure 2.16. Contoured endwall film-cooling effectiveness measurements (a-b) and predictions (c-d) using the SST k-ω model.

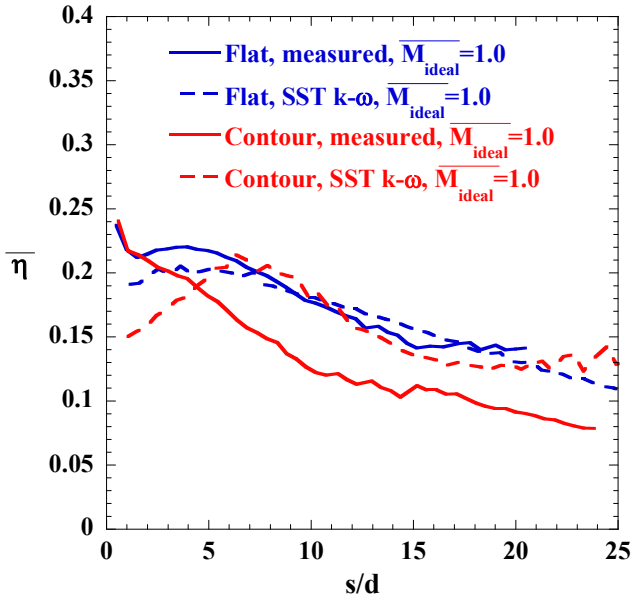

Figure 2.17. Laterally-averaged effectiveness down-stream of hole 3, for the contoured versus flat endwalls.

Paper 3: Investigation of the Three-Dimensional Boundary Layer on a Turbine Endwall with Non-axisymmetric Contouring

To be submitted to the *International Journal of Heat and Mass Transfer**

Abstract

The boundary layer on the endwall of an axial turbomachine passage is influenced by streamwise and cross-stream pressure gradients, as well as a large streamwise vortex, that develop in the passage. These influences distort the structure of the boundary layer and result in heat transfer and friction coefficients that differ significantly from simple two-dimensional boundary layers. Three-dimensional contouring of the endwall has been shown to reduce the strength of the large streamwise vortex and reduce endwall heat transfer, but the mechanisms of the reductions are not well understood, primarily due to an incomplete understanding of the complex nature of the endwall boundary layer.

This study describes three-component measurements of mean and fluctuating velocities in the passage of a turbine blade obtained with a laser Doppler velocimeter. Friction coefficients obtained with the oil film interferometry method were compared to previously measured heat transfer coefficients. Increased acceleration and skew in the turbulent boundary layer entering the blade passage resulted in decreased heat transfer for the contoured endwall compared with the flat endwall, although friction coefficients increased. Further into the passage, the strength of the large streamwise vortex was reduced with contouring. Regions where heat transfer was increased by endwall contouring corresponded to elevated turbulence levels compared to the flat endwall. The streamwise vortex progression toward the airfoil suction side at the exit of the passage was delayed and turbulent kinetic energy associated with strong spanwise flow was reduced with contouring.

*Co-author: Dr. Karen A. Thole, Mechanical & Nuclear Engineering Department, Penn State

Introduction

Three-dimensional boundary layers are found in many practical situations where a cross-stream pressure gradient exists to turn the flow, such as in curved channels, around the base of bridge piers, and at the endwall of axial turbomachine passages. Through a simple Euler analysis, it can be shown that the lower velocity of the wall boundary layer relative to the freestream results in a smaller radius of curvature than the freestream, when both are subjected to the same cross-stream pressure gradient. Skew between the freestream and near-wall flow direction develops, and the structure of the turbulence is distorted when compared to a simpler two-dimensional boundary layer.

The presence of a velocity component in the cross-stream direction implies mean streamwise vorticity in a three-dimensional boundary layer. For flow approaching an obstacle such as an axial turbine airfoil, the boundary layer along the endwall separates near the leading edge and rolls up into a vortex that is stretched around the obstacle in the streamwise direction. Previous studies have shown that the streamwise vorticity due to flow turning in an airfoil cascade passage merges with the streamwise vortex from the leading edge boundary layer separation to create a large streamwise vortex, also known as a passage vortex. Besides increasing skew, this vortex has been shown to impact endwall heat transfer. However, a clear link between the characteristics of the three-dimensional boundary layer, the effects of the passage vortex, and the associated endwall heat transfer has not yet been presented.

Previous research on three-dimensional contouring of the endwall surface has demonstrated reductions in the passage vortex strength when compared to a flat endwall. Elevations and depressions in the endwall shape locally decrease or increase the static pressure, respectively, to limit or distort the formation of the passage vortex. Generally the freestream flow remains the same; only the endwall structures are affected. It has been shown that the contouring also reduces endwall heat transfer, although the mechanisms behind this reduction are not yet clear.

The objective of this study was to perform a detailed examination of a three-dimensional boundary layer influenced by a large streamwise vortex. The application of endwall contouring provided a means of modifying the streamwise vortex to gauge its influence on endwall heat transfer and friction coefficients. Current predictive tools are generally deficient at capturing the

details of a three-dimensional endwall boundary layer and its influence on heat transfer, and the data set given will provide useful information to improve physical models.

Review of Literature

Flow near the endwall of an axial turbine is extremely complicated due to the interaction of cross-stream and streamwise pressure gradients, separation and reattachment of the endwall boundary layer, large vortical structures, high freestream turbulence, upstream airfoil wakes, transitional flow, compressibility effects, and so on. Despite a body of work addressing these effects on endwall flow, very few studies have examined the endwall boundary layer in detail. Research on isolated fundamental aspects of the endwall boundary layer have been reported, such as skewness and three-dimensionality caused by a transverse pressure gradient or a streamwise vortex; however, synergistic effects are important for an endwall boundary layer relevant to turbomachines. In particular, the focus of this work is to understand the convective heat transfer, which is significantly influenced by the large vortical structures in the passage.

A number of researchers have studied the characteristics of three-dimensional turbulent boundary layers. A three-dimensional boundary layer is termed as such due to the presence of a cross-flow velocity component (normal to the streamwise direction), which can be generated by transverse pressure gradients or by shear (such as on a rotating disk). This results in mean streamwise vorticity with a scale no larger than the size of the boundary layer. Anderson and Eaton [1] determined that the Reynolds shear stress vector lagged the strain rate vector in the three-dimensional boundary layer generated by a wedge in the flow, resulting in anisotropic eddy viscosity. Also, the ratio of the magnitude of the shear stress to the turbulent kinetic energy was lower for the three-dimensional boundary layer in comparison to two-dimensional boundary layers, implying reduced effectiveness of the boundary layer at generating Reynolds shear stresses. Olcmen and Simpson [2] presented an extensive study of the flow around a wing/body junction, where the transverse pressure gradient reverses sign. They determined that the ratio of cross-stream to streamwise eddy viscosity in the three-dimensional boundary layer scaled best in a coordinate system aligned with the wall shear direction. However, Olcmen and Simpson [3] found these coordinates did not universally collapse the data of others when they compared several three-dimensional turbulent boundary layer data sets. A review of several three-dimensional boundary layer data sets by Johnston and Flack [4] showed that the ratio of the shear

stress magnitude to the turbulent kinetic energy tended to decrease as the total skew angle between the freestream and the wall shear increased.

Only a few studies have considered heat transfer effects in three-dimensional turbulent boundary layers. Abrahamson and Eaton [5] proposed a vector formulation for the enthalpy thickness and showed that their measured heat transfer data agreed with two-dimensional correlations of Stanton number and Reynolds number based on the magnitude of the enthalpy thickness vector. Increasing the transverse pressure gradient increased the skew in the boundary layer and reduced heat transfer coefficients. Measurements by Lewis and Simpson [6] around a wing-body junction indicated that time-mean Stanton numbers decreased relative to the two-dimensional flat plate correlation for increasing boundary layer three-dimensionality, but profiles of temperature fluctuations were not affected.

Fundamental studies of a streamwise vortex embedded in a boundary layer have indicated that the vortex can have a significant impact on endwall heat transfer; although it should be noted that the streamwise vortex along the endwall in a turbine passage is generally larger than the boundary layer. Eibeck and Eaton [7] found that increasing levels of circulation produced by a delta wing in a two-dimensional boundary layer caused local Stanton numbers to asymptote to approximately 24% augmentation relative to a flat plate Stanton number in the downwash region of the vortex. Heat transfer effects of the streamwise vortex were attributed solely to its distortion of the mean flow, and not to turbulence enhancement. Wroblewski and Eibeck [8] conjectured that changes to the turbulence by the streamwise vortex promoted the transport of heat more than transport of momentum, which was supported by their determination that the thermal boundary layer was not thinned as much as the momentum boundary layer on the downwash side.

The combined effects of a streamwise vortex and a pressure-driven three-dimensional boundary layer were considered by Shizawa and Eaton [9]. A streamwise vortex with near-wall induced velocity in the same direction as the crossflow reduced the strength of ejection events. They also found that the three-dimensionality of the flow dissipated the streamwise vortex more quickly than a similar vortex in a two-dimensional flow.

The large-scale features of the endwall flow in a turbine cascade, which are collectively referred to as secondary flows, were investigated in detail by Langston, et al. [10]. Langston [11] proposed a model of the major secondary flow features, including a leading-edge horseshoe

vortex that develops from the three-dimensional separation ("saddle point") of the inlet boundary layer upstream of the airfoil. Although this vortex is analogous to the horseshoe vortex in front of a cylinder mounted normal to a wall, it develops in a region of flow asymmetry. The pressure side leg of the horseshoe vortex merges with a passage vortex arising from the streamline curvature in the passage. The suction side leg of the horseshoe vortex remains near the suction side-endwall corner and has the opposite sense of rotation to the passage vortex. These large vortical structures are linked to a loss of total pressure near the endwall (termed secondary loss) from the inlet to the exit of the cascade, as well as high heat transfer rates where they interact with the endwall.

Three-dimensional flowfield measurements given by Kang and Thole [12] verified the model of Langston [11]. They also showed the wall-normal component of the turbulence was larger than either the streamwise or cross-stream components, and that the turbulence intensity in the passage vortex core was around 26%, based on the inlet velocity. Although this was reported as turbulent kinetic energy, a later study by Radomsky and Thole [13] indicated that the fluctuations were more likely unsteadiness related to the instability of the horseshoe vortex. Radomsky and Thole [13] observed bi-modal probability density functions for the streamwise and spanwise velocity components in the horseshoe vortex upstream of the vane leading edge, which presumably would persist during the merger of the horseshoe vortex with the passage vortex downstream. Kang and Thole [12] noted heat transfer levels were higher where the passage vortex brought midspan flow down to the endwall, and lower where the vortex swept flow off the endwall.

Characterization of the endwall boundary layer in an airfoil cascade has only been attempted in a few studies. Single component hot-wire measurements in the cascade of Langston, et al. [10] indicated a very thin, possibly laminar boundary layer on the endwall downstream of the inlet boundary layer separation. Harrison [14] found that the momentum Reynolds number was less than Re_θ=200 over a large part of the endwall downstream of the horseshoe vortex separation. Hot-film signals in that region also exhibited much lower RMS values as compared to the upstream turbulent boundary layer. More recently, hot film signals presented by Vera, et al. [15] indicated low amplitudes near the pressure side, suggesting laminar-like flow. Signals increased in amplitude and unsteadiness from the pressure side to the suction side of the adjacent airfoil.

The detrimental effects of secondary flows in a turbine have prompted studies of endwall design methods that might mitigate those flows. One such method is three-dimensional (also termed non-axisymmetric) contouring of the endwall. In the most common implementation, a computational simulation of the turbine flowfield is coupled to optimization software to produce the three-dimensional shape. One of the first examples of this was presented by Harvey, et al. [16], whereby the optimization produced a three-dimensional blade endwall contour intended to minimize exit flow angle deviations and pitchwise static pressure gradients. The optimum design had convex endwall curvature near the pressure side and concave curvature at the suction side in the front of the passage to reduce cross-passage pressure gradients, while convex curvature near the trailing edge suction side reduced exit flow angle deviation. Experimental validation by Hartland, et al. [17] confirmed the general conclusions of Harvey, et al. [16], and found a 30% reduction in secondary losses for the contoured wall relative to a flat wall. Endwall contouring in the studies of Germain, et al. [18] and Schuepbach, et al. [19] produced an overall stage efficiency improvement of 1.0%±0.4% in a 1-1/2 stage turbine, which was largely attributed to reductions in the stator time-averaged and unsteady losses.

Praisner, et al. [20] and Knezevici, et al. [21] examined non-axisymmetric contouring for the same low-pressure turbine blade as in this study. Praisner, et al. [20] used computational optimization based on secondary loss reduction to design a non-axisymmetric endwall contour for the Pack-B airfoil. The Pack-B endwall contour reduced losses (4% predicted, 10% measured) and turbulent kinetic energy levels associated with the secondary flow, when compared to the flat endwall. Knezevici, et al. [21] presented oil flow visualization and seven-hole probe measurements that showed a reduction in passage vortex strength with the contour, although the corner vortex and near-wall passage crossflow were intensified near the trailing edge where the contour merged back to the flat endwall level.

Saha and Acharya [22], Lynch, et al. [23], and Lynch, et al. [24] considered the effect of non-axisymmetric contouring on endwall heat transfer. Saha and Acharya [22] computationally evaluated nine endwall shapes and found that the best design reduced overall heat transfer by 8%, with significant reductions of over 300% near the suction side leading edge and approximately 20% in the throat compared to a flat endwall. A low-pressure turbine blade contour studied by Lynch, et al. [23] (same as in this study) significantly decreased endwall heat transfer near the pressure side of the passage relative to a flat endwall, which was attributed to

reduced strength of the passage vortex. Although CFD predictions of the flat endwall heat transfer by Lynch, et al. [24] did not agree with the measurements of Lynch, et al. [23], trends of heat transfer augmentation due to contouring were reasonably captured.

The study presented in this paper is unique in several aspects. First, the large amount of skew present in the turbine blade passage exceeds the current level of skew that has been measured for three-dimensional boundary layers in the literature. Furthermore, there have been few measurements of the three-dimensional mean and turbulent flowfield in the forward region of a blade passage, where the passage vortex originates. Finally, there have been no direct measurements of the endwall boundary layer within a turbine cascade, particularly with the application of non-axisymmetric endwall contouring.

Experimental Methodology

A large scale turbine blade cascade was placed in a closed loop wind tunnel for this study, as shown in Figure 3.1a. The operation of the tunnel, as well as the cascade design and benchmarking, have been described previously by Lynch, et al. [23]. A turbulence grid with a bar width of 2.54 cm and 10.2 cm spacing between bar centers was placed approximately 11 axial chords upstream of the cascade to produce a freestream turbulence level of 4% at the cascade inlet plane. The linear cascade (Figure 3.1b) contained seven blades based on a low-pressure turbine airfoil geometry that has been studied extensively in the literature, particularly with regards to non-axisymmetric endwall contouring (Praisner, et al. [20], Knezevici, et al. [21], Lynch, et al. [23], Lynch, et al. [24]). Table 3.1 lists the geometrical parameters and operating conditions for the cascade. The cascade was scaled to 8.6 times engine scale and was operated at a Reynolds number matched to the engine condition.

The top endwall and a side wall of the cascade were constructed of glass for optical access with a laser Doppler velocimeter (LDV). The bottom endwall of the cascade, where measurements were made, was painted flat black and sanded smooth to create a low-reflectivity and hydrodynamically smooth surface. Two types of endwalls were tested in the cascade: a baseline flat endwall, and a three-dimensional non-axisymmetric contoured endwall. Figure 3.2a shows an isometric depiction of the non-axisymmetric endwall. Figure 3.2b presents height contours for the endwall with flowfield and boundary layer measurement locations overlaid, which are discussed in more detail in the next section. The non-axisymmetric contour was

designed by the methodology described by Praisner, et al. [20]. The contour shape contained an elevation near the pressure side leading edge of the airfoil, and a depression near the suction side leading edge, as well as an elevated ridge from the pressure to suction side through the passage. Maximum and minimum extents of the elevations and depressions were $0.06C_{ax}$ and $-0.04C_{ax}$ relative to the flat endwall, respectively. The contouring was contained between the inlet and exit planes of the cascade and merged smoothly to the flat endwall level outside of the blade passage.

The inlet boundary layer was measured at a location $2.85C_{ax}$ upstream of the cascade along the inlet flow direction, as indicated in Figure 3.1b. A 2-component LDV was used to measure streamwise and wall-normal velocities, with velocity bias correction by residence time weighting. Table 3.2 compares the various boundary layer parameters for stations located upstream of a blade leading edge (Y/P=0, 1) and between blade leading edges (Y/P=0.5). The boundary layer parameters agreed well and confirmed uniformity of the flow entering the cascade. The results also agreed fairly well with the measurements reported by Lynch, et al. [23].

Measurement Locations and Coordinate Systems

Flowfield measurements were obtained for two axial planes in the cascade to document the global flowfield, as shown in Figure 3.3a. One plane was located $0.2C_{ax}$ downstream of the leading edge plane of the cascade, and is denoted as Plane A. The other plane (Plane B) was located $1.03C_{ax}$ downstream of the leading edge, or approximately 5 mm downstream of the trailing edge. The local coordinate system (x, y, z) was aligned to the cascade coordinate system (X, Y, Z) for each plane, although the y-coordinate origin was shifted. For Plane A, the y-coordinate origin was set so that y/P=0 corresponded to the pressure side of the blade. For Plane B, the y-coordinate origin was fixed at the location of the blade trailing edge projected downstream along the design exit flow angle, such that y/P=0 corresponded approximately to the center of the blade wake. The z-coordinate origin was fixed to the flat endwall level, such that regions of the contoured endwall which were below the flat endwall level had negative z-coordinate values.

Mean velocities for each of the measurement planes were transformed from components aligned with the cascade coordinate system into streamwise and secondary velocity components aligned with the midspan (inviscid) flow direction by the method described by Kang and Thole [12]. The midspan flow direction was determined at each pitchwise location in the measurement plane by:

$$\beta_{ms} = \tan^{-1}\left(\frac{V_{ms}}{U_{ms}}\right) \tag{3.1}$$

The transformation from local velocities to secondary flow velocities was:

$$V_s = U\cos(\beta_{ms}) + V\sin(\beta_{ms}) \tag{3.2}$$

$$V_n = -U\sin(\beta_{ms}) + V\cos(\beta_{ms}) \tag{3.3}$$

$$V_z = W \tag{3.4}$$

Secondary flow vectors are plotted using the normal (V_n) and spanwise (V_z) components.

Endwall boundary layer profiles were obtained in Plane A, and also along a path defined by the direction of an endwall streakline obtained from oil flow visualization in the study of Lynch, et al. [23]. The endwall streakline path was chosen such that measurements would be obtained in a region of large boundary layer skew but away from endwall separation locations. Boundary layer measurements were attempted in Plane B, but preliminary results indicated that the boundary layer thickness was less than 3 mm ($\delta_{99}/S<0.005$). The closest reliable wall measurement at that location was limited to approximately 1 mm, so the boundary layer could not be resolved adequately. The locations of the boundary layer profiles are indicated in Figure 3.3b, and the coordinates of the profiles are shown in Table 3.3. The boundary layer measurements in the cascade coordinate system were rotated around the spanwise (z) axis into a coordinate system aligned with the freestream velocity direction at the measurement location. In the rotated coordinate system, x (and u) is the streamwise direction, y (and v) is the cross-stream direction, and z (and w) is the wall-normal (spanwise) direction, which is the same as for the cascade coordinate system. It is important to note, however, that for the boundary layer results the origin of the z-axis was defined relative to the wall at the measurement location.

Flowfield Measurements

Three-component flowfield measurements were obtained on the bottom endwall of the cascade with a laser Doppler velocimeter (LDV). An argon-ion laser supplied green (514.5 nm), blue (488.0 nm), and violet (476.5 nm) wavelengths. A Bragg cell split each wavelength into pairs of beams, where one beam in a pair was frequency-shifted at 40 MHz to resolve directional ambiguity. The beams were coupled into polarization-preserving fibers and transmitted to a two-component probe (green, blue wavelengths) and a single-component probe (violet wavelength). Each probe had a 750 mm focusing lens with a 2.6X beam expander, resulting in a half-angle of

4.92° between beam pairs and fringe spacings of 3.00 μm, 2.84 μm, and 2.78 μm for the green, blue, and violet wavelengths, respectively.

The probes are normally operated in backscatter mode to receive the scattered light, since the transmitting and receiving optics are contained in a single probe. For this study, however, the two probes were operated in sidescatter mode, where the receiving optics of one probe were used to collect the scattered light from the opposing probe. This was beneficial in reducing glare effects for the near-wall measurements, and had the added benefit of reducing the measurement volume size. The measurement volume size in the sidescatter mode had a diameter D=72.8 μm and a length L=200 μm. For location A3 with the largest measured shear, the dimensions normalized by inner scaling parameters were D^+=3 and L^+=8.

The light scattering particles consisted of atomized di-ethyl-hexyl sebacate with a diameter of approximately 1 μm. The particles were generated by a Laskin nozzle seeder and introduced upstream of the wind tunnel fan, so that they were fully mixed into the flow at the test section. Scattered light collected by the receiving optics was sent to photomultiplier tubes and the resulting signal was processed with an 8-bit digital signal processor.

Three-component coincident measurements were obtained by intersecting the measurement volumes of the green, blue, and violet beam pairs. Several non-orthogonal configurations were used for the flowfield measurements. To obtain measurements in the blade passage, the two probes were suspended above the top endwall and the beams passed through it; see Figure 3.4. The total angle between probes was approximately 31° to 35°, depending on the optical access available at a particular location. For locations near the blade pressure side and downstream of the cascade, the probes were also tilted by 7° (larger than the half-angle of the beam pairs) to minimize interference with the airfoil. Measurements upstream of the cascade were obtained through the side glass wall, with the probes tilted by 7° to eliminate interference by the bottom endwall. The angle between probes for those measurements was 31°. The various non-orthogonal configurations and the velocity transformations to cascade coordinates are described in detail in Appendix A.

The location of the wall was determined through two methods. The output signal from the photodetectors was monitored as the probe volume was moved to the wall. Also, the input power to the LDV was lowered and the beam crossing was visually monitored. Both methods

produced nearly identical results and repeatability tests indicated an uncertainty in wall position of less than ±100 μm (z^+~4 for highest measured shear at location A3).

At each measurement location, 20,000 coincident samples were obtained. Sampling rates ranged from approximately 50 samples/s near the wall to 200 samples/s in the freestream. Instantaneous velocity measurements were accepted when burst signals from each channel overlapped by less than 200% of their burst signal elapsed times. This essentially resulted in an adaptive coincidence window that became more restrictive for higher-velocity measurements, since the transit time of a particle is inversely related to its velocity. For low-velocity measurements (i.e., long burst times), the adaptive coincidence window method produced identical results to a fixed coincidence window of 10 μs. Measurements in non-orthogonal coordinates were transformed to the orthogonal blade cascade coordinates, and further transformed depending on the local coordinate system. Velocity bias correction was performed by using the inverse of the instantaneous velocity magnitude as a weighting factor (McLaughlin and Tiederman [25]).

A sequential perturbation analysis (Moffat [26]) was used to estimate uncertainty of the LDV measurements, which included the effect of measurement bias and angular uncertainty in the probe orientation on the transformed velocity components. Uncertainty in the probe orientation angles in the non-orthogonal setup was estimated to be ±0.5°, and the measurement bias was estimated as ±1% of the measured value. Precision uncertainties were estimated at a 95% confidence interval, and the root-sum-square of bias and precision uncertainties gave the total uncertainty. Table 3.4 lists the estimated total uncertainties for measurements obtained in a highly turbulent region (y/P=0.28, z/S=0.015) at station A3 in Plane A. Note that quantities involving the spanwise component of velocity (w) have higher uncertainty than the other velocity components since that component was the most sensitive to the angle between probes in the non-orthogonal configuration.

Wall Shear Stress Measurements

Endwall shear stress measurements were obtained using an oil film interferometry technique, in which the shear rate of an oil film is directly related to the shear stress acting on it. Naughton and Sheplak [27] provide a thorough review of the technique. Implementation on turbine cascade endwalls was described by Harrison [14], Holley, et al. [28], and Holley and Langston [29]. The method used in this study was described in detail by Lynch and Thole [30].

The time-averaged shear rate of the oil can be determined by measuring the change in height (thickness) of the film over a discrete time interval. The average shear rate multiplied by the oil viscosity gives the average shear stress acting on the surface of the film. This assumes that the pressure gradient, gravity, and inertial terms in a momentum balance on the film are negligible compared to the shear. An order-of-magnitude analysis using representative values pertinent to this study (h_{oil}=1 μm, ν_{oil}=100 cSt, τ_w=0.1 Pa, ρ_{oil}=1000 kg/m^3, dp/ds=100 Pa/m, g=10 m/s^2) confirmed that the Reynolds number of the oil film was less than 1 (inertial terms were negligible), and that the shear was three orders of magnitude larger than the pressure gradient term and an order of magnitude larger than the gravity term. Note that in our implementation gravity would be negligible regardless of the order-of-magnitude analysis since the cascade endwall was nominally parallel to ground (perpendicular to the gravity vector).

The height of the oil film is measured using interferometry, whereby illumination of the film by a monochromatic light source produces constructive and destructive interference bands. Figure 3.5a depicts the development of the interferogram bands in an oil film, and Figure 3.5b shows a sample interferogram. The equation used in this study to calculate wall shear (in the form of a non-dimensional friction coefficient) is:

$$C_f = \frac{L_f \frac{\lambda}{2} \sqrt{n_{oil}^2 - n_{air}^2 \sin^2 \theta_i}}{\int \frac{1}{2} \rho U_{in}^2 \frac{1}{\mu_{oil}} dt} \tag{3.5}$$

Eq. 6.5 is derived from a reduction of the Navier-Stokes equations for the oil film applied along an endwall streamline (limiting streamline). The direction of the limiting streamline was determined in this study by the shear direction of the oil film at the measurement point; see Figure 3.5b. The analysis requires measurement of the oil height only at the end of the wind tunnel run, since the conditions leading to the final oil film thickness are integrated over time.

The average distance between interferogram bands (L_f) was determined from the period of a sine wave fitted to the pixel intensity profile along the limiting streamline direction (Holley, et al. [28]). The location of the friction coefficient measurement was taken as the center of the intensity profile. The wavelength of light (λ) and the light incidence angle (θ_i), used to calculate the height of the oil film, were functions of the optical setup that produced the interferogram images. The oil viscosity (μ_{oil}) and cascade inlet dynamic pressure were functions of the run

time, since the oil viscosity is sensitive to temperature and the dynamic pressure varied from start-up to shut-down.

For implementation in the cascade, silicone oil droplets were applied to nickel foil patches adhered to the endwall surface. The nickel foil was 50 μm thick and the final thickness of the oil film was less than 1 μm; thus, the total thickness of the foil patch and oil film was not expected to disturb the flow ($z^+<2$ for the highest shear measured). The dynamic pressure and flow temperature were recorded throughout the run. Note that a typical run length to obtain measurable interferograms was approximately twenty minutes, with start-up and shutdown transients being less than 45 seconds of that time. The tunnel air temperature generally varied less than 2°C during a run, but the oil viscosity temperature sensitivity was still accounted for by the correlation of Naughton and Sheplak [27].

The foil patches were carefully removed after a test and immediately imaged in a fixture with a nearly monochromatic sodium vapor lamp (λ=589, 589.6 nm) to obtain the interferograms. Measurements were repeated several times with different oil viscosities, foil patch positions, and oil droplet placement techniques. Results were within experimental uncertainty for the technique.

Lynch and Thole [30] describe benchmarking of our implementation of the OFI method in determining friction factors in a fully developed channel. Additional benchmarking was performed for this study by comparing endwall shear stress obtained with OFI to the shear values derived from a fit to the log-law region of the two-dimensional boundary layer measured upstream of the cascade. OFI measurements were within 6% of the boundary layer-derived shear values at locations $5.4C_{ax}$ (Re_θ=1060), $3C_{ax}$ (Re_θ=1510), and $0.75C_{ax}$ (Re_θ=2090) upstream of the blade cascade.

The partial derivative method described by Moffat [26] was used to calculate uncertainties for the measurements of friction coefficient magnitude and direction. Table 3.4 lists the friction coefficient uncertainty at station A3. Directional uncertainty was estimated as $\partial\beta_w=\pm4°$. Magnitude uncertainty (including the effect of the limiting streamline direction uncertainty) was estimated as $\partial C_f=\pm8\%$ and was dominated by uncertainty in the interferogram spacing.

Results and Discussion

The results presented in this paper include flowfield measurements at two planes in the cascade, as well as boundary layer profiles at several locations on the endwall. The flow measurements are compared to friction coefficients and previously measured endwall heat transfer coefficients reported by Lynch, et al. [23]. Validation of the flowfield measurements was performed by comparing the streamwise mean velocity and flow angle to a benchmarked prediction of the cascade flow by Lynch, et al. [24]. Figure 3.6a and Figure 3.6b compare the measured streamwise velocity and flow angle at midspan to the prediction. Refer to Figure 3.3a for the definition of y/P for Planes A and B. Streamwise velocity in Figure 3.6a varies significantly across the passage for Plane A, and the blade wake is evident at Plane B. Note that the position of Plane B is very close to the trailing edge, which results in high gradients around the blade wake and increased uncertainty for those measurements. Mean flow angles in Figure 3.6b indicate that the cascade flow experiences more than 70° of turning from Plane A to B, although the variation of turning within a given plane is less than 10°. LDV measurements also show good agreement to the predictions for the mean flow angle.

Endwall oil flow patterns presented by Lynch, et al. [23] are reproduced in Figure 3.7a and Figure 3.7b for the flat and contoured endwalls, respectively. In their work, streaklines were drawn on the oil flow patterns and major secondary flow features associated with the passage and corner vortices were identified. In Figure 3.7, three-dimensional separation lines associated with the pressure and suction-side legs of the horseshoe vortex, as well as the flowfield measurement planes and boundary layer profile locations (see Figure 3.3), are added. The endwall flow pattern is helpful in interpreting the flowfield results presented next.

Flowfield and Heat Transfer Along an Endwall Streakline Path

Mean streamwise velocity profiles in Figure 3.8 were obtained by transforming measurements to the local freestream coordinate system at each of the three stations along the path of an endwall streakline. Table 3.5 summarizes the boundary layer parameters for each of the stations. Figure 3.8a presents the measurements in outer scaling variables, with a $1/7^{th}$ power law velocity profile for comparison. Freestream turbulence (5% at station S1) results in more full streamwise velocity profiles than the $1/7^{th}$ power law for station S1 upstream of the cascade. Profiles for the flat and contoured endwalls agree well for stations S1 and S2 since the flow has not yet encountered the effects of contouring and flow acceleration in the cascade. At station S3,

however, the streamwise velocity profiles for the flat and contoured endwalls show the effects of acceleration, with the contoured endwall flow experiencing higher acceleration. Figure 3.2b shows that station S3 is close to the depression in the contoured endwall near the suction side. Endwall streaklines around S3 in Figure 3.7 turn more sharply toward the suction side and converge rapidly for the contour versus the flat endwall, suggesting that the flow approaching the depression in the contour is diverted and accelerated toward the suction side.

To enable presentation of data in inner scaling parameters, friction velocities at stations S1-S3 were obtained by a Clauser fit to the velocity magnitude between $30<z^+<300$ (generally 8 points). Compton and Eaton [31] showed reasonable collapse of their three-dimensional boundary layer data to the law of the wall when plotted using velocity magnitude, although maximum skew in their study was limited to 24°. Table 3.5 lists the friction coefficient measured by the OFI method, as well as the friction coefficient obtained from the Clauser fit. For the upstream station S1, the OFI result is within experimental uncertainty of the Clauser fit result. At S3, the agreement is more poor, particularly for the contoured endwall, due to significant skew and acceleration that has developed. For consistency, however, the friction velocity from the Clauser fit is used in inner scaling plots that follow.

Figure 3.8b presents mean streamwise velocity scaled by the friction velocity from the Clauser fit. Spalding's law (Spalding [32]) is also included for reference. The streamwise velocity profiles at S1 and S2 agree with Spalding's law for both endwalls. Note that the freestream turbulence in this study depresses the wake of the boundary layer (Thole and Bogard [33]). The contoured endwall produces a stronger favorable pressure gradient by station S3 than the flat endwall, and the resulting profile falls below Spalding's law as expected (Volino and Simon [34]).

Flow entering the cascade is accelerated and turned by the blades, and the low-momentum fluid in the endwall boundary layer experiences a pitchwise pressure gradient that results in increasing cross-stream (pitchwise) velocities. Profiles of mean cross-stream velocity are shown in Figure 3.9 for the flat and contoured endwalls. At station S1 upstream of the cascade, cross-stream velocities are small for both endwalls. A small amount of skew has developed at S2, although there is still a negligible difference between the flat and contoured endwalls. At S3, there is a significant difference between the flat and contoured endwall profiles, where the contour results in nearly a 60% increase in peak cross-stream velocity. The larger

cross-stream velocity for the contour correlates well with the increased turning seen in the oil flow visualization results in Figure 3.7.

Figure 3.10 presents profiles of flow angle deviation at S1-S3 for the flat and contoured endwalls, which further illustrates the amount of skew that develops in the endwall boundary layer. Wall shear angles obtained from the OFI method are also indicated in the figure as the data points at $z/\delta_{99}=0.001$. The wall shear measurement location was arbitrarily chosen so that the data points could be plotted on the logarithmic abscissa, although note that $z/\delta_{99}=0.001$ corresponds to $z^+<2$ for the highest shear measured at S3. The mild pitchwise pressure gradient at S1 results in a maximum of 8° degrees of overturning for either endwall from Figure 3.10. As the pitchwise gradient increases further along the streakline path, the amount of skew increases, with a maximum of 24° at the wall for S2. Flow angle deviation is slightly higher for the contoured endwall. At S3, flow angle deviation is further increased for the contour versus the flat endwall. The wall shear angle is 39° larger than the freestream flow angle for the contoured endwall, and 36° larger for the flat endwall.

Turbulent kinetic energy profiles for the various endwall streakline stations are presented in Figure 3.11, where Figure 3.11a is based on freestream scaling parameters and Figure 3.11b is based on inner scaling parameters from the Clauser fit. In both figures, the turbulent kinetic energy profiles show a peak near the wall due to the production of turbulence in the overlap region of the boundary layer. Stations S1-S2 have similar levels of turbulent kinetic energy for either endwall geometry since the streamwise acceleration and three-dimensionality of the boundary layer is relatively mild at those stations. At S3, however, turbulent kinetic energy levels decrease due to the acceleration of the flow toward the suction side. The increased acceleration for the contoured endwall relative to a flat endwall results in a more significant decrease in turbulent kinetic energy. The decrease with contouring is particularly apparent on the inner scaling plot (Figure 3.11b), where the peak turbulent kinetic energy at S3 is 30% lower for the contour versus the flat endwall.

Endwall heat transfer (non-dimensionalized as a Stanton number) and friction coefficients are plotted in terms of a local Reynolds number along the endwall streakline path in Figure 3.12. Stanton numbers are plotted as a continuous line to indicate that they were obtained from the spatially-resolved measurements of Lynch, et al. [23], while the friction coefficients, obtained only at the boundary layer locations S1-S3, are plotted as discrete points. The length

scale in the definition of the Reynolds number is streamwise distance along the path, referenced to the virtual origin determined from the boundary layer measurement at S1. The velocity scale in the Reynolds number, Stanton number, and friction coefficient is the local freestream velocity, which was obtained from the prediction of the cascade midspan (inviscid) flowfield by Lynch, et al. [24]. Measured freestream velocities at S1-S3 agreed well with the inviscid prediction. Also included in Figure 3.12 are the correlations for a turbulent flat plate including the effect of the unheated starting length, as well as a correlation reported by Popiel and Boguslawski [35] for heat transfer in a skewed three-dimensional boundary layer developing on a rotating disk. Note that the three-dimensionality in that flow is shear-driven, while three-dimensionality in the flow in this study is pressure-driven.

Heat transfer coefficients in Figure 3.12 are similar between the flat and contoured endwalls at the start of the endwall streakline upstream of the cascade, and agree with the predicted levels for an unheated starting length for the thermal boundary layer. Further along the streakline path, St values for the flat and contoured endwalls are lower than predicted by the flat plate correlation, as the boundary layer becomes skewed by the pitchwise pressure gradient. Abrahamson and Eaton [5] and Lewis and Simpson [6] observed a similar decrease in heat transfer for a skewed three-dimensional boundary layer relative to a two-dimensional flat plate correlation. The contoured endwall exhibits a more marked decrease than the flat endwall due to higher turning of the flow that was presented previously, reaching levels consistent with the correlation of Popiel and Boguslawski [35] at a streakline Reynolds number of 1.3×10^6. Heat transfer levels increase for the contour further along the streakline due to the influence of the suction side leg of the horseshoe vortex, which will be addressed in more detail in the Plane A flowfield results.

Friction coefficients in Figure 3.12 agree well with the measured heat transfer at stations S1 and S2 upstream of the cascade, where the boundary layer is nominally two-dimensional and the cascade pressure gradient is still relatively mild. At station S3, however, friction coefficients increase for both endwalls, with a larger increase for the contoured endwall relative to the flat due to the increased acceleration of the near-wall flow mentioned earlier.

Plane A Flowfield and Endwall Heat Transfer

Figure 3.13 shows mean secondary velocity measurements at Plane A for the flat and contoured endwalls. The gray areas indicate the locations of the endwall and adjacent airfoils,

with the pressure and suction sides of the passage indicated by PS and SS, respectively. Note that due to limitations of optical access, measurements could not be obtained closer than y/P=0.14 from the pressure side or y/P=0.06 from the suction side. The secondary velocities in Figure 3.13 are normalized by the inlet freestream velocity, and a unit vector is included as a reference. Vertical lines in the figure indicate the locations of the boundary layer profiles presented later.

The flowfield results for the flat endwall (Figure 3.13a) are discussed first. In the freestream (above z/S=0.20), streamwise velocity contours indicate the low-velocity flow near the pressure side, and higher-velocity flow near the suction side due to acceleration around the airfoil. Below z/S=0.12, streamwise velocity decreases at a given pitchwise location due to the boundary layer at the endwall. Secondary velocity vectors indicate the presence of a vortex near the pressure side, centered around y/P=0.26, z/S=0.05, which brings fluid down to the endwall. Lynch, et al. [23] indicated high levels of endwall heat transfer near the pressure side for the flat endwall. Secondary vectors near the suction side indicate upward movement of fluid that is associated with the separation of the turbulent inlet boundary layer from the endwall.

The contoured endwall has a significant effect on the mean flowfield, as seen by comparing Figure 3.13a and b. The rise in the contour near the pressure side accelerates the near-wall flow and increases the streamwise velocity, but V_s/U_{in} contours near the depression indicate lower streamwise velocity compared to the flat endwall. Secondary vectors in Figure 3.13b indicate a much weaker vortex displaced further from the pressure side (center at y/P=0.3, z/S=0.06) than in the flat endwall measurements (Figure 3.13a). The secondary vectors also indicate a significant downward flow toward the middle of the passage, as the near-wall flow follows the wall down into the depression.

Turbulent kinetic energy normalized by the inlet freestream velocity is shown in Figure 3.14. A dashed box near the suction side endwall corner indicates the region presented in Figure 3.15, where the effect of the suction side horseshoe vortex is analyzed more closely. The overall flowfield results for the flat endwall (Figure 3.14a) indicate high levels of turbulent kinetic energy under the large vortex seen in the mean velocity results (Figure 3.13a). Peak turbulent kinetic energy levels correspond to a turbulence intensity of 11% based on the inlet freestream velocity. Kang and Thole [12] found a similar region of high turbulence under a large streamwise vortex located near the pressure side leading edge of a vane. A small circular region of high k/U_{in}^2 is also seen near the suction side of the passage, which corresponds to the suction side leg

of the horseshoe vortex. In comparison to the flat endwall, the contour (Figure 3.14b) has slightly higher peak k/U_{in}^2 levels near the pressure side, and a larger extent of high turbulent kinetic energy levels near the endwall across the passage. Turbulent kinetic energy associated with the suction side horseshoe vortex is also increased.

The effect of the contour on the suction side horseshoe vortex is more clear in Figure 3.15, which presents a magnified view of the suction side-endwall corner . Contours of turbulent kinetic energy are overlaid with the mean secondary flow vectors, and the boundary layer profile location A3 is indicated by the vertical dashed line. In Figure 3.15a, flat endwall secondary velocity vectors between $0.005<z/S=0.010$ indicate slight flow turning in the negative pitch direction caused by the sense of rotation of the suction side horseshoe vortex. Turbulent kinetic energy levels increase near the wall where the crossflow is forced to turn upward by the vortex. In contrast, secondary flow vectors for the contoured endwall in Figure 3.15b show a distinct vortex that is displaced away from the airfoil-endwall corner, with high levels of turbulent kinetic energy where it interacts with the near-wall crossflow. Comparison of the flat and contoured endwall separation lines in the oil flow results in Figure 3.7 also indicates that the suction side leg of the horseshoe vortex is displaced away from the blade. Note in Figure 3.7 that the saddle point is located farther upstream for the contour versus the flat endwall, which appears to make the trajectory of the suction side leg of the horseshoe vortex curve further away from the blade-endwall corner. Deceleration of flow around the suction side associated with the depression allows the suction side horseshoe vortex to move away from the airfoil-endwall corner where it normally resides.

Figure 3.16 shows endwall boundary layer profiles of streamwise mean velocity at stations A1-A3 in Plane A. Also included for reference is the $1/7^{th}$ power law profile for a turbulent boundary layer, and the Blasius laminar boundary layer profile. Table 3.6 summarizes the boundary layer parameters for A1-A3. At station A1, the streamwise velocity profile for the flat endwall falls between the turbulent and laminar zero-pressure-gradient profiles, although the streamwise momentum thickness Reynolds number and shape factor in Table 3.6 suggest that the flow is turbulent. The oil flow pattern in Figure 3.7a shows that station A1 is near the development of the passage vortex for the flat endwall. The laminar-like shape of the streamwise velocity at A1 near the wall in Figure 3.16 is due to flow being turned away from the inviscid streamwise direction by the rotation of the passage vortex. As expected from the flowfield result

in Figure 3.13b and the endwall oil flow in Figure 3.7b, the passage vortex is displaced away from the pressure side, reducing the effect of the passage vortex on the contour streamwise velocity profile at A1. Flow acceleration at the contour elevation near the pressure side decreases the momentum thickness Reynolds number and shape factor for the contour relative to the flat endwall in Table 3.6.

At station A2, the flat endwall streamwise profile is relatively close to the $1/7^{th}$ power law profile, but the contoured endwall profile has lower near-wall velocities. The displaced passage vortex, as well as deceleration of flow entering the contour depression, reduces the near-wall streamwise velocity. In contrast to station A1 results, the contour profile at A2 has a larger momentum thickness Reynolds number and shape factor than the flat endwall (see Table 3.6).

Streamwise velocity profiles at A3 are influenced by the acceleration of endwall flow toward the airfoil suction side (see Figure 3.7), as well as the effect of the suction side horseshoe vortex. The sweeping action of the stronger suction side horseshoe vortex associated with the contoured endwall turns near-wall flow away from the inviscid flow direction, compared to the flat endwall.

Figure 3.17 presents the cross-stream velocities at each of the measurement stations in Plane A. Note that the abscissa is plotted on a log scale to emphasize the near-wall region. At station A1, cross-stream velocities are extremely large, peaking at nearly 40% of the boundary layer edge velocity. The contour exhibits higher cross-stream velocity than the flat endwall, due to the acceleration of flow at the contour elevation. At station A2, the contour also has higher cross-stream velocity, but in this case it is due to the displaced passage vortex which turns flow away from the inviscid streamwise direction. The hooked profile at station A3 for the contour is a result of the influence of the suction side leg of the horseshoe vortex displaced awar from the suction side of the passage, as seen in Figure 3.15.

The mean flow angle relative to the midspan angle is shown in Figure 3.18. The data points at $z/\delta_{99}=0.001$ are the wall shear angles from the OFI measurements, where the spanwise location was arbitrarily chosen on the log scale abscissa as described for Figure 3.10. Station A1 profiles in Figure 3.18 show very large skew angles, exceeding 70° for the flat endwall. Due to the displacement and weakening of the passage vortex with endwall contouring, flow angle deviation is reduced at A1 but increased at A2 relative to the flat endwall. The profiles at station A3 indicate the effect of the suction side leg of the horseshoe vortex.

Endwall heat transfer (St) and friction coefficients (C_f) at Plane A are shown in Figure 3.19. The velocity scale for St and C_f is the local freestream velocity. Recall from Figure 3.6a that the inviscid streamwise velocity magnitude is lower near the pressure side than the suction side, which accentuates differences in St (or C_f) across the passage. Heat transfer coefficient levels for the flat endwall are high toward the pressure side of the passage (y/P=0), where the downward-turning fluid impinges on the endwall. Around y/P=0.7, St values are low where the turbulent boundary layer is skewed but not separated from the endwall. The heat transfer coefficient increases slightly near the suction side due to the downwash and increased turbulence of the suction side horseshoe vortex.

The flat endwall friction coefficient agrees reasonably well with the St number at station A1. At this location under the passage vortex, the flow is generally parallel to the wall and turbulent transport mechanisms of momentum and heat transfer are similar. At station A2, however, the flat endwall friction coefficient is higher than the heat transfer coefficient. Although part of the variation between St and C_f can be attributed to the cross-passage favorable pressure gradient, the oil flow visualization in Figure 3.7a indicates that A2 is slightly downstream of the pressure side horseshoe vortex separation line, which is associated with the pressure side leg of the horseshoe vortex. Holley and Langston [29] also indicate that friction coefficients around the separation line are higher on the downstream side where the vortex sweeps flow to the endwall. The friction coefficient for station A3 is higher than the endwall heat transfer coefficient due to the favorable pressure gradient accelerating the flow close to the suction side.

Contoured endwall heat transfer in Figure 3.19 is high near the pressure side and low around y/P=0.7, with levels similar to the flat endwall in those areas. From approximately $0.2<y/P<0.55$, however, the contour results in higher St values relative to the flat endwall. Comparison to the flowfield measurements suggests that the area of high streamwise velocity (Figure 3.13) and near-wall turbulent kinetic energy (Figure 3.14) between $0.2<y/P<0.55$ corresponds well to the increased heat transfer for the contour.

The contoured endwall friction coefficient in Figure 3.19 agrees well with St at station A1, and demonstrates an increase in C_f for the contour versus the flat endwall. The percent increase in C_f at station A1 is 23%, which compares well with the percent increase of 24% in St. At station A2, however, C_f and St have nearly the same magnitude for the contoured endwall,

unlike the situation for the flat endwall. Figure 3.7b indicates that the separation line has been displaced upstream with contouring, and thus the pressure side horseshoe vortex would be expected to have less of an influence on the wall shear at A2.

At station A3, the friction coefficient is higher than the corresponding Stanton number for the contoured endwall. The level of C_f is the same between the flat and contoured endwalls at this location. Although the magnitudes of C_f and St are different at station A3, both parameters indicate no significant difference between the flat and contoured endwalls. Strong flow acceleration close to the suction side has a significant role in minimizing differences between the two endwall geometries.

Plane B Flowfield and Endwall Heat Transfer

Mean streamwise velocity contours and mean secondary flow vectors are shown for Plane B in Figure 3.20. At ths plane, the contouring has merged with the flat endwall level. The vertical dashed lines in the figure indicate the projected location of the blade wake in the measurement plane. Note that discrepancies in the streamwise velocity contour levels in the blade wake are attributed to limited measurement resolution of the high gradients in the wake that was noted in Figure 3.6. Measurements obtained over one blade pitch from $-0.36<y/P<0.67$ were copied and shifted to generate Figure 3.20. The agreement between contours and secondary flow vectors at the overlap at y/P=0.67 indicate good periodicity for the cascade flow.

Secondary flow vectors in Figure 3.20a indicate that flow is directed downward to the endwall near the pressure side of the passage. A large vortical structure near the suction side of the passage is attributed to the passage vortex, with a center at approximately y/P=0.75, z/S=0.07. A low-streamwise-velocity region above the passage vortex is associated with the suction side horseshoe vortex that has swept up airfoil boundary layer fluid. Secondary velocity vectors show significant spanwise velocities around y/P=0.9, z/S=0.10 between the passage vortex and suction side horseshoe vortex, where fluid is swept between those two structures. Near the endwall another low-streamwise-velocity region is due to the corner vortex that remains close to the airfoil-endwall junction (see Figure 3.7).

The contoured endwall mean velocities in Figure 3.20b exhibit the same general features as the flat endwall, but with some important differences attributed primarily to the delay of the passage vortex in progressing to the suction side of the passage. The large vortical structure near the suction side is located further from the suction side and closer to the endwall (center at

y/P=0.65, z/S=0.06). The low-streamwise-velocity region above the passage vortex is also closer to the endwall. To further elucidate the the effect of the contour, a secondary kinetic energy coefficient (C_{SKE}) was computed from the mean secondary vectors as:

$$C_{SKE} = \frac{V_n^2 + V_z^2}{U_{in}^2} \tag{3.6}$$

Contours of C_{SKE} are plotted with the secondary velocity vectors overlaid in Figure 3.21. High values of C_{SKE} correspond to large secondary flow velocities. The large spanwise velocities near the suction side of the blade result in high C_{SKE} for the flat endwall in Figure 3.21. The sweeping effect of the passage vortex leads to high C_{SKE} near the endwall from $0.2<y/P<0.9$. In comparison, the contoured endwall (Figure 3.21b) has lower levels of spanwise velocity and C_{SKE} near the suction side at z/S=0.10, since the effect of the passage vortex is weaker at that location. At the endwall, however, the delayed passage vortex increases the skew in the near-wall flow and results in higher levels of C_{SKE} compared to the flat endwall. The effect of the contouring indicated by these measurements is consistent with the results of Knezevici, et al. [21] for the same cascade and contour geometry, and confirm the effect of the contour in delaying the development of the passage vortex.

Turbulent kinetic energy (TKE) at Plane B is shown in Figure 3.22. For the flat endwall (Figure 3.22a), high levels of TKE are present in the blade wake, as well as in the low-velocity region associated with the suction side horseshoe vortex. The high-spanwise-velocity region around y/P=0.9, z/S=0.10 also has high levels of turbulent kinetic energy. Near the endwall, the corner vortex produces high TKE, and moderate levels of turbulence extending across the passage are associated with the passage vortex. In comparison, the contoured endwall (Figure 3.22b) has slightly higher TKE associated with the passage vortex, since the vortex is closer to the endwall and induces higher secondary velocities. Also, turbulent kinetic energy associated with the high secondary kinetic energy region near the suction side of the blade is reduced with contouring, presumably due to reduced strength of the secondary flow. Finally, a small decrease in TKE is observed at the corner vortex with the application of endwall contouring.

Figure 3.23 shows endwall heat transfer at Plane B, where the velocity scale for St is the local freestream velocity magnitude. Also included on the plot are friction coefficient measurements. Flat endwall St levels are high around the blade wake due to the downwash of flow at the pressure side (Figure 3.20a). The high levels of turbulent kinetic energy in the corner

vortex on the suction side also contribute to increased heat transfer around that location. Contoured endwall St levels around the blade wake are slightly lower than for the flat endwall, probably due to reduced turbulent kinetic energy in the corner vortex noted earlier. Away from the blade wake, the contour does not exhibit a significant difference in endwall heat transfer relative to the flat endwall, despite the slight increase in turbulent kinetic energy associated with the passage vortex (Figure 3.22b). The location of the increased TKE lobe slightly off the endwall minimizes its influence on the endwall heat transfer.

Friction coefficient magnitudes agree fairly well with St levels near the pressure side and into the center of the passage. Figure 3.20a indicates flow is separating from the endwall around y/P=0.8 due to the roll-up of the passage vortex, and friction coefficients at that location in Figure 3.23 decrease accordingly. For the three measurement locations at Plane B, friction coefficients indicate no significant difference between the flat and contoured endwalls.

Conclusions

Mean and fluctuating velocity measurements obtained with a three-component laser Doppler velocimeter were presented for a turbine cascade with and without non-axisymmetric endwall contouring. The three-dimensional flowfield was measured at two planes in the cascade. Endwall boundary layer measurements were obtained along the path of an endwall streakline originating upstream of the cascade to determine the effect of skew on the approaching turbulent boundary layer. Boundary layer profiles were also obtained at three locations in the passage to understand the effect of the contour on the highly skewed endwall boundary layer. Friction coefficients at the selected boundary layer locations were measured with the oil film interferometry technique and compared to previously measured heat transfer coefficients.

Profiles of mean velocity along the endwall streakline path indicated significant streamwise acceleration and development of significant skew angles in the turbulent boundary layer approaching the cascade, for both flat and contoured endwalls. The contoured endwall resulted in higher streamwise acceleration and cross-stream velocities than the flat endwall, due to upstream displacement of the pressure side leg of the horseshoe vortex. The displacement was attributed to flow being diverted around the depression on the suction side of the passage. Both endwalls resulted in decreased peak turbulent kinetic energy near the wall as the flow was skewed and accelerated toward the suction side of the passage, but the reduction in turbulent

kinetic energy was larger for the contoured endwall in comparison to the flat. Endwall heat transfer levels along the streakline path were lower than the corresponding values in a two-dimensional zero-pressure-gradient boundary layer. The increased acceleration and skew caused by the contour further lowered endwall heat transfer but increased the friction coefficient, relative to the flat endwall.

Flowfield measurements in the forward portion of the passage indicated a reduction in passage vortex strength but a slight increase in near-wall turbulent kinetic energy for the contour compared to the flat endwall. A region of elevated endwall heat transfer seen in previously obtained results for the contour correlated well with the region of elevated turbulent kinetic energy. Boundary layer profiles indicated skew angles greater than 70° between the endwall and freestream for the flat endwall near the pressure side, reflecting the influence of the passage vortex. Near the suction side of the passage, the contoured endwall caused displacement of the suction side horseshoe vortex away from the airfoil-endwall corner and increased turbulent kinetic energy associated with the vortex, compared to the flat endwall.

At the exit of the cascade, the benefit of contouring was to delay the progress of the passage vortex toward the suction side of the passage. The delay resulted in a reduction of secondary kinetic energy and turbulent kinetic energy where the passage vortex interacted with flow on the suction side of the airfoil, compared to a flat endwall. Although turbulent kinetic energy levels near the endwall below the passage vortex were slightly higher with contouring, no significant difference in endwall heat transfer or friction coefficients was observed between the flat and contoured endwalls. A slight reduction in heat transfer with contouring was observed around the blade wake, due to a decrease in turbulent kinetic energy associated with the corner vortex at the suction side-endwall junction.

Overall, non-axisymmetric contouring acted to shift the horseshoe vortex away from the passage vortex and delay the development of the passage vortex. The upstream shift of the horseshoe vortex caused that feature to increase local heat transfer levels relative to the flat endwall, around the saddle point. However, the resulting smaller passage vortex with contouring had a reduced influence on the endwall boundary layer and lower levels of heat transfer in the passage.

Acknowledgments

We would like to thank United Technologies—Pratt & Whitney for their support of this work, and Eunice Allen-Bradley for performing the endwall contour design. We would also like to thank Dr. Brian Holley and Dr. Lee Langston for providing the raw materials for the OFI method.

Nomenclature

BL	boundary layer
C_{ax}	axial chord of blade
C_f	friction coefficient, $C_f = \frac{\tau_w}{1/2\,\rho U_{edge}^2}$
C_p	constant-pressure specific heat
C_{SKE}	mean secondary kinetic energy coefficient; see Eq. (3.6)
D	diameter of LDV measurement volume
g	gravitational acceleration (9.81 m/s^2)
h	heat transfer coefficient, $h = q''_w / (T_w - T_{in})$
H	boundary layer shape factor, $H=\delta^*/\theta$
HS	horseshoe vortex
k	turbulent kinetic energy (TKE), $k = 1/2\left(\overline{u'^2} + \overline{v'^2} + \overline{w'^2}\right)$
L	length of LDV measurement volume
L_f	average spacing between interferogram bands
n	index of refraction
P	blade pitch
p	static pressure
Pr	Prandtl number
PS	pressure side
q''_w	wall heat flux
Re_s	streamwise Reynolds number, $Re_s = sU_{edge} / \nu$
Re_θ	momentum thickness Reynolds number, $Re_\theta = \theta U_{edge} / \nu$
s	distance along streamwise direction

S	blade span
SS	suction side
St	Stanton number, $St = h/\rho C_p U_{edge}$
T	temperature
x, y, z	local coordinates; see Figure 3.3
X, Y, Z	blade cascade coordinates, where X is blade axial direction
u, v, w	velocity components in a local coordinate system; see Figure 3.3
U, V, W	velocity components in the cascade coordinate system
V_s, V_n, V_z	secondary velocity components; see Eq.'s (3.2-4)
u_τ	friction velocity, $u_\tau = \sqrt{\tau_w/\rho}$
U_{in}	magnitude of inlet streamwise velocity
U_{exit}	magnitude of exit streamwise velocity
U_{edge}	magnitude of local freestream velocity at the boundary layer edge

Greek

β	mean flow angle
δ_{99}	boundary layer thickness (99%)
δ^*	displacement thickness based on streamwise velocity, $\delta^* = \int_0^\infty \left(1 - \frac{u}{U_{edge}}\right) dz$
θ	momentum thickness based on streamwise velocity, $\theta = \int_0^\infty \frac{u}{U_{edge}} \left(1 - \frac{u}{U_{edge}}\right) dz$
θ_i	incidence angle of light
λ	wavelength of light
μ	dynamic viscosity
ν	kinematic viscosity
ρ	density
τ_w	wall shear stress

Subscripts

air	air conditions
edge	quantity at boundary layer edge

exit	exit freestream conditions
in	inlet freestream conditions
ms	midspan (inviscid) conditions
oil	silicone oil conditions
w	wall conditions

Superscripts

'	fluctuating quantity
+	inner wall coordinates (using friction velocity)
$\overline{(\,)}$	time-averaged quantity

References

[1] Anderson, S. D., and Eaton, J. K., 1989, "Reynolds Stress Development in Pressure-Driven Three-Dimensional Turbulent Boundary Layers," *Journal of Fluid Mechanics*, **202**, pp. 263-294.

[2] Olcmen, M. S., and Simpson, R. L., 1995, "An Experimental Study of a Three-Dimensional Pressure-Driven Turbulent Boundary Layer," *Journal of Fluid Mechanics*, **290**, pp. 225-262.

[3] Olcmen, M. S., and Simpson, R. L., 1992, "Perspective: On the near Wall Similarity of Three-Dimensional Turbulent Boundary Layers (Data Bank Contribution)," *Journal of Fluids Engineering*, **114**(4), pp. 487-495.

[4] Johnston, J. P., and Flack, K. A., 1996, "Review---Advances in Three-Dimensional Turbulent Boundary Layers with Emphasis on the Wall-Layer Regions," *Journal of Fluids Engineering*, **118**(2), pp. 219-232.

[5] Abrahamson, S. D., and Eaton, J. K., 1991, "Heat Transfer through a Pressure-Driven Three-Dimensional Boundary Layer," *Journal of Heat Transfer*, **113**(2), pp. 355-362.

[6] Lewis, D. J., and Simpson, R. L., 1998, "Turbulence Structure of Heat Transfer through a Three-Dimensional Turbulent Boundary Layer," *Journal of Thermophysics and Heat Transfer*, **12**(2), pp. 248-255.

[7] Eibeck, P. A., and Eaton, J. K., 1987, "Heat Transfer Effects of a Longitudinal Vortex Embedded in a Turbulent Boundary Layer," *Journal of Heat Transfer*, **109**(1), pp. 16-24.

[8] Wroblewski, D. E., and Eibeck, P. A., 1991, "Measurements of Turbulent Heat Transport in a Boundary Layer with an Embedded Streamwise Vortex," *International Journal of Heat and Mass Transfer*, **34**(7), pp. 1617-1631.

[9] Shizawa, T., and Eaton, J. K., 1992, "Turbulence Measurements for a Longitudinal Vortex Interacting with a Three-Dimensional Turbulent Boundary Layer," *AIAA Journal*, **30**(1), pp. 49-55.

[10] Langston, L. S., Nice, M. L., and Hooper, R. M., 1977, "Three-Dimensional Flow within a Turbine Cascade Passage," *Journal of Engineering for Power*, **99**, pp. 21-28.

[11] Langston, L. S., 1980, "Crossflows in a Turbine Cascade Passage," *Journal of Engineering for Power*, **102**, pp. 866-874.

[12] Kang, M. B., and Thole, K. A., 2000, "Flowfield Measurements in the Endwall Region of a Stator Vane," *Journal of Turbomachinery*, **122**(3), pp. 458-466.

[13] Radomsky, R. W., and Thole, K. A., 2000, "High Free-Steam Turbulence Effects on Endwall Heat Transfer for a Gas Turbine Stator Vane," *Journal of Turbomachinery*, **122**(4), pp. 699-708.

[14] Harrison, S., 1990, "Secondary Loss Generation in a Linear Cascade of High-Turning Turbine Blades," *Journal of Turbomachinery*, **112**(4), pp. 618-624.

[15] Vera, M., Blanco, E. D. L. R., Hodson, H., and Vazquez, R., 2009, "Endwall Boundary Layer Development in an Engine Representative Four-Stage Low Pressure Turbine Rig," *Journal of Turbomachinery*, **131**(1), pp. 011017.

[16] Harvey, N. W., Rose, M. G., Taylor, M. D., Shahpar, S., Hartland, J., and Gregory-Smith, D. G., 2000, "Nonaxisymmetric Turbine End Wall Design: Part I--- Three-Dimensional Linear Design System," *Journal of Turbomachinery*, **122**(2), pp. 278-285.

[17] Hartland, J. C., Gregory-Smith, D. G., Harvey, N. W., and Rose, M. G., 2000, "Nonaxisymmetric Turbine End Wall Design: Part II---Experimental Validation," *Journal of Turbomachinery*, **122**(2), pp. 286-293.

[18] Germain, T., Nagel, M., Raab, I., Schupbach, P., Abhari, R. S., and Rose, M., 2010, "Improving Efficiency of a High Work Turbine Using Nonaxisymmetric Endwalls--- Part I: Endwall Design and Performance," *Journal of Turbomachinery*, **132**(2), pp. 021007.

[19] Schuepbach, P., Abhari, R. S., Rose, M. G., Germain, T., Raab, I., and Gier, J., 2010, "Improving Efficiency of a High Work Turbine Using Nonaxisymmetric Endwalls---Part II: Time-Resolved Flow Physics," *Journal of Turbomachinery*, **132**(2), pp. 021008.

[20] Praisner, T. J., Allen-Bradley, E., Grover, E. A., Knezevici, D. C., and Sjolander, S. A., 2007, "Application of Non-Axisymmetric Endwall Contouring to Conventional and High-Lift Turbine Airfoils," Proc. ASME Turbo Expo 2007, Paper No. GT2007-27579.

[21] Knezevici, D. C., Sjolander, S. A., Praisner, T. J., Allen-Bradley, E., and Grover, E. A., 2010, "Measurements of Secondary Losses in a Turbine Cascade with the Implementation of Nonaxisymmetric Endwall Contouring," *Journal of Turbomachinery*, **132**(1), pp. 011013.

[22] Saha, A. K., and Acharya, S., 2008, "Computations of Turbulent Flow and Heat Transfer through a Three-Dimensional Nonaxisymmetric Blade Passage," *Journal of Turbomachinery*, **130**(3), pp. 031008.

[23] Lynch, S. P., Sundaram, N., Thole, K. A., Kohli, A., and Lehane, C., 2011, "Heat Transfer for a Turbine Blade with Nonaxisymmetric Endwall Contouring," *Journal of Turbomachinery*, **133**(1), pp. 011019-9.

[24] Lynch, S. P., Thole, K. A., Kohli, A., and Lehane, C., 2011, "Computational Predictions of Heat Transfer and Film-Cooling for a Turbine Blade with Nonaxisymmetric Endwall Contouring," *Journal of Turbomachinery*, **133**(4), pp. 041003-10.

[25] Mclaughlin, D. K., and Tiederman, W. G., 1973, "Biasing Correction for Individual Realization of Laser Anemometer Measurements in Turbulent Flows," *Physics of Fluids*, **16**(12), pp. 2082-2088.

[26] Moffat, R. J., 1988, "Describing the Uncertainties in Experimental Results," *Experimental Thermal and Fluid Science*, **1**, pp. 3-17.

[27] Naughton, J. W., and Sheplak, M., 2002, "Modern Developments in Shear-Stress Measurement," *Progress in Aerospace Sciences*, **38**(6-7), pp. 515-570.

[28] Holley, B. M., Becz, S., and Langston, L. S., 2006, "Measurement and Calculation of Turbine Cascade Endwall Pressure and Shear Stress," *Journal of Turbomachinery*, **128**(2), pp. 232-239.

[29] Holley, B. M., and Langston, L. S., 2009, "Surface Shear Stress and Pressure Measurements in a Turbine Cascade," *Journal of Turbomachinery*, **131**(3), pp. 031014-8.

[30] Lynch, S. P., and Thole, K. A., 2008, "The Effect of Combustor-Turbine Interface Gap Leakage on the Endwall Heat Transfer for a Nozzle Guide Vane," *Journal of Turbomachinery*, **130**(4), pp. 041019.

[31] Compton, D. A., and Eaton, J. K., 1997, "Near-Wall Measurements in a Three-Dimensional Turbulent Boundary Layer," *Journal of Fluid Mechanics*, **350**, pp. 189-208.

[32] Spalding, D. B., 1961, *Journal of Applied Mechanics*, **28**, pp. 455-457.

[33] Thole, K. A., and Bogard, D. G., 1996, "High Freestream Turbulence Effects on Turbulent Boundary Layers," *Journal of Fluids Engineering*, **118**(2), pp. 276-284.

[34] Volino, R. J., and Simon, T. W., 1997, "Velocity and Temperature Profiles in Turbulent Boundary Layer Flows Experiencing Streamwise Pressure Gradients," *Journal of Heat Transfer-Transactions of the ASME*, **119**(3), pp. 433-439.

[35] Popiel, C. O., and Boguslawski, L., 1975, "Local Heat-Transfer Coefficients on the Rotating Disk in Still Air," *International Journal of Heat and Mass Transfer*, **18**(1), pp. 167-170.

Table 3.1 Cascade Geometry

Scale	8.6X
Axial chord (C_{ax})	0.218 m
Span/axial chord (S/C_{ax})	2.50
Pitch/axial chord (P/C_{ax})	0.826
Inlet angle (β_{in}, relative to axial direction)	35°
Exit angle (β_{exit}, relative to axial direction)	60°
Zwiefel load coefficient	1.13
Inlet Reynolds number ($Re_{in}=U_{in}C_{ax}/\nu$)	$1.25x10^5$
Exit Reynolds number ($Re_{ex}=U_{exit}C_{ax}/\nu$)	$2.00x10^5$
Exit Mach number	0.04

Table 3.2 Inlet Boundary Layer Measurements at $2.85C_{ax}$ Upstream of Blade 3

Variable	**Y/P=0**	**Y/P=0.5**	**Y/P=1.0**	**Lynch, et al. [23]** (Y/P=1.0)
δ_{99}/S	0.065	0.068	0.076	0.061
θ/S	0.0049	0.0050	0.0051	0.0046
Re_θ	1500	1550	1540	1340
H	1.32	1.32	1.30	1.26
Tu	5.9%	5.7%	5.8%	5.9%
$C_f/2$	0.00229	0.00229	0.00231	0.00231

Table 3.3 Endwall Boundary Layer Locations in the Blade Passage (see Figure 3.3)

Name	**Cascade Coordinates**		**Local Coordinates**
	X/C_{ax}	**Y/P**	**y/P**
S1	-0.40	0.50	
S2	-0.15	0.48	
S3	0.03	0.51	
A1	0.2	0.19	0.28
A2	0.2	0.44	0.54
A3	0.2	0.65	0.74

Table 3.4 Estimated Uncertainties for Flowfield Measurements at a Highly Turbulent Location in Plane A

Variable	Mean	Uncertainty	% of Mean
u/U_{in}	0.436	±0.011	±2.6%
v/U_{in}	0.207	±0.0065	±3.1%
w/U_{in}	-0.030	±0.0053	±17.5%
β	25.4°	±0.5°	±2.0%
V_s/U_{in}	0.390	±0.041	±1.3%
V_n/U_{in}	0.283	±0.036	±1.6%
V_z/U_{in}	-0.030	±0.0053	±17.5%
k/U_{in}^2	0.023	±0.0011	±4.9%
$\overline{u'}/U_{in}$	0.143	±0.0037	±2.6%
$\overline{v'}/U_{in}$	0.130	±0.0034	±2.6%
$\overline{w'}/U_{in}$	0.089	±0.0028	±3.2%
$C_f/2$	0.00439	±3.51e-4	±8%
$\beta_w-\beta_{ms}$	64°	±4°	±6%

Table 3.5 Endwall Streakline Boundary Layer Parameters

Name	S1		S2		S3	
	Flat	Contour	Flat	Contour	Flat	Contour
U_{edge}/U_{in}	1.00	1.00	1.01	1.02	1.10	1.10
δ_{99}/S	0.096	0.099	0.095	0.096	0.112	0.112
θ/S	0.0078	0.0079	0.0081	0.0084	0.0090	0.0074
Re_θ	2140	2220	2230	2390	2680	2200
H	1.33	1.33	1.33	1.34	1.29	1.21
Tu	5.1%	5.5%	5.1%	5.4%	4.7%	4.8%
$C_f/2$, OFI	0.00214	0.00213	0.00217	0.00225	0.00244	0.00344
$C_f/2$, Clauser fit to velocity magnitude	0.00203	0.00200	0.00202	0.00193	0.00206	0.00250
β_{ms}	-35.1°	-35.1°	-31.8°	-31.4°	-26.1°	-25.8°
β_w	-27°	-26°	-9°	-7°	11°	13°

Table 3.6 Plane A Boundary Layer Parameters

Name	**A1**		**A2**		**A3**	
	Flat	**Contour**	**Flat**	**Contour**	**Flat**	**Contour**
U_{edge}/U_{in}	0.79	0.79	1.10	1.11	1.46	1.43
δ_{99}/S	0.091	0.072	0.124	0.128	0.159	0.194
θ/S	0.0100	0.0073	0.0100	0.0120	0.0110	0.0178
Re_θ	2230	1670	3050	3810	4370	7175
H	1.63	1.47	1.32	1.47	1.24	1.36
Tu	6.5%	6.2%	4.3%	4.3%	3.3%	3.3%
$C_f/2$, OFI	0.00337	0.00439	0.00310	0.00228	0.00277	0.00251
$C_f/2$, Clauser fit to velocity magnitude	0.00143	0.00201	0.00187	0.00140	0.00211	0.00137
β_{ms}	-10.4°	-10.6°	-10.5°	-9.9°	-14.9°	-17.0°
β_w	62°	53°	43°	54°	29°	48°

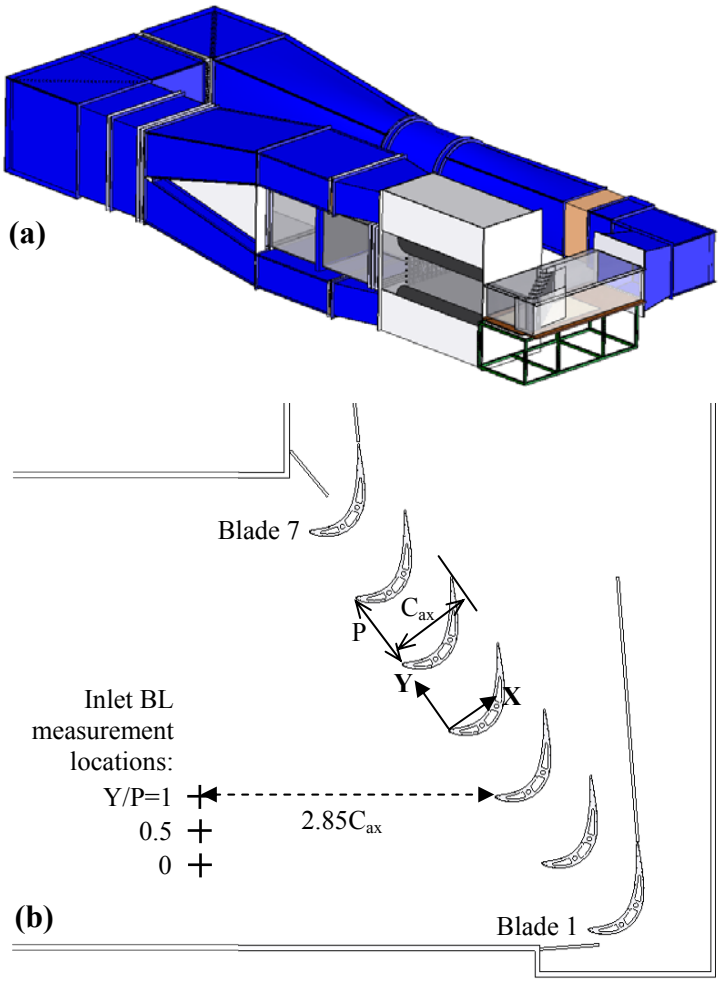

Figure 3.1. Depiction of (a) the low-speed wind tunnel with corner test section, and (b) the test section with inlet boundary layer measurement locations indicated.

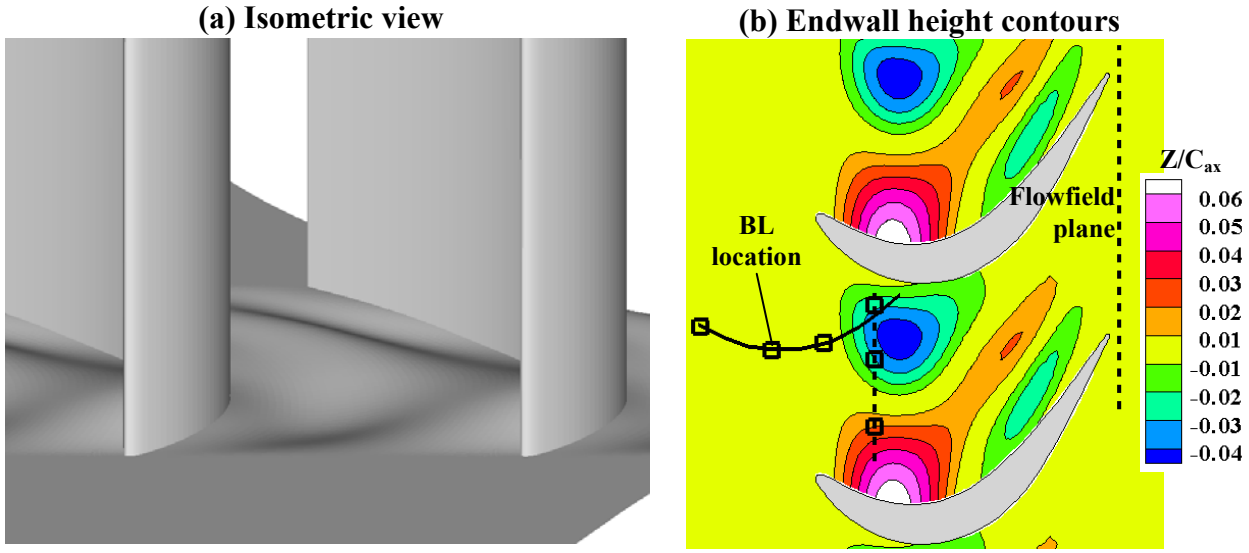

Figure 3.2. (a) An isometric view of the non-axisymmetric contoured endwall; and (b) contours of endwall height, with flowfield measurement locations overlaid (see Figure 3.3).

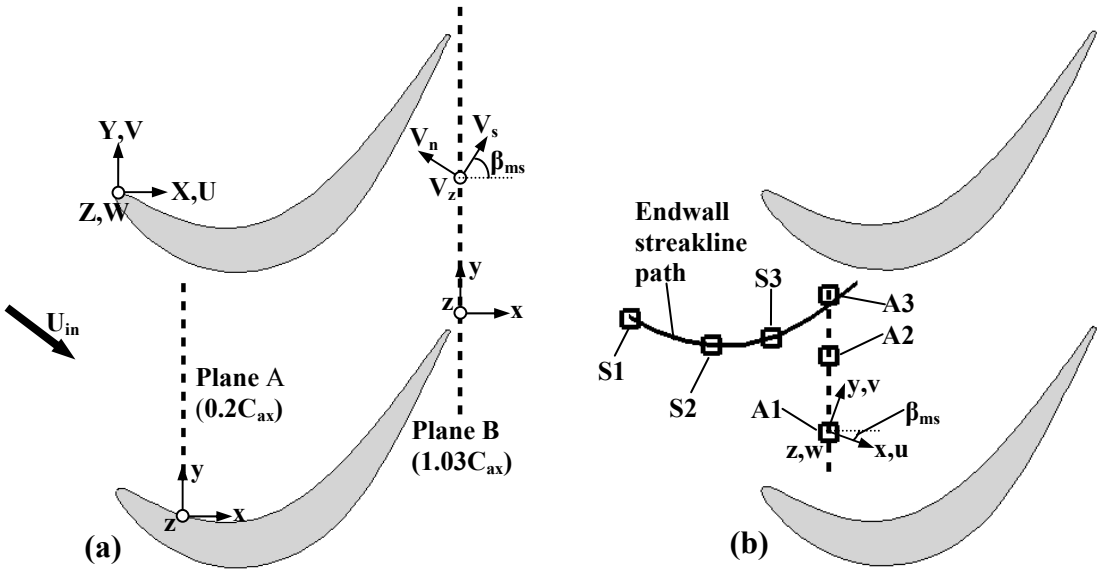

Figure 3.3. (a) Locations of flowfield measurement planes, where the local coordinate system is parallel to cascade coordinates; and (b) locations of endwall boundary layer measurements, where the local coordinate system is aligned to the local freestream velocity.

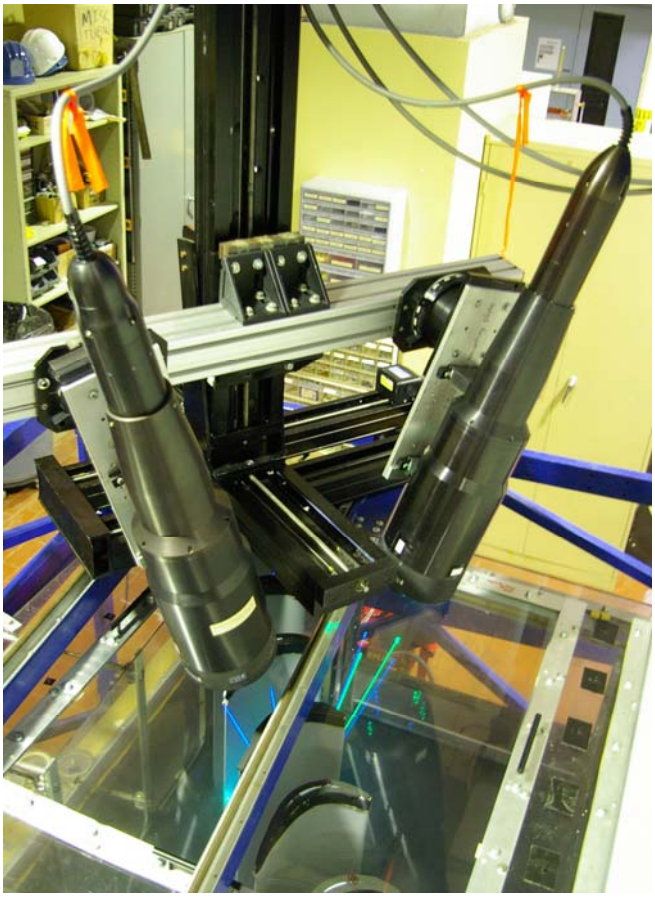

Figure 3.4. Non-orthogonal three-component LDV configuration for measurements in the blade passage.

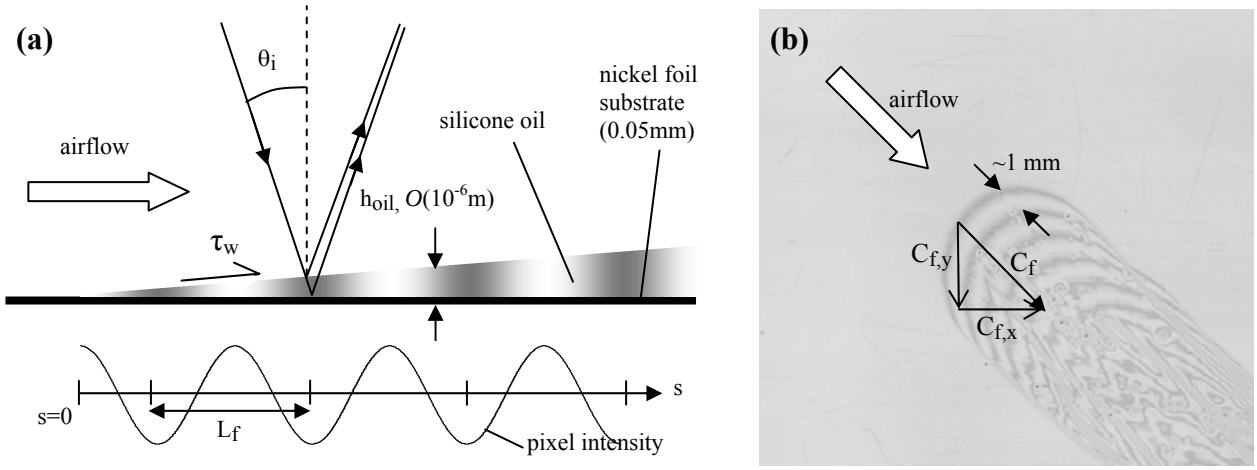

Figure 3.5. Schematic of oil film development due to shear (a); and a sample interferogram (b) which demonstrates friction coefficient directionality.

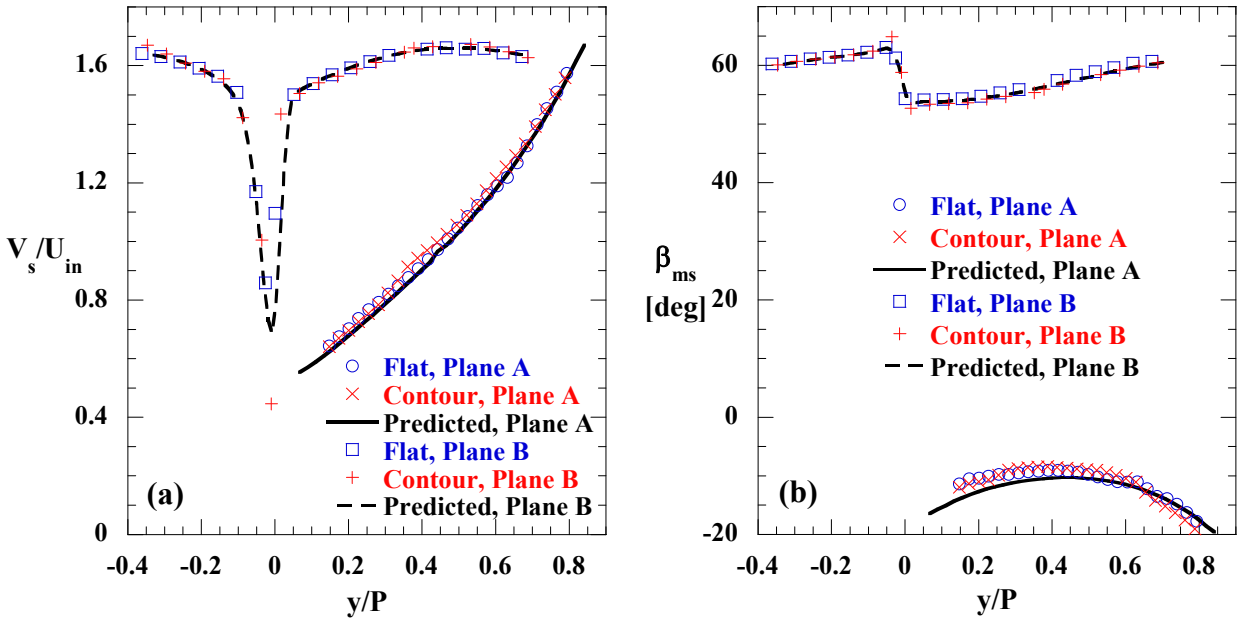

Figure 3.6. Measured (a) mean streamwise velocity and (b) mean flow angle at the blade midspan, compared to the prediction of Lynch, et al. [24].

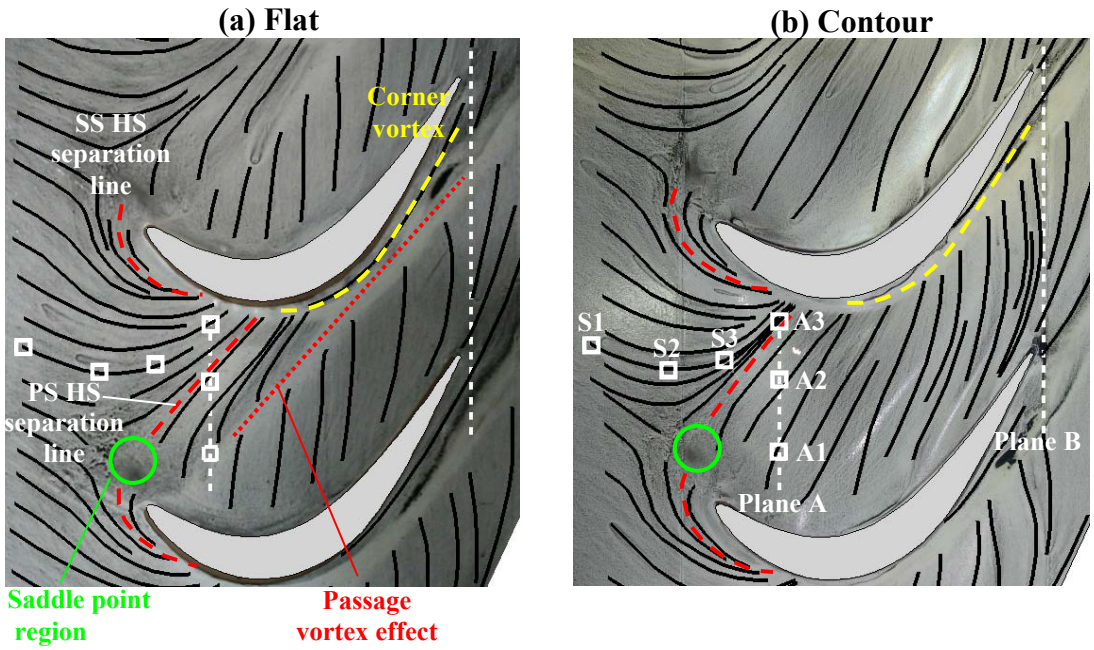

Figure 3.7. Endwall oil flow visualization of Lynch, et al. [23] for the (a) flat and (b) contoured endwalls, overlaid with the location of flowfield measurements in this study (see Figure 3.3).

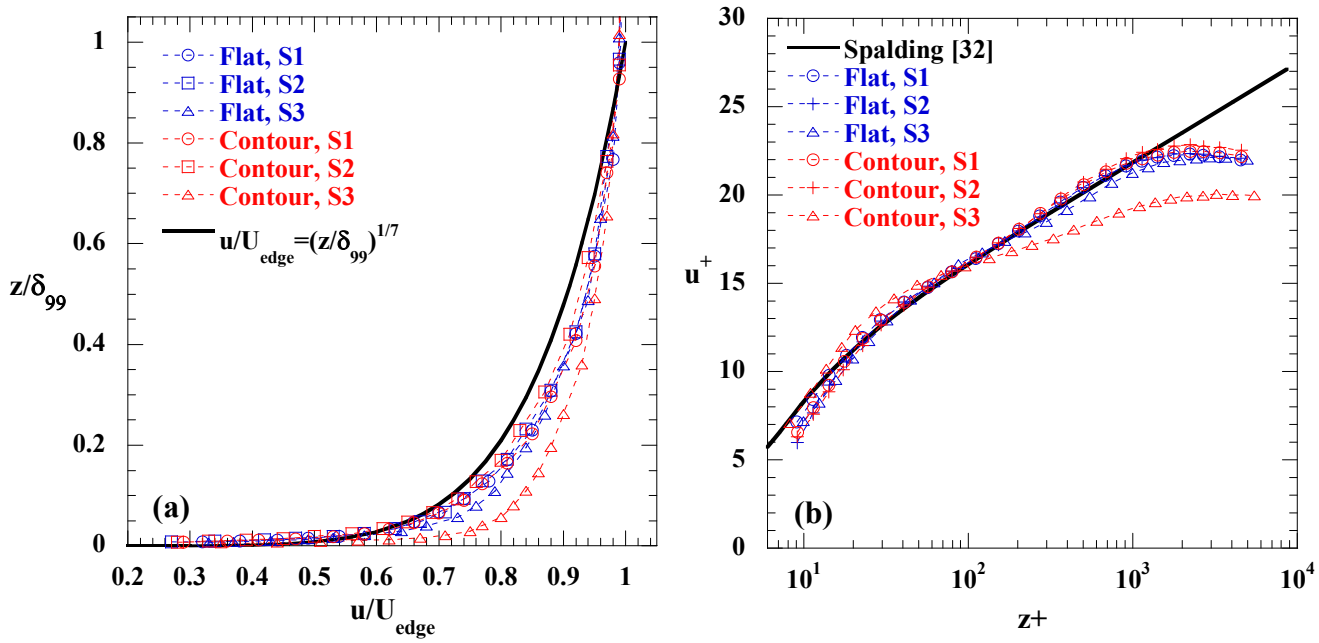

Figure 3.8. Boundary layer profiles of mean streamwise velocity along an endwall streakline path originating upstream of the cascade, plotted using (a) freestream scaling variables and (b) inner scaling variables.

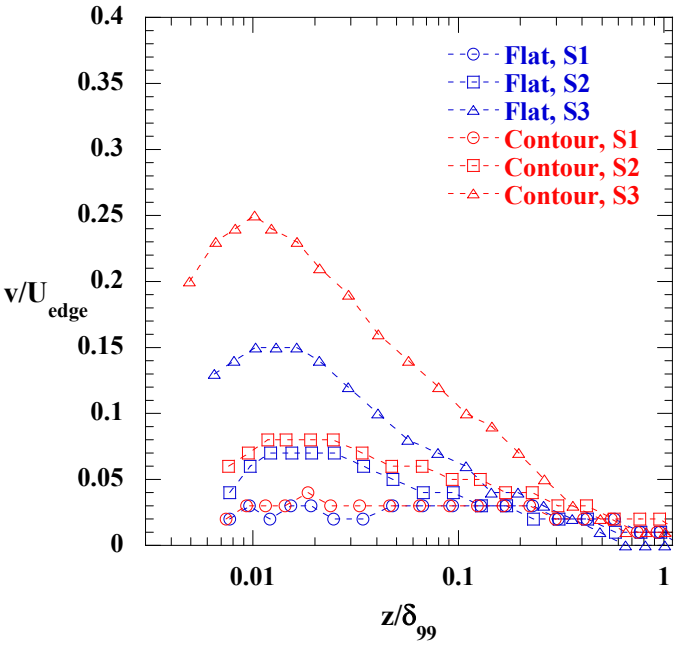

Figure 3.9. Boundary layer profiles of mean cross-stream velocity along an endwall streakline path originating upstream of the cascade.

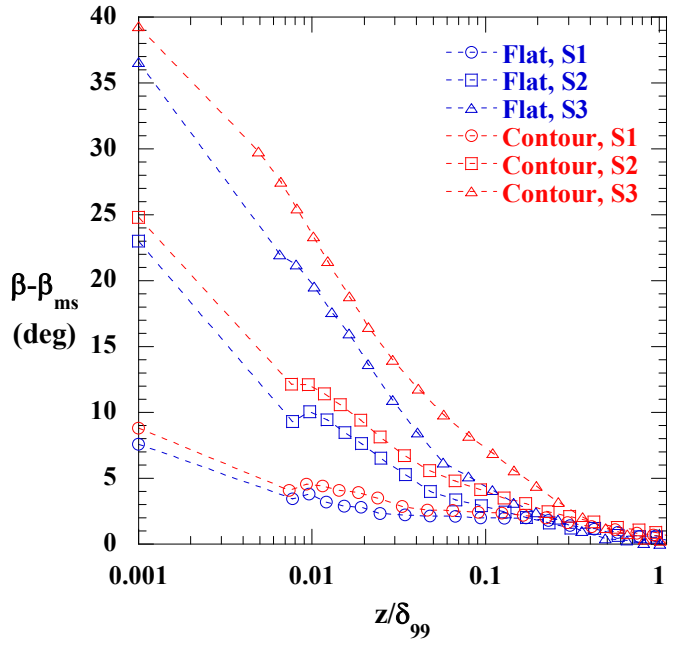

Figure 3.10. Boundary layer profiles of mean flow angle relative to the freestream angle along an endwall streakline path originating upstream of the cascade. The results at z/δ=0.001 are wall shear angles from the friction coefficient measurements.

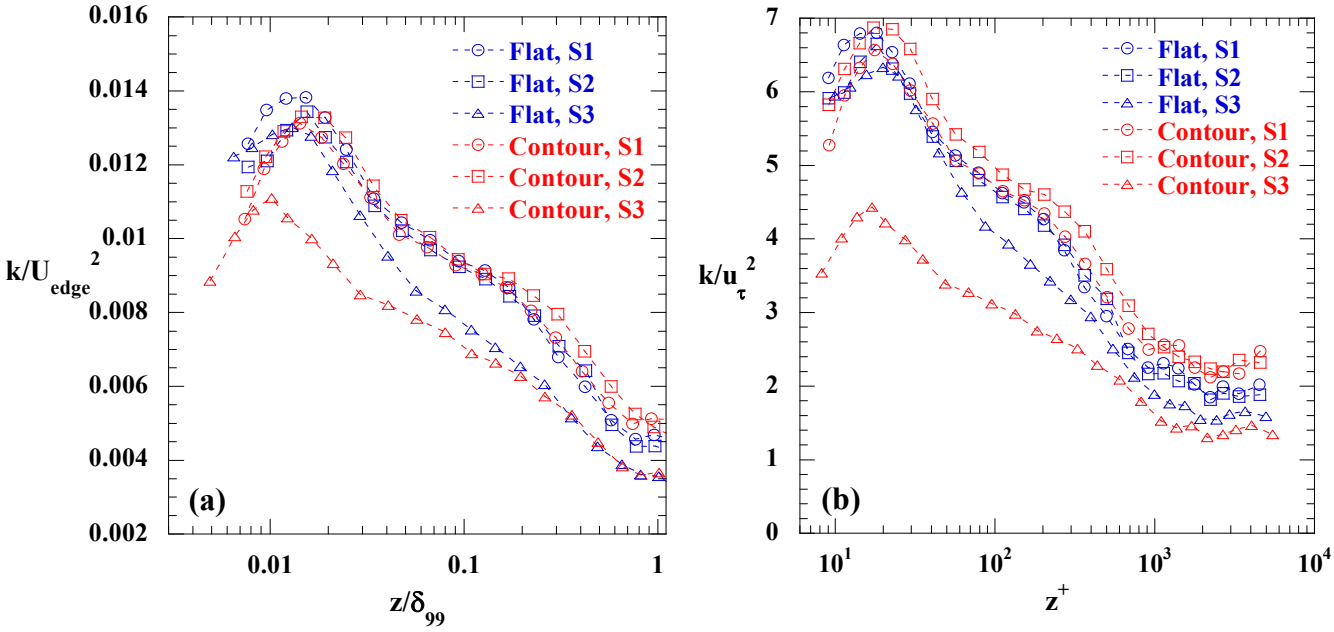

Figure 3.11. Boundary layer profiles of turbulent kinetic energy along an endwall streakline path originating upstream of the cascade, plotted using (a) freestream scaling variables and (b) inner scaling variables.

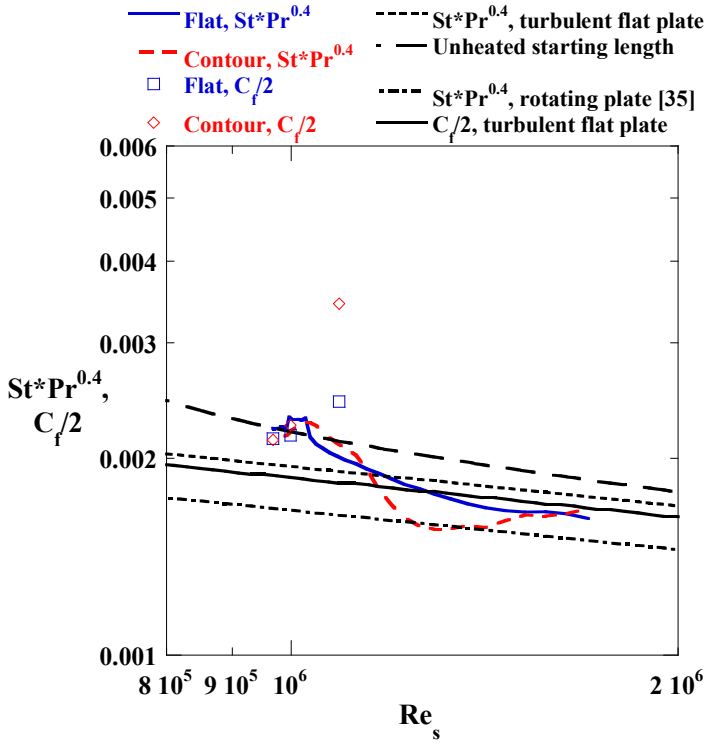

Figure 3.12. Endwall heat transfer and friction coefficients along an endwall streakline path, where the velocity scale for Re_s, St, and C_f is the local freestream velocity.

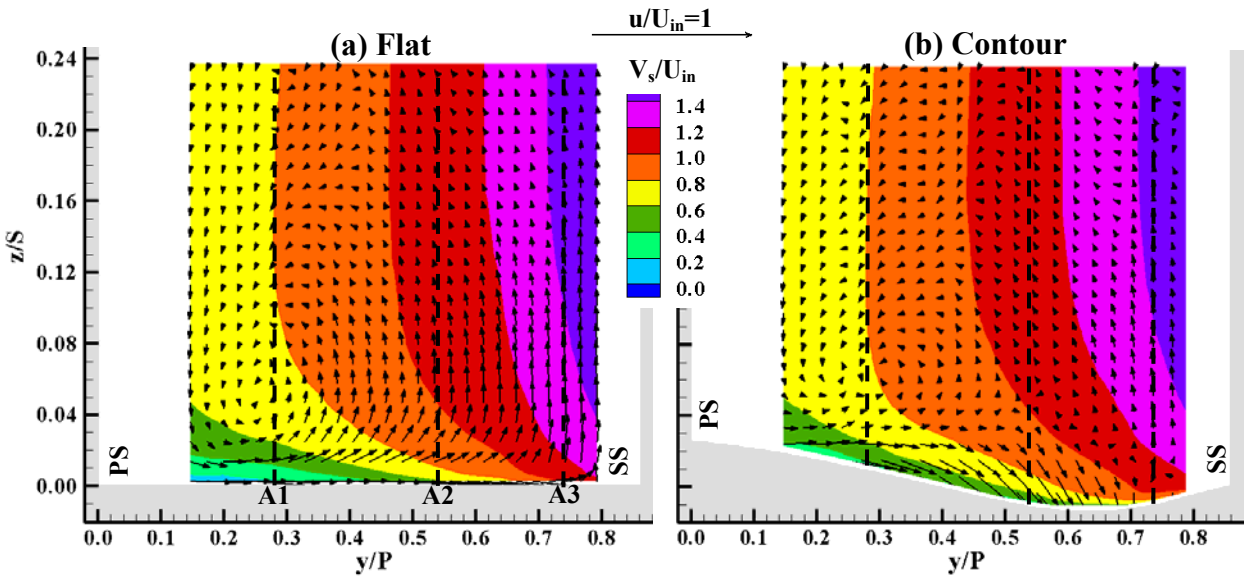

Figure 3.13. Contours of mean streamwise velocity and mean secondary velocity vectors at Plane A for the (a) flat and (b) contoured endwalls.

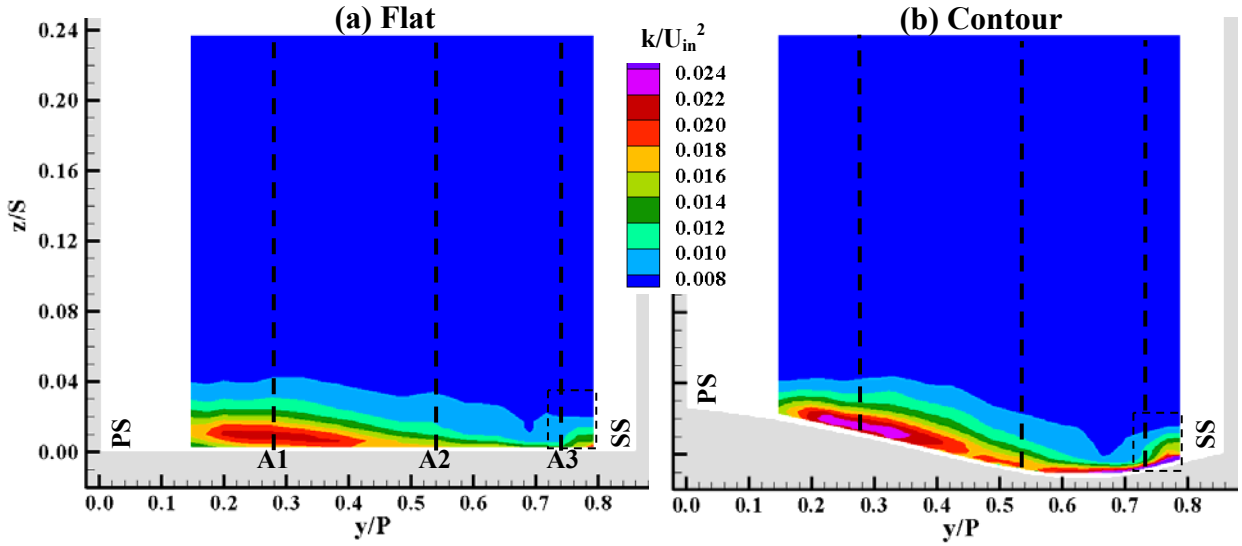

Figure 3.14. Contours of turbulent kinetic energy at Plane A for the (a) flat and (b) contoured endwalls.

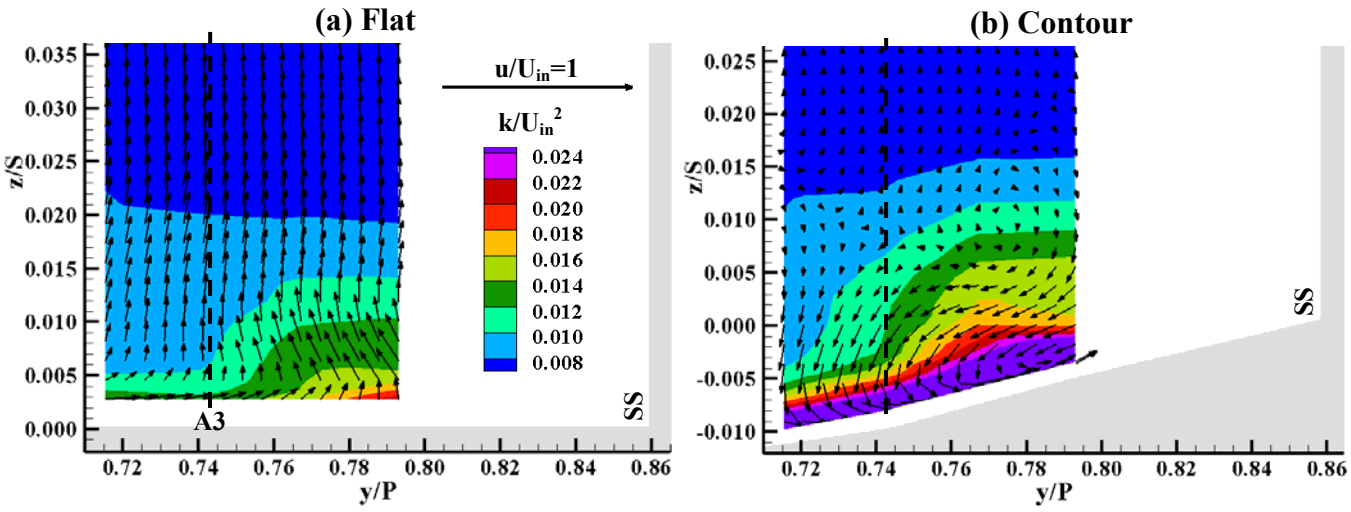

Figure 3.15. Contours of turbulent kinetic energy overlaid with mean secondary velocity vectors near the suction side-endwall corner for the (a) flat and (b) contoured endwalls.

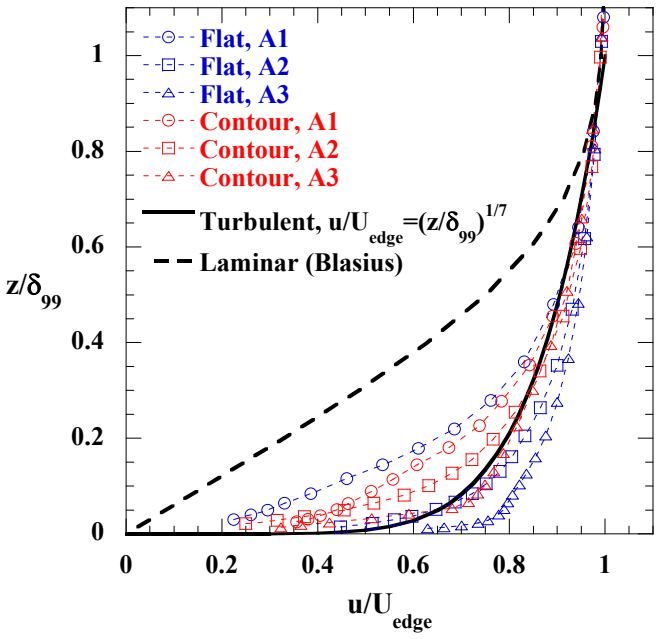

Figure 3.16. Boundary layer profiles of mean streamwise velocity in Plane A for the flat and contoured endwalls.

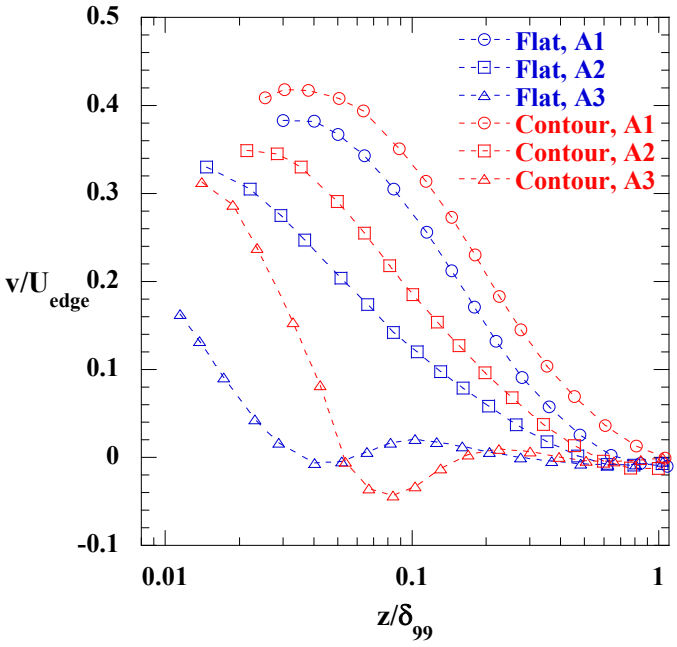

Figure 3.17. Boundary layer profiles of mean cross-stream velocity in Plane A for the flat and contoured endwalls.

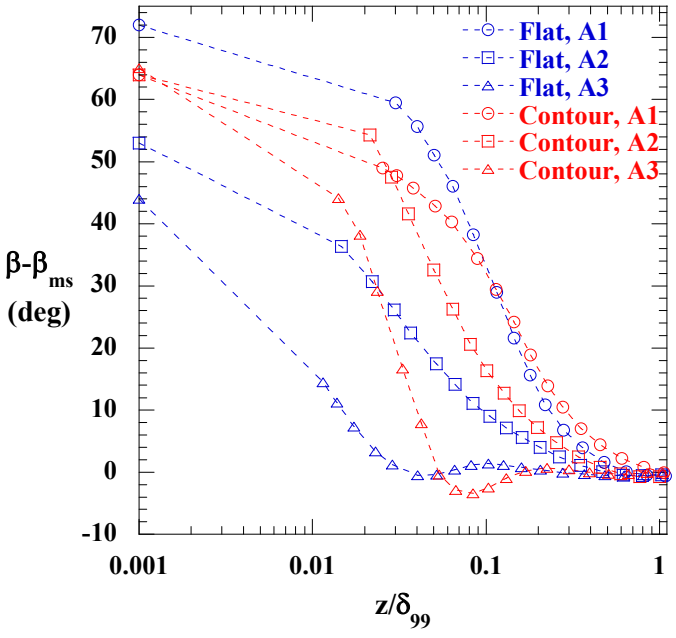

Figure 3.18. Boundary layer profiles of mean flow angle relative to the freestream angle in Plane A, for the flat and contoured endwalls. The results at z/δ=0.001 are wall shear angles from the friction coefficient measurements.

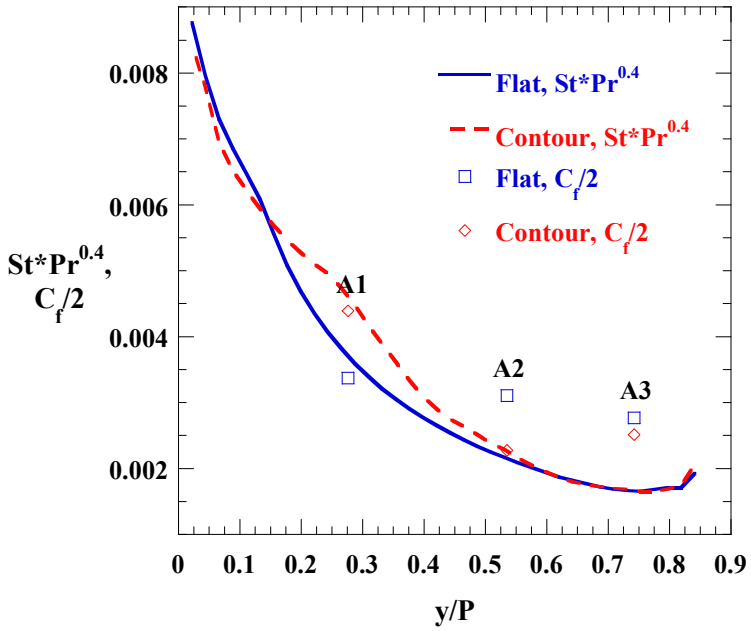

Figure 3.19. Endwall heat transfer and friction coefficients at Plane A, where the velocity scale for St and C_f is the local freestream velocity.

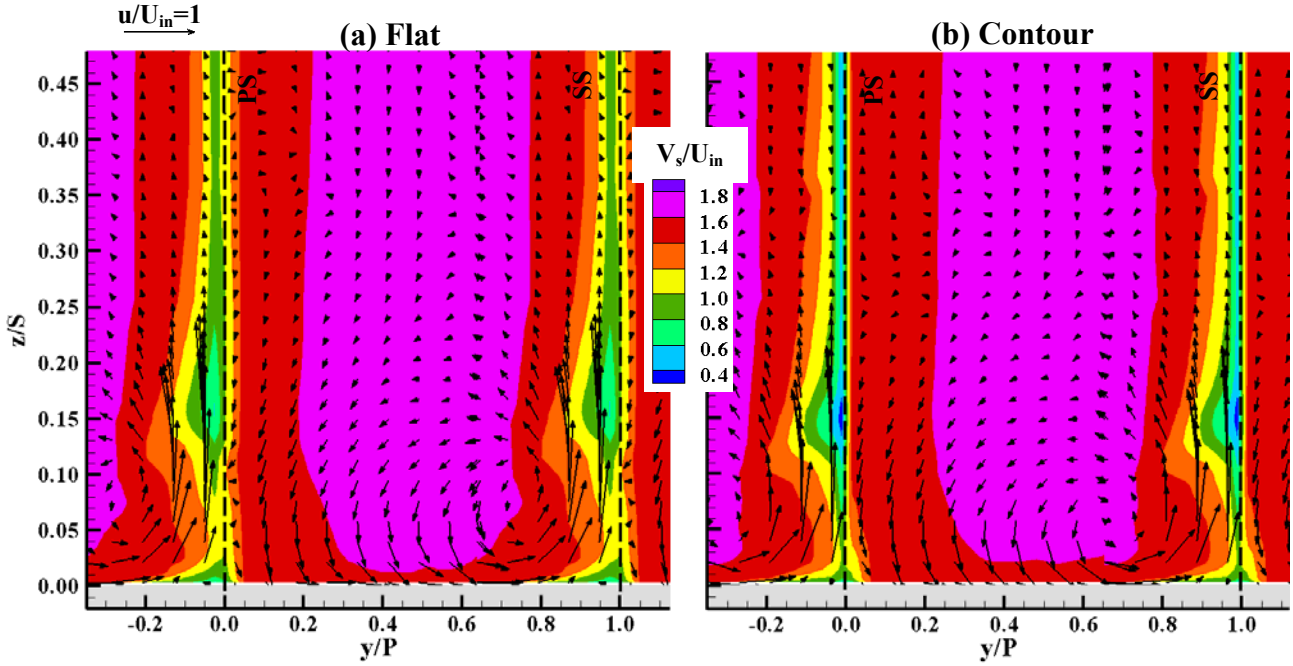

Figure 3.20. Contours of mean streamwise velocity and mean secondary velocity vectors at Plane B for the (a) flat and (b) contoured endwalls.

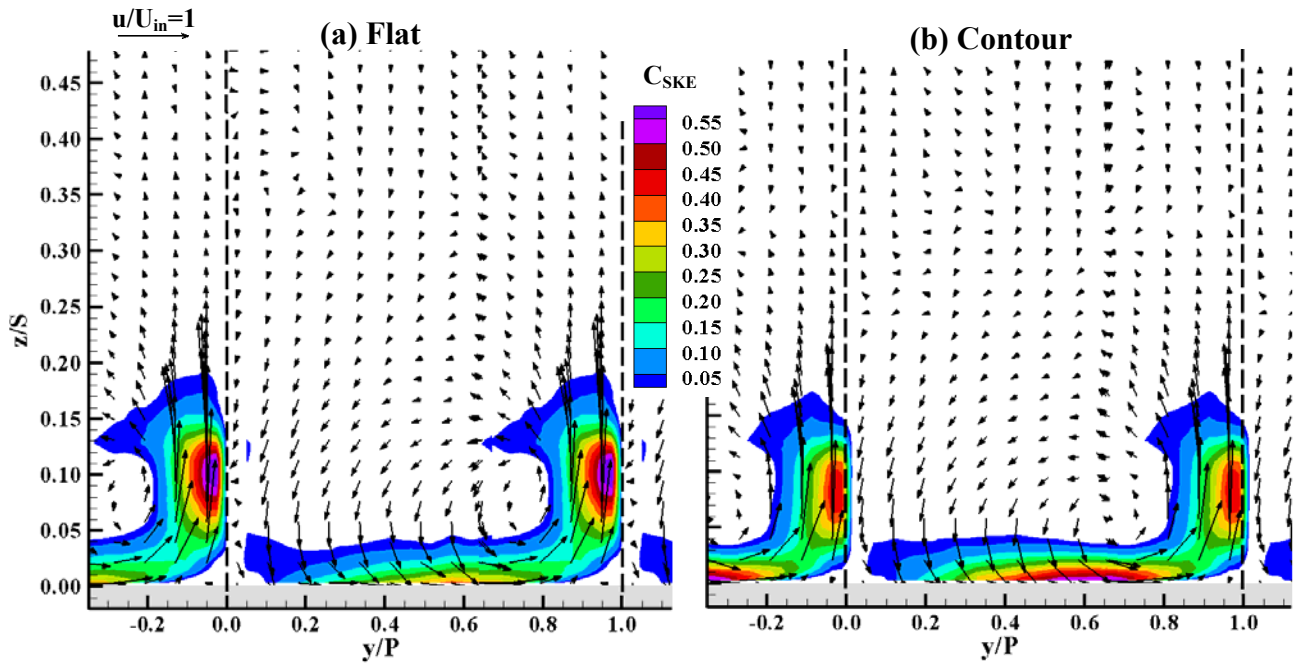

Figure 3.21. Contours of mean secondary kinetic energy at Plane B for the (a) flat and (b) contoured endwalls.

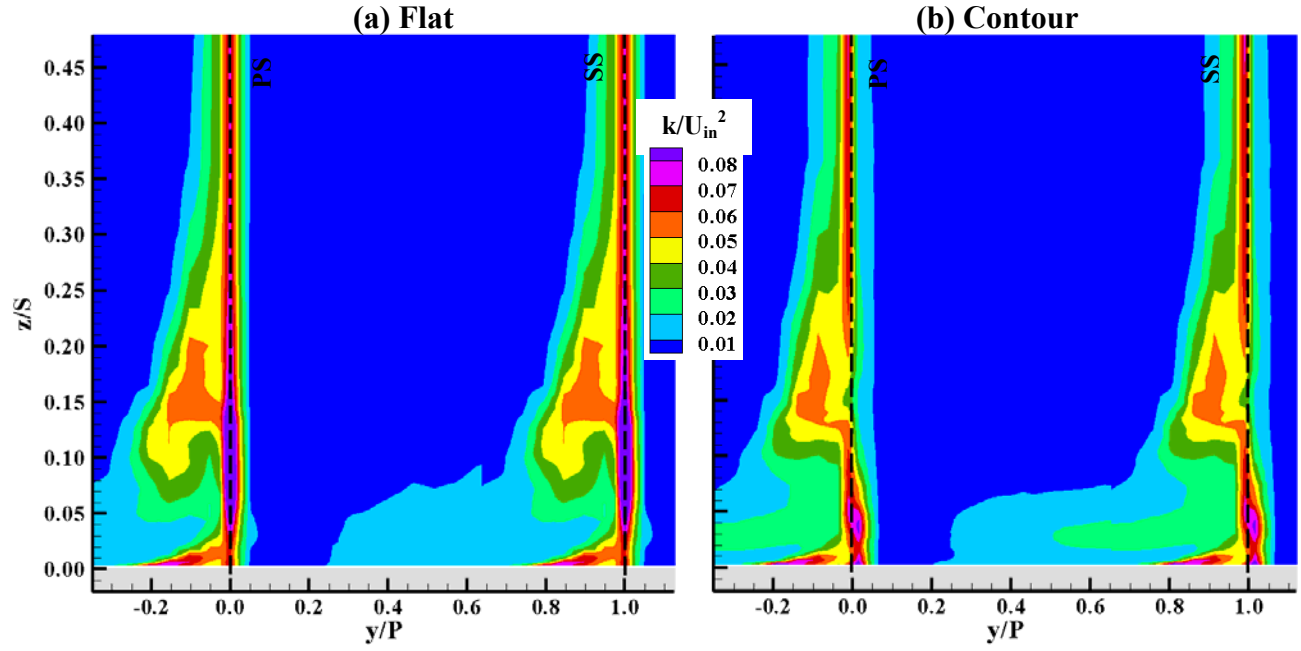

Figure 3.22. Contours of turbulent kinetic energy at Plane B for the (a) flat and (b) contoured endwalls.

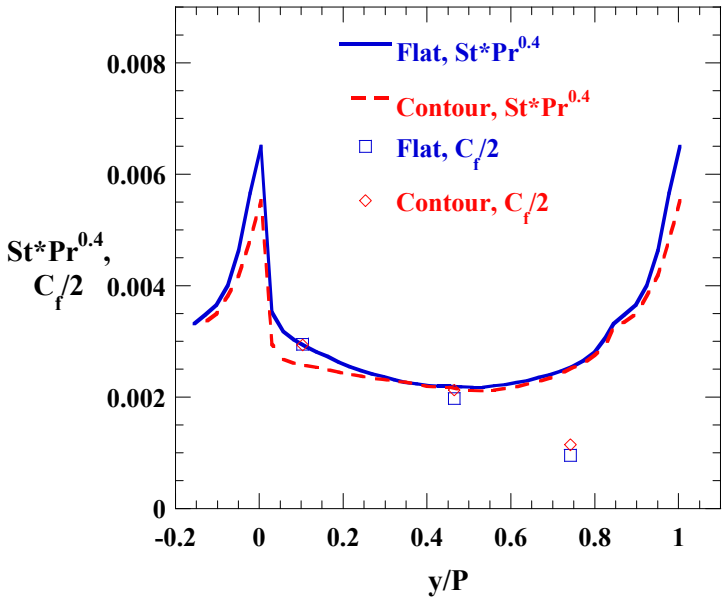

Figure 3.23. Endwall heat transfer and friction coefficients at Plane B, where the velocity scale for St and C_f is the local freestream velocity.

Paper 4: Endwall Heat Transfer for a Turbine Blade with an Upstream Cavity and Rim Seal Leakage

To be submitted to the *Journal of Turbomachinery**

Abstract

Aerodynamic loss and endwall heat transfer for a turbine blade are influenced by complex vortical flows that are generated at the airfoil-endwall junction. In an engine, those flows interact with clearance gaps between stationary and rotating components, as well as with leakage flow that is designed to exhaust through the gaps. Previous research has indicated that the mass flow ratio of the leakage and its relative circumferential (swirl) velocity can significantly influence the vortical flows.

This paper describes experimental measurements of endwall heat transfer for a high-pressure turbine blade with an endwall overlap geometry, as well as an upstream leakage feature that supplied swirled or unswirled leakage relative to the blade. Unswirled leakage represented flow with a circumferential velocity that was the same as the rotor hub speed, while swirled leakage simulated flow with a circumferential velocity that was lower than the rotor speed. For unswirled leakage, increasing its mass flow increased the magnitude and pitchwise uniformity of the heat transfer coefficient upstream of the blades although heat transfer further into the passage was unchanged. Leakage flow with swirl shifted the horseshoe vortex in the direction of swirl and increased heat transfer on the upstream blade endwall, as compared to unswirled leakage. For a nominal leakage mass flow ratio of 0.75%, swirled leakage did not increase area-averaged heat transfer relative to unswirled leakage. At a mass flow ratio of 1.0%, however, swirled leakage increased overall heat transfer by 4% due to an increase in the strength of the vortical flows.

*Co-authors: Dr. Karen A. Thole, Mechanical & Nuclear Engineering Department, Penn State
Dr. Atul Kohli, United Technologies--Pratt & Whitney
Dr. Christopher Lehane, United Technologies--Pratt & Whitney

Introduction

Heat transfer to gas turbine components is a critical issue at the high combustion gas temperatures typical of modern gas turbine engines. Rotor inlet temperatures are on the order of 1500°C, and it is estimated that a metal temperature increase of only 25°C can reduce part life to half of its design value (Han, et al. [1]); therefore, advanced reliable cooling schemes are necessary. A particularly challenging region to cool is the hub region of a turbine blade, also known as an endwall. Complex vortical flows at the airfoil-endwall junction, necessary clearance gaps between stationary and rotating components, and leakage flows from those gaps all play an important role in the heat transfer to the endwall.

Vortical flows at the airfoil-endwall junction, also termed secondary flows, are generated by the interaction of the endwall boundary layer with the airfoil leading edge, and by the cross-passage pressure gradient between adjacent airfoils. Models proposed by Langston [2], Sharma and Butler [3], Goldstein and Spores [4], and others have indicated the general structure of secondary flows. A horseshoe vortex is generated at the leading edge by the roll-up of the inlet boundary layer, and splits into pressure-side and suction-side legs. The pressure-side leg merges with a passage vortex that is drawn across the passage toward the aft suction side. A corner vortex develops at the suction side-endwall corner, downstream of the impingement of the passage vortex. Flow separation and reattachment, plus increased turbulence caused by secondary flows, results in high levels of endwall heat transfer.

Clearance gaps are required between the stationary and rotating components in an engine. Hot combustion gases must be prevented from escaping into the gaps and causing durability issues for components under the platform. One method of limiting hot gas leakage is to design an overlap in the stator and rotor endwalls, known as a rim seal. High-pressure compressor discharge flow is designed to exhaust through the rim seal to keep hot gases out. The leakage air can develop a significant circumferential (swirl) velocity due to viscous drag on the rotor wheel, or due to the manner of its injection below the rim seal. Flow separation and reattachment around the overlap, as well as swirled leakage flow, can interact with the secondary flow to impact endwall heat transfer.

The combined effect of the aforementioned influences on endwall heat transfer is not well understood. The intent of the work presented in this paper is to examine the effects of rim

seal leakage flow with and without swirl for a blade endwall with a realistic overlap geometry, through oil flow visualization and measurements of endwall heat transfer.

Review of Literature

Cavities or steps on the endwall upstream of a turbine can significantly change endwall secondary flows and their impact on aerodynamics and heat transfer. de la Rosa Blanco, et al. [5] determined that the passage vortex was shifted upstream for flow over a backward-facing step located upstream of a low-pressure turbine cascade, which reduced the interaction of the secondary flows with a pressure-side separation bubble and resulted in lower losses than a flat endwall or forward-facing step. A subsequent study (de la Rosa Blanco, et al. [6]) demonstrated that a cavity located downstream of the backward-facing step increased losses relative to a step without a cavity, due to ingestion and mixing in the cavity. Abo El Ella, et al. [7] also found that losses and flow overturning increased for an endwall with an upstream cavity relative to a smooth wall due to a separation bubble in the cavity that strengthened the passage vortex. Computational simulations by Marini and Girgis [8] indicated that eliminating a recessed cavity upstream of a rotor improved stage efficiency by reducing secondary mixing losses near the endwall. A loss breakdown scheme proposed by Gier, et al. [9] suggested that steps between turbine components were responsible for 20% of the loss increase between a smooth-flowpath model and a more realistic model with leakage interfaces.

In an endwall misalignment study by Piggush and Simon [10], a forward-facing step at the combustor-turbine interface slot in a nozzle guide vane cascade increased endwall heat transfer downstream of the step, relative to an aligned endwall. The increase for the forward-facing step was attributed to acceleration of the boundary layer over the step. The effect of steps at the combustor-turbine interface slot due to endwall misalignment was also studied by Cardwell, et al. [11]. A forward-facing step decreased slot coolant coverage downstream of the step due to increased mixing of slot coolant with the mainstream. A backward-facing step significantly increased coolant coverage due to reduced mixing, relative to an aligned endwall.

Leakage flow that is designed to exhaust from the clearance gap between the stator and rotor can have a circumferential velocity component due to drag on the rotor wheel or due to the manner of its injection. Generally, the leakage will have a lower circumferential velocity than the rotor wheel, which results in negative skew in the boundary layer approaching the blade. Walsh

and Gregory-Smith [12] demonstrated that an inlet boundary layer with negative skew significantly increased loss and vorticity downstream of a blade cascade by promoting earlier growth of secondary vortices. Reid, et al. [13] found that at a fixed leakage circumferential velocity, turbine stage efficiency decreased for increasing leakage mass flow ratios through a rim seal due to increased mixing losses. At a fixed mass flow ratio, increasing the circumferential velocity relative to the rotor decreased the near-wall incidence angle to the rotor and reduced the stage efficiency. de la Rosa Blanco, et al. [6] showed similar effects of leakage mass flow and swirl on aerodynamic loss for their low-pressure turbine cascade. Increasing stator-rotor leakage flow resulted in higher dissipation around the passage vortex and lower overall efficiency in rotating rig measurements by Schuepbach, et al. [14]. Rosic and Denton [15] placed miniature turning vanes on the stationary casing downstream of a rotor tip shroud to reduce near-wall swirl into the downstream stator and measured an increase of 0.4% in turbine efficiency. McLean, et al. [16] found that coolant injection into the stator-rotor wheelspace generally decreased total-to-total stage efficiency, although discrete-hole coolant injection on the stator hub improved stage efficiency by energizing the stator airfoil wake and the rotor hub boundary layer.

A few studies have also considered the thermal impact of stator-rotor leakage flow. Popovic and Hodson [17] concluded that blade endwall film cooling increased with leakage mass flow through a rim seal, but at the expense of increased aerodynamic losses. Increasing the amount of leakage swirl relative to the blade had little impact at low leakage mass flow ratios, but significantly increased coolant coverage and loss at high mass flow ratios due to a stronger interaction with the horseshoe vortex. Increasing amounts of stator-rotor leakage flow in a transonic turbine decreased rotor platform heat transfer and improved stage efficiency by acting as a blockage for the vane trailing edge shocks, in the study by Pau, et al. [18]. Film effectiveness measurements on a rotating turbine endwall by Suryanarayanan, et al. [19], as well as predictions by Yang, et al. [20], showed that stator-rotor gap leakage spread more uniformly over the endwall for increasing rotor rotational speeds, since the rotor relative incidence angle became more negative and the pitchwise static pressure variation near the stator-rotor gap decreased. Computational simulations by Shih and Lin [21] indicated that a negative flow incidence angle near the endwall, caused by mainstream flow swirl, reduced aerodynamic loss and endwall heat transfer for a nozzle guide vane relative to unswirled flow.

The previously referenced research suggests that backward-facing steps or cavities can improve endwall film cooling and aerodynamic performance relative to a flat wall. Upstream leakage flow with swirl generally reduces efficiency but increases platform cooling. However, there are very few studies that have considered endwall heat transfer with the combined effects of an upstream cavity and leakage swirl. The work presented in this paper attempts to understand the effect of those parameters through measurements of endwall heat transfer for a high-pressure turbine blade cascade that includes a realistic endwall upstream cavity geometry and varying leakage swirl.

Experimental Methodology

A large-scale, low-speed linear cascade was used to obtain measurements of endwall heat transfer at matched engine Reynolds number conditions. The cascade was connected to a closed-loop wind tunnel, depicted in Figure 4.1. The tunnel had a heat exchanger to control the flow temperature, and several screens upstream of the test section to ensure flow uniformity. Some flow was diverted into an upper bypass channel far upstream of the test section and extracted by a blower so that it could be sent to cascade leakage features.

The linear cascade contained six blades based on a high-pressure turbine airfoil geometry. The same airfoil geometry has been previously studied by MacIsaac, et al. [22]. Table 4.1 lists the geometric details of the cascade. The blades were fixed at the design inlet angle. Sidewall flaps and tailboards in the test section allowed control of the inlet velocity uniformity and periodicity in the cascade. The blades were constructed using stereolithography to give a smooth surface finish. Static pressure taps were designed into the stereolithography model at midspan to measure blade loading. Figure 4.2 shows measured blade static pressures, non-dimensionalized as a static pressure coefficient. The measurements demonstrated good agreement to the design blade loading, as well as periodicity for the central blades in the cascade.

The bottom endwall of the cascade was designed to simulate the platform (endwall) overlap between the stationary vane and rotating blade rows. The platform overlap geometry is depicted in Figure 4.3. The blade platform extended $0.57C_{ax}$ upstream of the blade leading edge and $0.27C_{ax}$ below the nominal endwall height, resulting in a cavity in the endwall known as a rim cavity. A smooth curve was used to transition from the lower upstream blade platform to the

nominal endwall height. Note that although the cascade was designed to simulate a rotor, no part of the test section, including the upstream (stator) platform, moved relative to the blades.

Turbine rim flow, which is designed to prevent ingestion of hot gas into the wheelspace between the rotor and stator, was simulated by a leakage feature placed upstream of the cascade. Two interchangeable stereolithography geometries were manufactured to test the effect of swirl in the rim seal leakage flow. The first geometry contained internal vanes that directed the leakage flow onto the blade platform with no swirl component (Figure 4.4a), thus simulating leakage flow with a tangential velocity matched to the rotor hub speed in the engine. Although the cascade measurements were performed in the rotating reference frame associated with the blades, the rim seal swirl velocity was characterized in the stationary reference frame of the engine. The case of no swirl relative to the blade will be denoted as "100% V_{wh}". Figure 4.4c depicts resultant velocity vectors, in the blade's frame of reference, for near-wall flow influenced by the rim seal leakage. U_{in} is the magnitude of the freestream velocity at the design inlet flow angle of β_{in}, U_{exit} is the magnitude of the cascade exit velocity at the design exit flow angle of β_{exit}, and V_{wh} is the speed of the rotor at the radius of the hub. Note that in the blade's frame of reference, V_{wh} would be the motion of the stator, although all parts of the test section were fixed in this cascade. Increasing mass flow ratios from the rim seal tend to increase the magnitude of the incident velocity, but reduce its incidence angle relative to β_{in}.

The second rim seal geometry contained internal turning vanes that imparted swirl to the leakage flow (Figure 4.4b), such that its tangential velocity was half of the rotor hub speed at the nominal net mass flow ratio of 0.75% MFR. This particular case is denoted as "50% V_{wh}". Because the turning vanes in the stereolithography model were stationary, the tangential velocity of the leakage flow was not independent of net mass flow. Instead, the tangential velocity relative to the blade increased with increasing net mass flow through the seal. This is representative of an engine condition whereby increased leakage flow will have more momentum to resist circumferential shearing by the spinning rotor disk and thus will have a higher tangential velocity relative to the blade when it exits the rim seal. Table 4.2 shows the leakage tangential velocities as a percent of V_{wh}, along with other blowing parameters, for the various net mass flow cases tested. It must be emphasized again that the leakage tangential velocities are based on the stationary reference frame, such that low leakage tangential velocities in the stationary reference frame correspond to high tangential velocities in the rotating reference frame of the

blade. The velocity triangle in Figure 4.4d illustrates this, where the 33% V_{wh} case in the blade reference frame has a large tangential component. It is obvious in Figure 4.4d that the incidence angle of the resultant near-wall velocity is significantly decreased for swirled rim seal leakage, relative to the design inlet angle (β_{in}).

Net mass flow through the rim seal was measured by a laminar flow element and supplied to a plenum mounted below the test section. Static pressure taps installed in the stereolithography models were used to check periodicity. The temperature of the leakage coolant was kept to within 0.4°C of the mainstream temperature, resulting in a density ratio of 1.0.

A turbulence grid was located $16C_{ax}$ upstream of the center blade of the cascade, resulting in a freestream turbulence level of 6% as measured with a laser Doppler velocimeter at $5C_{ax}$ upstream of the cascade. The turbulent boundary layer parameters are listed in Table 4.1.

Spatially-resolved heat transfer coefficient measurements were obtained by imaging surface temperatures on a uniform heat flux surface attached to the bottom endwall. The heater consisted of an inconel circuit with a thickness of 25 μm, which was encapsulated in kapton for a total thickness of 75 μm. A 37 μm layer of copper was attached to the flow surface of the heater to smooth out heat flux between the circuit gaps (Kang, et al. [23]). A thin layer of flat black paint was applied to the copper to increase emissivity for infrared measurements. Type-E thermocouples were thermally bonded to the underside of the heater for infrared image calibration.

A 3.2 mm thick stereolithography plate (k≈0.2 W/m-K) was constructed in the shape of the endwall shown in Figure 4.3 to ensure dimensional accuracy for the curved region upstream of the blade. Polyurethane foam (k≈0.032 W/m-K) was molded to the underside of the plate to minimize conduction losses for the heat transfer experiments. The minimum foam thickness was 20 mm at the upstream edge of the blade endwall. The heater was attached to the plate with double-sided tape.

Power supplied to the heater surface was calculated by measuring the circuit voltage and current. Circuit current was obtained by measuring the voltage across a precision resistor in series with the heater. The total heat flux of 900 W/m^2 supplied to the endwall was determined by dividing the power by the heater area. To obtain convective heat flux, conductive and radiative losses were subtracted from the total heat flux. Conductive losses were estimated locally by a one-dimensional conduction analysis to be less than 1.5% of the total heat flux.

Radiative losses were also estimated locally to be less than 15%, assuming that the surroundings behaved as a blackbody at the freestream temperature of 295 K. Local loss corrections were highest in regions of high endwall temperatures.

Infrared camera images were obtained at several locations throughout the cascade to provide a complete map of the endwall heat transfer. At each location, five images were captured to reduce measurement uncertainty. The averaged result was calibrated by adjusting surface emissivity and background temperature until the heater top surface temperature matched measurements from the underside-mounted thermocouples. A conduction bias of 0.8°C between the top surface and underside-mounted thermocouples was accounted for in the calibration. Typical emissivity and background temperature for the calibrated images was 0.96 and 16°C, respectively, which compared well to published emissivity for black paint (~0.96) and the cascade freestream temperature of 21°C. Calibrated images generally agreed to within 0.5°C of the thermocouple measurements. The camera field of view was 320 x 240 pixels, with a resolution of 1.4 pixels/mm. No correction was performed for perspective distortion of the images at the upstream cavity since the small variation in camera standoff distance did not affect its focus.

Uncertainty was estimated using the partial derivative method (Moffat [24]). The largest source of error was the measurement of surface temperature with the infrared camera. Bias and precision uncertainties for that parameter were 0.8°C and 0.3°C, respectively. Total uncertainty in the heat transfer coefficient, based on a 95% confidence interval, was 5.0% at a high value of Nu=410.

Results and Discussion

The oil flow pattern and heat transfer for a turbine blade endwall with a representative upstream cavity and rim seal leakage are discussed first. The effect of varying net leakage mass flow without leakage swirl is then considered, followed by a discussion of the effects of swirl in the rim seal leakage flow.

Comparison of Endwall Oil Flow and Heat Transfer for No Swirl

Oil flow visualization was performed on the endwall using a mixture of black paint, oil, and kerosene. The mixture was applied to removable shelf paper placed over the endwall heaters. The final pattern was photographed after approximately two hours to achieve steady-state. Figure

4.5a shows a photograph of the oil flow pattern for rim seal leakage without swirl, at the nominal leakage mass flow ratio of 0.75%. Arrow-tipped streaklines and dashed vortex path lines were drawn on the low-contrast image to elucidate the patterns. Note that streaklines were not drawn in regions where the flow pattern was not clear, such as very low velocity regions upstream of the blades where separated flow was likely recirculating in the rim cavity.

The endwall oil flow pattern in Figure 4.5a exhibits features similar to classical secondary flow theories; however, the complexity of the upstream cavity and rim seal leakage result in some important differences. A saddle point, indicating the roll-up of the inlet boundary layer into the horseshoe vortex system, is seen far upstream of the blade leading edge, about midway across the pitch. Oil flow visualization results of Abo El Ella, et al. [7] for a similar upstream cavity geometry, and those of de la Rosa Blanco, et al. [6] for a backward-facing step upstream of the blade, indicated that the saddle point and the horseshoe vortex system moved away from the blade leading edge compared to a smooth endwall. Their results also suggested that the pressure side leg of the horseshoe vortex was strengthened by interaction with a recirculation vortex in the cavity. In Figure 4.5a, a cleared region just downstream of the saddle point that sweeps through the passage is attributed to the strong pressure side leg of the horseshoe vortex, which merges with the passage vortex. The suction side leg of the horseshoe vortex appears to move away from the blade leading edge, nearly to the flat portion of the upstream blade platform, before it turns sharply toward the blade suction side. It separates off of the endwall (as indicated by converging streaklines) at the lowest pitchwise point of the airfoil and climbs the airfoil suction side. The passage vortex impinges on the suction side of the airfoil further downstream, and the strong impingement generates a corner vortex that remains close to the airfoil-endwall corner. Downstream of the trailing edge, the corner vortex turns sharply due to flow separation behind the relatively thick trailing edge. Streaklines originating near the pressure side sweep toward the suction side due to the effect of the cross-passage pressure gradient on the new endwall boundary layer in this region.

Contours of endwall heat transfer are shown in Figure 4.5b for the nominal case of 0.75% leakage mass flow ratio with no swirl relative to the blade (100% V_{wh}). Streaklines from Figure 4.5a are overlaid to indicate the effects of the secondary flows on endwall heat transfer. Periodic islands of low heat transfer are seen on the upstream blade platform, where rim seal leakage flow and inlet boundary layer flow separate around the saddle point. The horseshoe vortex drives flow

down the blade span, where it impinges on the endwall and results in high gradients of heat transfer around the blade leading edge. High Nusselt numbers are visible near the blade stagnation, as well as around the suction side where the suction side horseshoe vortex turns sharply toward the blade. The impingement of the passage vortex on the suction side of the blade, and the corner vortex that is generated, both result in a region of high heat transfer downstream of where the suction side horseshoe vortex separates from the endwall. Low heat transfer contours that sweep through the passage, along the path of the cleared region in the oil flow, correspond to separation induced by the pressure-side horseshoe vortex and passage vortex. Heat transfer levels are highest in the blade wake, where divergence of the streaklines indicates flow reattaching to the endwall due to the passage vortex and the counter-rotating corner vortex.

Effect of Upstream Leakage Net Mass Flow for No Swirl

Oil flow visualization patterns for 0% and 0.75% MFR are shown in Figure 4.6. Note that for the 0% MFR case, no net flow was supplied to the plenum but mainstream flow could still be ingested and ejected through the rim seal into a closed plenum. The streaklines in Figure 4.6 show very similar patterns between the two cases, suggesting that 0.75% MFR rim seal leakage does not have a strong effect on the endwall flow relative to the rim cavity and horseshoe vortex effects. It appears that 0.75% MFR causes a slight upstream shift of the saddle point region (in the negative streamwise direction) compared to 0% MFR. Although the limited resolution of oil flow visualization makes it difficult to argue this conclusively, Paniagua, et al. [25] observed the same trend for increasing net leakage flow upstream of their transonic rotating turbine blade, and inferred that the leakage increases the strength of the horseshoe vortex.

Figure 4.7 shows contours of endwall heat transfer for varying net leakage mass flow ratio from the rim seal with unswirled flow (100% V_{wh}). In general, increasing the leakage mass flow ratio increases heat transfer on the upstream blade platform and around the blade leading edge, but has little effect further into the passage. The islands of low heat transfer on the upstream platform between the blades decrease in size between Figure 4.7a (0% MFR) and Figure 4.7d (1.0% MFR) due to increased near-wall velocity with leakage injection. A band of low heat transfer sweeps downstream of the islands of low heat transfer into the center of the passage for leakage above 0% MFR. As mentioned earlier, the band of low heat transfer corresponds to the liftoff induced by the pressure-side horseshoe vortex and passage vortex, and as the horseshoe vortex strengthens with increased leakage, so does the amount of flow that

separates from the endwall. Heat transfer values around the blade leading edge-endwall-junction, particularly at the stagnation point and along the suction side, increase with increasing leakage mass flow ratios. The suction side leg of the horseshoe vortex may be strengthened by the leakage, but it also appears to be pushed closer to the airfoil-endwall junction, resulting in high heat transfer around the suction side.

Nusselt number values shown in Figure 4.8 were extracted from the contours in Figure 4.7 along a pitchwise line located $0.3C_{ax}$ upstream of the blades. Figure 4.8 indicates the pitchwise variation in heat transfer on the upstream rim. For 0% MFR, peak Nu values are relatively low, but peak-to-peak variation in Nu is high. As the MFR increases to 0.35%, both the high and low peak Nu increase, indicating a higher average heat transfer, which is consistent with the increased magnitude of the resultant velocity vector in the blade velocity triangle in Figure 4.4c. This trend continues as leakage MFR increases to 0.75% and 1.0%, and peak-to-peak variation in Nu becomes smaller. Note that the maximum Nu values do not increase as fast as the minimum values when comparing 0.75% to 1.0% MFR. The blade potential field and the large secondary flow vortices cause significant pitchwise variation in the leakage flow, but flow becomes more evenly distributed along the rim seal for increasing mass flow ratios.

Endwall heat transfer was also extracted from the contours in Figure 4.7 along the paths of inviscid streamlines obtained from a two-dimensional simulation of the cascade. The streamline paths were named according to their pitchwise location at the point where the paths passed through the inlet plane of the cascade. Figure 4.9 shows Nu values along the 0.25P and 0.75P streamline paths, where small inset diagrams indicate the respective streamline paths relative to the blades. The abscissa of the figures is the x-coordinate along the streamline normalized by the blade axial chord, so that $X/C_{ax}=0$ corresponds to the inlet plane and $X/C_{ax}=1$ corresponds to the exit plane of the cascade. At each streamwise location along a path, Nu values from each of the three passages seen in Figure 4.7 were averaged to obtain a single value at that streamwise location.

The 0.25P streamline path in Figure 4.9a passes close to the pressure side of the blade. Upstream of the blades, increasing leakage mass flow results in increased Nu values. Also, the minimum Nu around $X/C_{ax}=-0.3$ appears to be pushed further downstream. A peak in heat transfer around $X/C_{ax}=0$ is attributed to the effect of the downwash of the horseshoe vortex, and there appears to be no significant effect of leakage mass flow in this region. Further into the

passage, heat transfer levels are similar between the various leakage MFR cases, suggesting that strong secondary flows override any effect of increasing leakage flow. Heat transfer levels rise toward the exit of the passage, peaking in the blade wake at X/C_{ax}=1.

Figure 4.9b shows Nu values along the 0.75P streamline path passing near the suction side of the blade. Again, the effect of increasing leakage MFR is visible as increasing Nu values upstream of the blades. Around X/C_{ax}=0.1, the streamline path passes through a region of high Nu attributed to the suction side horseshoe vortex turning toward the blade-endwall junction. Another peak in heat transfer is seen around X/C_{ax}=0.6, where the passage vortex impinges on the blade suction side. No significant difference (outside experimental uncertainty) is seen between the various net MFR cases at locations downstream of X/C_{ax}=-0.1, due to the minimal effect of the rim seal leakage on the endwall secondary flows.

Effect of Upstream Leakage Swirl

The effect of rim seal leakage flow with a tangential velocity of 50% V_{wh} can be seen by comparing the oil flow results in Figure 4.10. The most obvious change is a shift in the saddle point in the direction of the swirl in Figure 4.10b. Leakage with a velocity component in the positive pitchwise direction reduces the momentum of the near-wall flow and promotes earlier separation of the inlet boundary layer. The path of the pressure side leg of the horseshoe vortex in Figure 4.10b is also displaced in the direction of swirl for the forward part of the passage; however, strong acceleration further in the passage results in similar oil flow patterns for the two leakage flow cases.

Figure 4.11 shows contours of endwall heat transfer for leakage at 0.75% MFR with and without swirl. Endwall heat transfer upstream of the blade is increased for 50% V_{wh} leakage due to the additional tangential component of leakage velocity. Also, the region of high heat transfer gradients around the blade stagnation in Figure 4.11b appears to be extended away from the leading edge, in the direction of the leakage swirl. This is consistent with the oil flow visualization in Figure 4.10 indicating a displacement of the horseshoe vortex away from the airfoil leading edge by swirled leakage flow.

The displacement of the horseshoe vortex has a noticeable impact on several other regions of the endwall in the forward portion of the passage. The band of low Nu that extends into the center of the passage in Figure 4.11a appears to have been eliminated in Figure 4.11b. The shift of the pressure-side leg of the horseshoe vortex toward the suction-side leg on the

adjacent airfoil reduces the size of the region of separating flow between those vortices. Near the pressure side of the endwall in Figure 4.11b, Nu values are slightly lower for 50% V_{wh} leakage compared to 100% V_{wh} leakage (Figure 4.11a). The displacement of the pressure side horseshoe/passage vortex away from the blade pressure side reduces its downwash on the pressure side-endwall junction. Further into the passage, the strong pressure gradients that drive secondary flows result in similar endwall heat transfer levels between the two cases.

Endwall heat transfer with and without swirl is shown for a low net leakage mass flow ratio of 0.35% in Figure 4.12. Recall that the fixed turning vanes in the swirling rim seal geometry (Figure 4.4b) meant that the tangential velocity of the leakage flow relative to the blade decreased with decreasing net mass flow, and that the convention of reporting tangential velocity in the stationary frame means that the swirl velocity in this case is characterized as 77% V_{wh}. In Figure 4.12, the upstream blade endwall heat transfer is slightly higher for rim seal leakage at 77% V_{wh}, compared to 100% V_{wh}. Nu values elsewhere in the passage are similar between Figure 4.12a and b due to the strong effects of the passage vortex.

The effect of rim seal leakage swirl at a high MFR of 1.0% is shown in Figure 4.13. Leakage with high swirl (33% V_{wh}) relative to the blade results in a significant increase in Nu values on the upstream blade platform due to the high tangential velocity. Heat transfer is also noticeably increased around the blade leading edge in Figure 4.13b relative to Figure 4.13a. The horseshoe vortex is significantly displaced in the direction of swirl, but it may also be increased in strength for this MFR/swirl velocity combination. This is supported by the observation that the endwall heat transfer near the pressure side has not generally been reduced, unlike the trend for 0.75% MFR (Figure 4.11).

Figure 4.14 shows the pitchwise variation of Nu, without and with leakage swirl, on the upstream blade platform at X/C_{ax}=-0.3. Only the 0.75% MFR and 1.0% MFR cases are shown since the swirl had more of an effect at those MFR's. At 0.75% MFR, the peaks and valleys of Nu have been shifted by about 0.15P in the positive pitchwise direction and the magnitudes of those extrema are increased for 50% V_{wh} leakage compared to 100% V_{wh} leakage. At 1.0% MFR and 33% V_{wh}, the valleys in Nu are shifted in the positive pitchwise direction, but the peaks are not, compared to 1.0% MFR at 100% V_{wh}. The peaks in Nu occur where the suction side horseshoe vortex sweeps around the blade leading edge, and at a high MFR of 1.0%, the increase in the horseshoe vortex size offsets its pitchwise displacement due to rim seal swirl. Increased

heat transfer for 33% V_{wh} leakage versus 100% V_{wh} leakage is attributed to both a stronger suction side horseshoe vortex and increased tangential velocity of the leakage.

Endwall heat transfer along the inviscid streamline paths is plotted in Figure 4.15. For the pressure-side streamline path (Figure 4.15a), swirled leakage flow (50% V_{wh}) at 0.75% MFR results in higher heat transfer upstream of the blade but a slight decrease in heat transfer from X/C_{ax}=0.2 to 0.7, compared to unswirled leakage (100% V_{wh}). Swirled leakage (33% V_{wh}) at 1.0% MFR also increases heat transfer upstream of the blade, but pressure side Nu levels are nominally the same between swirled and unswirled leakage along the 0.25P streamline.

Suction-side heat transfer through the passage is nominally the same between the unswirled and swirled leakage at 0.75% MFR, except around X/C_{ax}=0.5 to 0.8. At X/C_{ax}=0.5, the passage vortex impinges on the suction side of the blade and a corner vortex is typically generated. The change in the trajectory of the pressure side horseshoe vortex causes it to approach the blade suction side at a slightly reduced angle for 50% V_{wh} leakage, compared to unswirled leakage (Figure 4.10b). Sieverding [26] indicates that this would reduce the strength of the corner vortex. This same effect of reduced corner vortex strength with swirled leakage flow is also seen by comparing Figure 4.15a and b for 1.0% MFR.

The percent increase in area-averaged heat transfer, relative to the no net leakage case, is shown in Figure 4.16. The averaging area for a single blade passage (depicted in the inset in Figure 4.16) extended upstream to the front end of the blade platform (X/C_{ax}=-0.47) and downstream to X/C_{ax}=1.3. Individual passage averages for each of the three blade passages were averaged to give an overall result for the cascade at that leakage condition. Figure 4.16 shows that average Nu increases with leakage MFR, regardless of rim seal swirl condition. At a low MFR of 0.35%, the effect of the swirl is to slightly decrease overall heat transfer compared to unswirled flow, although the percent difference between the two is small. At the nominal MFR of 0.75%, there is no difference in area-averaged endwall heat transfer between unswirled and swirled leakage, suggesting that the swirl does not significantly interact with the secondary flow. Only at the highest MFR of 1.0% does the swirled leakage result in higher heat transfer than unswirled leakage. Since the leakage tangential velocity is coupled to MFR, it is unclear from these results if area-averaged Nu would increase for high leakage swirl at the nominal MFR of 0.75%.

In an engine, matching the tangential velocity of the rim seal leakage to the rotor hub speed may be difficult, or not possible. Also, a minimum amount of rim seal leakage flow may be necessary to prevent hot gas ingestion. The results presented here suggest that heat transfer coefficients increase with increasing swirl relative to the blade and with increasing leakage mass flow ratio, however, which presents an optimization challenge to the turbine designer. Fortunately there are a couple of mitigating factors: the effects of the leakage are largely confined to the forward portion of the platform, where heat transfer coefficients are nominally low; and the leakage flow is cooler than the mainstream gases and will provide some cooling to the endwall, although it is likely that the large horseshoe vortex system shown in Figure 4.5 will limit its coverage. It does appear from these results that a designer should attempt to avoid high leakage MFR with high levels of swirl relative to the blade.

Conclusions

Oil flow visualization and endwall heat transfer measurements were made for a turbine cascade containing high-pressure blades and an endwall with a representative upstream cavity and rim seal. The effect of leakage flow through the rim seal was determined by varying the net mass flow, as well as its tangential velocity (swirl) relative to the blades.

Secondary flow structures and their effect on the endwall heat transfer were clearly visible when the oil flow visualization streaklines were overlaid on measured heat transfer contours. Flow separation in the upstream cavity resulted in low heat transfer upstream of the blades. The suction side leg of the horseshoe vortex was located away from the leading edge of the blade, and a cleared region in the passage correlated with the path of the passage vortex.

For rim seal leakage with no swirl relative to the blades, increasing the net leakage mass flow strengthened the horseshoe vortex and shifted the saddle point slightly upstream. Heat transfer on the endwall upstream of the blades increased in magnitude but the pitchwise variation in heat transfer decreased with increasing mass flow. The suction side horseshoe vortex was pushed closer to the airfoil leading edge-endwall junction for increasing mass flow ratios, but heat transfer levels in the passage did not show any significant variation. Area-averaged heat transfer increased for high leakage flows, relative to no net leakage.

Comparison of the endwall oil flow patterns with and without swirl indicated that the saddle point upstream of the blades was shifted in the direction of swirl (toward the suction side),

although the secondary flow pattern was not significantly different further into the passage. Endwall heat transfer contours indicated that the displacement of the horseshoe vortex reduced heat transfer near the pressure side, but increased it around the suction side leading edge for swirled leakage versus unswirled leakage. Area-averaged heat transfer, however, was unchanged between swirled and unswirled leakage at low mass flow ratios.

At the highest leakage mass flow ratio, the large tangential velocity of the rim seal leakage significantly increased Nu values on the upstream endwall and near the blade pressure side, suggesting that this leakage flowrate and swirl combination strengthened the horseshoe vortex. Area-averaged heat transfer increased by nearly 4% for swirled leakage versus unswirled leakage.

Acknowledgments

We would like to thank United Technologies—Pratt & Whitney for their support of this work, and acknowledge the assistance of Scott Fishbone in the construction of the test section.

Nomenclature

C	true chord of blade
C_{ax}	axial chord of blade
C_D	discharge coefficient, $C_D = \dot{m}_{c,actual} / \dot{m}_{c,ideal}$
C_p	static pressure coefficient, $C_p = (P_s - P_{s,in}) / 0.5\rho U_{in}^2$
h	heat transfer coefficient, $h = q''_w / (T_w - T_{in})$
H	boundary layer shape factor
HS	horseshoe vortex
I	momentum flux ratio, $I = \rho_c U_c^2 / \rho_{in} U_{in}^2$
k	thermal conductivity
$\dot{m}$	mass flow rate
M	blowing ratio, $M = \rho_c U_c / \rho_{in} U_{in}$
MFR	mass flow ratio, $MFR = \dot{m}_c / \dot{m}_{in}$
Nu	Nusselt number, $Nu = hC_{ax} / k_{air}$
P	blade pitch

P_s	static pressure
PS	pressure side
P_{tot}	total pressure
q''_w	wall heat flux
Re_θ	momentum thickness Reynolds number, $Re_\theta = \theta U_{in} / \nu$
S	blade span
SS	suction side
T	temperature
X, Y, Z	global coordinates, where X is blade axial direction
U, V, W	velocity components aligned with global coordinates
U_{in}	magnitude of inlet streamwise velocity
U_{exit}	magnitude of exit streamwise velocity
V_{wh}	Circumferential speed of the blade wheel at the hub

Greek

β	flow angle
δ_{99}	boundary layer thickness (99%)
θ	momentum thickness
ν	kinematic viscosity
ρ	density

Subscripts/Superscripts

c	leakage coolant conditions
exit	exit conditions
in	inlet conditions
w	wall conditions
$\overline{\overline{(\ )}}$	area-average, $\overline{\overline{(\ )}} = \dfrac{\int (\ ) \partial X \partial Y}{\int \partial X \partial Y}$

References

[1] Han, J. C., Dutta, S., and Ekkad, S., 2000, Taylor & Francis, New York, NY, USA, Chap. 1.

[2] Langston, L. S., 1980, "Crossflows in a Turbine Cascade Passage," *Journal of Engineering for Power*, **102**, pp. 866-874.

[3] Sharma, O. P., and Butler, T. L., 1987, "Predictions of Endwall Losses and Secondary Flows in Axial Flow Turbine Cascades," *Journal of Turbomachinery*, **109**(2), pp. 229-236.

[4] Goldstein, R. J., and Spores, R. A., 1988, "Turbulent Transport on the Endwall in the Region between Adjacent Turbine Blades," *Journal of Heat Transfer*, **110**(4a), pp. 862-869.

[5] De La Rosa Blanco, E., Hodson, H. P., and Vazquez, R., 2005, "Effect of Upstream Platform Geometry on the Endwall Flows of a Turbine Cascade," Proc. ASME Turbo Expo 2005, Paper No. GT2005-68938.

[6] De La Rosa Blanco, E., Hodson, H. P., and Vazquez, R., 2009, "Effect of the Leakage Flows and the Upstream Platform Geometry on the Endwall Flows of a Turbine Cascade," *Journal of Turbomachinery*, **131**(1), pp. 011004.

[7] Abo El Ella, H. M., Sjolander, S. A., and Praisner, T. J., 2010, "Effects of an Upstream Cavity on the Secondary Flow in a Transonic Turbine Cascade," Proc. ASME Turbo Expo 2010, Paper No. GT2010-22843.

[8] Marini, R., and Girgis, S., 2007, "The Effect of Blade Leading Edge Platform Shape on Upstream Disk Cavity to Mainstream Flow Interaction of a High-Pressure Turbine Stage," Proc. ASME Turbo Expo 2007, Paper No. GT2007-27429.

[9] Gier, J., Stubert, B., Brouillet, B., and De Vito, L., 2005, "Interaction of Shroud Leakage Flow and Main Flow in a Three-Stage LP Turbine," *Journal of Turbomachinery*, **127**(4), pp. 649-658.

[10] Piggush, J. D., and Simon, T. W., 2007, "Heat Transfer Measurements in a First-Stage Nozzle Cascade Having Endwall Contouring: Misalignment and Leakage Studies," *Journal of Turbomachinery*, **129**(4), pp. 782-790.

[11] Cardwell, N. D., Sundaram, N., and Thole, K. A., 2006, "Effect of Midpassage Gap, Endwall Misalignment, and Roughness on Endwall Film-Cooling," *Journal of Turbomachinery*, **128**(1), pp. 62-70.

[12] Walsh, J. A., and Gregory-Smith, D. G., 1990, "Inlet Skew and the Growth of Secondary Losses and Vorticity in a Turbine Cascade," *Journal of Turbomachinery*, **112**(4), pp. 633-642.

[13] Reid, K., Denton, J. D., Pullan, G., Curtis, E., and Longley, J., 2006, "The Effect of Stator-Rotor Hub Sealing Flow on the Mainstream Aerodynamics of a Turbine," Proc. ASME Turbo Expo 2006, Paper No. GT2006-90838.

[14] Schuepbach, P., Abhari, R. S., Rose, M. G., Germain, T., Raab, I., and Gier, J., 2010, "Effects of Suction and Injection Purge-Flow on the Secondary Flow Structures of a High-Work Turbine," *Journal of Turbomachinery*, **132**(2), pp. 021021.

[15] Rosic, B., and Denton, J. D., 2008, "Control of Shroud Leakage Loss by Reducing Circumferential Mixing," *Journal of Turbomachinery*, **130**(2), pp. 021010-7.

[16] Mclean, C., Camci, C., and Glezer, B., 2001, "Mainstream Aerodynamic Effects Due to Wheelspace Coolant Injection in a High-Pressure Turbine Stage: Part I---Aerodynamic Measurements in the Stationary Frame," *Journal of Turbomachinery*, **123**(4), pp. 687-696.

[17] Popovic, I., and Hodson, H. P., 2010, "Aerothermal Impact of the Interaction between Hub Leakage and Mainstream Flows in Highly-Loaded HP Turbine Blades," Proc. ASME Turbo Expo 2010, Paper No. GT2010-22311.

[18] Pau, M., Paniagua, G., Delhaye, D., Loma, A. D. L., and Ginibre, P., 2010, "Aerothermal Impact of Stator-Rim Purge Flow and Rotor-Platform Film Cooling on a Transonic Turbine Stage," *Journal of Turbomachinery*, **132**(2), pp. 021006.

[19] Suryanarayanan, A., Mhetras, S. P., Schobeiri, M. T., and Han, J. C., 2009, "Film-Cooling Effectiveness on a Rotating Blade Platform," *Journal of Turbomachinery*, **131**(1), pp. 011014.

[20] Yang, H., Chen, C.-H., and Han, J. C., 2006, "Numerical Study of a Rotating Blade Platform with Film Cooling from Cavity Purge Flow in a 1- ½ Turbine Stage," Proc. ASME Turbo Expo 2006, Paper No. GT2006-90322.

[21] Shih, T. I.-P., and Lin, Y.-L., 2003, "Controlling Secondary-Flow Structure by Leading-Edge Airfoil Fillet and Inlet Swirl to Reduce Aerodynamic Loss and Surface Heat Transfer," *Journal of Turbomachinery*, **125**(1), pp. 48-56.

[22] Macisaac, G. D., Sjolander, S. A., and Praisner, T. J., 2010, "Measurements of Losses and Reynolds Stresses in the Secondary Flow Downstream of a Low-Speed Linear Turbine Cascade," Proc. ASME Turbo Expo 2010, Paper No. GT2010-22727.

[23] Kang, M. B., Kohli, A., and Thole, K. A., 1999, "Heat Transfer and Flowfield Measurements in the Leading Edge Region of a Stator Vane Endwall," *Journal of Turbomachinery*, **121**(3), pp. 558-568.

[24] Moffat, R. J., 1988, "Describing the Uncertainties in Experimental Results," *Experimental Thermal and Fluid Science*, **1**, pp. 3-17.

[25] Paniagua, G., Denos, R., and Almeida, S., 2004, "Effect of the Hub Endwall Cavity Flow on the Flow-Field of a Transonic High-Pressure Turbine," *Journal of Turbomachinery*, **126**(4), pp. 578-586.

[26] Sieverding, C. H., 1985, "Recent Progress in the Understanding of Basic Aspects of Secondary Flows in Turbine Blade Passages," *Journal of Engineering for Gas Turbines and Power*, **107**(2), pp. 248-257.

Table 4.1 Cascade Geometry and Operating Conditions

Scale	6X
Axial chord (C_{ax})	0.1524 m
Span/axial chord (S/C_{ax})	3.6
Pitch/axial chord (P/C_{ax})	1.48
Inlet angle (β_{in}, relative to axial direction)	31.5°
Exit angle (β_{exit}, relative to axial direction)	73.2°
Zwiefel load coefficient (Zw)	0.97
Inlet Reynolds number ($Re_{in}=U_{in}C_{ax}/\nu$)	70,000
Exit Reynolds number ($Re_{ex}=U_{exit}C_{ax}/\nu$)	200,000
Exit Mach number	0.06
Inlet boundary layer thickness at $X/C_{ax}=-5$ (δ_{99}/S)	0.08
Momentum thickness (θ/S)	0.0064
Momentum thickness Re number ($Re_{ex}=U_{in}\theta/\nu$)	1450
Shape factor (H)	1.35

Table 4.2 Flow Conditions Through the Two Rim Seal Geometries

	Unswirled leakage (C_D=0.63)			**Swirled leakage (C_D=0.52)**		
MFR (% of inlet)	**Leakage tangential velocity**	**Blowing ratio (M)**	**Momentum flux ratio (I)**	**Leakage tangential velocity**	**Blowing ratio (M)**	**Momentum flux ratio (I)**
0%	--	0	0	--	0	0
0.35%	100% V_{wh}	0.28	0.08	77% V_{wh}	0.25	0.06
0.75%	100% V_{wh}	0.31	0.10	50% V_{wh}	0.29	0.09
1.0%	100% V_{wh}	0.38	0.14	33% V_{wh}	0.37	0.14

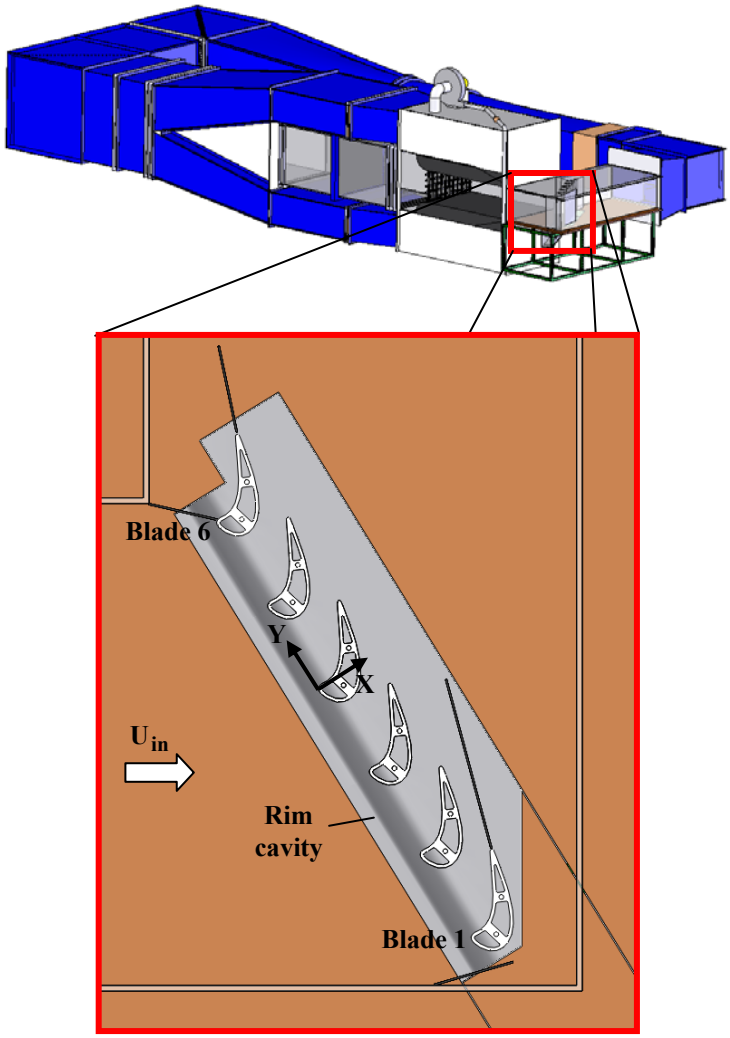

Figure 4.1. Depiction of the low-speed wind tunnel and large-scale test section.

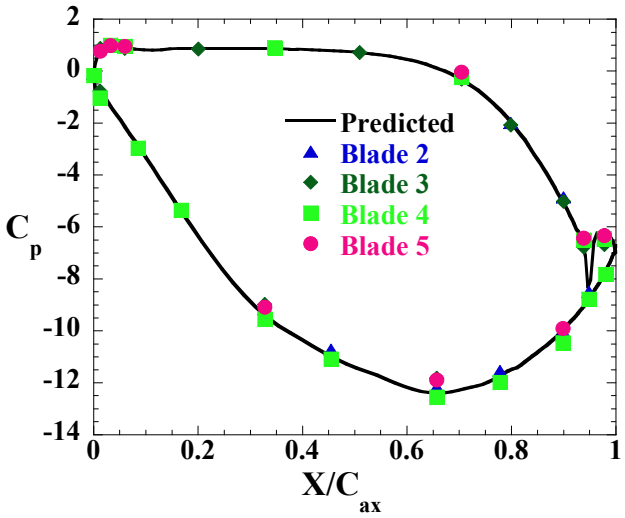

Figure 4.2. Static pressure coefficient measured at midspan for the central blades in the cascade.

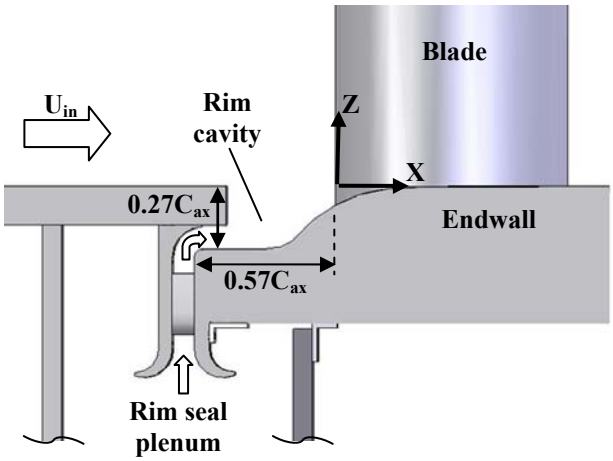

Figure 4.3. Depiction of the rim cavity and rim seal leakage geometry on the endwall upstream of the blades.

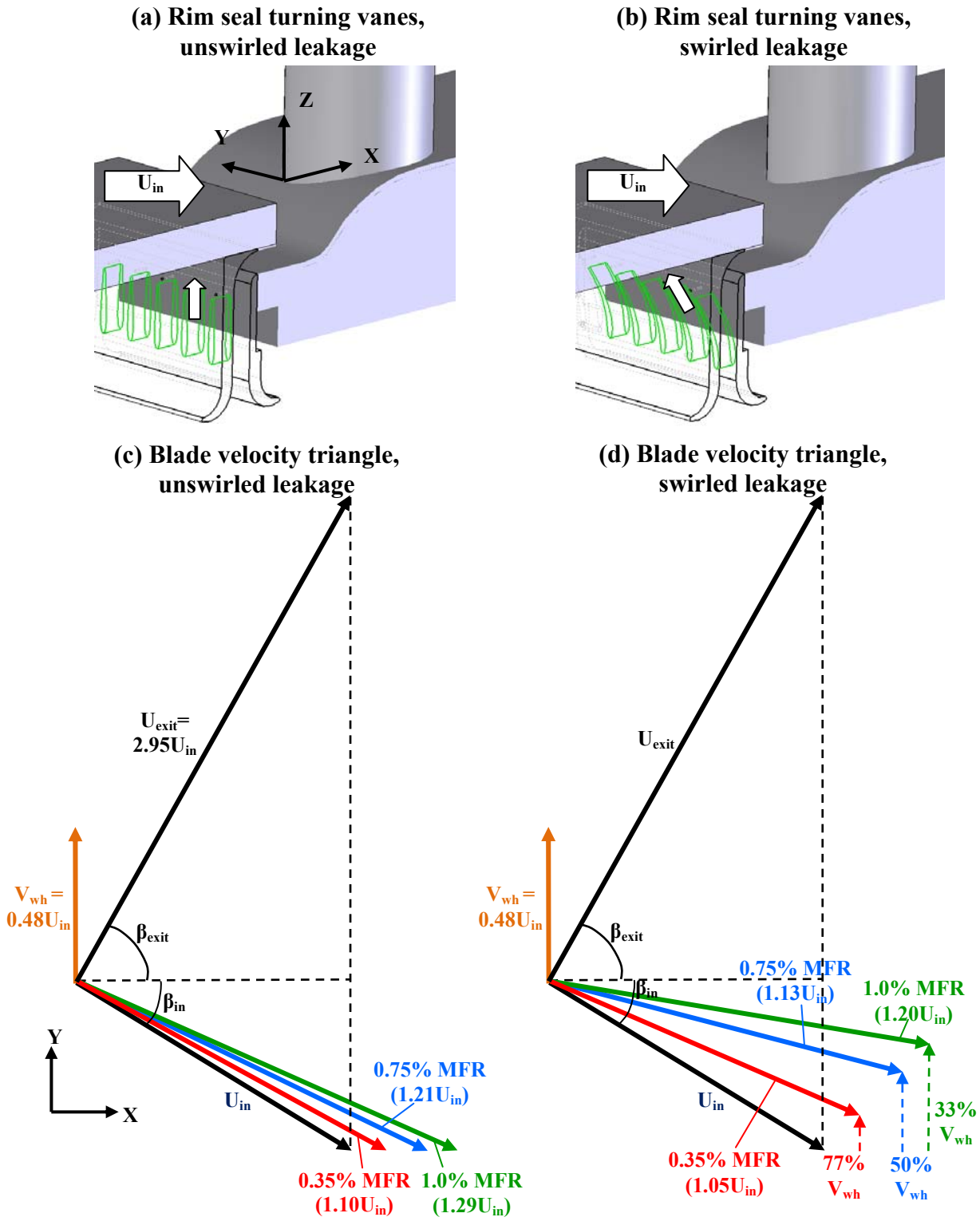

Figure 4.4. Depictions of the turning vanes inside the rim seal for (a) unswirled and (b) swirled leakage; and resultant velocity vectors in the blade reference frame with the addition of (c) unswirled and (d) swirled rim seal leakage.

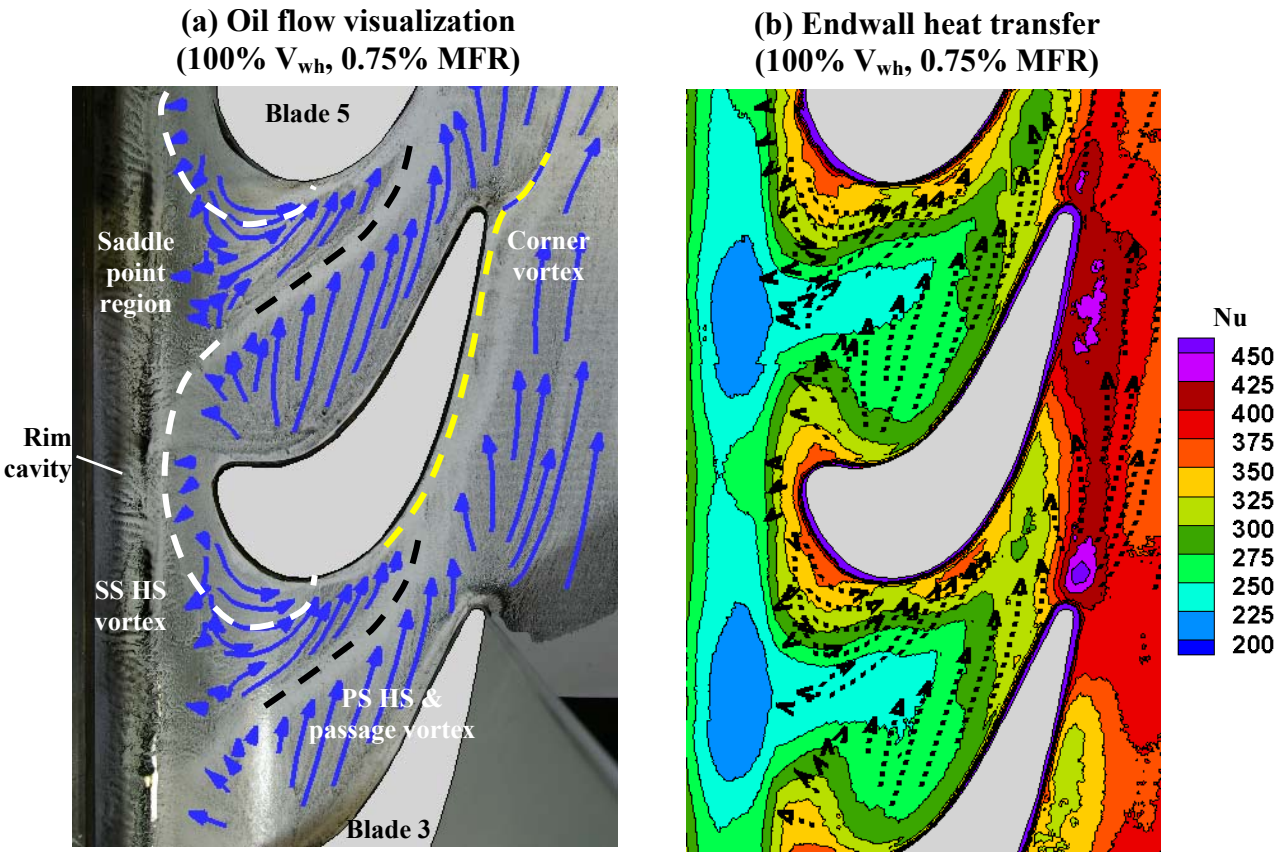

Figure 4.5. (a) Endwall oil flow visualization with streaklines and vortex paths indicated; (b) endwall heat transfer contours with streaklines overlaid.

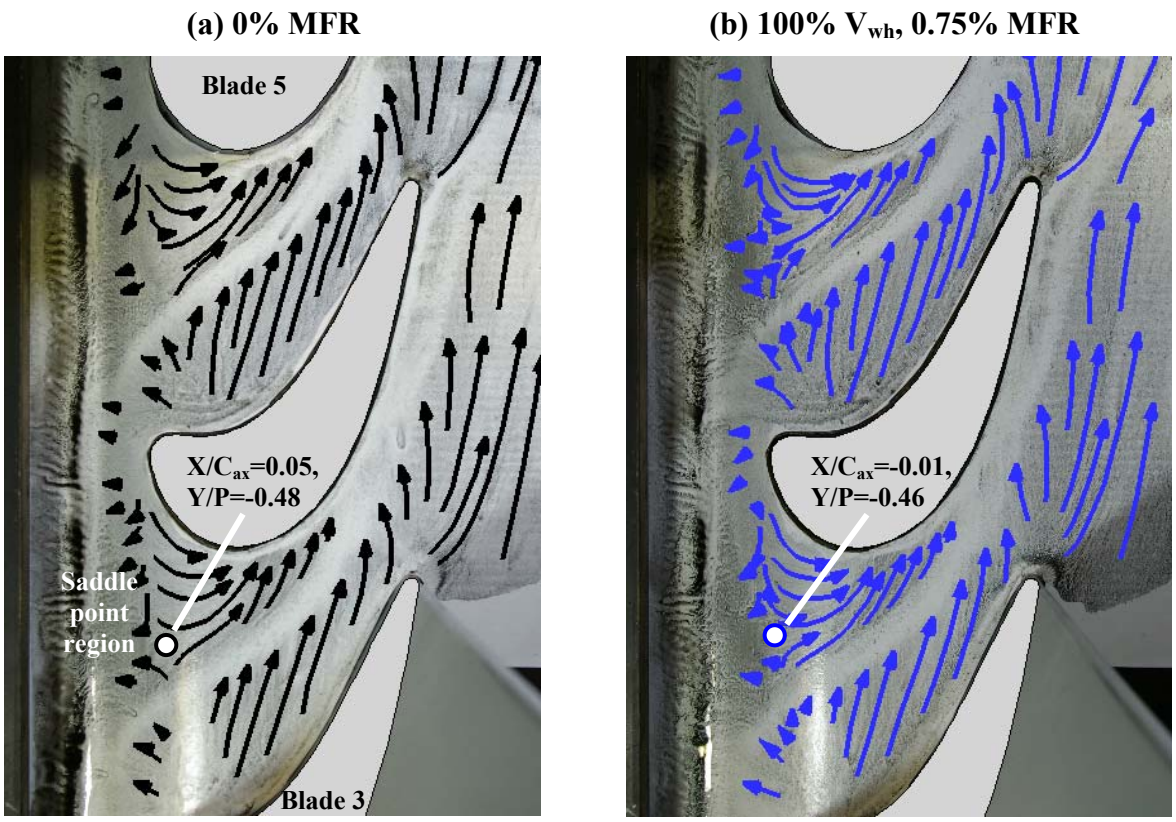

Figure 4.6. Endwall oil flow visualization for rim seal net leakage mass flow ratios of (a) 0% and (b) 0.75%, without swirl.

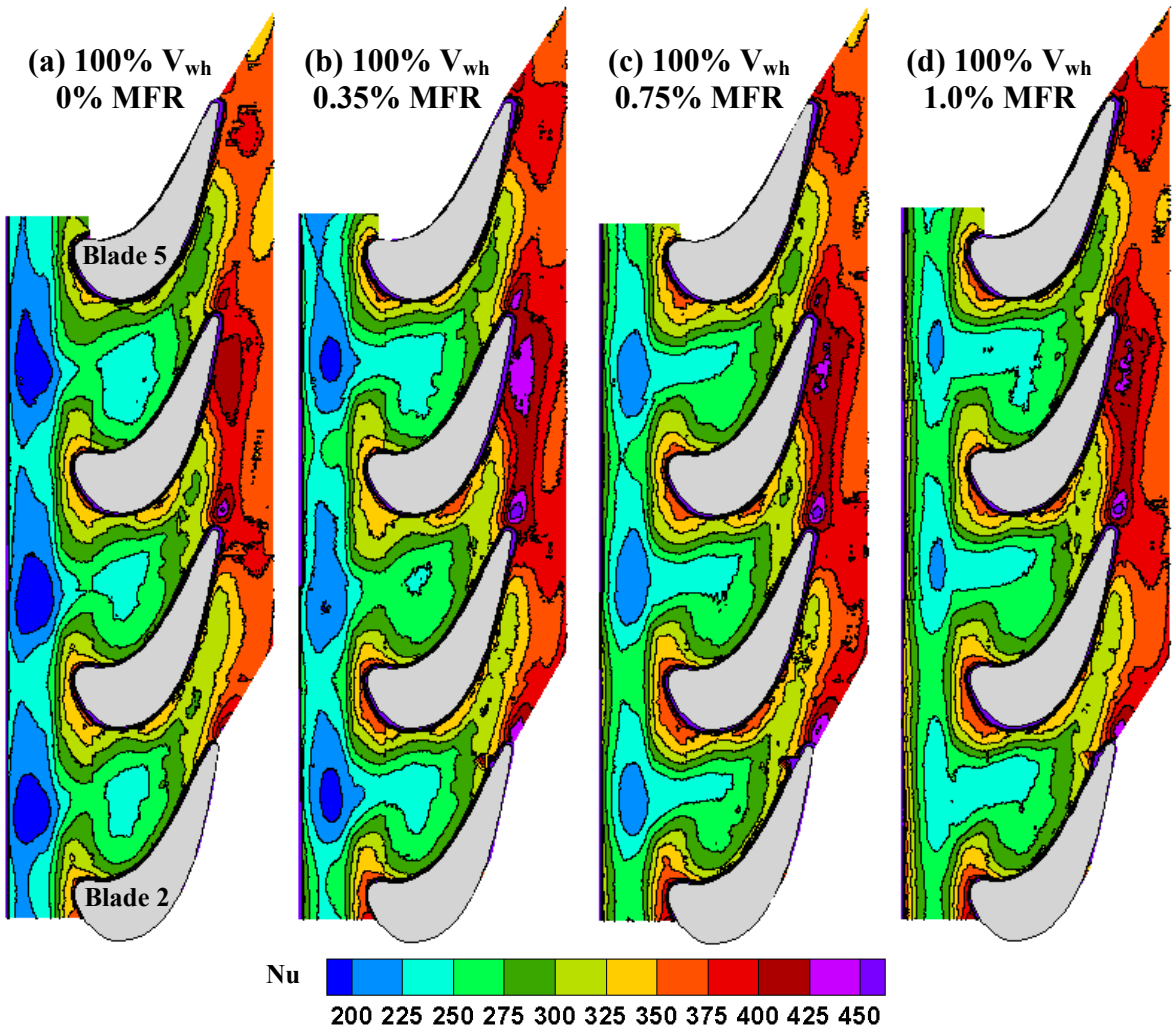

Figure 4.7. Contours of endwall Nu for net rim seal leakage mass flow ratios of (a) 0%, (b) 0.35%, (c) 0.75%, and (d) 1.0%, with no leakage swirl.

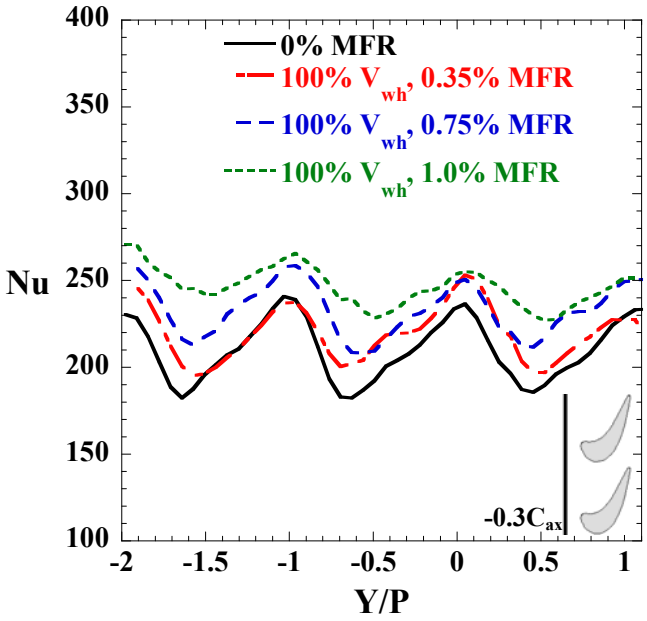

Figure 4.8. Endwall heat transfer on the upstream blade platform for varying rim seal MFR and no swirl, extracted along a pitchwise line at X/C_{ax}=-0.3.

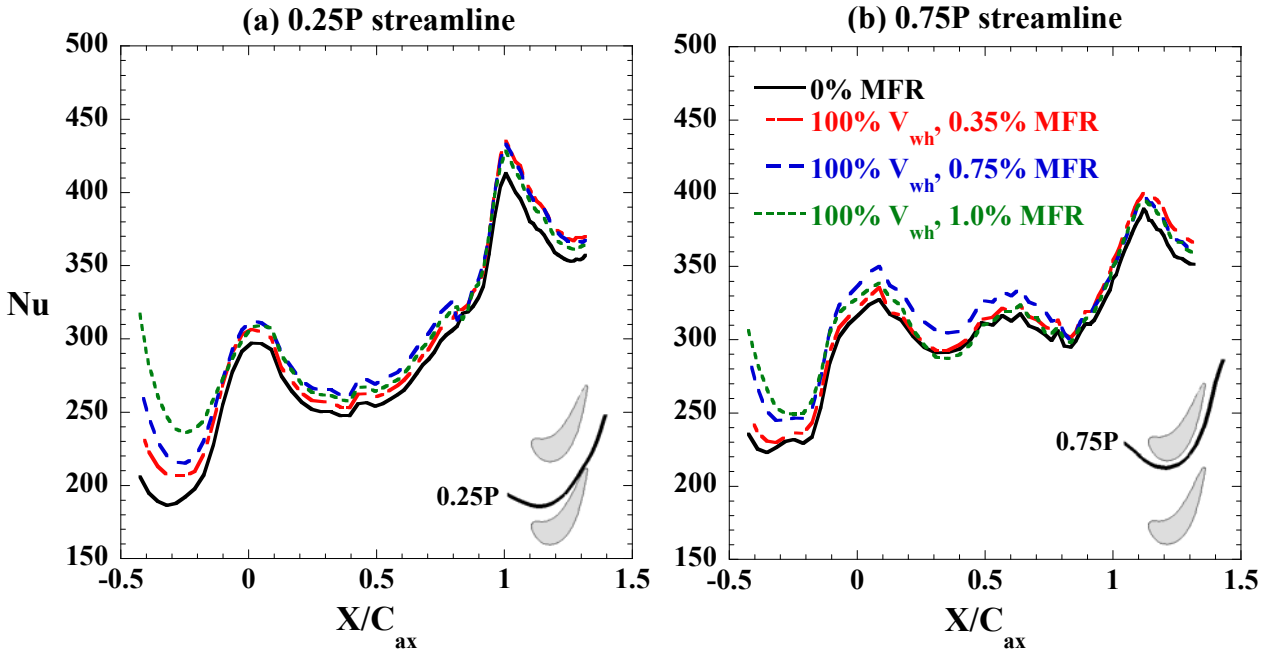

Figure 4.9. Endwall heat transfer for varying rim seal MFR and no swirl, extracted along inviscid streamline paths passing through (a) 0.25P and (b) 0.75P.

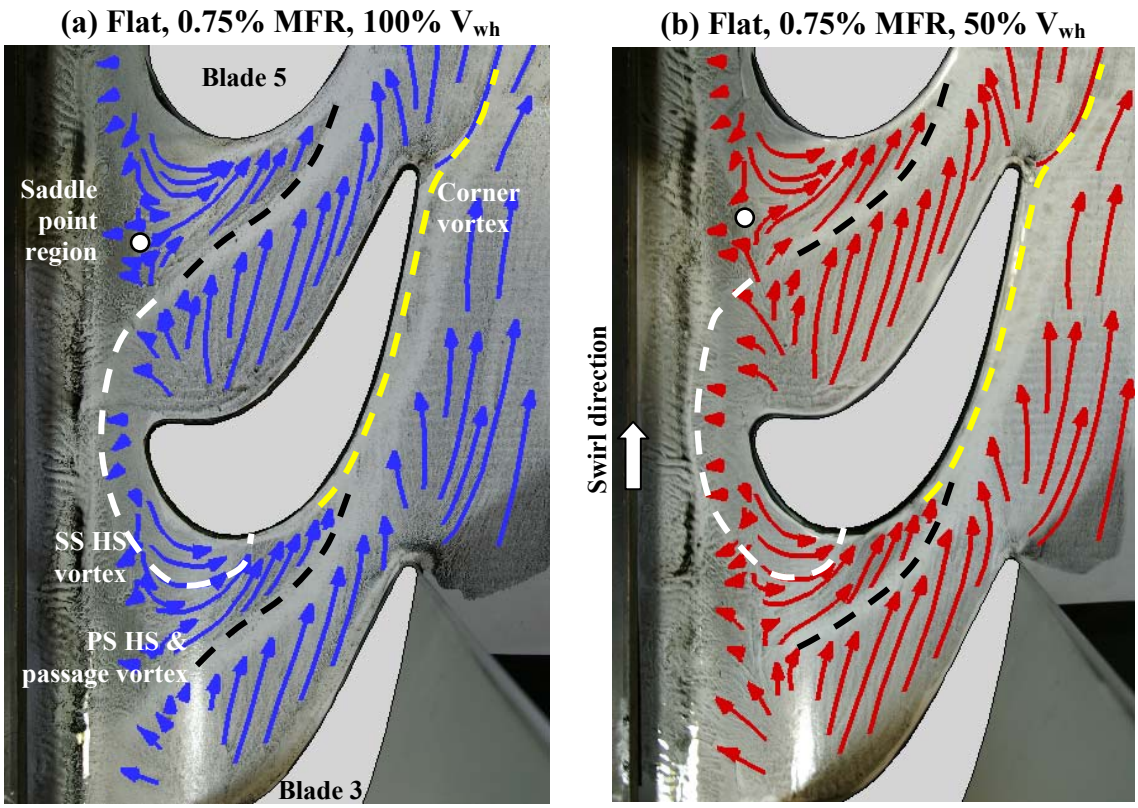

Figure 4.10. Oil flow visualization for upstream rim seal leakage at 0.75% MFR (a) with no swirl relative to the blade (100% V_{wh}), and (b) with swirl at 50% V_{wh}.

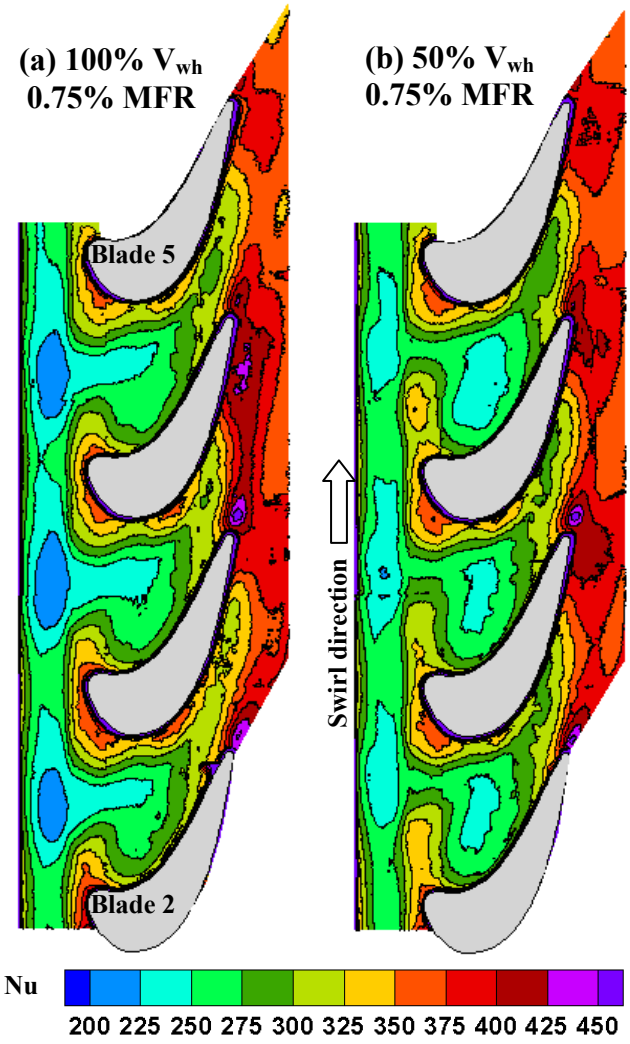

Figure 4.11. Endwall heat transfer contours for 0.75% MFR upstream rim seal leakage (a) without swirl (100% V_{wh}), and (b) with swirl (50% V_{wh}).

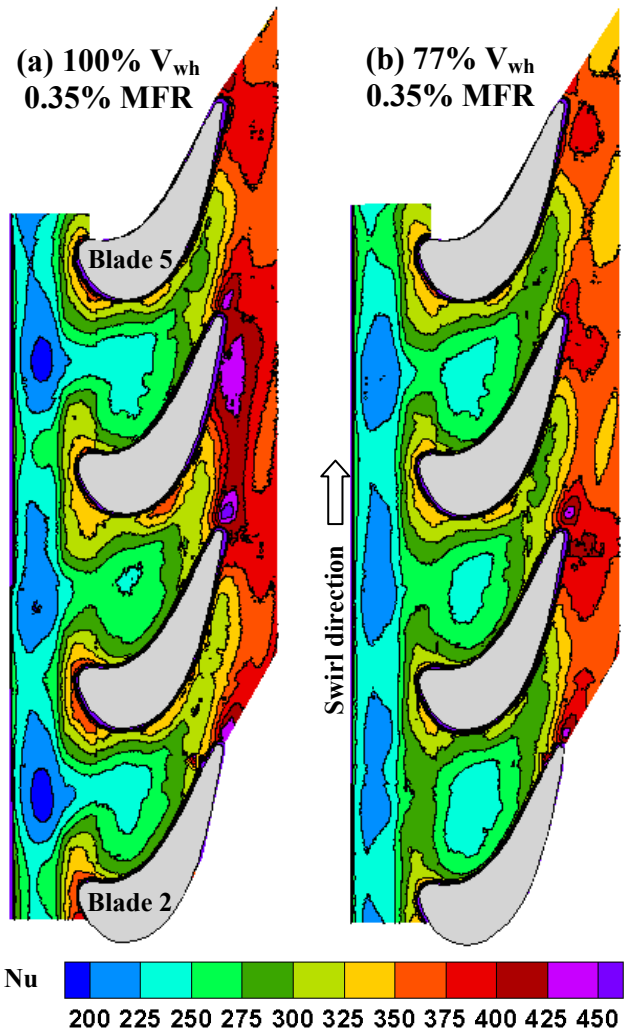

Figure 4.12. Endwall heat transfer contours for 0.35% upstream rim seal leakage (a) without swirl (100% V_{wh}), and (b) with swirl (77% V_{wh}).

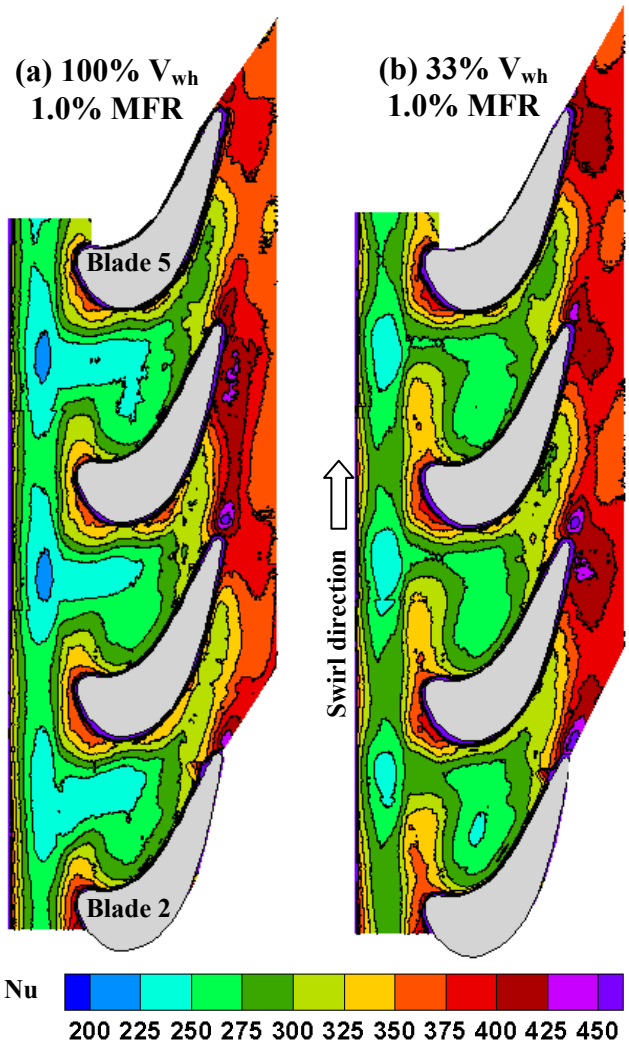

Figure 4.13. Endwall heat transfer contours for 1.0% upstream rim seal leakage (a) without swirl (100% V_{wh}), and (b) with swirl (33% V_{wh}).

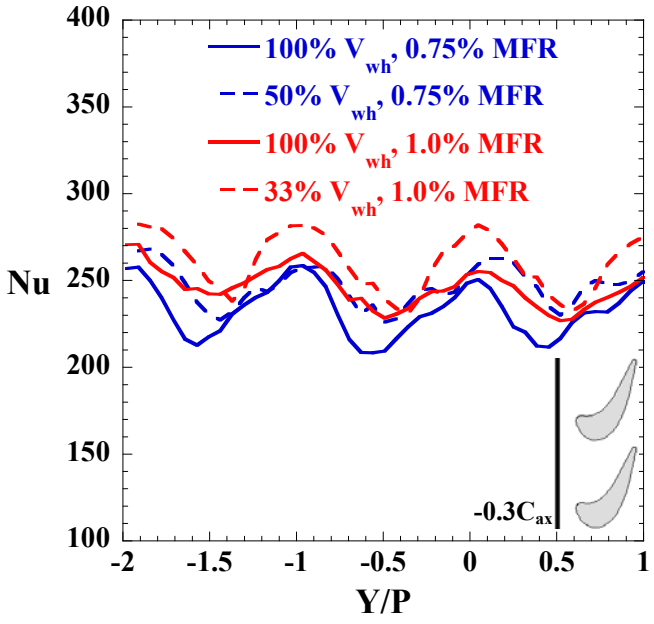

Figure 4.14. Endwall heat transfer on the upstream blade platform for varying rim seal swirl, extracted along a pitchwise line at X/C_{ax}=-0.3.

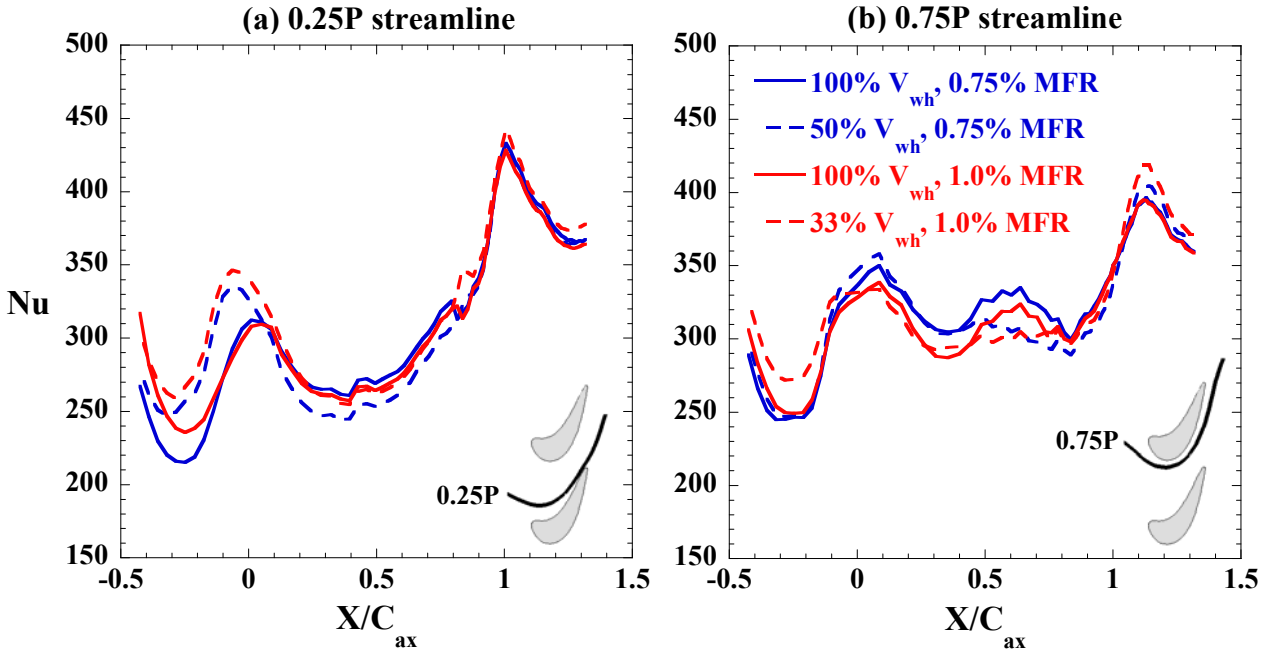

Figure 4.15. Endwall heat transfer for varying rim seal swirl, extracted along inviscid streamline paths passing through (a) 0.25P and (b) 0.75P.

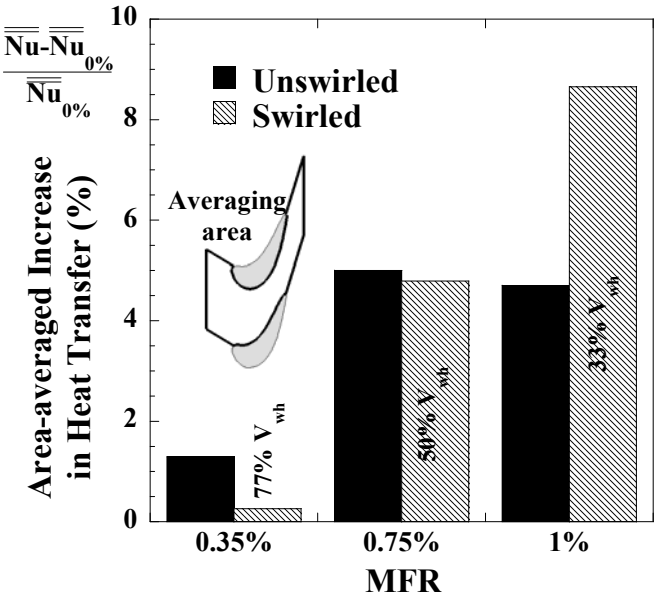

Figure 4.16. Percent increase in area-averaged endwall heat transfer relative to the 0% MFR case.

Paper 5: Measurements of Aerodynamic Loss for a Turbine Blade with Endwall Leakage Features and Contouring

To be submitted to the *Journal of Turbomachinery**

Abstract

Secondary flows near the endwall of a turbine blade contribute to a loss in aerodynamic performance in the engine, and it is desirable to reduce or minimize those flows. Further reductions in performance occur when the secondary flows interact with leakage flow from necessary clearance features present at the blade endwall. Relatively cool air from the compressor is designed to exhaust through the clearance gap between the blade rotor and an upstream stator to prevent hot gas ingestion into the wheelspace. The cool air is also designed to exhaust through the gaps between adjacent blade platforms, which are present when individual blades are installed in the rotor.

Non-axisymmetric endwall contouring has been shown to reduce the strength of secondary flows near the endwall, but relatively little research has been done to test the sensitivity of the contouring to the endwall leakage features. This paper describes aerodynamic measurements taken downstream of a cascade with representative leakage features. In general, upstream leakage flow with a tangential velocity half that of the blade wheelspeed increased aerodynamic loss, relative to leakage that was matched to the blade wheelspeed. Non-axisymmetric contouring for an endwall without a platform gap reduced underturning of the flow but had no effect on overall loss, relative to a flat endwall without a gap. A contoured endwall with a platform gap had 12% higher mixed-out loss than a contoured endwall without a gap.

*Co-authors: Dr. Karen A. Thole, Mechanical & Nuclear Engineering Department, Penn State
Dr. Atul Kohli, United Technologies--Pratt & Whitney
Dr. Christopher Lehane, United Technologies--Pratt & Whitney

Introduction

Modern turbines are able to achieve high levels of aerodynamic efficiency at high loading due to advanced component design; however, further improvements are possible by manipulating the complex flows generated at the hub and tip endwalls of turbine airfoils. These flows originate from the roll-up of the incoming endwall boundary layer into a horseshoe vortex. The legs of the vortex pass around the suction and pressure sides of the airfoil and sweep up boundary layer fluid. The new boundary layer downstream of the inlet separation is susceptible to the strong cross-passage pressure gradients and is swept across the passage into a passage vortex, which merges with the pressure side leg of the horseshoe vortex. Mixing and diffusion of the vortical flows generates aerodynamic loss that is detrimental to component efficiency. This loss is generally termed secondary loss. Denton [1] states that secondary losses can contribute up to 30% of the total component loss.

In an engine, losses can be exacerbated by interaction of the secondary flows with clearance features that are necessary between the stationary and rotating parts of the turbine. One such feature is known as the rim seal, where the downstream edge of a stator platform overlaps the upstream rim of the rotor platform. Purge flow from the compressor is designed to exhaust into the wheelspace below the stator-rotor platforms and then exit out of the rim seal, to prevent hot gas ingestion into the wheelspace. At the rim seal, the purge flow is typically non-uniform due to circumferential static pressure variation imposed by stator wakes or the blade potential field (bow-wave) effects. Furthermore, the purge flow can have a significant circumferential velocity depending on how it is injected into the wheelspace and how much it is spun up by the rotating blade wheel. The interaction of this flow with the developing horseshoe vortex is complex and is a source of additional loss.

Another clearance feature present in turbines is a gap between adjacent blade platforms. This gap occurs because turbine components are generally manufactured as single or double-airfoil units that are individually assembled on the wheel. Purge flow is also designed to exhaust from this gap, where it influences the development and progression of secondary flows in the passage.

A successful method of reducing aerodynamic loss resulting from secondary flows is the application of non-axisymmetric contouring of the endwall. Complex curved endwall shapes are

typically designed via computational optimization to minimize cross-passage pressure gradients and reduce the strength of the passage vortex. However, the complexity of the simulations is generally restricted to reduce turnaround time, and it is not clear how sensitive the designs are to realistic turbine leakage features. The intent of the work presented in this paper was to understand the effect of interactions between realistic leakage features and non-axisymmetric contouring through flowfield measurements at the exit of a cascade.

Review of Literature

Aerodynamic performance of axial flow turbines has been shown to be significantly impacted by the presence of steps or cavities around rotor-stator leakage features. Flow visualization by Abo El Ella, et al. [2] indicated a significant endwall flow separation induced by a cavity upstream of a blade cascade, which strengthened the pressure side leg of the leading edge horseshoe vortex and resulted in higher total pressure loss and flow overturning relative to a smooth wall. Computational simulations by Marini and Girgis [3] indicated that eliminating a recessed cavity on the platform upstream of the blade increased stage efficiency and reduced its sensitivity to varying leakage mass flow. de la Rosa Blanco, et al. [4] found that a backward-facing step upstream of a low-pressure turbine blade resulted in lower losses relative to a forward-facing step for any leakage mass flow or swirl condition. For the backward-facing step, the horseshoe vortex separation line moved farther upstream and limited the interaction of the secondary flows with a pressure-surface separation bubble.

An additional source of loss generation occurs when leakage flow from an upstream cavity interacts with the mainstream. Denton [1] postulated through thermodynamic arguments that the majority of mixing loss generated by leakage flow injected at an angle to mainstream flow was due to differences in swirl velocities. A study by Hunter and Manwaring [5] concluded that the primary source of loss from shroud leakage flow was the mixing of leakage tangential velocity with the mainstream tangential velocity. Rosic and Denton [6] found that miniature turning vanes on the stationary casing downstream of a rotor tip shroud reduced near-wall swirl into the downstream stator and increased turbine efficiency by up to 0.4%. In the study of Paniagua, et al. [7], an increase in leakage mass flow reduced leakage tangential velocity and decreased both the mean flow incidence angle and its time-resolved variation near the blade hub. This reduced the rotor loading in that region, although flow overturning and loss downstream of

the rotor were not reduced. Computational simulations of freestream swirl in a nozzle guide vane by Shih and Lin [8] indicated that a negative incidence angle near the endwall resulted in higher static pressure on the suction side of the passage and earlier separation of secondary flows from the endwall. Walsh and Gregory-Smith [9] also concluded that an inlet boundary layer with negative skew increased secondary flows by causing earlier development of the vortical structures.

Several researchers have found that aerodynamic performance appears to be relatively independent of leakage conditions at low leakage mass flow rates or low relative tangential velocity. de la Rosa Blanco, et al. [4] found that increasing the leakage mass flow or relative tangential velocity from an upstream slot resulted in increased aerodynamic loss; however, at a given massflow, losses did not vary for relative velocities below 60% of the wheelspeed. Popovic and Hodson [10] concluded that coolant coverage and loss were not significantly affected by variation in relative tangential velocity for low to moderate leakage mass flows. Reid, et al. [11] found for a single-stage turbine that efficiency was nearly independent of leakage flow tangential velocity at low leakage mass flow.

Another turbine leakage feature known to contribute to aerodynamic loss is the inter-platform gap between airfoil segments. Reid, et al. [12] found that turbine efficiency was decreased significantly by the presence of a platform gap in the endwall, but efficiency was not sensitive to platform gap leakage flowrate. A later study by Reid, et al. [13] varied the location and angle of the platform gap and determined an improvement in stage efficiency for a gap located in a region of relatively constant static pressure. Piggush and Simon [14] found through a sensitivity study that aerodynamic loss was most significantly impacted by increasing platform gap leakage flow, although the gap was covered for the low flowrate condition and thus the effect of the gap geometry was not distinguishable from the effect of varying leakage flow. A subsequent study (Piggush and Simon [15]) addressed this by maintaining the platform gap open while varying net flowrate, and found that losses increased as platform gap flow increased. The complexity of mainstream flow interaction with the platform gap was indicated by Lynch and Thole [16], where flow was ingested in the forward part of the gap and ejected at the passage throat resulting in a vortical structure that increased endwall heat transfer.

For idealized endwalls without leakage features, non-axisymmetric endwall contouring has been shown to be an effective method to control secondary flows. The complex three-

dimensional shape is generally designed through an optimization routine coupled to a steady-state computational fluid dynamics simulation. Harvey, et al. [17] presented a computational optimization methodology intended to reduce the cross-passage pressure gradient and weaken secondary flows. Cascade measurements by Hartland, et al. [18] demonstrated a reduction in the cross-passage gradient and decreased aerodynamic loss. A computational optimization was used to design non-axisymmetric endwalls for a 1.5 stage turbine in the study by Germain, et al. [19]. Experimental validation by Schuepbach, et al. [20] indicated a 1.0% increase in turbine efficiency. A contour design methodology presented by Praisner, et al. [21] for low-pressure turbines was used to design endwalls in the studies of Knezevici, et al. [22] and Knezevici, et al. [23]. Overall, contouring reduced secondary kinetic energy and total pressure loss by delaying the migration of the passage vortex across the passage.

The effect of non-axisymmetric contouring may be more complicated than a reduction in the cross-passage pressure gradient. Knezevici, et al. [22] indicated that the contour inhibited the merger of the pressure side leg of the horseshoe vortex with the passage vortex. Poehler, et al. [24] also concluded that endwall contouring decoupled the pressure-side horseshoe vortex and passage vortex, which contributed to reduced total pressure unsteadiness and improved efficiency in a 1 ½ stage turbine. Torre, et al. [25] found for their solid-thin low pressure turbine cascade that the suction side leg of the horseshoe vortex was strengthened with contouring, which prevented the pressure side leg from migrating across the passage. Smoke visualization at a low Reynolds number by Gustafson, et al. [26] indicated that the saddle point and pressure side leg of the horseshoe vortex were displaced upstream with the application of endwall contouring.

Most contour designs only consider a single operating point, and it might be expected that for off-design airfoil loading, the effectiveness of a non-axisymmetric contour could suffer. Snedden, et al. [27] considered off-design operating conditions of a 1 ½ stage turbine by varying the rotor speed. Efficiency was slightly improved with endwall contouring for low and design-level loading, but was decreased for high loading. In a study by Vazquez and Fidalgo [28], the performance benefit of a non-axisymmetric contoured endwall did not vary with Reynolds number, but for increasing Mach number, the contoured endwall exhibited higher losses than the baseline as the airfoil became more aft-loaded.

The previously referenced research suggests that leakage cavities and flow from those cavities generally reduces aerodynamic performance, but endwall contouring generally improves

performance. It is not clear how these factors interact. This study attempts to answer that question through measurements of flow and aerodynamic loss at the exit of a high-pressure turbine blade cascade. This study is unique in the literature due to its inclusion of a realistic endwall upstream cavity geometry, varying leakage swirl, and non-axisymmetric endwall contouring.

Experimental Methodology

Aerodynamic loss measurements were obtained downstream of a large-scale low-speed linear cascade matched to engine Reynolds numbers. Flow through the cascade was supplied by a closed-loop wind tunnel. Figure 5.1 shows the tunnel and the cascade. A blower on the top of the tunnel extracted flow to be sent to cascade leakage features.

The linear cascade consisted of six blades based on the near-hub geometry for a high-pressure turbine airfoil. The same airfoil geometry was also studied by MacIsaac, et al. [29]. Table 5.1 lists the geometric details of the cascade in this study. Sidewall flaps and tailboards in the test section allowed control of the inlet velocity uniformity and periodicity in the cascade. The blades were constructed via stereolithography and given a smooth surface finish. The design of the blades included static pressure taps at midspan to measure blade loading. Lynch, et al. [30] and Lynch, et al. [31] describe a similar cascade design for a low-pressure turbine airfoil (Pack-B) with endwall contouring.

The bottom endwall of the cascade was designed to simulate the platform overlap in a real engine between the stationary vane and the rotating blade rows. Figure 5.2 depicts the platform overlap geometry, also known as a rim cavity. The blade platform extended $0.57C_{ax}$ upstream of the blade leading edge and $0.27C_{ax}$ below the nominal endwall height. A smooth curve was used to transition from the lowered upstream blade platform to the nominal endwall height. Note that although the cascade simulated a rotor, no parts of the cascade, including the upstream (stator) platform, moved relative to the blades.

A leakage feature was placed upstream of the blade platform to simulate the rim leakage flow that prevents ingestion of hot gas into the wheelspace. Two different stereolithography models were constructed to funnel leakage flow onto the blade platform. The first geometry contained small vanes that directed the leakage flow onto the blade platform with no swirl component (Figure 5.3a), thus simulating leakage flow with tangential velocity that was matched

to the rotor wheel speed. This case will be denoted as "100% V_{wh}". The blade velocity triangle depicted in Figure 5.3c shows representative vectors for the near-wall velocities, in the reference frame of the rotor. The speed of the rotor at the radius of the rim is denoted as V_{wh}. The inlet (U_{in}) and outlet (U_{exit}) freestream velocities are shown in black with their incidence angles relative to the axial direction (see Table 5.1 for values). The average velocity magnitude of the leakage flow (V_{leak}) was calculated using the net mass flow of 0.75% of the mainstream and the metering area of the rim seal slot. The resultant velocity near the endwall due to leakage, depicted in red, indicates a larger magnitude but a slightly reduced incidence angle compared to the freestream velocity.

The second rim seal geometry contained small vanes that imparted swirl to the leakage flow (Figure 5.3b), such that the tangential velocity of the leakage flow was half of the rotor wheel speed. This case is denoted as "50% V_{wh}". The blade velocity triangle in Figure 5.3d indicates that the magnitude of the resultant near-wall velocity is slightly reduced compared to Figure 5.3c, but the incidence angle has been significantly reduced by 17° relative to the freestream velocity. A negative incidence angle would be expected to raise the pressure on the suction side of the airfoil (reduce the cross-passage pressure gradient) near the endwall.

Flow to the rim seal was supplied by a plenum mounted below the test section. Static pressure taps installed in the stereolithography models were used to check periodicity. The net mass flow supplied to the plenum was measured by a laminar flow element, and was kept constant in this study at 0.75% of the mainstream flow. The temperature of the mainstream and coolant were maintained at 295 K, resulting in a density ratio of 1.0. The blowing ratio and momentum flux ratio were 0.3 and 0.08, respectively.

Two types of endwalls were tested in the cascade passage: a flat endwall depicted in Figure 5.2; and a non-axisymmetric contoured endwall depicted in Figure 5.4a. Both endwalls had the same upstream blade platform geometry described above. The non-axisymmetric endwall was designed using the methodology described by Praisner, et al. [21] for upstream leakage conditions of 0.75% mass flow at 50% V_{wh} relative tangential velocity. Non-axisymmetric contouring began at $0.1C_{ax}$ upstream of the leading edge and merged to the nominal endwall level at the exit of the blade passage. Maximum and minimum heights of the contouring were $+0.04C_{ax}$ near the leading edge suction side, and $-0.04C_{ax}$ near the center of the passage, respectively. It is interesting to note that the endwall contour in this study differs from typical

designs in that there is a hill near the leading edge suction side. Knezevici, et al. [23] and Lynch, et al. [30] studied a contour for a low-pressure turbine airfoil (Pack-B) that was produced by the same design methodology as in this study, although upstream leakage features were not considered in the Pack-B contour design. The Pack-B contour had a depression ("valley") near the suction side leading edge, instead of a hill. Upstream leakage features appear to play a significant role in the generation of optimal endwall contour shapes.

The effect of a gap between adjacent blade platforms was only considered for the non-axisymmetric contoured endwall. The geometry of the platform gap is depicted in Figure 5.4, and gaps were located in every passage except between blades 1 and 2, where the gap would pass below the outer airfoil tailboard. The gaps were taped over for the studies without gap leakage flow, and are indicated as "no gap" in the figure legends in this paper. A thin strip seal was attached to the underside of the platform gap (see Figure 5.4b-c) to simulate the effect of a similar component in the engine which limits leakage flow into and out of the gap. Flow to each of the four platform gaps was supplied to individual plenums mounted on the underside of the test section, and net flowrates were measured with a laminar flow element. Net flow from the platform gaps was fixed at 0.3% of the mainstream mass flow.

Measurements of flow angles, velocity magnitude, and total and static pressures were obtained with a five-hole cobra-type probe both upstream and downstream of the cascade. The probe had a diameter of 2.1 mm and was inserted from the top endwall. It was operated in non-nulling mode by post-processing measured pressures with a calibration map for recovery of total pressure, static pressure, yaw, and pitch. The calibration was performed over ±50° in pitch and yaw, in increments of 3° outside of ±20°, and increments of 0.5° within ±20°. When taking measurements, the probe was oriented in the flow such that the maximum flow angle relative to the probe head was less than ±20°.

Cascade exit measurements were obtained at $1.3C_{ax}$ downstream of the leading edge by traversing the five-hole probe pitchwise across the center passage in the cascade, and spanwise from Z/S=0.016 to Z/S=0.5 (see Figure 5.1). Over 1000 measurements were obtained in the flowfield, concentrated in regions of high gradients near the endwall and in the blade wake.

Pressures from each of the five probe ports were captured with individual differential transducers ranging from ±125 Pa to 0-1250 Pa, such that the maximum range of measured pressures from a given port were just within the range of the transducer. At each measurement

point, 20,000 samples were acquired at a sampling rate of 500 Hz. Transducer bias uncertainty due to calibration, linearity, and hysteresis was ±0.25% full-scale, while probe calibration bias uncertainty was estimated at ±0.3% of the measured dynamic pressure. Maximum precision uncertainty in any of the five measured pressures was 1% of the exit midspan dynamic pressure, and it occurred in the highly turbulent region between the passage and suction side horseshoe vortex cores (Y/P≈0.17, Z/S≈0.11). Estimated total uncertainties at a 95% confidence interval for dynamic and total pressures were ±1.4% and ±1.2% of midspan dynamic pressure at the measurement plane (X/C_{ax}=1.3), respectively. The sequential perturbation analysis described by Moffat [32] was used to estimate uncertainties for derived quantities, which are listed in Table 5.2.

A turbulence grid was located $16C_{ax}$ upstream of the center blade of the cascade, resulting in a freestream turbulence level of 6% that was measured with a laser Doppler velocimeter at $5C_{ax}$ upstream of the cascade. The inlet turbulent boundary layer was characterized at $1.1C_{ax}$ upstream of the cascade with the five-hole probe, at a pitchwise location directly upstream of the leading edge of blade 3. Table 5.1 lists the measured boundary layer parameters.

Blade surface static pressure at midspan, non-dimensionalized as a pressure coefficient, is shown in Figure 5.5. The measurements demonstrated good agreement to the predicted blade loading and periodicity for the central blades in the cascade.

Data Analysis

Several derived quantities were obtained by post-processing the five-hole probe pressure and velocity data. A total pressure loss coefficient (C_{Ptot}) was computed by using the inlet total pressure at midspan, measured $1.1C_{ax}$ upstream of the cascade, as a reference pressure:

$$C_{Ptot} = \left(P_{tot} - P_{tot,in}\right) \Big/ 0.5\rho U_{in}^2 \tag{5.1}$$

This pressure loss coefficient was used in contour plots and pitchwise mass-averaged plots. For mass-averaged results, a loss coefficient normalized by the midspan mass-averaged exit dynamic pressure (Y_o) was used:

$$Y_o = \left(P_{tot} - P_{tot,in}\right) \Big/ \left(\overline{P_{tot,exit,ms}} - \overline{P_{s,exit,ms}}\right) \tag{5.2}$$

Inlet loss to the cascade was determined as the mass-average of the total pressure loss across the inlet boundary layer with the total pressure gains in the leakage plenums, similar to the method

of Friedrichs, et al. [33]. The net loss generated in the cascade was calculated as the difference between the mass-averaged total pressure loss at the measurement plane and the inlet loss. Net loss was further broken down into loss due to the boundary layer on the airfoil, termed profile loss, and all other remaining losses associated with the secondary flow generated at the endwall, termed secondary loss. Profile loss was determined by mass-averaging from Z/S=0.36 to midspan, outside of the region influenced by secondary flow. Subtraction of the profile loss from the net loss produced the secondary loss.

Streamwise vorticity was determined by the method described by Gregory-Smith, et al. [34], in which the pitchwise component of vorticity (ω_y) is calculated with the incompressible Helmholtz equation, and the angle of the streamwise direction ($\bar{\bar{\beta}}_{exit}$) is the mass-averaged midspan exit yaw angle:

$$\omega_s = \omega_x \sin\bar{\bar{\beta}}_{exit} - \omega_y \cos\bar{\bar{\beta}}_{exit} \tag{5.3}$$

Gradients were computed from the measured data using second-order-accurate finite difference approximations. Streamwise vorticity was non-dimensionalized into a coefficient ($C_{\omega s}$) by using the blade true chord and inlet freestream velocity magnitude:

$$C_{\omega s} = \frac{\omega_s C}{U_{in}} \tag{5.4}$$

Secondary kinetic energy is defined as the sum of the square of the mean velocity components of the flow that are perpendicular to the primary (inviscid) flow direction. These components were determined by transforming the velocity vectors in the blade coordinate system into a coordinate system aligned with the mass-averaged midspan flow direction:

$$V_n = -U\sin\bar{\bar{\beta}}_{exit} + V\cos\bar{\bar{\beta}}_{exit} \tag{5.5}$$

$$V_z = W \tag{5.6}$$

A coefficient of secondary kinetic energy (C_{SKE}) was calculated by normalizing with the inlet freestream velocity magnitude:

$$C_{SKE} = \left(V_n^2 + V_z^2\right) \Big/ U_{in}^2 \tag{5.7}$$

Results and Discussion

The effect of swirl in the upstream rim cavity leakage flow for the nominal flat wall is discussed first, followed by a comparison of the flat endwall to the non-axisymmetric endwall contour without a platform gap. The effect of a platform gap with leakage flow is considered for the non-axisymmetric contour, and the overall plane-mass-averaged and mixed-out loss results for all configurations are discussed.

Effect of Upstream Leakage Swirl for a Flat Endwall

Figure 5.6 presents oil flow visualization for the flat endwall for 100% V_{wh} and 50% V_{wh} leakage at 0.75% MFR. To perform the flow visualization, a mixture of black paint, kerosene, and oil was painted on white shelf paper covering the endwall. The flow pattern was photographed after running the cascade at the design Reynolds number for approximately two hours. Due to the low contrast of the image, arrows have been drawn to indicate the pattern. Dashed lines have also been drawn on the figure to indicate separation lines associated with the secondary flow vortices. Note that no arrows were drawn on the flat portion of the platform upstream of the blades, since the flow pattern was not discernable in this low-velocity region.

Some features of classical endwall secondary flow are visible in the endwall streakline patterns for the 100% V_{wh} leakage case in Figure 5.6a. A saddle point region is visible upstream of the blade leading edge, where the incoming flow separates into a horseshoe vortex. Flow visualization by Abo El Ella, et al. [2] for a similar upstream cavity shape indicated that the saddle point merges with a vortex caused by the rollup of flow separating off of the upstream endwall as it drops into the cavity. This results in a strong pressure side horseshoe vortex and passage vortex, which are visible as a cleared region sweeping through the cascade (illustrated by the black dashed line in Figure 5.6a). Those vortices also contribute to the development of a corner vortex near the blade suction side (yellow dashed line), which turns sharply downstream of the trailing edge to a separation behind the trailing edge. Near the pressure side of the blade in the passage, the cross-passage pressure gradient drives low-momentum endwall boundary layer fluid toward the suction side of the passage.

The primary difference between 100% V_{wh} leakage flow in Figure 5.6a and the 50% V_{wh} case in Figure 5.6b is a displacement of the saddle point region in the direction of the swirl. The blade velocity triangles in Figure 5.3d indicate that the additional tangential component of

leakage velocity for 50% V_{wh} leakage reduces the magnitude of the resultant vector and leads to an earlier separation of the endwall flow, since that flow has reduced momentum.

Although it is less clear than the saddle point effect, the oil flow pattern also suggests that the suction side leg of the horseshoe vortex impinges on the blade slightly farther upstream for 50% V_{wh} leakage (Figure 5.6b) than for 100% V_{wh} leakage (Figure 5.6a). Classical secondary flow theory indicates that the vortex migrates up the airfoil span downstream of that point. No oil flow visualization was done on the airfoil, but flowfield results presented later confirm that the loss cores associated with the endwall vortical structures are displaced slightly further from the endwall for 50% V_{wh} leakage. Strong pressure gradients further in the passage constrain the path of secondary flows, which appear similar between the two leakage swirl cases.

Flowfield measurements at X/C_{ax}=1.3 for the six cases in this study are presented in Figure 5.7 and Figure 5.8. The six cases considered included three endwall configurations (flat, contoured without a platform gap, and contoured with a platform gap), each with the two upstream rim seal leakage swirl conditions (100% V_{wh}, 50% V_{wh}). In this figure and all subsequent figures, the cases for the contoured endwall without a platform gap are indicated in the legend as "no gap". Also note that the net mass flow from the upstream rim seal was kept constant at 0.75% of the mainstream mass flow for all cases. Figure 5.7 shows color contours of streamwise vorticity coefficient ($C_{\omega s}$) overlaid with line contours of total pressure loss coefficient (C_{Ptot}), while Figure 5.8 shows color contours of secondary kinetic energy coefficient (C_{SKE}) with secondary flow vectors interpolated to a uniform grid for display clarity. The figures are oriented such that the viewer is looking upstream at the oncoming flow, with the suction side toward the left and the pressure side toward the right (see Figure 5.7a).

In Figure 5.7a, the vertical band of total pressure loss around Y/P=0.25 is associated with the wake of the airfoil. Secondary flow structures generated at the endwall are visible as cores of total pressure loss and streamwise vorticity. Features with negative streamwise vorticity, located around Y/P=0.18, Z/S=0.12, are associated with the suction side leg of the horseshoe vortex, which moves upward away from the endwall along the suction side of the airfoil and sweeps up airfoil boundary layer fluid. The features with positive streamwise vorticity are associated with the passage vortex, which sweeps up inlet boundary layer fluid and endwall boundary layer fluid in the passage to create the large lobe of total pressure loss from Y/P=0 to 0.1, and 0.6 to 1.0. A thin region of negative streamwise vorticity near the endwall consists of the corner vortex and

the skewed endwall boundary layer. The corner vortex is small and very close to the endwall, making it difficult to discern from the endwall boundary layer, but its likely position is indicated in Figure 5.7a. Note that the five-hole probe diameter was too large to obtain measurements within the thin endwall boundary layer.

Comparison of Figure 5.7a to Figure 5.7b indicates that only subtle differences are visible between the secondary flow structures for rim seal flow without and with swirl. The center of the loss core associated with negative streamwise vorticity in Figure 5.7b is slightly farther from the endwall (Z/S=0.14) compared to the loss core in Figure 5.7a (Z/S=0.12). Also, the loss core associated with the passage vortex (positive streamwise vorticity) appears to have shifted slightly further off the endwall in Figure 5.7b, compared to Figure 5.7a, although the magnitudes of the loss cores are not significantly different. These results are similar to the findings of McLean, et al. [35], where the spanwise location of peak mass-averaged loss downstream of a turbine stage with wheelspace cooling was displaced slightly away from the endwall but the magnitude was unchanged.

Figure 5.8a shows the secondary flow vectors and secondary kinetic energy for the flat endwall with leakage flow at 100% V_{wh}. High values of C_{SKE} are present around Y/P=0.1 and Z/S=0.08, where the vectors indicate high secondary flow velocities between the two vortical structures. C_{SKE} is also high near the endwall, where the influences of the passage vortex and the cross-passage pressure gradient on the endwall boundary layer result in large cross-stream velocities. For a flat endwall with 50% V_{wh} leakage, Figure 5.8b indicates lower levels of secondary kinetic energy in the peak C_{SKE} at Y/P=0.1 and a shift away from the endwall to Z/S=0.10, when compared to Figure 5.8a. Figure 5.8b also shows lower secondary kinetic energy near the endwall from Y/P=0.6 to 0.8, in comparison to Figure 5.8a. Secondary flow vectors in that region indicate that the induced downwash velocity of the passage vortex is smaller for the flat endwall with 50% V_{wh} leakage, compared to 100% V_{wh} leakage. Yaw and pitch angles relative to midspan values are extracted at Y/P=0.75 and plotted versus span in Figure 5.9. 50% V_{wh} leakage results in less negative pitch angles (reduced turning of the flow toward the wall) below Z/S=0.06, compared to 100% V_{wh} leakage. Below Z/S=0.04, 50% V_{wh} leakage shows smaller values of yaw angle deviation (reduced overturning of the flow toward the blade suction side). The blade velocity triangles in Figure 5.2 indicate that the additional tangential component of 50% V_{wh} leakage reduces the incidence angle of the flow entering the cascade. Perdichizzi and

Dossena [36] found that negative incidence resulted in reduced under- and overturning compared to 0° incidence.

Effect of Non-Axisymmetric Contouring

In Figure 5.7c and d, the non-axisymmetric endwall contour does not display significant differences in magnitude or structure of total pressure loss or streamwise vorticity around the suction side horseshoe vortex or passage vortex cores, relative to a flat endwall. Recall that both endwalls had the same upstream cavity geometry. It is likely that the dominating factor in the development of the endwall secondary flow is the upstream cavity geometry. Abo El Ella, et al. [2] indicated that the presence of a similar upstream cavity geometry significantly increased the size and strength of the passage vortex, even without leakage flow. Geometric or flow constraints in the contour optimization process may limit the contour design such that significant changes in loss are not achievable. The design methodology of Praisner, et al. [21], used for the contour in this study, had a constraint to limit overturning near the wall. Furthermore, observations indicate that the separated flow in the upstream cavity is highly unsteady. Any correlated effects of that unsteadiness with the passage vortex were not captured by an optimization process using steady CFD.

The only significant impact of contouring occurs near the endwall around Y/P=0.45, Z/S=0.02 for 100% V_{wh} leakage (Figure 5.7c), where the contour appears to increase loss associated with the corner vortex. Knezevici, et al. [23] found that losses very near the wall (Z/S<0.02) increased with endwall contouring for their cascade without upstream leakage features. The corner vortex losses, however, are relatively unchanged (within the uncertainty of the measurements) for the contour design case of 50% V_{wh} leakage. Swirled upstream leakage flow (50% V_{wh}) changes the trajectory of the passage vortex in the forward portion of the passage in Figure 5.6b and may slightly reduce the angle at which it impinges on the suction side of the airfoil. Sieverding [37] states that a reduced impact angle weakens the corner vortex, and thus it might be less influenced by contouring.

Total pressure loss coefficients were pitchwise mass-averaged and plotted versus the normalized span direction in Figure 5.10. Two peaks are distinguishable, corresponding to the suction side horseshoe vortex away from the endwall and the passage vortex nearer to the endwall. High levels of loss below Z/S=0.03 are due to the endwall boundary layer as well as the corner vortex. For either endwall geometry, 50% V_{wh} leakage shifts the peak losses away from

the endwall and increases loss between Z/S=0.10 to 0.20 compared to 100% V_{wh} leakage. Losses are slightly higher between Z/S=0.12 to 0.16 for the contoured endwall versus the flat endwall at 50% V_{wh} swirl. This may be due to a stronger suction side horseshoe vortex caused by the contour hill near the suction side leading edge in Figure 5.4a. A hill in a contour is intended to locally accelerate the flow, which would increase the strength of the suction side horseshoe vortex and its ability to entrain airfoil boundary layer fluid. Below Z/S=0.1, the contour at 50% V_{wh} leakage shows a very slight reduction in losses relative to the flat endwall. The same trend of increased loss around the suction side horseshoe vortex (Z/S=0.10 to 0.14) occurs with contouring and 100% V_{wh} leakage, compared to a flat endwall; however, the contour also increases loss below Z/S=0.04, which is tied to the increased corner vortex losses mentioned earlier.

Secondary kinetic energy contours in Figure 5.8 indicate that non-axisymmetric contouring slightly increases the peak C_{SKE} around Y/P=0.1, Z/S=0.08, relative to a flat endwall. For 100% V_{wh} leakage, the contoured endwall (Figure 5.8c) results in a 9% increase in the peak C_{SKE} relative to Figure 5.8a, and for 50% V_{wh} leakage, peak C_{SKE} was increased with contouring by about 18%. The suction side horseshoe vortex, which is augmented by the contour hill mentioned earlier, results in larger secondary kinetic energy levels. Contouring results in decreased C_{SKE} between the passage vortex and the endwall (around Y/P=0.8, Z/S=0.04) for 100% V_{wh} leakage, which the secondary flow vectors indicate is largely due to a reduction in downward-directed (V_z) flow in that region. Based on the loss results for Figure 5.7c discussed earlier, the corner vortex for 100% V_{wh} leakage with contouring appears to be slightly stronger, and since it rotates in a direction opposite to the passage vortex, it would be expected to counteract the influence of that structure near the endwall.

The global effect of contouring on secondary kinetic energy can be seen in the pitchwise mass-averaged results in Figure 5.11. The contour with swirled leakage (50% V_{wh}) results in slightly higher C_{SKE} than the flat endwall from Z/S=0.10 to 0.16, which is attributed to the suction side horseshoe vortex. Secondary kinetic energy below Z/S=0.08 is also slightly higher for the contour versus the flat endwall for 50% V_{wh} leakage. Knezevici, et al. [23] indicated the same trend of higher C_{SKE} with contouring near the endwall and attributed it to accelerations induced by the merging of the contour to the nominal flat level at the cascade exit. Endwall contouring with 100% V_{wh} leakage also slightly increases secondary kinetic energy around the

suction side horseshoe vortex (Z/S=0.08 to 0.14), but below Z/S=0.08, the contour shows reduced $C_{SKE,}$ relative to a flat endwall. The stronger corner vortex for the contour with 100% V_{wh} leakage contributes to the reduction in C_{SKE} near the endwall.

Figure 5.12 shows pitchwise-mass-averaged yaw angle deviation for the flat and contoured endwalls at the two leakage swirl conditions. Note that the reference yaw angle is the mass-averaged yaw at midspan. The contour reduces underturning at a given span location by up to 2 degrees between Z/S=0.08 to 0.12 for either leakage swirl condition. The passage vortex is the dominating feature in this region of the span. The application of endwall contouring in this cascade appears to slightly reduce its strength, and its effect on exit yaw angle. Based on the previous discussions, at least part of the reduction in the passage vortex strength is probably due to increases in the suction side horseshoe and corner vortices.

Effect of a Platform Gap on a Contoured Endwall

Measurements of total pressure loss coefficient and streamwise vorticity coefficient are presented in Figure 5.7e-f for the contoured endwall with a platform gap. A net leakage flowrate of 0.3% of the passage mainstream flow was provided to the gap plenums in each blade passage. The presence of the gap and its net leakage flow results in a large increase in total pressure loss and streamwise vorticity in the passage, compared to a contour without a gap in Figure 5.7c-d. Note that the non-axisymmetric contour design was not optimized with a gap, although the results shown here indicate that the effect of the gap is more significant than the effect of contouring. For either of the leakage swirl conditions, the gap (Figure 5.7e-f) increases the peak total pressure loss by almost 30% in the loss core associated with negative streamwise vorticity, and the size of the vortical structure has increased. The region of positive streamwise vorticity associated with the passage vortex has increased in intensity, and the peak loss is also higher. In Figure 5.13, pitchwise-mass-averaged total pressure loss clearly indicates the increased loss for an endwall with a gap compared to a continuous contoured endwall. The ejection of flow from the gap appears to displace the peak loss from Z/S=0.11 to 0.14 for the 100% V_{wh} leakage case, such that the peak is located at the same spanwise location as for 50% V_{wh} leakage.

Comparison of Figure 5.8c to Figure 5.8e, and Figure 5.8d to Figure 5.8f, reveals a significant increase in secondary kinetic energy for the endwall with a gap, both in the peak C_{SKE} away from the endwall and also below Z/S=0.05. The secondary velocity vectors in the near-wall region indicate higher pitchwise velocity that corresponds to stronger crossflow from the

pressure to suction sides of the passage. In Figure 5.14, the peak near-wall C_{SKE} (around Z/S=0.04) has increased by approximately 40% for the endwall with a platform gap and no upstream swirl (100% V_{wh}), relative to a continuous wall. In contrast, peak near-wall C_{SKE} is only 15% larger for 50% V_{wh} leakage with a gap, relative to a continuous wall. The larger increase of 40% in peak C_{SKE} for 100% V_{wh} leakage, relative to the increase for 50% V_{wh} leakage, is attributed to the differences in the near-wall blade loading for unswirled and swirled leakage. As explained earlier, 50% V_{wh} leakage increases the static pressure around the suction side leading edge. This in turn would reduce the streamwise pressure gradient that drives the platform gap ingestion/ejection flow. It is possible that less near-wall flow is ingested into the platform gap for 50% V_{wh} leakage, and thus the ejected gap flow has less of an influence on the passage vortex.

Pitchwise-mass-averaged yaw angle deviation is presented in Figure 5.15 for the contoured endwall with and without a gap. In general, the gap results in increased over- and under-turning for a given upstream leakage swirl condition. As was noted in the C_{SKE} results, the amount of increase in over- or under-turning with a gap appears to be slightly less for 50% V_{wh} leakage than for 100% V_{wh} leakage, due to reduced interaction of the gap leakage flow with the cascade secondary flow.

Overall Mass-Averaged Losses

Figure 5.16 presents mass-averaged results over a single passage for the measurement plane located at X/C_{ax}=1.3. Definitions for the various loss terms were given in the Experimental Methodology section. For the flat endwall, net total pressure loss across the cascade was increased by about 10% for swirled rim seal leakage (50% V_{wh}), compared to unswirled leakage (100% V_{wh}). This is consistent with previous studies indicating a modest overall loss increase with increasing relative tangential velocity for small to moderate amounts of leakage mass flow (<1%). In terms of secondary loss, however, the 50% V_{wh} case resulted in a 30% increase. The mixing losses described by Denton [1] are certainly increased when the leakage flow has additional swirl, although the results of Popovic and Hodson [10] indicate that interaction with the endwall secondary flow is perhaps more significant.

At the design condition of 50% V_{wh} for the upstream leakage, the contoured endwall without a gap resulted in a small improvement for both net loss (-4%) and secondary loss (-7%)

over the flat endwall in Figure 5.16. The off-design condition of 100% V_{wh} leakage resulted in a small increase in net loss (+3%) with contouring and a modest increase of +16% in secondary loss, relative to a flat endwall. This suggests that non-axisymmetric endwall contouring may be sensitive to off-design conditions.

Figure 5.16 also shows that a platform gap in the contoured endwall resulted in large increases in loss relative to a continuous contoured endwall. For upstream leakage without swirl (100% V_{wh}), net loss increased by 16% and secondary loss increased by 58% for the endwall with a gap. Upstream leakage with swirl relative to the blade (50% V_{wh}) resulted in a net loss increase of 12% and a secondary loss increase of 38% for the endwall with a gap, relative to a continuous contour. When comparing losses between the two upstream swirl cases with an endwall gap, however, the effect of swirl was negligible. It appears that the mechanism of ingestion of near-wall flow into the forward portion of the gap and ejection from the gap downstream, as described by Cardwell, et al. [38] and Reid, et al. [12], tends to negate any differences in loss generation caused by upstream leakage swirl.

Mixed-out losses are compared to the net mass-averaged losses at the measurement plane (X/C_{ax}=1.3) in Figure 5.17. The mixed-out analysis was performed using constant-area mixing with no frictional losses, and was done to account for additional losses that would be generated due to mixing out of the secondary flow. Mixed-out net losses indicate no significant improvement of endwall contouring over a flat endwall for a given upstream swirl condition. This could be due to increased overturning very near the wall for the contour, which is a consequence of the merging of the contour back to a nominal endwall height. MacIsaac, et al. [29], however, noted for the same airfoil as in this study, that secondary kinetic energy contributed to only about half of the difference between plane mass-averaged and mixed-out losses, with the remainder being static pressure recovery and mixing of primary kinetic energy.

Figure 5.17 also indicates that when comparing a contour with a platform gap to a continuous contour, mixed-out losses increase by about the same percentage (~12% for 50% V_{wh}, and ~16% for 100% V_{wh}) as mass-averaged losses. This implies that the additional secondary kinetic energy generated by the gap (Figure 5.14) is not a significant contribution to mixing loss in this cascade, and supports the hypothesis of MacIsaac, et al. [29] that pressure recovery and primary kinetic energy mixing are significant factors for this airfoil geometry.

Conclusions

Endwall oil flow visualization and flowfield measurements at X/C_{ax}=1.3 downstream of the cascade were presented for a high-pressure turbine blade with an upstream cavity and purge flow through realistic leakage features. Two upstream rim seal purge flow conditions were considered: flow with no tangential velocity relative to the blade (100% V_{wh}), and flow with a tangential velocity at half of the wheel speed (50% V_{wh}). Both cases had a net mass flow rate of 0.75% of the mainstream mass flow. Two types of endwalls were also investigated in the passage downstream of the rim seal cavity: an endwall with a flat profile; and a non-axisymmetric contoured endwall. The effect of a platform gap through the passage, with 0.3% net mass flow, was considered for the non-axisymmetric contoured endwall.

Oil flow visualization for the flat endwall indicated that rim seal leakage flow with tangential velocity relative to the blade (50% V_{wh}) shifted the saddle point region in the direction of the tangential velocity relative to leakage with no tangential velocity (100% V_{wh}). Contours of the flowfield downstream of the cascade showed a slight shift toward midspan for the loss cores and peak secondary kinetic energy for 50% V_{wh} leakage, but no significant difference in magnitudes of those features. Mass-averaged and mixed-out losses over the measurement plane were higher for 50% V_{wh} leakage relative to the no-swirl (100% V_{wh}) case.

Contour plots of the exit flowfield did not indicate a significant effect of non-axisymmetric endwall contouring on total pressure loss or streamwise vorticity features relative to a flat endwall. A strong passage vortex due to separated upstream cavity flow, as well as constraints in the endwall contour design, limited the effect of the contouring on the primary flowfield features. A hill near the suction side leading edge of the endwall contour was conjectured to strengthen the suction side horseshoe vortex, which increased secondary kinetic energy and loss associated with that vortex. Underturning of the exit flow associated with the passage vortex was reduced with contouring, however, which would provide some benefit to downstream airfoils. At the design condition of 50% V_{wh} leakage for the contour, mass-averaged losses showed a nearly insignificant improvement for non-axisymmetric contoured endwalls, but at the off-design condition of 100% V_{wh} leakage, the contour resulted in slightly higher losses.

The presence of a platform gap with leakage in a contoured endwall significantly increased peak total pressure loss and secondary kinetic energy relative to a continuous contoured endwall. Mass-averaged losses for the endwall with a gap were nearly the same

regardless of upstream leakage swirl condition, indicating that the gap is the most significant factor in the generation of loss.

Acknowledgments

We would like to thank United Technologies—Pratt & Whitney for their support of this work, and acknowledge the assistance of Scott Fishbone in the construction of the test section.

Nomenclature

C	true chord of blade
C_{ax}	axial chord of blade
C_p	static pressure coefficient, $C_p = \left(P_s - P_{s,in}\right) \big/ 0.5\rho U_{in}^2$
C_{Ptot}	total pressure loss coefficient based on inlet dynamic pressure, Eq. (5.1)
C_{SKE}	secondary kinetic energy coefficient, Eq. (5.7)
$C_{\omega s}$	streamwise vorticity coefficient, Eq. (5.4)
H	boundary layer shape factor
HS	horseshoe vortex
MFR	mass flow ratio, $MFR = \dot{m}_{leak} / \dot{m}_{in}$
P	blade pitch
P_s	static pressure
PS	pressure side
P_{tot}	total pressure
Re_θ	momentum thickness Reynolds number, $Re_\theta = \theta U_{in} / \nu$
S	blade span
SS	suction side
X, Y, Z	global coordinates, where X is blade axial direction
U, V, W	velocity components aligned with global coordinates
U_{in}	magnitude of inlet streamwise velocity
U_{exit}	magnitude of exit streamwise velocity
V_{leak}	magnitude of upstream rim leakage velocity
V_n	pitchwise component of mean velocity on a plane normal to the mass-averaged velocity vector, Eq. (5.5)

V_{wh}	Circumferential speed of the blade wheel at the hub
V_z	spanwise component of mean velocity on a plane normal to the mass-averaged velocity vector, Eq. (5.6)
Y_o	Total pressure loss based on exit dynamic pressure, Eq. (5.2)
Zw	Zweifel load coefficient, $Zw = 2\frac{P}{C_{ax}}\cos^2\beta_{exit}\left(\frac{U_{x,in}}{U_{x,exit}}\tan\beta_{in} + \tan\beta_{exit}\right)$

Greek

$\bar{\beta}_{exit}$	mass-averaged measured exit yaw angle
β	design flow yaw angle
δ_{99}	boundary layer thickness (99%)
θ	momentum thickness
ν	kinematic viscosity
ρ	density
ω_s	streamwise vorticity, Eq. (5.3)
ω_x	axial vorticity, $\omega_x = \frac{\partial W}{\partial y} - \frac{\partial V}{\partial z}$
ω_y	pitchwise vorticity, $\omega_y = \left(\frac{1}{\rho}\frac{\partial P_{tot}}{\partial z} - V\cdot\omega_x\right)\cdot\left(\frac{1}{U_x}\right)$

Subscripts/Superscripts

exit	exit conditions
in	inlet conditions
ms	local midspan conditions
net	net mass-averaged total pressure loss across cascade
profile	profile loss consisting of airfoil boundary layer loss only (i.e., midspan)
secondary	secondary loss comprised of all losses other than profile loss
x	aligned with axial direction
$\overline{(...)}$	pitchwise-mass-averaged quantity, $\overline{(...)} = \int_{Y/P=0}^{1}\rho U_x(...)\partial Y \Big/ \int_{Y/P=0}^{1}\rho U_x\partial Y$

$\overline{(...)}$ plane-mass-averaged quantity,

$$\overline{(...)} = \int_{Z/S=0}^{0.5} \int_{Y/P=0}^{1} \rho U_X (...) \partial Y \partial Z \Big/ \int_{Z/S=0}^{0.5} \int_{Y/P=0}^{1} \rho U_X \partial Y \partial Z$$

References

[1] Denton, J. D., 1993, "The 1993 IGTI Scholar Lecture: Loss Mechanisms in Turbomachines," *Journal of Turbomachinery*, **115**(4), pp. 621-656.

[2] Abo El Ella, H. M., Sjolander, S. A., and Praisner, T. J., 2010, "Effects of an Upstream Cavity on the Secondary Flow in a Transonic Turbine Cascade," Proc. ASME Turbo Expo 2010, Paper No. GT2010-22843.

[3] Marini, R., and Girgis, S., 2007, "The Effect of Blade Leading Edge Platform Shape on Upstream Disk Cavity to Mainstream Flow Interaction of a High-Pressure Turbine Stage," Proc. ASME Turbo Expo 2007, Paper No. GT2007-27429.

[4] De La Rosa Blanco, E., Hodson, H. P., and Vazquez, R., 2009, "Effect of the Leakage Flows and the Upstream Platform Geometry on the Endwall Flows of a Turbine Cascade," *Journal of Turbomachinery*, **131**(1), pp. 011004.

[5] Hunter, S. D., and Manwaring, S. R., 2000, "Endwall Cavity Flow Effects on Gaspath Aerodynamics in an Axial Flow Turbine: Part I - Experimental and Numerical Investigation," Proc. ASME Turbo Expo 2000, Paper No. 2000-GT-651.

[6] Rosic, B., and Denton, J. D., 2008, "Control of Shroud Leakage Loss by Reducing Circumferential Mixing," *Journal of Turbomachinery*, **130**(2), pp. 021010-7.

[7] Paniagua, G., Denos, R., and Almeida, S., 2004, "Effect of the Hub Endwall Cavity Flow on the Flow-Field of a Transonic High-Pressure Turbine," *Journal of Turbomachinery*, **126**(4), pp. 578-586.

[8] Shih, T. I.-P., and Lin, Y.-L., 2003, "Controlling Secondary-Flow Structure by Leading-Edge Airfoil Fillet and Inlet Swirl to Reduce Aerodynamic Loss and Surface Heat Transfer," *Journal of Turbomachinery*, **125**(1), pp. 48-56.

[9] Walsh, J. A., and Gregory-Smith, D. G., 1990, "Inlet Skew and the Growth of Secondary Losses and Vorticity in a Turbine Cascade," *Journal of Turbomachinery*, **112**(4), pp. 633-642.

[10] Popovic, I., and Hodson, H. P., 2010, "Aerothermal Impact of the Interaction between Hub Leakage and Mainstream Flows in Highly-Loaded HP Turbine Blades," Proc. ASME Turbo Expo 2010, Paper No. GT2010-22311.

[11] Reid, K., Denton, J. D., Pullan, G., Curtis, E., and Longley, J., 2006, "The Effect of Stator-Rotor Hub Sealing Flow on the Mainstream Aerodynamics of a Turbine," Proc. ASME Turbo Expo 2006, Paper No. GT2006-90838.

[12] Reid, K., Denton, J., Pullan, G., Curtis, E., and Longley, J., 2007, "The Interaction of Turbine Inter-Platform Leakage Flow with the Mainstream Flow," *Journal of Turbomachinery*, **129**(2), pp. 303-310.

[13] Reid, K., Denton, J. D., Pullan, G., Curtis, E., and Longley, J., 2006, "Reducing the Performance Penalty Due to Turbine Inter-Platform Gaps," Proc. ASME Turbo Expo 2006, Paper No. GT2006-90839.

[14] Piggush, J., and Simon, T. W., 2005, "Flow Measurements in a First Stage Nozzle Cascade Having Endwall Contouring, Leakage and Assembly Features," Proc. ASME Turbo Expo 2005, Paper No. GT2005-68340.

[15] Piggush, J., and Simon, T. W., 2005, "Flow Measurements in a First Stage Nozzle Cascade Having Leakage and Assembly Features: Effects of Endwall Steps and Leakage on Aerodynamic Losses," Proc. ASME International Mechanical Engineering Congress and Expo, Paper No. IMECE2005-83032.

[16] Lynch, S. P., and Thole, K. A., 2009, "The Effect of the Combustor-Turbine Slot and Mid-Passage Gap on Vane Endwall Heat Transfer," Proc. ASME International Mechanical Engineering Congress & Expo 2009, Paper No. IMECE2009-12847.

[17] Harvey, N. W., Rose, M. G., Taylor, M. D., Shahpar, S., Hartland, J., and Gregory-Smith, D. G., 2000, "Nonaxisymmetric Turbine End Wall Design: Part I--- Three-Dimensional Linear Design System," *Journal of Turbomachinery*, **122**(2), pp. 278-285.

[18] Hartland, J. C., Gregory-Smith, D. G., Harvey, N. W., and Rose, M. G., 2000, "Nonaxisymmetric Turbine End Wall Design: Part II---Experimental Validation," *Journal of Turbomachinery*, **122**(2), pp. 286-293.

[19] Germain, T., Nagel, M., Raab, I., Schupbach, P., Abhari, R. S., and Rose, M., 2010, "Improving Efficiency of a High Work Turbine Using Nonaxisymmetric Endwalls--- Part I: Endwall Design and Performance," *Journal of Turbomachinery*, **132**(2), pp. 021007.

[20] Schuepbach, P., Abhari, R. S., Rose, M. G., Germain, T., Raab, I., and Gier, J., 2010, "Improving Efficiency of a High Work Turbine Using Nonaxisymmetric Endwalls---Part II: Time-Resolved Flow Physics," *Journal of Turbomachinery*, **132**(2), pp. 021008.

[21] Praisner, T. J., Allen-Bradley, E., Grover, E. A., Knezevici, D. C., and Sjolander, S. A., 2007, "Application of Non-Axisymmetric Endwall Contouring to Conventional and High-Lift Turbine Airfoils," Proc. ASME Turbo Expo 2007, Paper No. GT2007-27579.

[22] Knezevici, D. C., Sjolander, S. A., Praisner, T. J., Allen-Bradley, E., and Grover, E. A., 2009, "Measurements of Secondary Losses in a High-Lift Front-Loaded Turbine Cascade with the Implementation of Non-Axisymmetric Endwall Contouring," Proc. ASME Turbo Expo 2009, Paper No. GT2009-59677.

[23] Knezevici, D. C., Sjolander, S. A., Praisner, T. J., Allen-Bradley, E., and Grover, E. A., 2010, "Measurements of Secondary Losses in a Turbine Cascade with the Implementation of Nonaxisymmetric Endwall Contouring," *Journal of Turbomachinery*, **132**(1), pp. 011013.

[24] Poehler, T., Gier, J., and Jeschke, P., 2010, "Numerical and Experimental Analysis of the Effects of Non-Axisymmetric Contoured Stator Endwalls in an Axial Turbine," Proc. ASME Turbo Expo 2010, Paper No. GT2010-23350.

[25] Torre, D., Vazquez, R., Blanco, E. D. L. R., and Hodson, H. P., 2011, "A New Alternative for Reduction in Secondary Flows in Low Pressure Turbines," *Journal of Turbomachinery*, **133**(1), pp. 011029-10.

[26] Gustafson, R., Mahmood, G. I., and Acharya, S., 2007, "Aerodynamic Measurements in a Linear Turbine Blade Passage with Three-Dimensional Endwall Contouring," Proc. ASME Turbo Expo 2007, Paper No. GT2007-28073.

[27] Snedden, G., Dunn, D., Ingram, G., and Gregory-Smith, D., 2010, "The Performance of a Generic Non-Axisymmetric End Wal in a Single Stage, Rotating Turbine at on and Off-Design Conditions," Proc. ASME Turbo Expo 2010, Paper No. GT2010-22006.

[28] Vazquez, R., and Fidalgo, V. J., 2010, "The Effect of Reynolds and Mach Number on End-Wall Profiling Performance," Proc. ASME Turbo Expo 2010, Paper No. GT2010-22765.

[29] Macisaac, G. D., Sjolander, S. A., and Praisner, T. J., 2010, "Measurements of Losses and Reynolds Stresses in the Secondary Flow Downstream of a Low-Speed Linear Turbine Cascade," Proc. ASME Turbo Expo 2010, Paper No. GT2010-22727.

[30] Lynch, S. P., Sundaram, N., Thole, K. A., Kohli, A., and Lehane, C., 2011, "Heat Transfer for a Turbine Blade with Nonaxisymmetric Endwall Contouring," *Journal of Turbomachinery*, **133**(1), pp. 011019-9.

[31] Lynch, S. P., Thole, K. A., Kohli, A., and Lehane, C., 2010, "Computational Predictions of Heat Transfer and Film-Cooling for a Turbine Blade with Non-Axisymmetric Endwall Contouring," Proc. ASME Turbo Expo 2010, Paper No. GT2010-22984.

[32] Moffat, R. J., 1988, "Describing the Uncertainties in Experimental Results," *Experimental Thermal and Fluid Science*, **1**, pp. 3-17.

[33] Friedrichs, S., Hodson, H. P., and Dawes, W. N., 1997, "Aerodynamic Aspects of Endwall Film-Cooling," *Journal of Turbomachinery*, **119**(4), pp. 786-793.

[34] Gregory-Smith, D. G., Graves, C. P., and Walsh, J. A., 1988, "Growth of Secondary Losses and Vorticity in an Axial Turbine Cascade," *Journal of Turbomachinery*, **110**(1), pp. 1-8.

[35] Mclean, C., Camci, C., and Glezer, B., 2001, "Mainstream Aerodynamic Effects Due to Wheelspace Coolant Injection in a High-Pressure Turbine Stage: Part I---Aerodynamic Measurements in the Stationary Frame," *Journal of Turbomachinery*, **123**(4), pp. 687-696.

[36] Perdichizzi, A., and Dossena, V., 1993, "Incidence Angle and Pitch--Chord Effects on Secondary Flows Downstream of a Turbine Cascade," *Journal of Turbomachinery*, **115**(3), pp. 383-391.

[37] Sieverding, C. H., 1985, "Recent Progress in the Understanding of Basic Aspects of Secondary Flows in Turbine Blade Passages," *Journal of Engineering for Gas Turbines and Power*, **107**(2), pp. 248-257.

[38] Cardwell, N. D., Sundaram, N., and Thole, K. A., 2006, "Effect of Midpassage Gap, Endwall Misalignment, and Roughness on Endwall Film-Cooling," *Journal of Turbomachinery*, **128**(1), pp. 62-70.

Table 5.1 Cascade Geometry and Operating Conditions

Scale relative to engine	6X
Axial chord (C_{ax})	0.1524 m
Span/axial chord (S/C_{ax})	3.6
Pitch/axial chord (P/C_{ax})	1.48
Inlet angle (β_{in}, relative to axial direction)	31.5°
Exit angle (β_{exit}, relative to axial direction)	73.2°
Zweifel load coefficient (Zw)	0.97
Inlet Reynolds number ($Re_{in}=U_{in}C_{ax}/\nu$)	70,000
Exit Reynolds number ($Re_{ex}=U_{exit}C_{ax}/\nu$)	200,000
Exit Mach number	0.06
Inlet boundary layer thickness (δ_{99}/S)	0.13
Momentum thickness (θ/S)	0.0082
Momentum thickness Re number ($Re_{\theta}=U_{in}\theta/\nu$)	1990
Shape factor (H)	1.32

Table 5.2 Uncertainties for Variables Derived from Probe Measurements in a Highly Turbulent Region at Y/P=0.17, Z/S=0.11

Variable	**Value**	**Absolute Uncertainty**	**Percent Uncertainty**
Yaw	64.8°	0.7°	1%
Pitch	5.9°	0.3°	4.5%
V_n	-2.7 m/s	0.25 m/s	9.3%
V_z	2.1 m/s	0.10 m/s	4.4%
C_{SKE}	0.245	0.026	10.8%
$C_{\omega s}$	-9.09	0.080	1.7%
C_{Ptot}	1.7	0.11	6.4%
Y_{loss}	0.19	0.012	6.4%

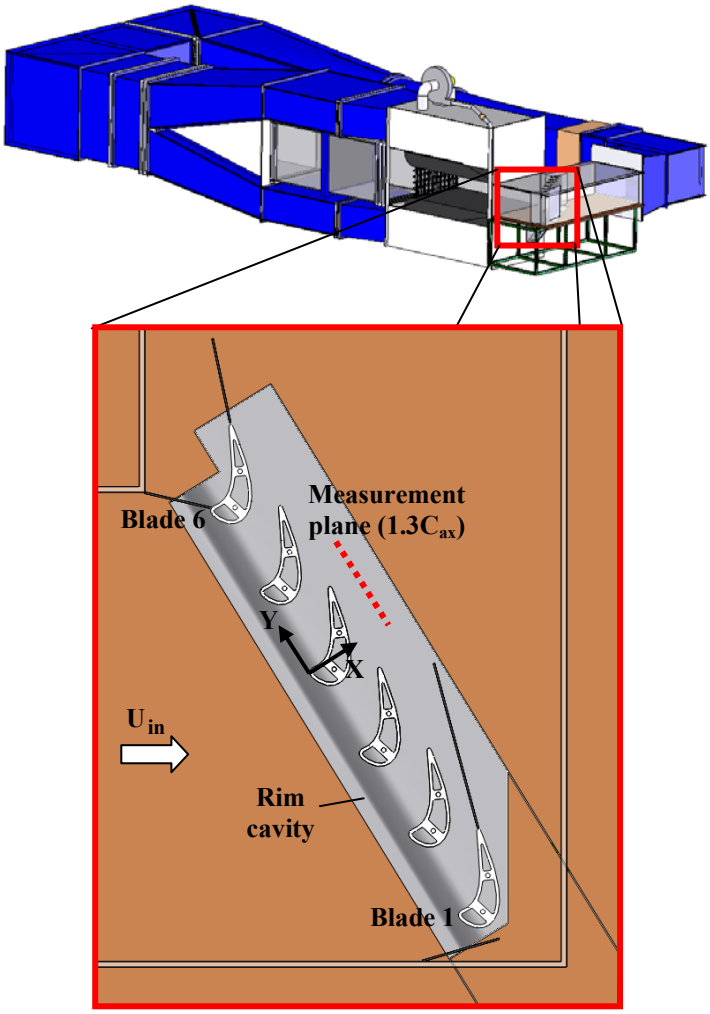

Figure 5.1. Depiction of the low-speed wind tunnel and large-scale test section.

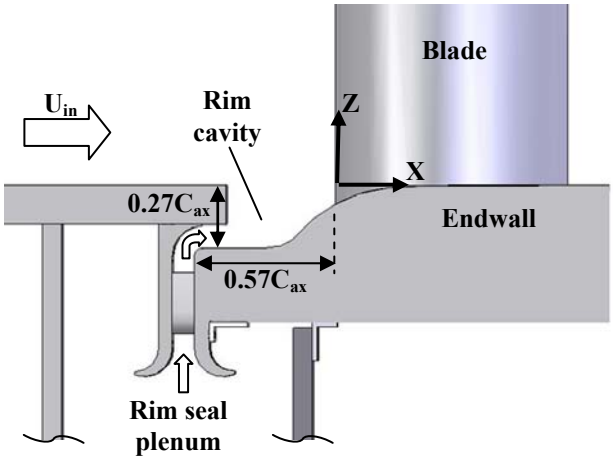

Figure 5.2. Depiction of the endwall rim cavity and rim seal upstream of the cascade.

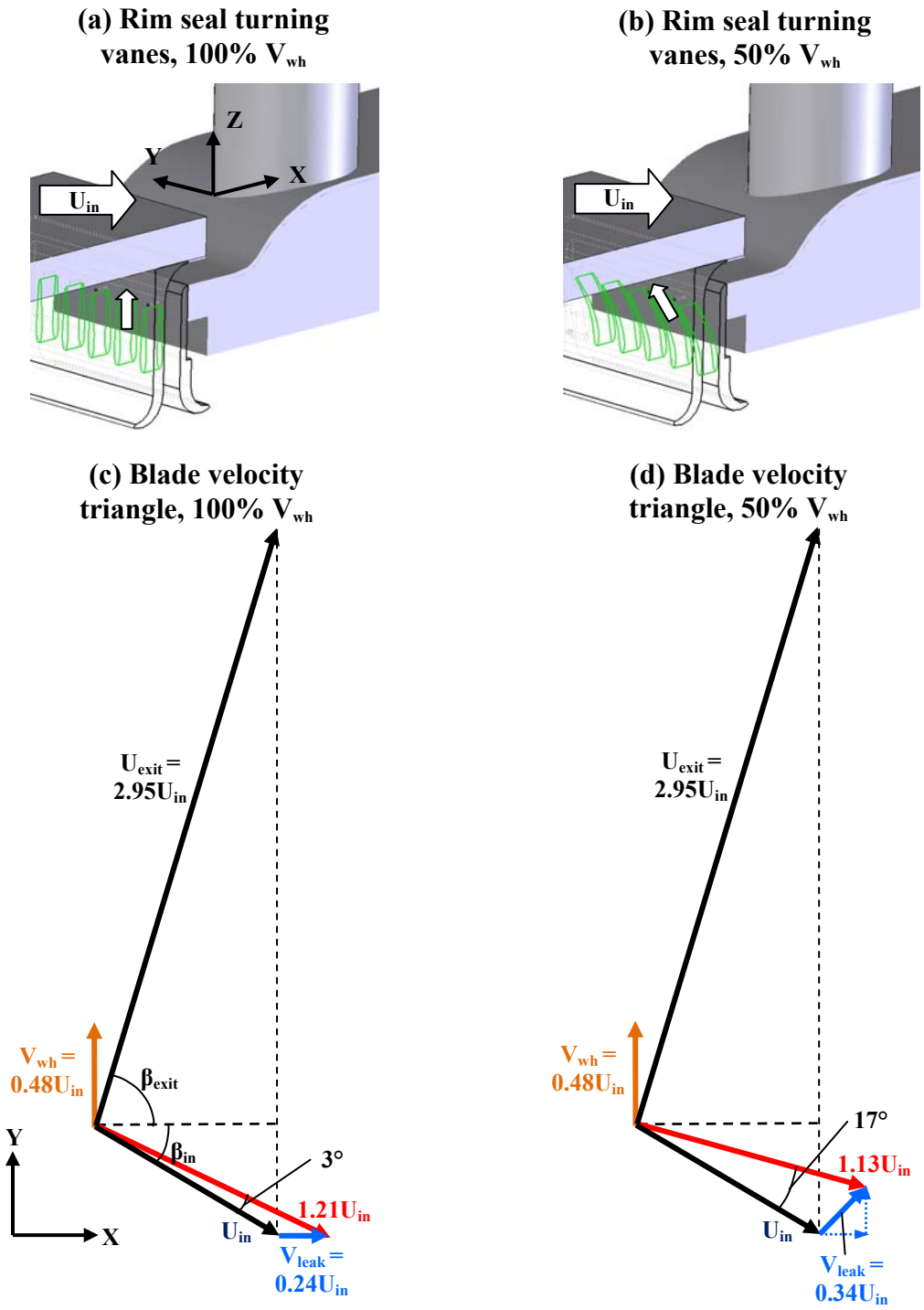

Figure 5.3. Depictions of the internal turning vanes for rim seal leakage at (a) 100% V_{wh} and (b) 50% V_{wh}; and velocity triangles (blade reference frame) near the endwall for (c) 100% V_{wh} and (d) 50% V_{wh}. The incident velocity to the blade near the endwall due to the addition of rim seal leakage is shown in red.

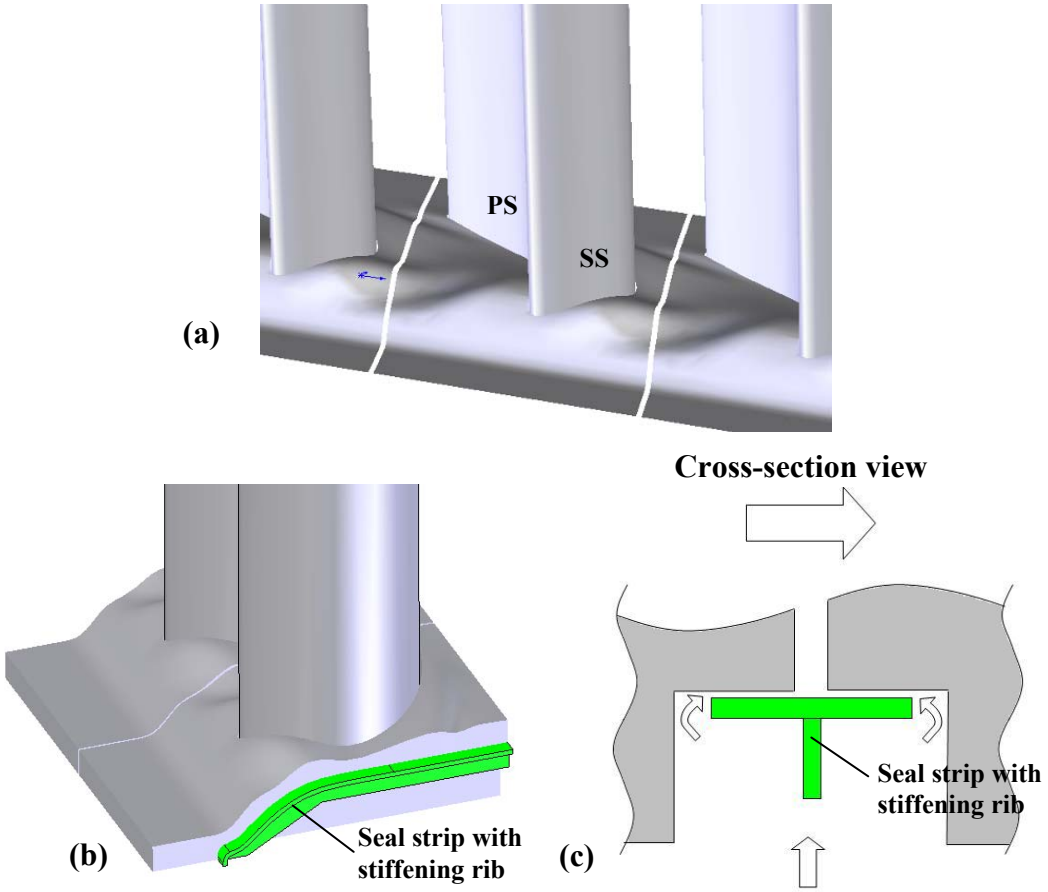

Figure 5.4. Depictions of the (a) non-axisymmetric endwall contour with platform gap; (b) side view of gap with seal strip; and (c) cross-section view of gap.

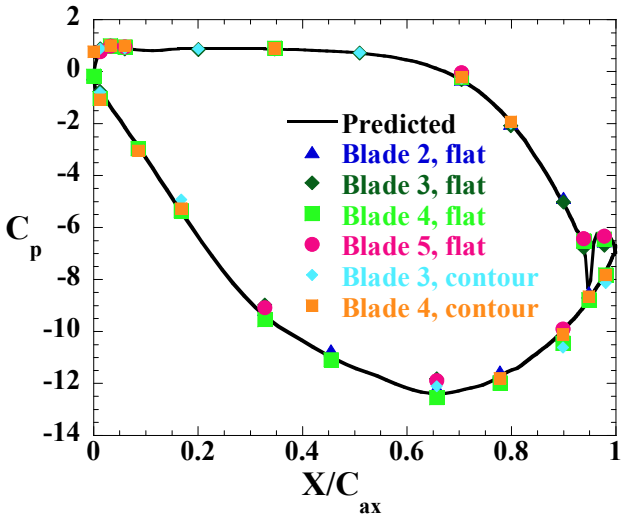

Figure 5.5. Midspan blade static pressure coefficient for various blades in the cascade.

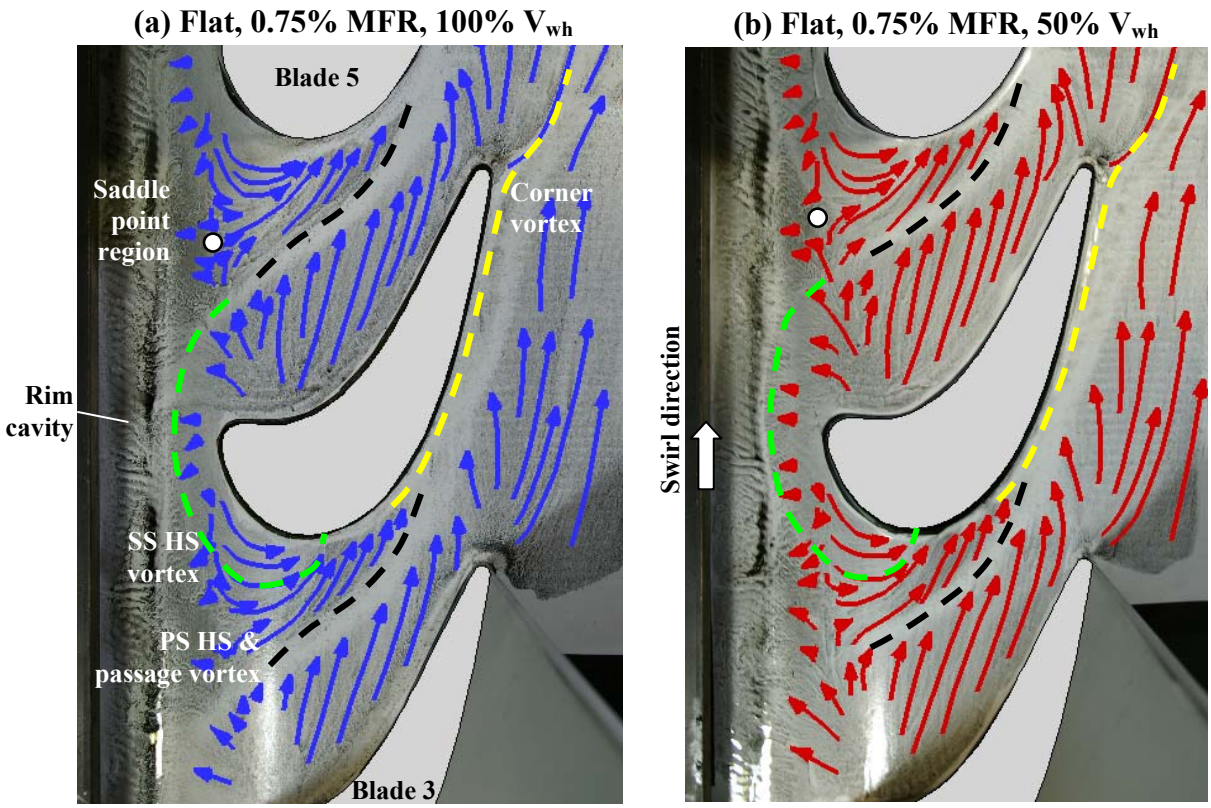

Figure 5.6. Oil flow visualization for the flat endwall, where streakline patterns are highlighted with arrows and separation lines are indicated by dashed lines.

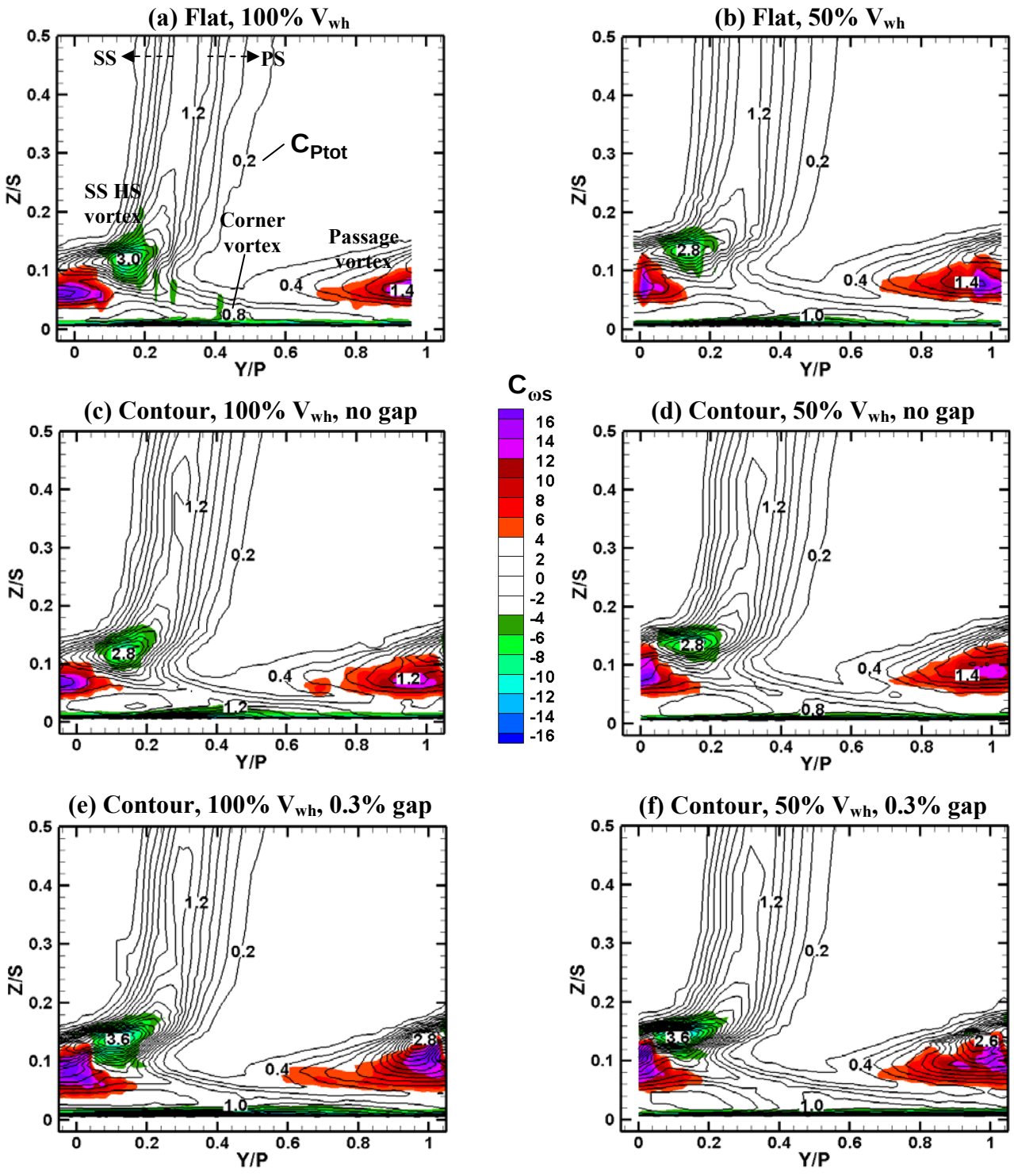

Figure 5.7. Line contours of total pressure coefficient (C_{Ptot}), with color contours of streamwise vorticity coefficient ($C_{\omega s}$) at X/C_{ax}=1.3, for the (a) flat endwall, 100% V_{wh}; (b) flat endwall, 50% V_{wh}; (c) contoured endwall without a gap, 100% V_{wh}; (d) contoured endwall without a gap, 50% V_{wh}; (e) contoured endwall with a gap at 0.3% MFR, 100% V_{wh}; and (f) contoured endwall with a gap at 0.3% MFR, 50% V_{wh}.

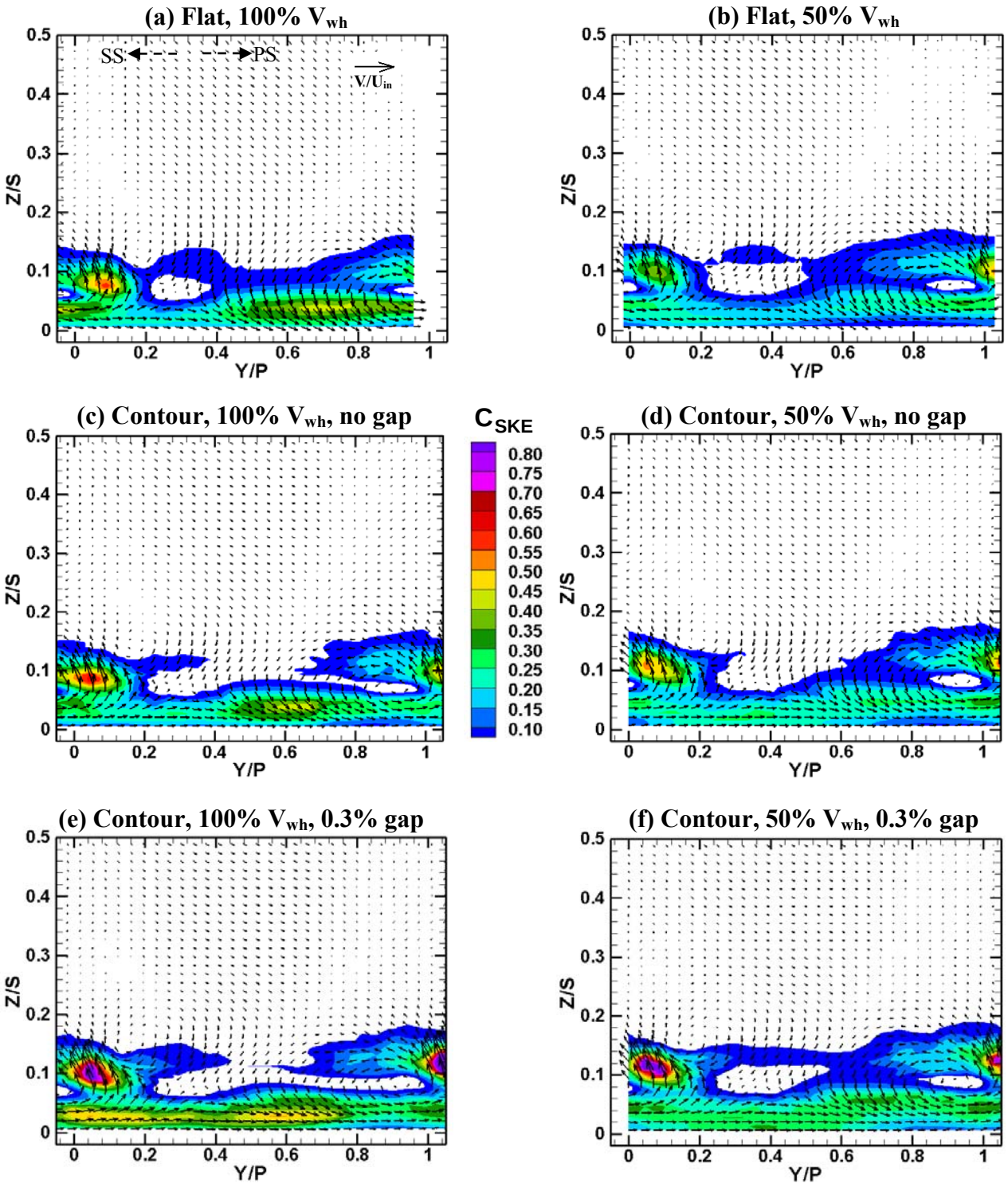

Figure 5.8. Contours of secondary kinetic energy coefficient (C_{SKE}) overlaid with secondary velocity vectors at X/C_{ax}=1.3, for the (a) flat endwall, 100% V_{wh}; (b) flat endwall, 50% V_{wh}; (c) contoured endwall without a gap, 100% V_{wh}; (d) contoured endwall without a gap, 50% V_{wh}; (e) contoured endwall with a gap at 0.3% MFR, 100% V_{wh}; and (f) contoured endwall with a gap at 0.3% MFR, 50% V_{wh}.

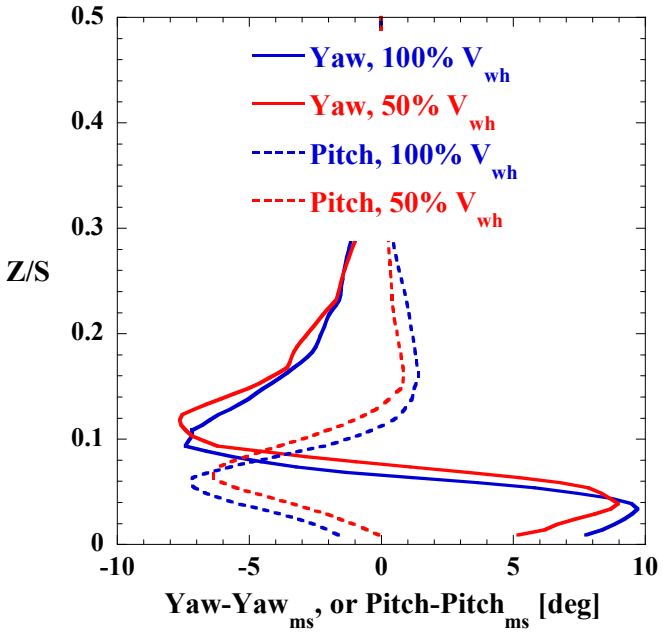

Figure 5.9. Spanwise variation of yaw and pitch angles (relative to midspan) at Y/P=0.75, for the flat endwall with 100% and 50% V_{wh} leakage flow.

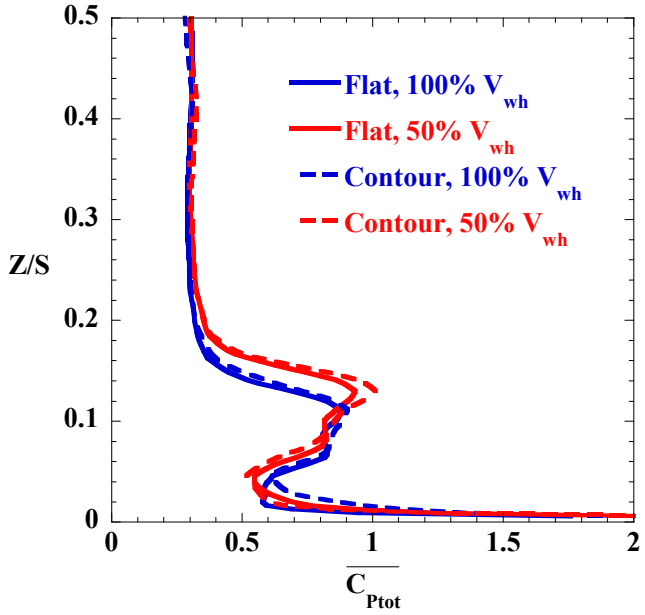

Figure 5.10. Pitchwise-mass-averaged total pressure loss coefficient for the flat endwall and the contoured endwall without a platform gap.

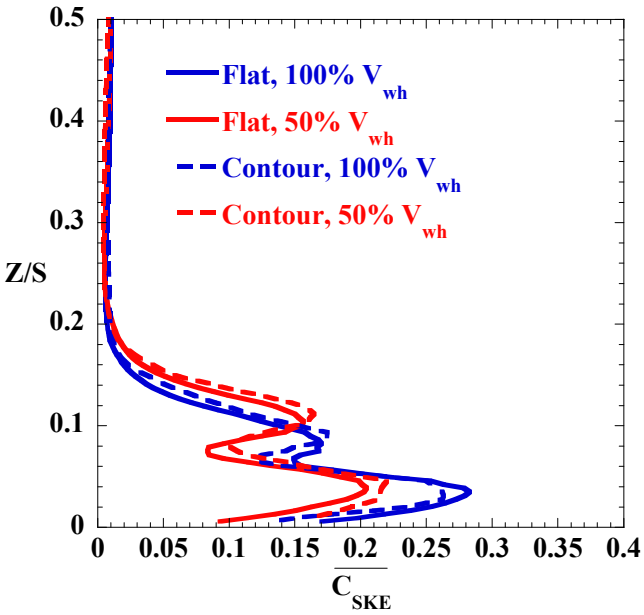

Figure 5.11. Pitchwise-mass-averaged secondary kinetic energy coefficient for the flat endwall and the contoured endwall without a platform gap.

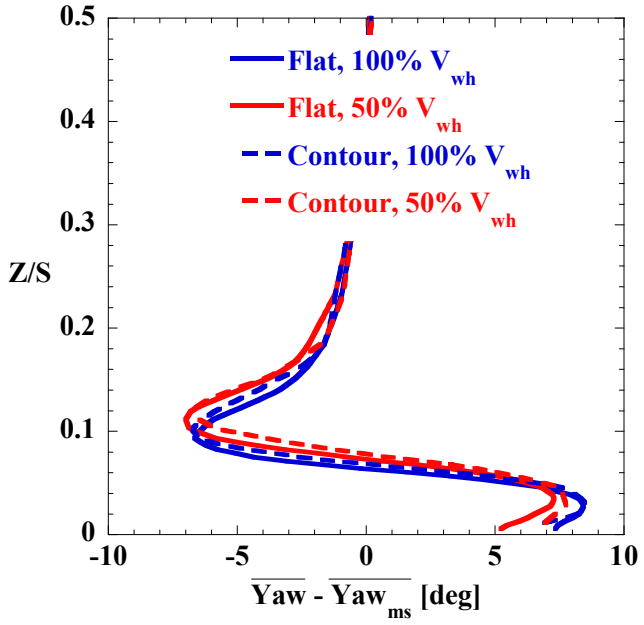

Figure 5.12. Pitchwise-mass-averaged yaw angle deviation for the flat endwall and the contoured endwall without a platform gap.

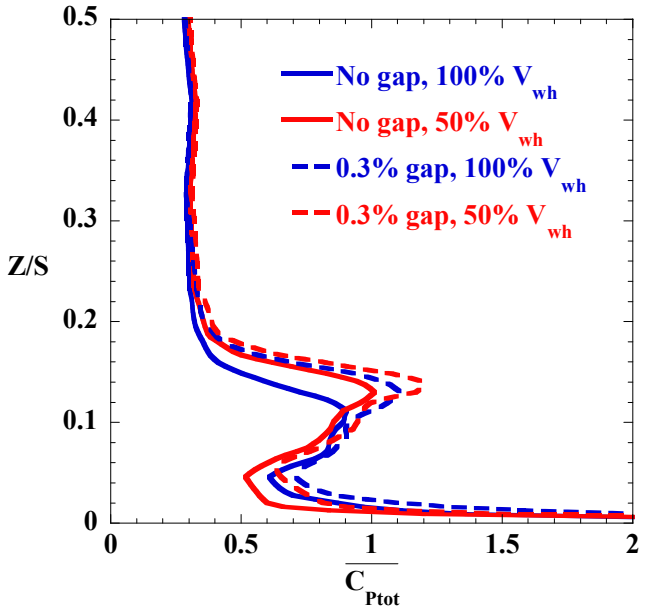

Figure 5.13. Pitchwise-mass-averaged total pressure loss coefficient for a contour with and without a platform gap.

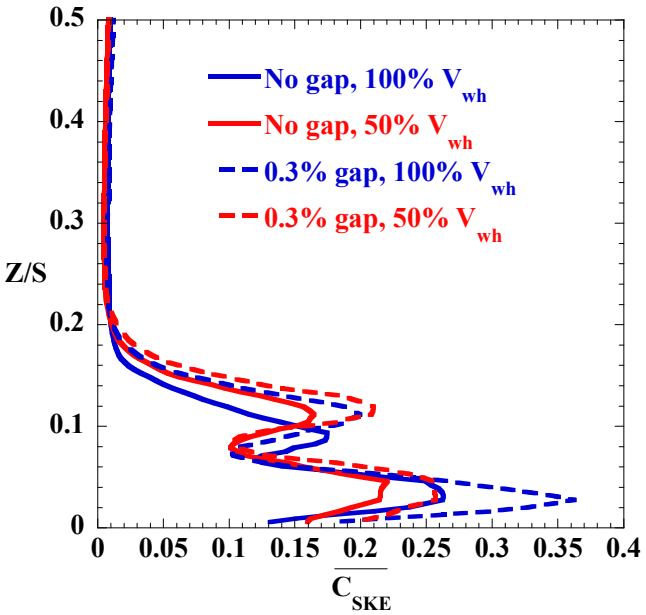

Figure 5.14. Pitchwise-mass-averaged secondary kinetic energy coefficient for the contoured endwall with and without a platform gap.

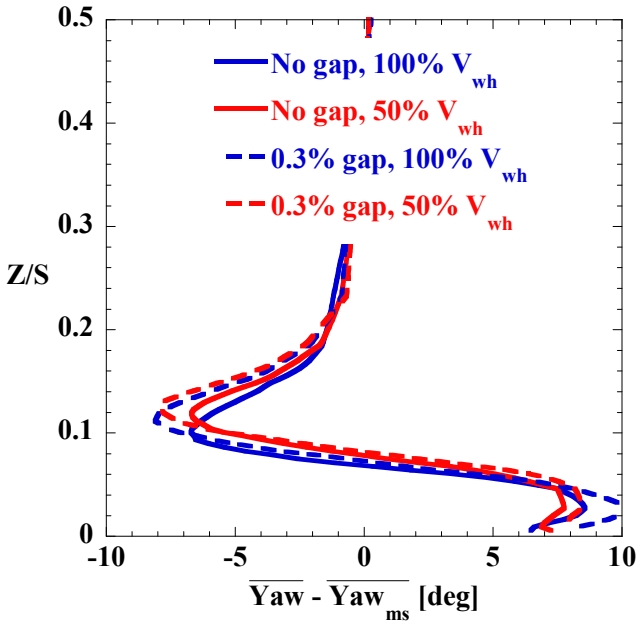

Figure 5.15. Pitchwise-mass-averaged yaw angle deviation for the contoured endwall with and without a platform gap.

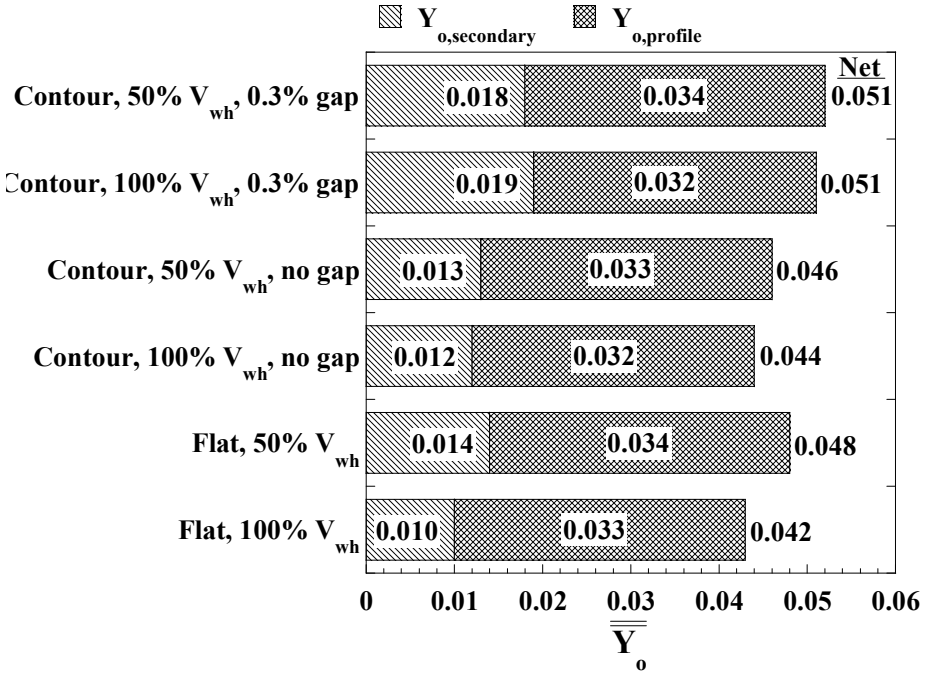

Figure 5.16. Overall mass-averaged results at the measurement plane (X/C_{ax}=1.3), separated into profile and secondary loss contributions.

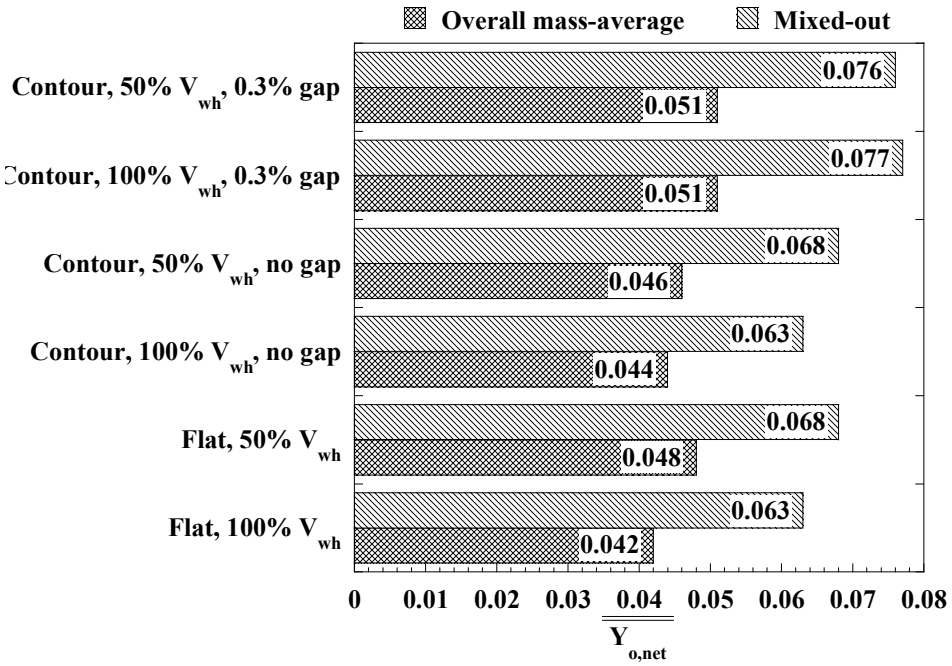

Figure 5.17. Comparison of overall mass-averaged and mixed-out net losses.

Paper 6: Heat Transfer and Film-Cooling for a Turbine Blade with Endwall Leakage Features and Contouring

To be submitted to the *Journal of Turbomachinery**

Abstract

Turbine blade components in an engine are typically designed with gaps between parts due to manufacturing, assembly, and operational considerations. Coolant is provided to these gaps to limit the ingestion of hot combustion gases. The interaction of the gaps, their leakage flows, and the complex vortical flow at the endwall of a turbine blade can significantly impact endwall heat transfer coefficients and the effectiveness of the leakage flow in providing localized cooling. Non-axisymmetric contouring of the endwall has been shown to reduce heat transfer coefficients and improve film coverage, but it is not clear how the contouring and the gap leakage might interact. To understand some of the effects, measurements of endwall heat transfer and film cooling effectiveness were performed in a scaled blade cascade. The endwall consisted of a non-axisymmetric contour in the passage. A rim seal with a cavity, representing the overlap interface between a stator and rotor, was included upstream of the blades. A platform gap through the passage, representing the mating interface between adjacent blades in a wheel, was also modeled. The effects of leakage flow through the platform gap, and vertical misalignment of the blade endwalls that might occur due to differential thermal expansion, were tested in this study. Results indicated that endwall heat transfer coefficients increased with increasing platform gap flow, but net heat flux to the endwall was reduced due to high film cooling effectiveness of the leakage flow. A vertical misalignment that resulted in a forward-facing step at the platform gap slightly increased endwall heat transfer and reduced film cooling effectiveness, although misalignment was a less significant effect than net platform gap flowrate.

*Co-authors: Dr. Karen A. Thole, Mechanical & Nuclear Engineering Department, Penn State
Dr. Atul Kohli, United Technologies--Pratt & Whitney
Dr. Christopher Lehane, United Technologies--Pratt & Whitney

Introduction

The desire to improve turbine engine efficiencies drives designs toward higher turbine inlet temperatures and lower required coolant for hot gas path hardware. Turbine hardware downstream of the combustor is subjected to combustion gas temperatures in excess of the metal melting temperature, and cooling is required to maintain part durability, especially for the highly stressed rotating components. The coolant, generally extracted from the compressor, results in an efficiency penalty since it provides no useful work in the turbine, and thus it is desirable to minimize the amount needed.

Gaps between turbine components are present in an engine due to manufacturing and assembly constraints or the necessity of stationary-rotating component clearances. High-pressure coolant is provided to the gaps to minimize hot gas ingestion into the core of the engine where materials are less able to withstand high temperatures. The stationary-rotating clearance gap between the stator and rotor, referred to as a rim seal in this paper, is often designed as a backward-facing step, where recirculating fluid downstream of the step helps to limit hot gas ingestion. The high pressure coolant supplied to the rim seal can also have a tangential component of velocity relative to the rotor due to the rotational speed of the wheel and the manner of injection of the coolant.

Another gap in the rotor endwall, referred to as a platform gap in this paper, is present between airfoils that are assembled individually on the wheel of a high-pressure turbine blade section. The platform gap between components is a necessary consequence of the manufacturing and assembly process, but also helps to accommodate thermal expansion over the wide range of turbine operating conditions.

As previously mentioned, coolant is designed to leak through these leakage paths to prevent hot gas ingestion, but has the inherent advantage that the fluid can be used to provide cooling coverage for the component. Until fairly recently, however, these leakage paths were mostly neglected in studies of endwall heat transfer and turbine aerodynamic loss. Recent studies outlined in the literature review indicate that the presence of the rim seal and platform gap and their leakage flows can have a significant impact on endwall film-cooling effectiveness and heat transfer.

Non-axisymmetric (three-dimensional) contouring of the endwall has also been recently shown to impact endwall heat transfer coefficients and film cooling. The shape of the contour is designed to reduce the cross-passage pressure gradient and the strength of the vortical secondary flows. This is beneficial for the aerodynamic performance of the turbine, but also has been shown to reduce heat transfer coefficients and improve film cooling coverage relative to flat endwalls. It is not clear, however, how the effects of contouring relate to realistic turbine configurations.

For the work presented here, a realistic blade endwall was studied in a scaled-up cascade. The endwall included non-axisymmetric contouring in the passage. A rim seal, with representative leakage mass flow rates and tangential velocity of the leakage flow, was included upstream of the blade. A platform gap through the passage, also with representative leakage mass flow rates, was modeled. The effect of leakage flow through the platform gap and misalignment of the endwalls, as might occur due to thermal expansion, will be discussed in this paper.

Review of Literature

A range of studies have been presented in the literature concerning the effect of turbine component interface gaps on turbine aerodynamics, heat transfer, and film-cooling. For a gap located upstream of an airfoil, such as between a combustor and a vane, or between a rotor and stator, the interaction of the leakage flow with the vortical flow generated at the endwall-airfoil junction has been shown to have a significant effect on turbine aerodynamics and heat transfer. Piggush and Simon [1] indicated an increase in loss roughly following the increase in momentum flux ratio for leakage flow through an upstream slot simulating the combustor-vane gap. Turbine stage efficiency decreased with increasing stator-rotor leakage flowrate in the study by Reid, et al. [2]. Simulations showed an increase in entropy generation (loss generation) where the leakage flow mixed into the freestream. Popovic and Hodson [3] concluded that blade endwall film cooling increased with leakage mass flow through an upstream rotor rim seal, but at the expense of increased aerodynamic losses. A study by Papa, et al. [4] showed higher endwall heat transfer but more uniform film cooling coverage for a blade endwall with increasing upstream slot blowing ratio.

A platform gap between individual turbine components in a wheel has also been shown to significantly influence aerodynamic loss and endwall heat transfer. Reid, et al. [5] measured a

0.46% drop in turbine efficiency due to the presence of a platform gap, even with no net flow through the gap. The losses were attributed to mixing within the gap, and were shown to be relatively independent of platform gap net flowrate. Film cooling effectiveness coverage was significantly reduced on a vane endwall with a platform gap, relative to a continuous endwall, in a study by Cardwell, et al. [6]. Gap flow temperatures indicated ingestion of coolant into the forward portion of the gap where it mixed with freestream fluid before being ejected near the throat. A study by Piggush and Simon [7] indicated a significant increase in vane endwall heat transfer where the platform gap leakage flow was ejected onto the endwall, compared to a smooth endwall. Lynch and Thole [8] found that ingestion and ejection of flow in the platform gap correlated well with high heat transfer coefficients on the inner channel walls of the platform gap.

Misalignment of engine components, arising from differential thermal stresses or assembly tolerances, results in steps in the flowpath, which have been examined for their effect on aerodynamics and heat transfer. de la Rosa Blanco, et al. [9] concluded that a small backward-facing step located upstream of a blade cascade reduced losses relative to a flat endwall, but a forward-facing step increased losses due to increased interaction between the horseshoe vortex and a pressure side separation bubble. A forward-facing step at the combustor-turbine interface slot increased vane endwall heat transfer relative to an aligned endwall in the study by Piggush and Simon [10]. The increase for the forward-facing step was attributed to acceleration of the boundary layer over the step. A related study with the same vane geometry (Piggush and Simon [11]) concluded that a forward-facing step (as seen by the endwall crossflow) at the platform gap in the passage increased net heat flux to the endwall, but a backward facing step slightly decreased heat flux relative to an aligned endwall. Film cooling measurements by Cardwell, et al. [6] showed that a backward-facing step at the combustor-turbine interface slot dramatically improved coolant coverage downstream of the step relative to an aligned endwall, due to reduced mixing of the coolant with the mainstream gases.

Many of the aforementioned heat transfer and film cooling studies have considered vanes with relatively simple upstream combustor-turbine interface geometries. Only one study (Popovic and Hodson [3]) combined the effects of realistic upstream conditions for a blade, such as a rim seal with a cavity at the stator-rotor interface, leakage flow through the rim seal, and a tangential velocity component in the leakage flow which arises due to the relative motion of the

rotor. No studies have been presented which include realistic turbine gaps and non-axisymmetric endwall contouring. This study builds on the work of Popovic and Hodson [3] by adding a platform gap, and by examining the effects of platform gap leakage flow and misalignment on endwall heat transfer and film cooling.

Experimental Methodology

Heat transfer and film cooling measurements were obtained on the endwall of a large-scale low-speed linear cascade that was matched to engine Reynolds number conditions. Flow through the cascade was provided by a closed-loop wind tunnel shown in Figure 6.1. Some flow was diverted into an upper bypass channel far upstream of the cascade and extracted by a blower so that it could be sent to cascade leakage features. For film cooling studies, heat exchangers in the bypass channel were connected to a 40 kW chiller unit to cool leakage air, and the mainstream was equipped with a 55 kW electric heater bank to heat mainstream air to approximately 46°C, such that a temperature differential of approximately 25°C was achieved. The density ratio of the coolant for those studies was 1.08. For heat transfer studies, the heat exchangers were used to keep the leakage air temperature to within 0.5°C of the mainstream temperature (density ratio of 1.0).

The design and construction of the linear cascade is described in Papers 4 and 5 of this dissertation, and only a short treatment will be given here. The cascade contained six blades based on a high-pressure turbine airfoil geometry, which was also studied by MacIsaac, et al. [12]. Table 6.1 lists the geometric details of the cascade. The blades were constructed using stereolithography, with static pressure taps integrally designed. Measured blade static pressures presented previously were shown to closely match the design conditions (see Paper 5).

A turbulent boundary layer was measured with a laser Doppler velocimeter at $5C_{ax}$ upstream of the cascade, on the bottom endwall. The turbulent boundary layer parameters are listed in Table 6.1. A turbulence grid located $16C_{ax}$ upstream of the center blade of the cascade resulted in a freestream turbulence level of 6% at the boundary layer measurement location.

Upstream of the blades, the platform (endwall) overlap between the stationary vane and rotating blade rows was simulated as shown in Figure 6.2. The blade platform extended $0.57C_{ax}$ upstream of the blade leading edge and $0.27C_{ax}$ below the nominal endwall height, resulting in a cavity in the endwall known as a rim cavity. A smooth curve was used to transition from the

lowered upstream blade platform to the start of the non-axisymmetric endwall contouring in the passage. Although the cascade was designed to simulate a rotor, no part of the test section, including the upstream (stator) platform, moved relative to the blades.

Rim seal flow was simulated by a leakage feature placed upstream of the cascade. In this study, swirled leakage relative to the blade was simulated, such as would occur in an engine when there is a mismatch between the rotor hub speed and the tangential velocity of the leakage flow. As shown in Figure 6.3a, the leakage feature contained internal turning vanes that imparted swirl to the leakage flow, such that its tangential velocity was half of the rotor hub speed (50% V_{wh}) at the nominal net mass flow ratio of 0.75% MFR.

Figure 6.3b depicts the velocity triangle and near-wall resultant velocity vector influenced by rim seal leakage, in the blade's frame of reference. U_{in} is the magnitude of the freestream velocity at the design inlet flow angle of β_{in}, and U_{exit} is the magnitude of the cascade exit velocity at the design exit flow angle of β_{exit}, and V_{wh} is the speed of the rotor at the radius of the hub. Note that in the blade's frame of reference, V_{wh} would be the motion of the stator, although all parts of the test section were fixed in this cascade. It is obvious in Figure 6.3b that the incidence angle of the resultant near-wall velocity is decreased for swirled rim seal leakage, relative to the design inlet angle (β_{in}).

The rim seal leakage mass flow ratio was kept constant at 0.75% MFR for all cases in this study. The average coolant velocity (U_c) through the rim seal was calculated using the measured mass flow through the metering area of the rim seal (A_{rim}):

$$U_c = \frac{\dot{m}_c}{\rho_c A_{rim}} \tag{6.1}$$

The local blowing ratio of M=0.29 and momentum flux ratio of I=0.09 were referenced to the local freestream velocity, which was estimated using Bernoulli's equation with the measured inlet freestream total pressure and measured local static pressure ($P_{s,loc}$) at the rim seal exit:

$$U \approx \sqrt{\frac{2}{\rho_{in}}\left(P_{tot,in} - P_{s,loc}\right)} \tag{6.2}$$

The local blowing ratio (M) and the local momentum flux ratio (I) were defined as:

$$M = \frac{\rho_c U_c}{\rho_{in} U} \tag{6.3}$$

$$I = \frac{\rho_c U_c^2}{\rho_{in} U^2} \tag{6.4}$$

Net mass flow through the rim seal was measured by a laminar flow element and supplied to a plenum mounted below the test section. Static pressure taps were used to check periodicity.

A non-axisymmetric contoured endwall, designed using the methodology described by Praisner, et al. [13], was employed in the passage of the cascade (see Figure 6.4a). Non-axisymmetric contouring began at $0.1C_{ax}$ upstream of the leading edge and merged to the nominal endwall level at the exit of the blade passage. Maximum and minimum heights of the contouring, relative to a nominal flat wall with the same upstream geometry (see Paper 5), were $+0.04C_{ax}$ near the leading edge suction side, and $-0.04C_{ax}$ near the center of the passage, respectively. Note that the endwall contour in this study differs from typical designs in that there is a hill near the leading edge suction side, as opposed to the depression found in most other contour designs (Harvey, et al. [14], Praisner, et al. [13]). For this endwall, inclusion of the upstream rim seal and its leakage flow appears to play a significant role in the generation of the optimal endwall contour shape. The contour in this study was designed for nominal rim seal leakage conditions of 0.75% MFR, with a swirl velocity of 50% V_{wh}. The platform gap, however, was not included in the optimization.

The effect of a gap between adjacent blade platforms was considered for all cases in this study. The geometry of the platform gap is depicted in Figure 6.4, and gaps were located in every passage except between blades 1 and 2, where the gap would pass below the outer airfoil tailboard. A thin strip seal was attached to the underside of the platform gap (see Figure 6.4b-c) to simulate the effect of a similar component in the engine which limits leakage flow into and out of the gap. Platform gap leakage flow was isolated from the rim seal leakage flow to enable independent control. Net leakage mass flow was supplied to individual plenums located under the test section (see Figure 6.2). Total mass flow supplied to all four gap plenums was measured with a laminar flow element. Valves were used to split the flow evenly among the four plenums, as determined by equalizing the pressures in each of the plenums. Net gap leakage flowrates are reported in this paper as a percentage of a single blade passage mass flow rate. Net flowrates

ranged from 0% to 0.6%, where the 0% net flow was achieved by closing a valve in the supply line for each gap plenum. Note that mainstream flow could still be ingested into the forward portion of the gap and ejected further downstream, but no net flow was introduced.

An estimation of the gap leakage velocities along the gap length was performed using the measured plenum pressure and net gap mass flow. At a given position along the gap, a local inviscid leakage velocity ($V_{gap,inv}$) was calculated using the measured platform gap plenum total pressure ($P_{tot,c}$) and the local freestream static pressure ($P_{s,loc}$) obtained from a 2-D simulation of the cascade:

$$V_{gap,inv} = \sqrt{\frac{2}{\rho_c}\left(P_{tot,c} - P_{s,loc}\right)} \tag{6.5}$$

The local inviscid leakage velocities were averaged over the entire length of the gap and the average ($\overline{V}_{gap,inv}$) was used in the formula for net mass flow from the gap:

$$\dot{m}_{gap} = C_D \dot{m}_{ideal} = C_D\left(\rho_c \overline{V}_{gap,inv} A_{gap}\right) \tag{6.6}$$

where C_D is the global discharge coefficient relating the inviscid mass flow to the actual net mass flow. Since the net mass flow ($\dot{m}_{gap}$) was measured, C_D was iterated until Eq. 6.6 was satisfied. Values for global C_D were approximately 0.24 for 0.3% and 0.6% gap MFR. Note that the global C_D for the platform does not generally conform to a standard interpretation of a discharge coefficient, since the gap can ingest and eject flow. The normalized gap velocity plotted in Figure 6.5 was obtained by multiplying the local inviscid velocity by the global discharge coefficient of 0.24 found through the iteration process:

$$\frac{V_{gap}}{U_{in}} = \frac{C_D V_{gap,inv}}{U_{in}} \tag{6.7}$$

Gap leakage velocities for the three net leakage flowrates tested in this study are shown in Figure 6.5. For 0% gap MFR, gap leakage velocities are negative up to $x_{gap}/L=0.42$, implying ingestion of the mainstream gases into the gap plenum. Further along the gap, velocities are positive where the leakage flow is ejected out of the gap due to low freestream static pressure. As the net MFR is increased to 0.3%, ingestion is eliminated over the entire gap length, but the ejection velocity of the leakage flow is small, especially in the forward portion of the gap. Note that this analysis does not account for unsteady effects or for a difference between the endwall static pressure and the inviscid freestream static pressure. For the highest leakage MFR of 0.6%,

ejection velocities are nearly uniform over the entire gap length and are on the order of the cascade inlet velocity.

The effect of vertical misalignment of adjacent endwalls was tested in the cascade for the platforms attached to blades 3 and 4 (center blades). Figure 6.6 shows the alignment modes considered in this study, where the magnitude of misalignment was $0.03C_{ax}$ (1% of the blade span). The aligned mode (Figure 6.6a) represented no difference in height between any of the blade platforms, or between the platforms and the upstream endwall.

The misalignment was achieved by lowering the center blade platforms by $0.03C_{ax}$ (Figure 6.6b). This resulted in a backward-facing step for flow entering the blade cascade, as well as for secondary flow sweeping from the pressure to suction side of the passage between blades 2 and 3. Note that the secondary flow in the passage between blades 4 and 5 experiences a forward-facing step for this misalignment. As indicated in Figure 6.6b, the seal strips underneath the platform gaps were tilted to simulate the effect of centrifugal forces in the rotor that would force the strip to conform to the upper wall of the platform gap cavity.

For the film cooling effectiveness studies, supplemental film cooling holes ($d/C_{ax}=0.020$) were drilled in the endwall around the platform gap. Figure 6.7 depicts the holes, with the injection directions shown by the blue arrows. Holes were grouped by their location: six holes near the pressure side of the blade platform are designated as film cooling group #1 (FC1), two holes by the suction side trailing edge are designated as FC2, and four holes by the suction side of the blade platform are designated as FC3. Table 6.2 lists the L/d ratios and local surface angles of the holes.

Each group of holes had its own separate plenum for independent control, and four endwalls were constructed for film cooling tests; thus, there were four FC1 plenums, four FC2 plenums, and three FC3 plenums underneath the cascade (no film cooling was supplied on the suction side of blade 2's platform). In a manner similar to the platform gap flow supply, the total mass flow supplied to the four FC1 plenums was measured with a laminar flow element and then split evenly by equalizing the pressures in each of the FC1 plenums. The same methodology was employed for FC2 and FC3 plenum flows.

The mass flow ratios and respective blowing parameters for each of the film cooling groups are listed in Table 6.3. The average coolant velocity for a given film cooling group

(necessary to determine blowing and momentum flux ratios) was determined by the total mass flow divided by the sum of the hole metering areas:

$$U_c = \frac{\dot{m}_c}{\rho_c \sum_{i=1}^{N} A_h} \tag{6.8}$$

The average local freestream velocity was determined by using the average of the static pressures at each of the hole exit locations, as determined from a 2-D CFD simulation of the cascade, in Bernoulli's equation:

$$U \approx \sqrt{\frac{2}{\rho_{in}} \left(P_{tot,in} - \frac{\sum_{i=1}^{N} P_{s,loc,i}}{N} \right)} \tag{6.9}$$

Heat Transfer Measurements

Infrared thermography was used to determine heat transfer coefficients by capturing spatially-resolved surface temperatures on a uniform heat flux surface (heater) attached to the endwall. Heater design and attachment to the non-axisymmetric contour was based on the methodology developed by Lynch, et al. [15]. Total heater thickness, including the inconel circuit and the encapsulating kapton, was 75 μm. A 37 μm layer of copper was attached to the flow surface of the heater to smooth out heat flux between the circuit gaps (Kang, et al. [16]). Flat black paint was applied to the copper to increase emissivity for infrared measurements, and type-E thermocouples were thermally bonded to the underside of the heater for infrared image calibration.

A 3 mm thick stereolithography plate (k≈0.2 W/m-K) was constructed in the shape of the contoured endwall shown in Figure 6.4a. Polyurethane foam (k≈0.032 W/m-K) was molded to the underside of the plate to minimize conduction losses for the heat transfer experiments. The minimum foam thickness was 20 mm at the upstream edge of the blade endwall. The heater was bonded to the stereolithography plate via a vacuum-bag process (Lynch, et al. [15]).

Heat flux was calculated by measuring the circuit voltage and current and dividing by the heater area, where current was measured by the voltage drop across a precision resistor in series with the heater. Conductive and radiative losses were subtracted from the total heat flux. Conductive losses were estimated locally by a one-dimensional conduction analysis to be less than 1.5% of the total heat flux. Radiative losses were also estimated locally to be less than 15%,

assuming that the surroundings behaved as a blackbody at the freestream temperature of 295 K. Local loss corrections were highest in regions of high endwall temperatures (~315 K).

Infrared camera images were obtained at several locations throughout the cascade to provide a complete map of the endwall heat transfer. At each location, five images were captured to reduce measurement uncertainty. The averaged result was calibrated by adjusting surface emissivity and background temperature until the heater top surface temperature matched measurements from the underside-mounted thermocouples. A conduction bias of 0.8°C between the top surface and underside-mounted thermocouples was accounted for in the calibration. Typical emissivity and background temperature for the calibrated images was 0.96 and 16°C, respectively, which compared well to published emissivity for black paint (~0.96) and the cascade freestream temperature of 21°C. Calibrated images generally agreed to within 0.5°C of the thermocouple measurements. The camera field of view was 320 x 240 pixels, with a resolution of 1.4 pixels/mm. No correction was performed for perspective distortion of the images at the upstream cavity or along the contoured endwall since the small variation in camera standoff distance did not affect its focus.

The reference temperature in the definition of the heat transfer coefficient (T_{in}) was determined as the average of the measured freestream temperature, the rim seal plenum temperature, and the gap supply line temperature immediately upstream of the gap plenums. Variation among the averaged temperatures was kept to within 0.5°C. The ingestion mechanism of the platform gap (Cardwell, et al. [6]) caused the gap plenum temperatures to be approximately 1°C higher than the reference temperature for the nominal gap leakage flowrate of 0.3% MFR, which was why gap plenum temperatures were not used in determining the reference temperature. Since the lowest endwall temperature was at least 10°C above the reference temperature, the slightly increased temperature of ejected gap flow was calculated to have a minimal effect (nearly the same order as the experimental uncertainty) on the measured heat transfer coefficient.

Uncertainty was estimated using the partial derivative method (Moffat [17]). The largest source of error was the measurement of surface temperature with the infrared camera. Bias and precision uncertainties for that parameter were 0.8°C and 0.3°C, respectively. Total uncertainty in the heat transfer coefficient, based on a 95% confidence interval, was 5.0% at a value of Nu=410.

Adiabatic Effectiveness Measurements

Infrared thermography was also used to obtain film cooling effectiveness measurements by capturing spatially-resolved surface temperatures on an adiabatic (foam) endwall. A mold was used to cast polyurethane foam into the shape of the bottom endwall of the cascade (Figure 6.4b). The flow surface of the foam was painted flat black for high emissivity, and type-E thermocouples for infrared image calibration were installed flush with the endwall surface.

Infrared images were obtained in the same manner as for the heat transfer measurements. Calibration with the embedded endwall thermocouples yielded an average emissivity of 0.94 and an average background temperature of 47°C (nominal inlet freestream temperature was T_{in}=47°C). The calibrated images were assembled into a temperature map and converted to adiabatic effectiveness using the measured freestream temperature and a coolant reference temperature.

The coolant reference temperature (T_c) in the definition of adiabatic effectiveness was the average of the temperatures in the rim seal plenum and the film cooling plenums, as well as the temperature of the flow in the supply line leading to the platform gap plenums. Variation among the averaged coolant temperatures was less than 0.5°C. The ingestion mechanism of the platform gap resulted in gap plenum temperatures that were about 1.5°C above the supply line temperature for the nominal gap net flowrate of 0.3% MFR, which was why the gap plenum temperatures were not used to determine the reference temperature.

Uncertainty in the effectiveness measurements was estimated in the same manner as for the heat transfer measurements. The largest contribution to uncertainty was the surface temperature measured with the IR camera, which had an estimated bias uncertainty of 0.6°C and a precision uncertainty (95% confidence interval) of 0.3°C. Total uncertainty in effectiveness was $\partial\eta=\pm0.04$ at a value of $\eta=0.25$.

Results and Discussion for Aligned Endwalls

Measurements of endwall heat transfer and film cooling effectiveness are first compared to the endwall flow pattern visualized by oil flow. The effect of increasing the platform gap leakage flow is then discussed, followed by a discussion of the effect of platform misalignment.

Comparison of Oil Flow Visualization, Heat Transfer, and Film Effectiveness

Oil flow visualization was performed to obtain endwall flow patterns caused by secondary flows. The visualization was done with nominal leakage flowrates of 0.75% MFR for the rim seal and 0.3% MFR for the platform gap. The endwalls were painted white, and mixture of black paint, motor oil, and kerosene was uniformly applied. Images of the resulting streak pattern were captured after the pattern reached a steady-state condition (approximately two hours). Streaklines were drawn over the top of the image to enhance the flow pattern, as shown in Figure 6.8a. Dashed lines indicate the paths of the vortical secondary flow structures. No streaklines were drawn on the upstream platform, since a pattern was not discernable to low-velocity separated flow in the rim cavity. Oil flow visualization by Abo El Ella, et al. [18] for a similar rim cavity shape also indicates a recirculation zone in that region.

Major features identified in the oil flow pattern in Figure 6.8a are similar to those in classical secondary flow descriptions, including a saddle point region upstream of the blade where the incoming boundary layer separates from the endwall to create the horseshoe vortex. The legs of the horseshoe vortex wrap around the blade, and the pressure-side leg merges with the passage vortex. The impingement of the passage vortex on the blade suction side generates a corner vortex, which remains near the blade-endwall junction. For the non-axisymmetric endwall contour in this study, the bulge near the suction side leading edge (see Figure 6.4a) displaces the suction side horseshoe vortex away from the blade. It eventually turns sharply toward the blade and impinges on the blade suction side. In the passage near the blade pressure side, the strong cross-passage pressure gradient results in a high level of turning toward the adjacent suction side for the new endwall boundary layer downstream of the horseshoe vortex, relative to the inviscid flow direction.

Previous work presented in Paper 4 indicated that the addition of rim seal leakage flow had a small effect on the oil flow pattern and endwall heat transfer, mostly around the forward portion of the passage. Swirled rim seal leakage flow tended to shift the saddle point in the direction of swirl, compared to unswirled leakage, but did not have a significant effect on the endwall oil flow pattern or overall heat transfer for the nominal leakage MFR of 0.75%.

The effect of the platform gap is not immediately obvious in the oil flow pattern, but some observations are made. Streaklines upstream of the saddle point appear to be diverted from crossing over the gap, suggesting a small amount of leakage is emanating from the gap and

blocking near-wall flow. Estimated gap leakage velocities in Figure 6.5 also indicate ejection over the entire gap length for the nominal gap MFR of 0.3%. Further downstream in the throat region, a small pool of oil and paint collects on the suction side platform near the gap (see Figure 6.8a). The pool appears to be located in a region between the passage vortex trajectory and the wake from the trailing edge of the blade. Figure 6.5 shows a slight dip in the ejection velocity around $x_{gap}/L=0.9$, which corresponds to the location of the pool. Lynch and Thole [19] describe a vortical structure that is generated at the throat as the gap leakage is ejected into the mainstream flow. The vortical structure occurs near the peak in ejection velocity around $x_{gap}/L=0.85$ in Figure 6.5, and the sweeping action of the vortical structure brings oil toward the pool.

Figure 6.8b shows contours of endwall heat transfer with the streaklines from Figure 6.8a overlaid to enable interpretation of secondary flow effects. The white line through the passage indicates the location of the platform gap, and the arrow on the left side of the figure indicates the direction of rim seal swirl. The rim cavity upstream of the blade experiences relatively low heat transfer due to the low-velocity separated flow present in that region. Flow approaching the saddle point crosses over the platform gap, which disturbs the boundary layer and increases heat transfer on the downstream side of the gap, right around the saddle point. Around the leading edge, heat transfer levels are high due to the downwash of the horseshoe vortex legs at the airfoil-endwall junction, particularly along the suction side.

Along the pressure side further into the passage, heat transfer levels are relatively low in the new endwall boundary layer developing downstream of the horseshoe vortex. Streamwise acceleration toward the throat of the passage causes the heat transfer coefficient to increase. As the endwall boundary layer crosses over the platform gap, heat transfer rises to very high levels on the downstream side of the gap. A combination of factors contributes to the significant heat transfer increase across the gap. The endwall boundary layer is tripped by the physical presence of the gap; however, Figure 6.5 also indicates that fluid in the gap is ejected in the low-pressure region around the throat, which results in high turbulence levels and the generation of a vortical structure described by Lynch and Thole [19]. Heat transfer downstream of the gap decreases as the thermal boundary layer re-develops, but starts to increase slightly near the suction side trailing edge as the corner vortex grows.

Film cooling effectiveness contours are shown in Figure 6.8c, with the oil flow streaklines overlaid to enable correlation with secondary flow features. Areas with high effectiveness values indicate where the coolant lowers the adiabatic wall temperature and reduces the driving potential for heat transfer to the endwall. The rim seal leakage upstream of the blade provides some cooling on the platform, although the secondary flows severely constrain the extent of coverage. Most of the rim seal coolant is channeled toward the saddle point and separates from the endwall, providing little coverage around the leading edge or the pressure side of the passage. Any rim seal leakage that might be ingested into the forward portion of the platform gap is convected along the gap and ejected near the throat, which results in a region of high effectiveness on the suction side platform. Net flow introduced into the gap plenum also preferentially leaks out in the throat region, since the endwall static pressure is lowest there. A streak of high effectiveness persists along the blade suction side in Figure 6.8c, which is attributed to the vortical structure mentioned earlier. Note that the four film cooling holes located on the suction side platform appear redundant in terms of providing coolant coverage; however, in the engine the flow through those holes also acts as a heat sink helping to remove heat from the platform metal.

Effect of Platform Gap Leakage Flow

Contours of endwall heat transfer are shown in Figure 6.9 for increasing net gap flowrates. The nominal rim seal leakage flowrate of 0.75% MFR with swirl (50% V_{wh}) was maintained for all cases, and thus heat transfer upstream of the blades is expected to be the same. Around the location of the saddle point, heat transfer levels do not change significantly between 0% and 0.3% gap MFR, and increase slightly between 0.3% and 0.6% MFR as the gap ejection velocity increases (refer to Figure 6.5). Heat transfer along the pressure side of the passage in Figure 6.9 is unchanged by increasing gap flow since secondary flows prevent it from penetrating to that region. Around the throat on the suction side blade platform, however, heat transfer levels rise noticeably with increasing gap MFR. Increasing the amount of flow ejected results in a stronger vortical structure and increased turbulence.

Figure 6.10 shows endwall Nusselt numbers extracted from Figure 6.9 along the path of an inviscid streamline passing through the center of the passage (0.50P) at the inlet plane. The abscissa of the plot is the X-coordinate along the streamline normalized by the blade axial chord, such that $X/C_{ax}=0$ corresponds to the inlet plane of the cascade and $X/C_{ax}=1$ corresponds to the

exit plane. The vertical bars are the regions where the streamline passes over the platform gap. For a given location along the streamline path, heat transfer values from each of the three blade passages were averaged to obtain a representative value for that streamwise location.

Heat transfer levels upstream of the passage are the same for the range of platform gap flowrates in Figure 6.10 due to similar rim seal conditions, as described earlier. Heat transfer increases along the streamline path approaching the first gap crossing (X/C_{ax}=-0.18), due to reattachment of the recirculating rim cavity flow on the upstream endwall. Downstream of the first gap crossing, Nusselt values are slightly higher for 0.6% gap MFR compared to the other leakage MFR's due to the larger gap ejection velocity. Heat transfer levels decrease along the pressure side up to X/C_{ax}=0.5, and then begin to increase again as the flow accelerates toward the throat. After the second gap crossing at X/C_{ax}=0.85, heat transfer coefficients for 0% gap MFR rise to levels nearly four times higher than the value on the upstream blade platform (X/C_{ax}=-0.4). Increasing the gap MFR to 0.6% results in a 50% increase immediately downstream of the gap relative to 0% gap MFR, and a 500% increase over the heat transfer levels on the upstream blade platform. Certainly this is undesirable for part durability due to the potential for high heat loads and large temperature gradients in the component metal. Heat transfer levels decay rapidly further along the streamline path, reaching nearly the same level regardless of gap MFR at the exit plane (X/C_{ax}=1).

To visualize the region of influence of the gap leakage, contours of heat transfer augmentation were calculated by taking the ratio of heat transfer with gap MFR to heat transfer with no net gap MFR (0% gap). Figure 6.11 shows the contours of heat transfer augmentation for 0.3% and 0.6% gap MFR, where values above 1.0 indicate an increase in heat transfer relative to the 0% gap MFR case. Over the majority of the upstream half of the passage, increasing the gap MFR does not significantly increase or decrease endwall heat transfer. Along the suction side platform around the throat, however, heat transfer augmentation levels are approximately 1.3-1.4 for 0.3% gap MFR, and 1.4-1.5 for 0.6% gap MFR. The highest heat transfer augmentation generally occurs immediately downstream of the throat since leakage flow preferentially ejects from the gap at that location, but heat transfer is augmented on the suction side blade platform along nearly the entire downstream half of the platform gap's length through the passage.

Film cooling effectiveness contours in Figure 6.12 give an indication of the effectiveness of gap leakage in reducing the adiabatic wall temperature. For no net gap flow (0% MFR),

Figure 6.12a indicates that cooling due to the rim seal leakage is ingested into the forward portion of the gap, providing very little coverage over a significant portion of the endwall. As the ingested coolant is convected along the gap, its temperature increases due to mixing with the hot mainstream gases. The ingested flow is ejected out of the gap at the throat and provides some cooling to the suction side platform, although a good portion of the cooling also comes from the four film cooling holes in that region.

As the gap net MFR is increased to 0.3% (Figure 6.12b), the gap ejects coolant over its entire length, which is reflected in the higher effectiveness values around the gap. Cooling effectiveness is also significantly increased on the suction side platform around the throat since the net outflow limits mixing of the coolant with the hot mainstream gas before it exits onto the blade platform. Cooling effectiveness levels decay rapidly downstream of the gap due to high levels of turbulence and mixing with the mainstream. From 0.3% MFR (Figure 6.12b) to 0.6% MFR (Figure 6.12c), there does not appear to be a significant difference in cooling effectiveness for the forward portion of the passage or immediately downstream of the throat.

Figure 6.13 presents cooling effectiveness values along the inviscid streamline path for the three gap flow cases. Effectiveness on the upstream platform is high due to the rim seal leakage flow, but decays as the streamline progresses toward the platform gap. Immediately downstream of the first platform gap crossing (X/C_{ax}=-0.18), the 0.3% and 0.6% gap MFR cases indicate higher effectiveness levels than the 0% MFR case due to ejected gap flow. Cooling effectiveness decays along the streamline into the passage for all gap MFR's due to the sweeping effect of the secondary flows that prevents coolant from penetrating toward the pressure side of the platform; however, cooling persists farther along the streamline path for 0.6% gap MFR, compared to 0.3% or 0%. The spike in effectiveness at X/C_{ax}=0.7 is where the streamline crosses a film cooling hole on the pressure side platform. Downstream of the second gap crossing (X/C_{ax}=0.85), a net gap MFR of 0.3% causes higher effectiveness levels on the blade platform relative to 0% gap MFR, due to both increased coolant mass flow and reduced mixing within the platform gap. Increasing the gap MFR to 0.6% does not appear to significantly improve cooling effectiveness downstream of the second gap crossing relative to 0.3%, however; effectiveness levels are already high and introducing more coolant is unnecessary.

Figure 6.14 shows contours of net heat flux reduction (NHFR) for 0.3% and 0.6% gap MFR, where net heat flux reduction (Sen, et al. [20]) is defined as:

$$NHFR = 1 - \frac{h}{h_{0\%}}(1 - \eta\theta) \tag{6.10}$$

The heat transfer coefficient ratio with gap flow relative to 0% gap MFR ($h/h_{0\%}$) was presented in Figure 6.11, and the effectiveness (η) was presented in Figure 6.12. Note that the heat transfer coefficient measurements were performed without film cooling holes. Our analysis for NHFR assumed that the heat transfer coefficient augmentation for the film cooling holes was 1.0; measurements by Sen, et al. [20] and Baldauf, et al. [21] for moderate blowing ratios indicated that heat transfer augmentation for circular film cooling holes was generally below 1.1, so our assumption was deemed reasonable. The non-dimensional metal temperature (θ) was estimated to be a constant value of 1.6 per the recommendations of Sen, et al. [20]. Net heat flux reduction values less than 0 are undesirable, since they indicate where the cooling scheme results in higher heat flux to the part than the uncooled scheme. This would occur if the heat transfer coefficient augmentation increases without a significant increase in cooling effectiveness. In contrast, NHFR values greater than 0 indicate a benefit of the cooling with regards to heat flux experienced by the part.

Net heat flux reduction for 0.3% gap MFR is shown in Figure 6.14a. The contours are similar to the results for film cooling effectiveness (Figure 6.12b), especially on the upstream half of the platform, since the heat transfer augmentation is nominally equal to one there. Despite a significant increase in heat transfer augmentation on the suction side platform (see Figure 6.11a), the high effectiveness levels of the ejected platform gap flow result in high net heat flux reduction values and reduced heat flux to the metal, relative to the 0% gap MFR case. The contours in Figure 6.14b for 0.6% gap MFR closely resemble the results for 0.3% gap MFR, indicating that an increase in heat transfer coefficients due to higher gap MFR is offset by increased cooling.

The overall effect of increasing gap leakage flow was determined by performing an area-weighted average of the endwall heat transfer and film cooling effectiveness results over the entire platform. Figure 6.15 shows the percent increase in area-averaged Nusselt number and area-averaged film effectiveness for the two net gap flowrates, relative to 0% gap MFR. Also included in the figure is the area-weighted average NHFR. The inset in the figure indicates the averaging area. Platform averages for each of the three platforms were then averaged to get an overall result. At the nominal gap MFR of 0.3%, area-averaged endwall heat transfer increased

by 6% but film effectiveness increased by 17% relative to 0% gap MFR, suggesting that the additional cooling massflow could reduce the overall heat load on the part. In fact, the area-averaged NHFR in Figure 6.15 was 0.33, indicating a reduction in heat flux to the endwall for the nominal gap MFR case.

For the higher gap MFR of 0.6%, heat transfer increased by 8% but overall cooling increased by 27%, relative to the 0% gap MFR case. Most of the additional cooling benefit for 0.6% gap MFR versus 0.3% gap MFR is probably due to higher effectiveness around the upstream portion of the platform gap (see Figure 6.13). The average NHFR for 0.6% gap MFR was 0.35, which is only slightly higher than for 0.3% gap MFR. For a turbine designer desiring to conserve coolant massflow without sacrificing part durability, there appears to be no significant benefit in increasing the platform gap net massflow above 0.3%.

Results and Discussion for Misaligned Endwalls

The effect of vertical misalignment of the blade platforms on the endwall heat transfer is shown in Figure 6.16. Recall that the platforms connected to blades 3 and 4 were vertically misaligned by $-0.03C_{ax}$ relative to the adjacent platforms. The misaligned platforms are designated in Figure 6.16b as "Down" to indicate that they were lowered. The white arrows in Figure 6.16b indicate the direction of flow at the throat and the step condition that the flow encounters is labeled on the side of that figure. Figure 6.16c-f contains close-up views of the endwall misalignment regions, where Figure 6.16c and d are comparisons of the aligned and forward-facing step region, respectively, and Figure 6.16e and f are comparisons of the aligned and backward-facing step region.

Comparison of the overall endwall heat transfer for the aligned case (Figure 6.16a) to the misaligned case (Figure 6.16b) indicates that misalignment does not have a significant impact on the global heat transfer pattern. The presence of the gap and leakage flow ejected from it plays a larger role in disrupting the endwall boundary layer than a misalignment.

Examination of the close-up views, however, indicates that misalignment has a slight effect on local heat transfer around the gap. In the close-up view of the forward-facing step region in Figure 6.16d, heat transfer levels on the suction side platform are slightly higher immediately downstream of the gap relative to the aligned endwall (Figure 6.16c). The forward-facing step misalignment acts to trip the crossflow boundary layer particularly in locations where

the gap ejection velocity is low, such as around the middle of the gap's length through the passage. The backward-facing misalignment (Figure 6.16f), however, reduces local heat transfer levels on the suction side platform immediately downstream of the gap relative to the aligned endwall (Figure 6.16e). In this case, the backward-facing step results in a small low-velocity recirculation region downstream of the step that results in low heat transfer levels, similar to the results of Vogel and Eaton [22] downstream of a two-dimensional backward-facing step.

Figure 6.17 shows contours of endwall film cooling effectiveness for the aligned and misaligned cases, with close-ups of the forward-facing step region (Figure 6.17c and d) and the backward-facing step region (Figure 6.17e and f). The downward-misaligned platforms are indicated in the figures, and the direction of endwall crossflow across a misalignment step is indicated by the black arrows in Figure 6.17b. In contrast to the heat transfer results discussed earlier, misalignment does appear to affect a large region of the endwall downstream of the step. In Figure 6.17b, the suction-side platform of blade 3 experiences higher effectiveness levels downstream of the backward-facing step that persist along most of the suction side-endwall junction, compared to the aligned endwall (Figure 6.17a). Cardwell, et al. [6] and Piggush and Simon [23] found a similar trend of improved cooling for a backward-facing step in nozzle guide vane cascades.

The film-cooling jets on the suction side of the platform (FC3) in the close-up images in Figure 6.17c-f help to illustrate the effects of backward- and forward-facing steps on the local effectiveness. For the backward-facing step in Figure 6.17f, the film cooling jets on the suction side platform are directed toward the platform gap (in the opposite direction to the crossflow) due to the recirculation region immediately downstream of the backward-facing step. Coolant from the platform gap and the suction side platform holes is more evenly dispersed over the suction side platform when compared to the aligned case in Figure 6.17e, although effectiveness levels are reduced due to increased mixing with the freestream.

The forward-facing step misalignment also reduces effectiveness levels on the suction side platform as seen in Figure 6.17d. For this misalignment configuration, platform gap cooling is lifted off the endwall as the crossflow separates over the forward-facing step, which reduces the effectiveness immediately downstream of the gap. The separated coolant does result in slightly higher effectiveness further downstream relative to the aligned endwall (Figure 6.17e) as it mixes with the mainstream flow.

Area-averaged increase in heat transfer or effectiveness due to misalignment is shown in Figure 6.18. The inset in the figure shows the averaging area consisting of the aft portion of the suction side platform, which experiences the highest heat transfer levels. Percent increase in heat transfer or cooling effectiveness is indicated for each of the misalignment configurations. Overall, the effect of misalignment is small, especially when compared to the effect of increasing platform gap MFR (Figure 6.15). The backward-facing step reduces area-averaged heat transfer on the suction side platform, but also reduces average effectiveness due to mixing of the platform gap leakage flow in the recirculation region downstream of the step. The forward-facing step appears to be undesirable for two reasons: it increases average heat transfer and reduces average cooling effectiveness on the suction side platform relative to an aligned endwall.

Conclusions

Endwall heat transfer and film cooling effectiveness measurements were presented for a turbine blade with a realistic platform geometry that included an upstream rim seal cavity, three-dimensional non-axisymmetric endwall contouring, and a platform gap between adjacent blade endwalls. Leakage flows at representative engine mass flow rates were provided at the upstream rim seal and through the platform gap. The effect of vertical misalignment of individual blade platforms was also investigated.

Oil flow visualization revealed the features of secondary flow influenced by the upstream rim cavity, contoured endwall, and platform gap. Low-velocity recirculating flow was present in the upstream rim cavity. The endwall contour elevation around the suction side leading edge appeared to displace the suction side horseshoe vortex away from the airfoil-endwall junction. The sweeping action of a vortex generated by the platform gap leakage flow resulted in a pool of oil near the throat of the passage.

The oil flow visualization patterns compared well to the measured endwall heat transfer, with the effect of the horseshoe vortex legs indicated by high heat transfer levels around the leading edge. Boundary layer disturbance due to the platform gap and leakage flow emanating from it resulted in very high heat transfer levels downstream of the gap. Endwall film effectiveness coverage was limited by the horseshoe vortex, although leakage from the platform gap provided cooling in the throat region where heat transfer levels were high.

Increasing the platform gap leakage flowrate resulted in significantly higher heat transfer levels on the suction side platform due to increased strength of the vortical flow feature caused by the gap exit flow. Increased gap flow also resulted in more coolant present near the endwall, however, as film cooling effectiveness levels also increased around the platform gap. For the highest gap net flowrate of 0.6% MFR, platform area-averaged heat transfer increased by 8%, but effectiveness increased by 27%, relative to a gap without net leakage flow. Net heat flux to the endwall was reduced by platform gap leakage, but was not significantly reduced for gap flowrates above 0.3% MFR.

Vertical misalignment of the endwall that resulted in a backward-facing step for the passage crossflow slightly decreased endwall heat transfer and film effectiveness downstream of the step, relative to an aligned endwall. A small recirculation region downstream of the step reduced endwall heat transfer but increased the mixing of the coolant with the mainstream flow. Vertical misalignment that resulted in a forward-facing step for the crossflow slightly increased heat transfer and decreased film cooling effectiveness downstream of the step due to enhanced flow separation relative to an aligned endwall. Area-averaged results indicated that misalignment effects were less significant than platform gap net leakage flow effects.

Although the effect of the non-axisymmetric contour on the endwall heat transfer or film cooling was not directly tested, previous work in this dissertation suggests that the presence of the rim cavity and platform gap play a dominant role in the endwall flow pattern. The contour studied here may not significantly affect the endwall heat transfer or film cooling, compared to the effect of the leakage features. Further work in this area is necessary.

Acknowledgments

We would like to thank United Technologies—Pratt & Whitney for their support of this work, and acknowledge the assistance of Scott Fishbone in the construction of the test section.

Nomenclature

A_{gap}	metering area (flow area) of gap
A_h	metering area of film cooling hole
A_{rim}	metering area of rim seal leakage flow
C	true chord of blade

C_{ax}	axial chord of blade
C_D	discharge coefficient, $C_D = \dot{m}_{c,actual} / \dot{m}_{c,ideal}$
d	diameter of film cooling hole
h	heat transfer coefficient, $h = q''_w / (T_w - T_{in})$
H	boundary layer shape factor
HS	horseshoe vortex
I	momentum flux ratio based on local conditions, see Eq. (6.4)
k	thermal conductivity
L	length of film cooling hole, or length of platform gap through passage
$\dot{m}$	mass flow rate
M	blowing ratio based on local conditions, see Eq. (6.3)
MFR	mass flow ratio, $MFR = \dot{m}_c / \dot{m}_{in}$
N	number of film cooling holes in a group
NHFR	net heat flux reduction, see Eq. (6.10)
Nu	Nusselt number, $Nu = hC_{ax} / k_{air}$
P	blade pitch
P_s	static pressure
PS	pressure side
P_{tot}	total pressure
q''_w	convective wall heat flux
Re_θ	momentum thickness Reynolds number, $Re_\theta = \theta U_{in} / \nu$
S	blade span
SS	suction side
T	temperature
X, Y, Z	global coordinates, where X is blade axial direction
U	average velocity magnitude
V_{gap}	platform gap ingestion/ejection velocity (Z-direction component)
V_{wh}	circumferential speed of the blade wheel at the hub
x_{gap}	distance along platform gap

Greek

β	design flow (yaw) angle
δ_{99}	boundary layer thickness (99%)
η	adiabatic effectiveness, $\eta = (T_{in} - T_w)/(T_{in} - T_c)$
θ	momentum thickness, or nondimensional metal temperature, $\theta = (T_{in} - T_c)/(T_{in} - T_{w,metal})$
ν	kinematic viscosity
ρ	density

Subscripts/Superscripts

0%	case without film cooling flow
c	leakage coolant conditions
exit	exit freestream conditions
f	case with film-cooling flow
in	inlet freestream conditions
inv	inviscid conditions
loc	local conditions
w	wall conditions
$\overline{(\ )}$	average, $\overline{(\ )} = \dfrac{\sum_i^N (\ )_i}{N}$
$\overline{\overline{(\ )}}$	area-average, $\overline{\overline{(\ )}} = \dfrac{\iint (\ )\partial X \partial Y}{\iint \partial X \partial Y}$

References

[1] Piggush, J., and Simon, T. W., 2005, "Flow Measurements in a First Stage Nozzle Cascade Having Leakage and Assembly Features: Effects of Endwall Steps and Leakage on Aerodynamic Losses," Proc. ASME International Mechanical Engineering Congress and Expo, Paper No. IMECE2005-83032.

[2] Reid, K., Denton, J. D., Pullan, G., Curtis, E., and Longley, J., 2006, "The Effect of Stator-Rotor Hub Sealing Flow on the Mainstream Aerodynamics of a Turbine," Proc. ASME Turbo Expo 2006, Paper No. GT2006-90838.

[3] Popovic, I., and Hodson, H. P., 2010, "Aerothermal Impact of the Interaction between Hub Leakage and Mainstream Flows in Highly-Loaded HP Turbine Blades," Proc. ASME Turbo Expo 2010, Paper No. GT2010-22311.

[4] Papa, M., Srinivasan, V., and Goldstein, R. J., 2010, "Film Cooling Effect of Rotor-Stator Purge Flow on Endwall Heat/Mass Transfer," Proc. ASME Turbo Expo 2010, Paper No. GT2010-23178.

[5] Reid, K., Denton, J., Pullan, G., Curtis, E., and Longley, J., 2007, "The Interaction of Turbine Inter-Platform Leakage Flow with the Mainstream Flow," *Journal of Turbomachinery*, **129**(2), pp. 303-310.

[6] Cardwell, N. D., Sundaram, N., and Thole, K. A., 2006, "Effect of Midpassage Gap, Endwall Misalignment, and Roughness on Endwall Film-Cooling," *Journal of Turbomachinery*, **128**(1), pp. 62-70.

[7] Piggush, J., and Simon, T. W., 2005, "Heat Transfer Measurements in a First Stage Nozzle Cascade Having Endwall Contouring, Leakage and Assembly Features," Proc. 2005 ASME Summer Heat Transfer Conference, Paper No. HT2005-72573.

[8] Lynch, S. P., and Thole, K. A., 2011, "The Effect of the Combustor-Turbine Slot and Midpassage Gap on Vane Endwall Heat Transfer," *Journal of Turbomachinery*, **133**(4), pp. 041002-9.

[9] De La Rosa Blanco, E., Hodson, H. P., and Vazquez, R., 2005, "Effect of Upstream Platform Geometry on the Endwall Flows of a Turbine Cascade," Proc. ASME Turbo Expo 2005, Paper No. GT2005-68938.

[10] Piggush, J. D., and Simon, T. W., 2007, "Heat Transfer Measurements in a First-Stage Nozzle Cascade Having Endwall Contouring: Misalignment and Leakage Studies," *Journal of Turbomachinery*, **129**(4), pp. 782-790.

[11] Piggush, J. D., and Simon, T. W., 2007, "Measurements of Net Change in Heat Flux as a Result of Leakage and Steps on the Contoured Endwall of a Gas Turbine First Stage Nozzle," *Applied Thermal Engineering*, **27**(4), pp. 722-730.

[12] Macisaac, G. D., Sjolander, S. A., and Praisner, T. J., 2010, "Measurements of Losses and Reynolds Stresses in the Secondary Flow Downstream of a Low-Speed Linear Turbine Cascade," Proc. ASME Turbo Expo 2010, Paper No. GT2010-22727.

[13] Praisner, T. J., Allen-Bradley, E., Grover, E. A., Knezevici, D. C., and Sjolander, S. A., 2007, "Application of Non-Axisymmetric Endwall Contouring to Conventional and High-Lift Turbine Airfoils," Proc. ASME Turbo Expo 2007, Paper No. GT2007-27579.

[14] Harvey, N. W., Rose, M. G., Taylor, M. D., Shahpar, S., Hartland, J., and Gregory-Smith, D. G., 2000, "Nonaxisymmetric Turbine End Wall Design: Part I--- Three-Dimensional Linear Design System," *Journal of Turbomachinery*, **122**(2), pp. 278-285.

[15] Lynch, S. P., Sundaram, N., Thole, K. A., Kohli, A., and Lehane, C., 2011, "Heat Transfer for a Turbine Blade with Nonaxisymmetric Endwall Contouring," *Journal of Turbomachinery*, **133**(1), pp. 011019-9.

[16] Kang, M. B., Kohli, A., and Thole, K. A., 1999, "Heat Transfer and Flowfield Measurements in the Leading Edge Region of a Stator Vane Endwall," *Journal of Turbomachinery*, **121**(3), pp. 558-568.

[17] Moffat, R. J., 1988, "Describing the Uncertainties in Experimental Results," *Experimental Thermal and Fluid Science*, **1**, pp. 3-17.

[18] Abo El Ella, H. M., Sjolander, S. A., and Praisner, T. J., 2010, "Effects of an Upstream Cavity on the Secondary Flow in a Transonic Turbine Cascade," Proc. ASME Turbo Expo 2010, Paper No. GT2010-22843.

[19] Lynch, S. P., and Thole, K. A., 2009, "The Effect of the Combustor-Turbine Slot and Mid-Passage Gap on Vane Endwall Heat Transfer," Proc. ASME International Mechanical Engineering Congress & Expo 2009, Paper No. IMECE2009-12847.

[20] Sen, B., Schmidt, D. L., and Bogard, D. G., 1996, "Film Cooling with Compound Angle Holes: Heat Transfer," *Journal of Turbomachinery*, **118**(4), pp. 800-806.

[21] Baldauf, S., Scheurlen, M., Schulz, A., and Wittig, S., 2002, "Heat Flux Reduction from Film Cooling and Correlation of Heat Transfer Coefficients from Thermographic Measurements at Enginelike Conditions," *Journal of Turbomachinery-Transactions of the ASME*, **124**(4), pp. 699-709.

[22] Vogel, J. C., and Eaton, J. K., 1985, "Combined Heat Transfer and Fluid Dynamic Measurements Downstream of a Backward-Facing Step," *Journal of Heat Transfer*, **107**(4), pp. 922-929.

[23] Piggush, J., and Simon, T. W., 2006, "Adiabatic Effectiveness Measurements in a First Stage Nozzle Cascade Having Endwall Contouring, Leakage and Assembly Features," Proc. ASME Turbo Expo 2006, Paper No. GT2006-90576.

Table 6.1 Cascade Geometry and Operating Conditions

Scale relative to engine	6X
Axial chord (C_{ax})	0.1524 m
Span/axial chord (S/C_{ax})	3.6
Pitch/axial chord (P/C_{ax})	1.48
Inlet angle (β_{in}, relative to axial direction)	31.5°
Exit angle (β_{exit}, relative to axial direction)	73.2°
Zwiefel load coefficient (Zw)	0.97
Inlet Reynolds number ($Re_{in}=U_{in}C_{ax}/\nu$)	70,000
Exit Reynolds number ($Re_{ex}=U_{exit}C_{ax}/\nu$)	200,000
Exit Mach number	0.06
Inlet boundary layer thickness at $X/C_{ax}=-5$ (δ_{99}/S)	0.08
Momentum thickness (θ/S)	0.0064
Momentum thickness Re number ($Re_{ex}=U_{in}\theta/\nu$)	1450
Shape factor (H)	1.35

Table 6.2 Film Cooling Geometry

Hole #	Film cooling group	L/d	Surface angle
1	FC1	13	22°
2	FC1	14	27°
3	FC1	14	30°
4	FC1	14	30°
5	FC1	12	36°
6	FC1	11	44°
7	FC2	11	40°
8	FC2	12	40°
9	FC3	23	22°
10	FC3	23	35°
11	FC3	20	35°
12	FC3	17	35°

Table 6.3 Film Cooling Group Flow Conditions

Film cooling group	MFR (% of inlet)	Blowing ratio (M_{loc})	Momentum flux ratio (I_{loc})
FC1	0.1%	1.5	2.1
FC2	0.05%	1.6	2.3
FC3	0.1%	1.6	2.3

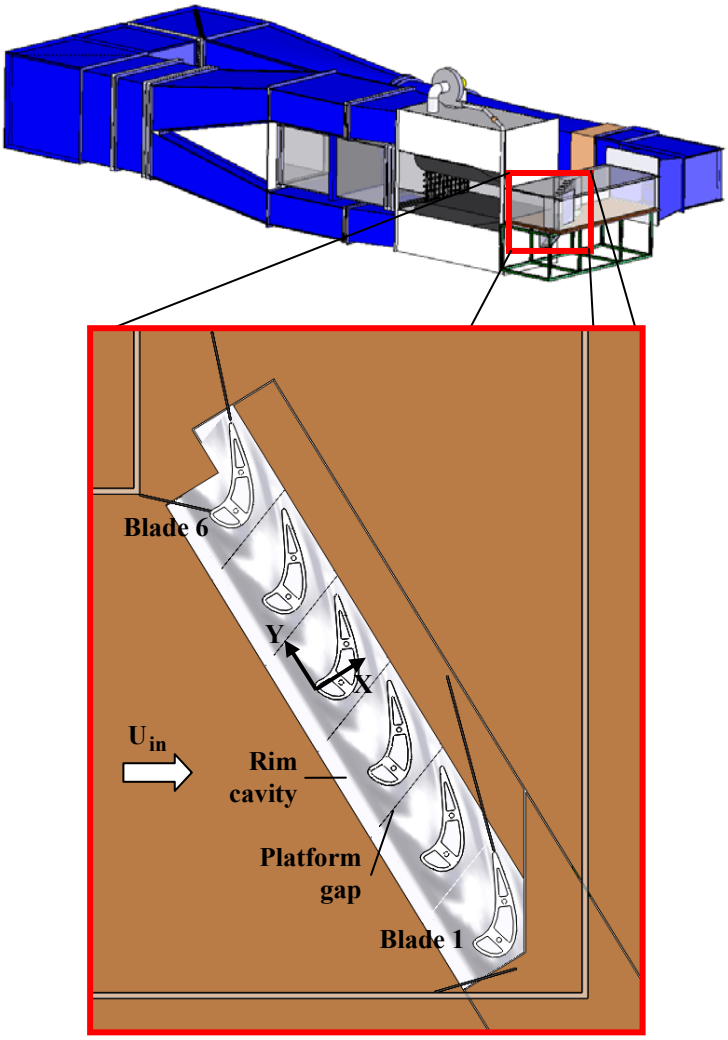

Figure 6.1. Depiction of the low-speed wind tunnel and large-scale test section.

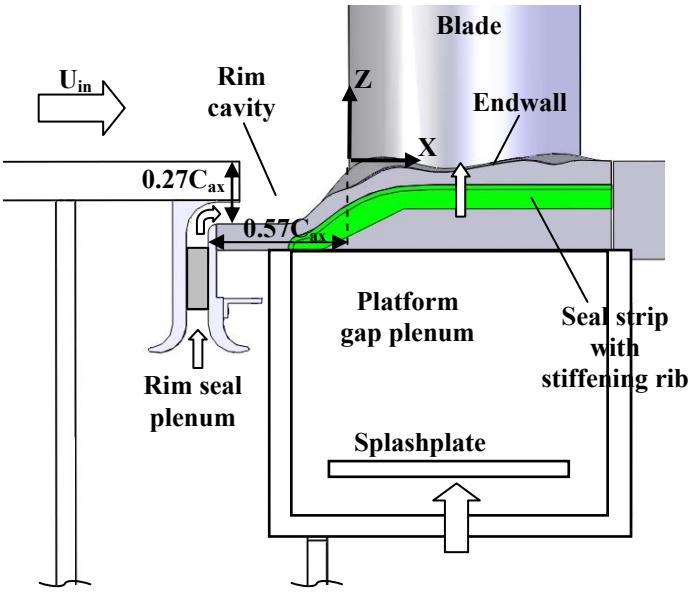

Figure 6.2. Depiction of the rim cavity, rim seal leakage geometry, and platform gap leakage geometry in the cascade.

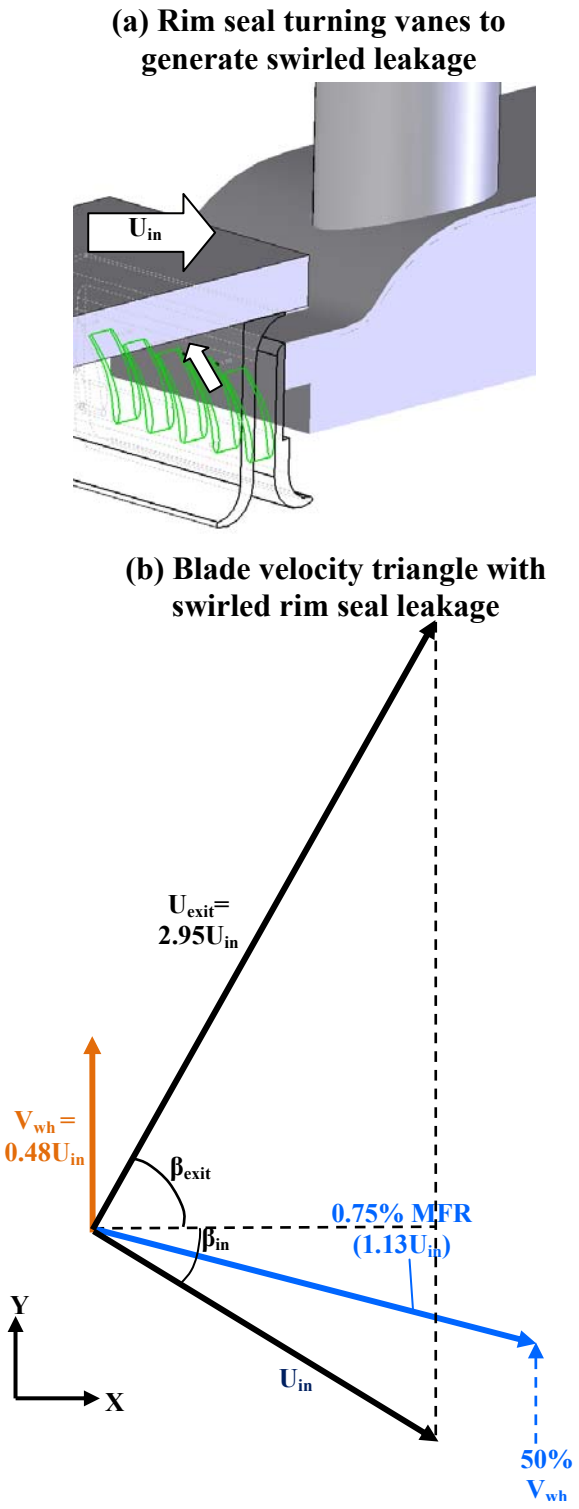

Figure 6.3. (a) Depiction of the turning vanes inside the rim seal that generate swirled leakage; and (b) velocity vectors in the blade reference frame with the effect of the effect of the swirled rim seal leakage on the near wall flow.

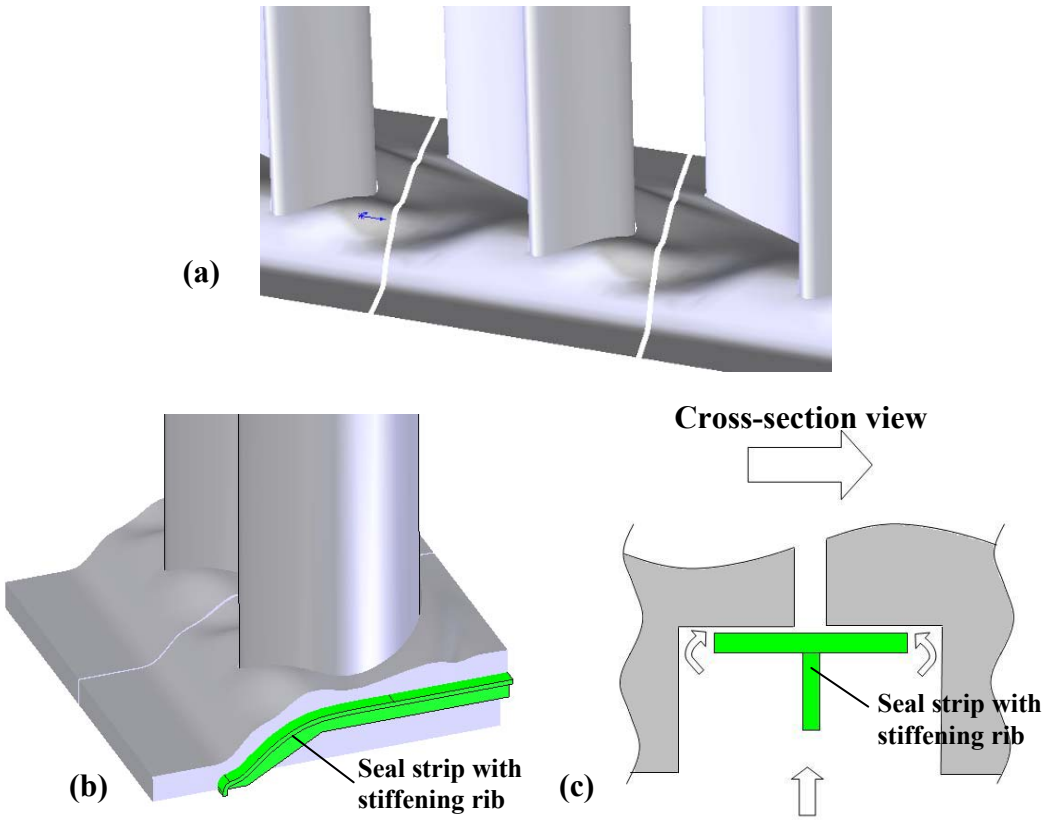

Figure 6.4. Depictions of the (a) non-axisymmetric endwall contour with platform gap; (b) side view of gap with seal strip; and (c) cross-section view of gap.

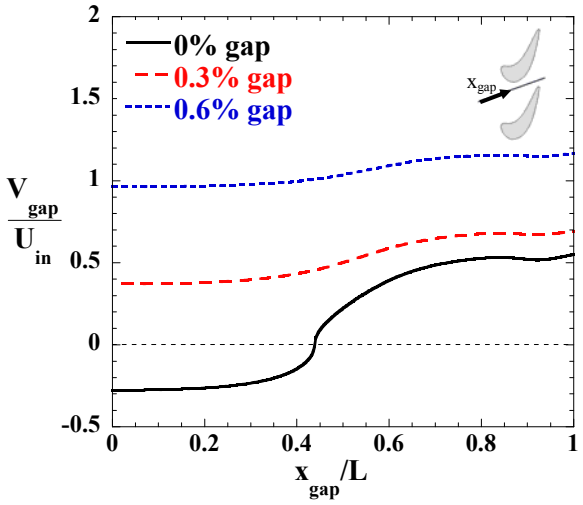

Figure 6.5. Estimated platform gap leakage velocities along the gap length for various net leakage flowrates.

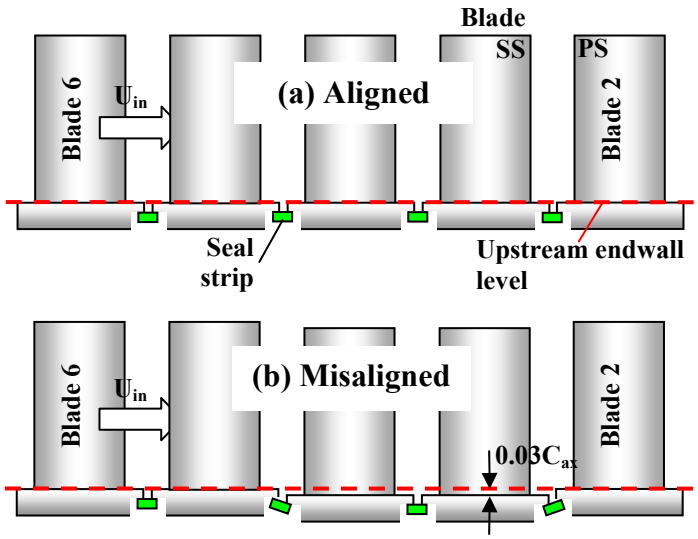

Figure 6.6. Upstream view of the aligned and misaligned endwall modes.

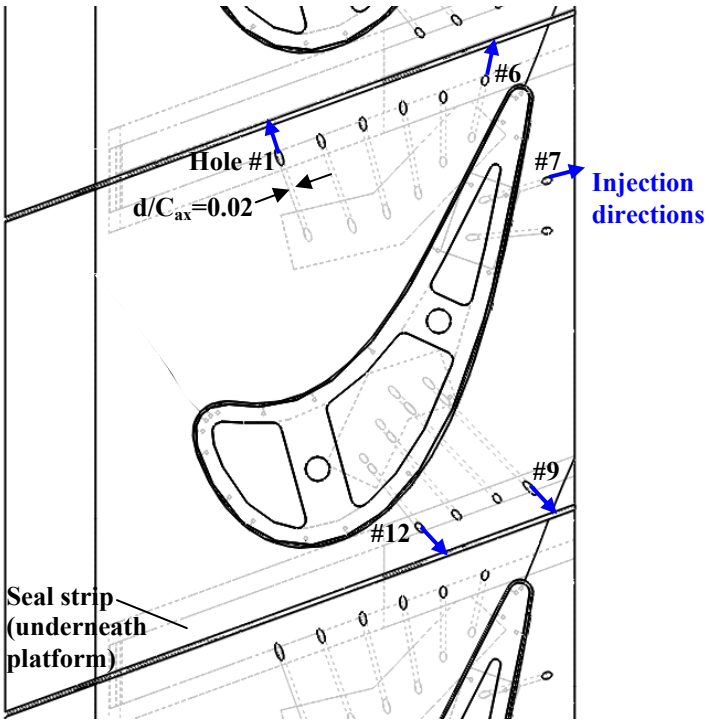

Figure 6.7. Endwall film cooling hole geometry, with injection directions indicated (also see Table 6.2).

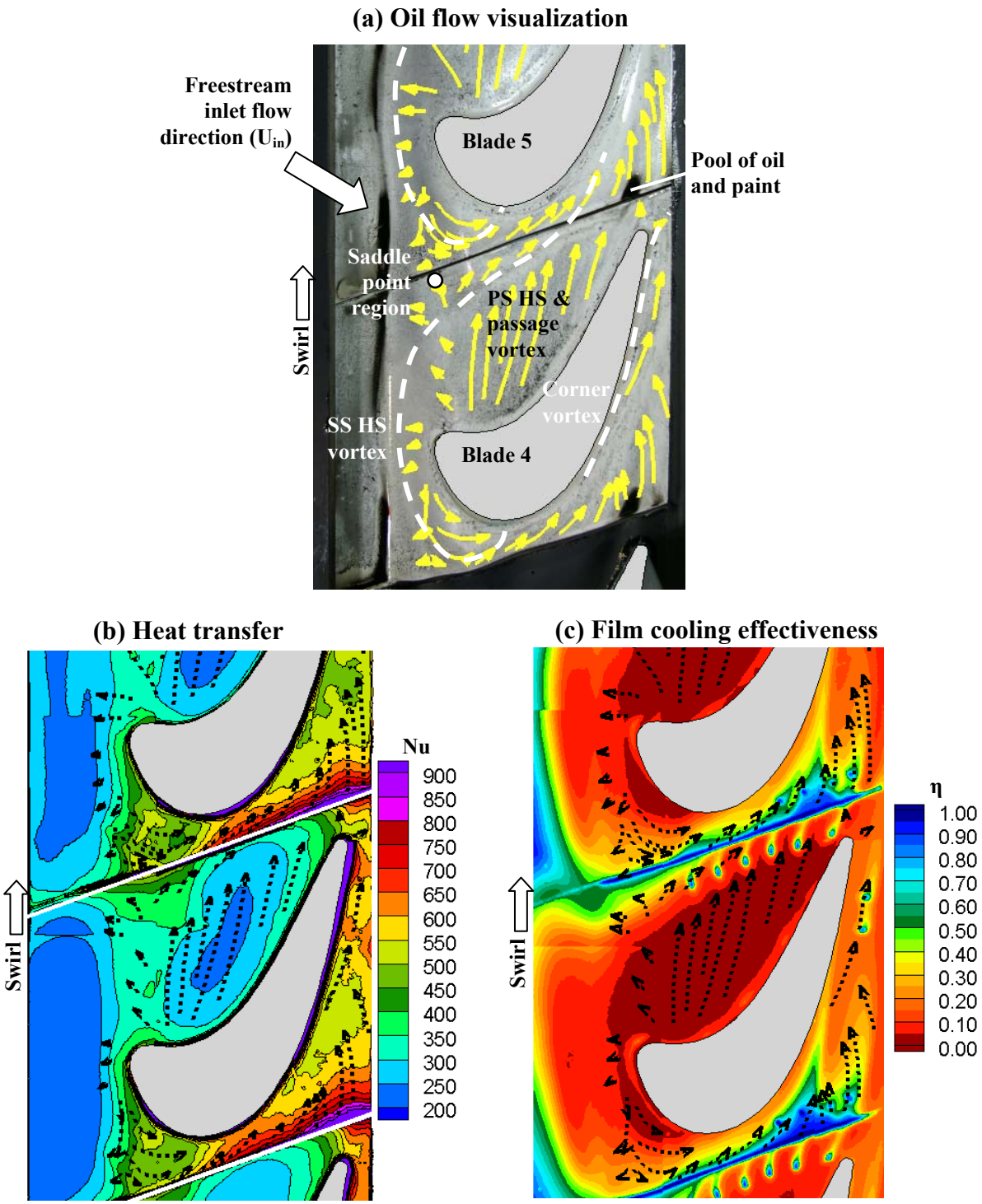

Figure 6.8. Comparison of (a) oil flow visualization, (b) endwall heat transfer, and (c) film-cooling effectiveness for the nominal case of 0.75% MFR swirled rim seal flow (50% V_{wh}) and 0.3% MFR platform gap flow.

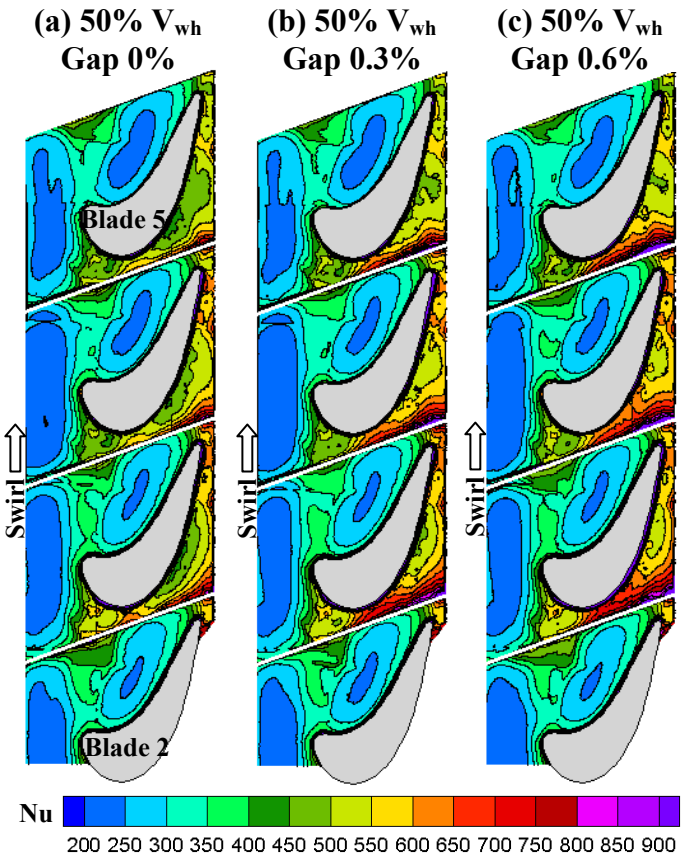

Figure 6.9. Endwall heat transfer contours for 0.75% MFR rim seal leakage with swirl and platform gap MFR of (a) 0%, (b) 0.3%, and (c) 0.6%.

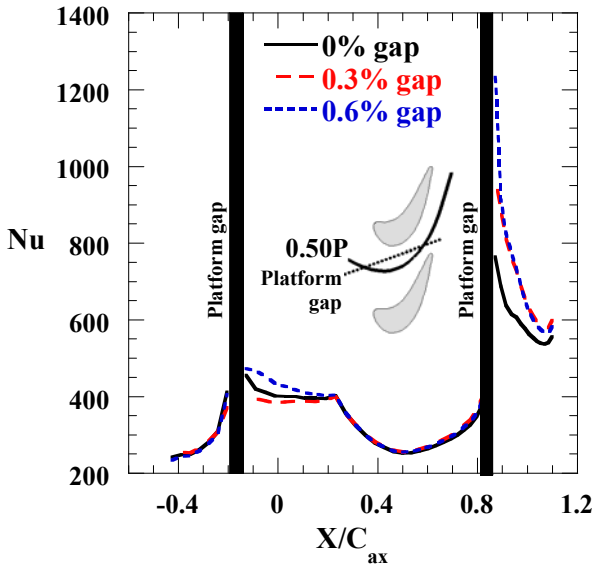

Figure 6.10. Endwall heat transfer for varying platform gap MFR, extracted along an inviscid streamline path passing through the center of the passage (0.50P).

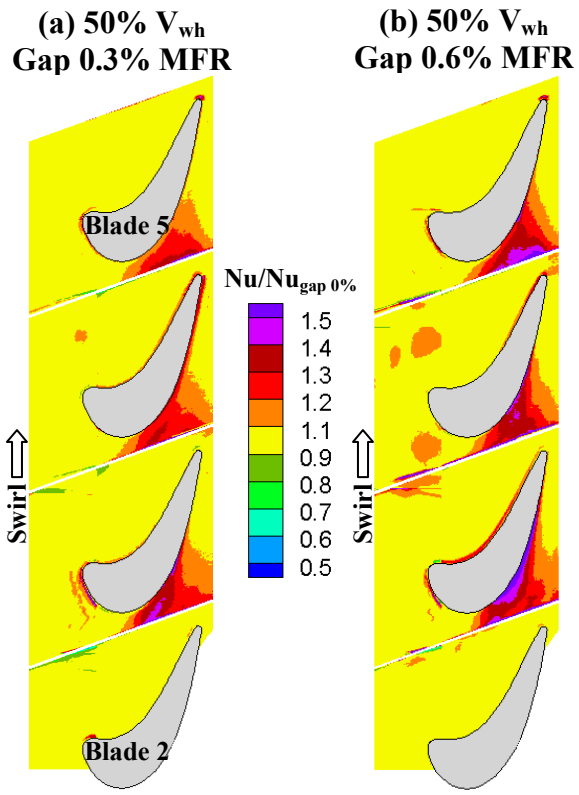

Figure 6.11. Heat transfer augmentation with net gap flow relative to heat transfer with 0% net gap flow, for net gap MFR's of (a) 0.3% and (b) 0.6%.

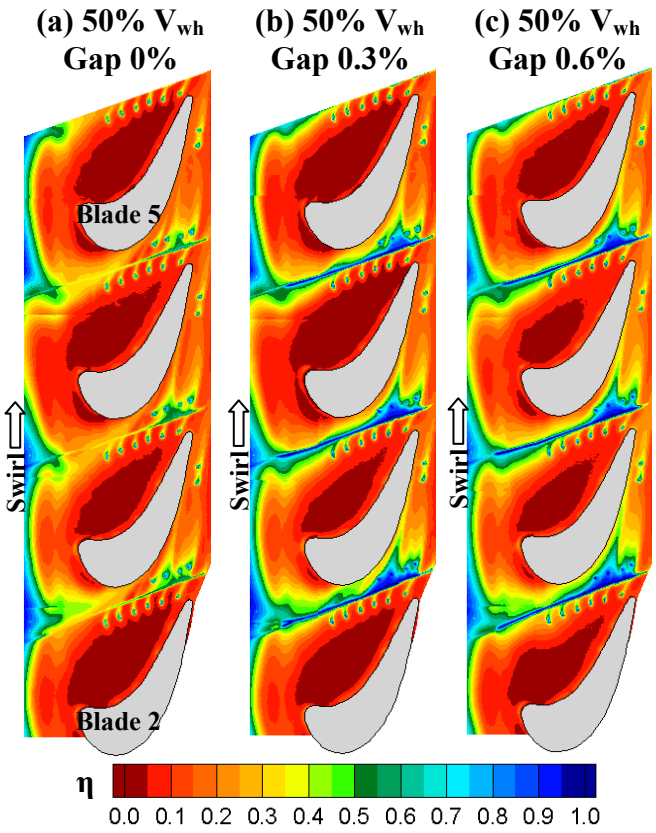

Figure 6.12. Film cooling effectiveness for 0.75% MFR rim seal leakage with swirl (50% V_{wh}) and net gap MFR of (a) 0%, (b) 0.3%, and (c) 0.6%.

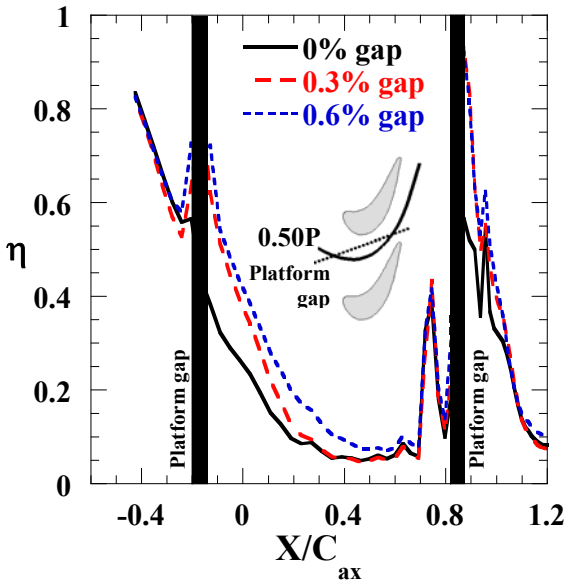

Figure 6.13. Endwall film cooling effectiveness for varying gap MFR, plotted along an inviscid streamline path passing through the center of the passage.

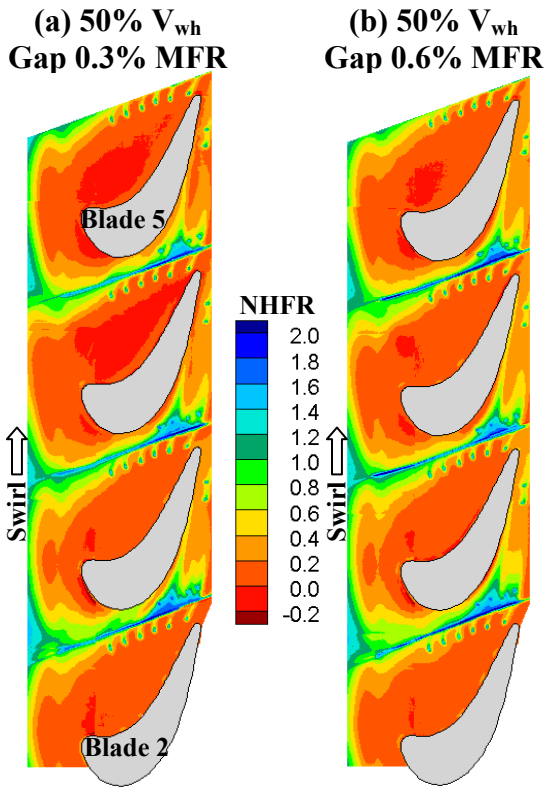

Figure 6.14. Net heat flux reduction with the addition of gap leakage flow, for (a) 0.3% gap MFR, and (b) 0.6% gap MFR.

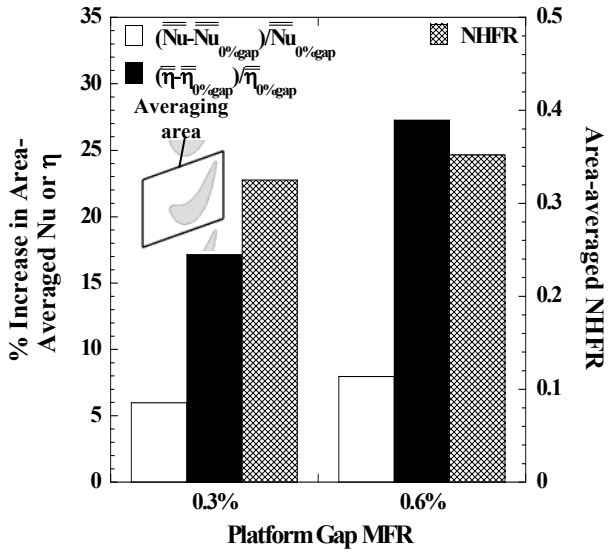

Figure 6.15. Percent increase in area-averaged endwall heat transfer and film-cooling effectiveness, and resulting area-averaged NHFR, for increasing platform gap flow relative to 0% gap MFR.

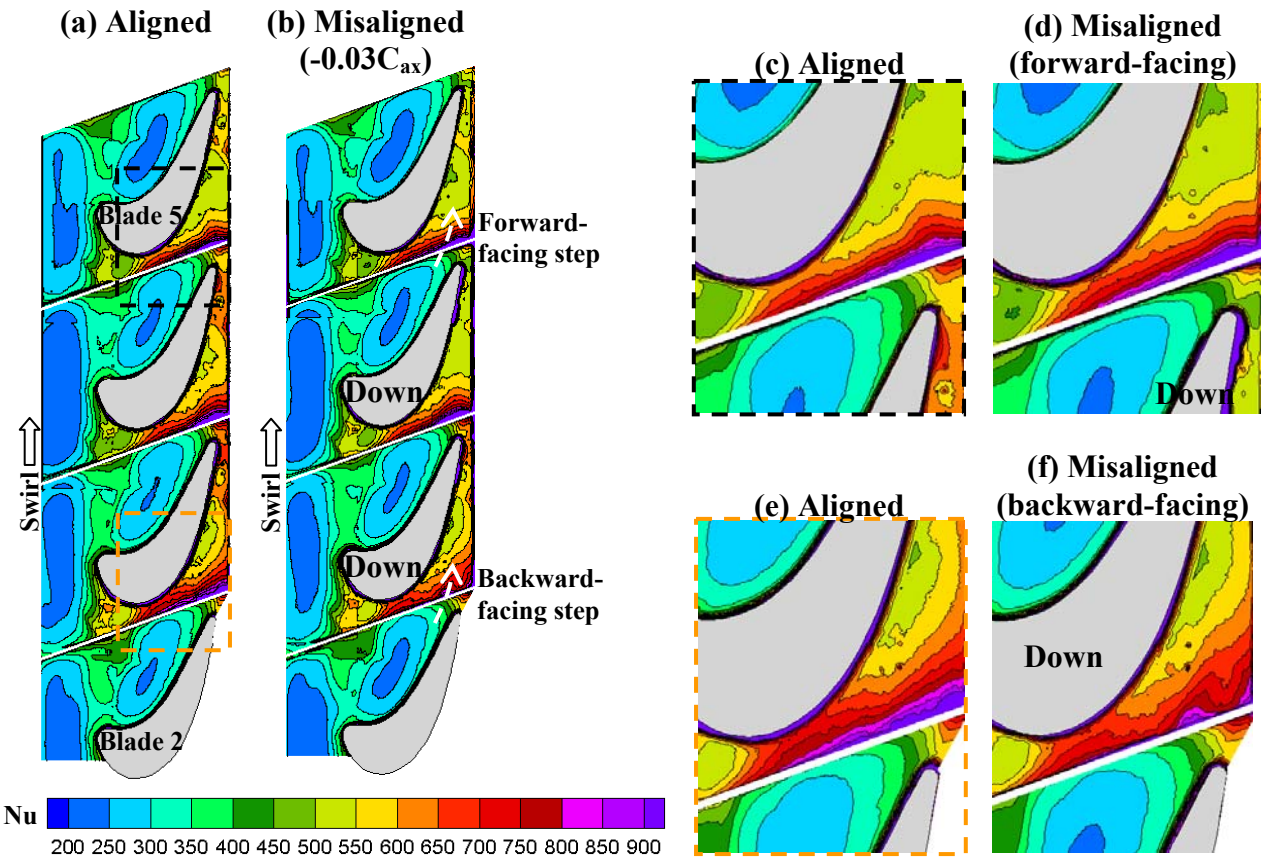

Figure 6.16. Endwall heat transfer contours for (a) aligned platforms and (b) misaligned platforms; close-up views of the endwall for the (c) aligned and (d) forward-facing step misalignment; and close-up views for the (e) aligned and (f) backward-facing step misalignment.

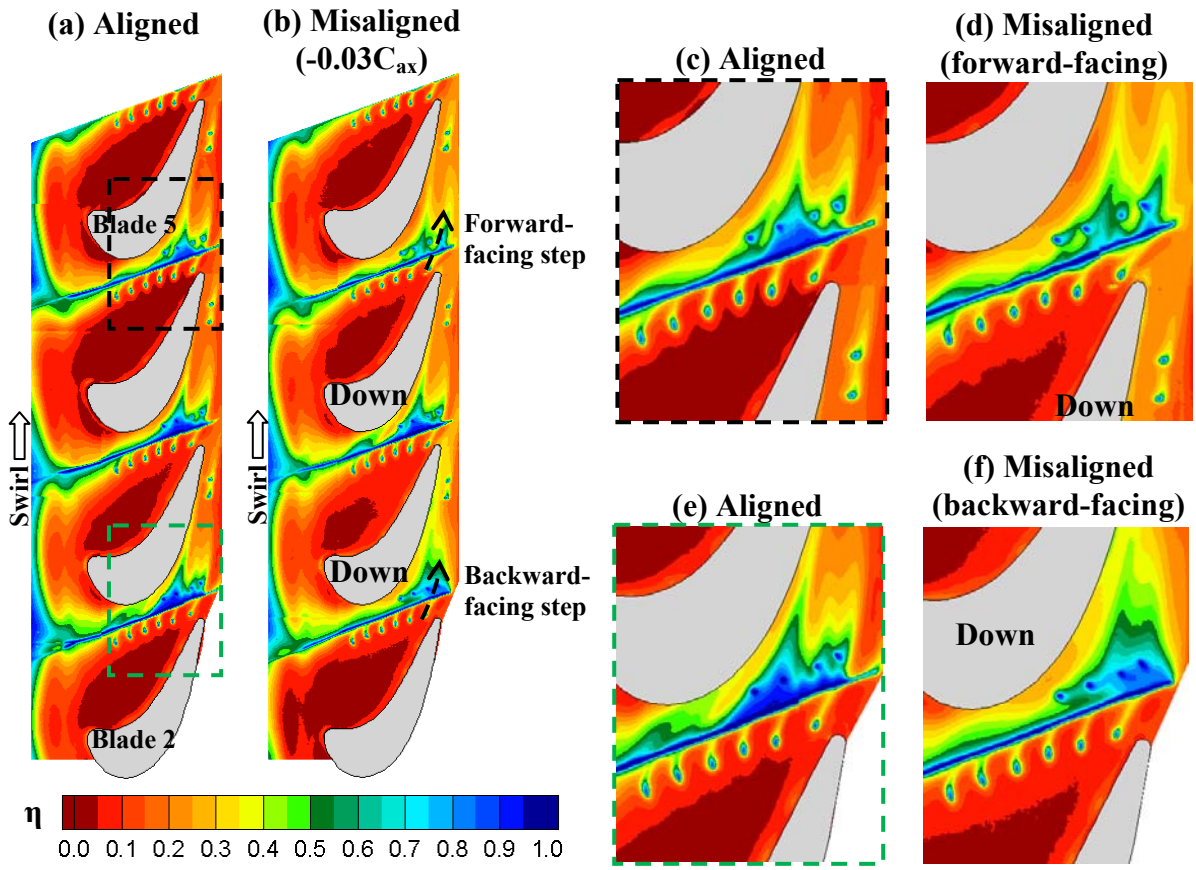

Figure 6.17. Film cooling effectiveness contours for (a) aligned platforms and (b) misaligned platforms; close-up views of the endwall for the (c) aligned and (d) forward-facing step misalignment; and close-up views for the (e) aligned and (f) backward-facing step misalignment.

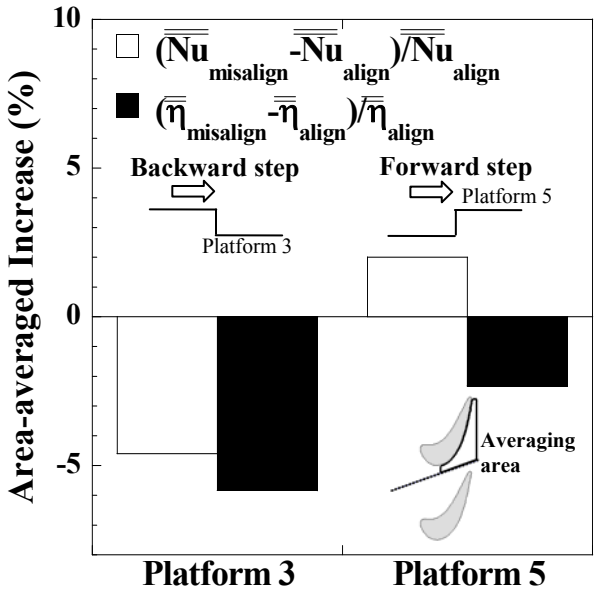

Figure 6.18. Percent increase in area-averaged endwall heat transfer and film cooling effectiveness for platform misalignment, relative to aligned endwalls.

Conclusions and Recommendations for Future Work

Measurements of endwall heat transfer, film cooling effectiveness, total pressure loss, and all three components of mean and fluctuating flowfields were obtained to document the influence of non-axisymmetric endwall contouring on the endwall boundary layer in a turbine passage. Two blade cascades were constructed to study the physics of contouring and determine the sensitivity of the secondary flows to endwall geometry changes. One cascade was designed for detailed studies of the endwall boundary layer, including spatially resolved heat transfer and three-component boundary layer measurements with a laser Doppler velocimeter. The second cascade was used to test the effectiveness of non-axisymmetric contouring in conjunction with realistic turbine leakage gaps, such as between the stator and rotor, or between adjacent airfoils in a wheel. Aerodynamic loss measurements and spatially resolved heat transfer and film cooling measurements were obtained for various combinations of leakage interface geometries and leakage flow rates.

Initial studies without the effect of realistic leakage features were performed to understand how secondary flows influence the three-dimensional endwall boundary layer in a turbine passage. For a baseline flat endwall, the turbulent boundary layer entering the passage was accelerated and developed significant levels of skew as it was turned toward the suction side. The increased three-dimensionality of the boundary layer reduced the heat transfer relative to a two-dimensional zero-pressure-gradient boundary layer. However, the downwash associated with a large passage vortex caused high heat transfer levels near the pressure side-endwall junction in the passage.

The addition of a non-axisymmetric contour was intended to perturb the passage vortex to further understand its influence on endwall heat transfer. With endwall contouring, the incoming boundary layer was further accelerated and skewed, with a subsequent decrease in heat transfer. Although the contour displaced the horseshoe vortex upstream and resulted in higher endwall heat transfer levels around the saddle point, it reduced the interaction of the horseshoe and passage vortices, and delayed the development of the passage vortex through the passage. These effects resulted in reduced endwall heat transfer near the pressure side-endwall junction, relative to the flat endwall. Secondary kinetic energy and turbulent kinetic energy, both of which

contribute to aerodynamic loss generation, were reduced at the exit of the cascade with contouring.

The effectiveness of non-axisymmetric contouring in a more realistic turbine environment provided an opportunity to probe the physics of contouring. A rim seal with an upstream cavity was studied to determine the sensitivity of contouring to horseshoe vortex development. The upstream cavity caused early separation and shifted the saddle point toward the adjacent blade suction side. A strong passage vortex was generated from the separated cavity flow, which limited the impact of the constrained contour design. For the contour studied, no significant improvement was indicated relative to a flat endwall, and in an off-design case of unswirled leakage from the rim seal, the contour resulted in slightly higher aerodynamic loss relative to a flat endwall. Although it was not possible to ascertain the vertical position of the secondary flows from the measurements obtained in this portion of the study, it is likely that the leakage could have displaced the vortical structures away from the endwall and limited their influence.

A platform gap through the passage acted as a means of perturbing the passage vortex development. Leakage from the gap was a significant factor in high levels of endwall heat transfer and aerodynamic loss, although net heat flux to the endwall was reduced due to high levels of cooling effectiveness. The endwall contour was not designed around the platform gap and its lack of improved aerodynamic loss relative to the flat endwall made it unlikely that it would have a positive benefit on endwall heat transfer.

Overall, this work demonstrated that contouring can have a positive benefit on endwall heat transfer by reducing the development of the passage vortex and its interaction with the horseshoe vortex. However, realistic endwall geometry features can reduce contouring effectiveness due to significant interactions with secondary flows. Careful consideration of the various influences on secondary flow development is important to optimize mitigation strategies such as non-axisymmetric endwall contouring.

The results summarized above were presented in six papers. The design and benchmarking of a low-pressure turbine blade cascade for high-resolution measurements of the three-dimensional endwall boundary layer was described in the first paper. Oil flow visualization for a baseline flat endwall indicated a strong passage vortex originating near the pressure side leading edge and significant overturning of endwall streamlines near the blade pressure side. Flat

endwall heat transfer levels were high around the leading edge and near the pressure side where the secondary flow turned fluid down to the endwall. With the application of non-axisymmetric endwall contouring, the effect of the passage vortex and streamline overturning was diminished in the oil flow visualization. Heat transfer augmentation with contouring was presented, where the results were a fraction of the local value of heat transfer for the flat endwall. Heat transfer relative to the flat endwall increased near the leading edge, but decreased by 20% near the blade pressure side where flat endwall levels were high. The flat endwall heat transfer pattern and the relative effect of the contour were not sensitive to cascade Reynolds number.

Computational simulations of the flat and non-axisymmetric contoured endwalls were performed to test the capabilities of steady Reynolds-Averaged Navier Stokes (RANS) simulations to accurately predict the cascade flowfield and three-dimensional boundary layer. The computations, described in the second paper, compared two turbulence models (SST k-ω and realizable k-ε) to measurements of the endwall heat transfer and film cooling effectiveness, as well as to the exit flowfield presented previously in the literature. The SST k-ω model reasonably predicted the structure of the exit flowfield but overpredicted total pressure loss, and significantly overpredicted flat endwall heat transfer in the passage. The realizable k-ε model did not accurately capture the exit flowfield, and also overpredicted endwall heat transfer. The measured trends of heat transfer augmentation near the leading edge and reduction near the pressure side with the application of endwall contouring were generally reproduced in the simulations, although the levels were overpredicted. Measurements and predictions of film effectiveness showed that coolant coverage area decreased with contouring due to reduced cross-passage flow. It was concluded that the effects of the three-dimensional boundary layer on the endwall heat transfer were not adequately captured in the isotropic eddy viscosity-based closure models, and more information about the boundary layer was needed to improve modeling.

To address the general lack of information about the endwall boundary layer in a turbine passage, three-component measurements of mean and turbulent quantities were obtained with a laser Doppler velocimeter at selected locations. The oil film interferometry technique was also employed to obtain mean shear stress. The third paper discusses the methodology and results of that work. Profiles of mean velocity along the path of an endwall streakline entering the passage indicated streamwise acceleration and development of significant skew angles in the turbulent boundary layer, which correlated with a drop in endwall heat transfer levels below the

corresponding values in a two-dimensional zero-pressure-gradient boundary layer. In the forward portion of the passage, flowfield measurements indicated a reduction in passage vortex size but a slight increase in near-wall turbulent kinetic energy for the contour compared to the flat endwall. A region of elevated endwall heat transfer for the contour correlated well with the region of elevated turbulent kinetic energy. At the exit of the cascade, contouring delayed the progress of the passage vortex toward the suction side of the passage, which reduced secondary kinetic energy and turbulent kinetic energy compared to a flat endwall. Due to the position of the passage vortex away from the endwall, however, no significant difference in heat transfer or friction coefficients was observed at the exit plane between the flat and contoured endwalls. Overall, the contouring increased heat transfer in the forward portion of the passage due to displacement of the horseshoe vortex, but decreased heat transfer further into the passage due to delayed development of the passage vortex.

Before considering the combined effects of leakage features and non-axisymmetric endwall contouring, a study was done to understand the effect of the stator-rotor interface, known as a rim seal, on a flat endwall. The results of that study are reported in the fourth paper. Oil flow visualization and endwall heat transfer measurements were obtained for a flat endwall with a representative upstream cavity and rim seal, which could supply unswirled or swirled leakage flow. Flow separation in the upstream cavity resulted in low heat transfer upstream of the blades and shifted the suction side leg of the horseshoe vortex away from the leading edge of the blade. For unswirled leakage, increasing the net leakage mass flow pushed the suction side horseshoe vortex closer to the blade and increased heat transfer on the endwall upstream of the blades, but heat transfer levels in the passage did not show any significant variation. Comparison of the endwall oil flow patterns with and without swirl indicated that the saddle point upstream of the blades was shifted in the direction of swirl (toward the suction side), resulting in an increase in endwall heat transfer around the suction side leading edge. Variations in the rim seal leakage massflow or swirl had little effect in the passage, however, suggesting that uncertainty in those leakage conditions might not critically affect the design of a non-axisymmetric contour.

The sensitivity of contouring to leakage features was explored further through measurements of aerodynamic loss, reported in the fifth paper. The upstream cavity and rim seal with and without swirl were modeled, and the effect of a platform gap was also considered. Swirled rim seal leakage relative to the blade resulted in increased losses compared to unswirled

leakage. For the contour versus a flat endwall, no significant difference was observed in total pressure loss or streamwise vorticity features in the exit flowfield, although underturning of the exit flow associated with the passage vortex was slightly reduced. It was conjectured that a strong passage vortex due to separated upstream cavity flow, as well as constraints in the endwall contour design, limited the effect of the contouring on the secondary flows. The contour resulted in slightly higher mass-averaged losses compared to a flat endwall at the off-design condition of no rim seal swirl relative to the blades, which indicated negative sensitivity of the contouring to leakage conditions. However, the most significant effect was the presence of a platform gap with leakage, which significantly increased peak total pressure loss and secondary kinetic energy relative to a continuous endwall.

The study of the platform gap significance was extended in the work described in the sixth paper. Endwall heat transfer and film cooling effectiveness measurements were presented for the contoured endwall with the upstream rim seal and platform gap. Boundary layer disturbance due to the platform gap and leakage flow emanating from it resulted in very high heat transfer levels downstream of the gap. Increasing the platform gap leakage flowrate resulted in significantly higher heat transfer levels on the suction side platform due to increased strength of the vortical flow feature caused by the gap exit flow. Increased gap flow also resulted in more coolant present near the endwall, however, as film cooling effectiveness levels also increased around the platform gap, and net heat flux to the endwall was reduced. Vertical misalignment of the endwall, which might occur due to thermal expansion or installation differences between adjacent blades, had a measurable effect but was less significant than varying platform gap leakage flowrates. A forward-facing step misalignment, as seen by the endwall crossflow, slightly increased heat transfer and decreased film cooling effectiveness downstream of the step, due to increased flow separation relative to an aligned endwall.

Recommendations for Future Work

Although the goal of this study was to capture significantly more detail of the endwall boundary layer in a turbine cascade than has ever been obtained, more work could be done in this area. Additional flowfield measurements in the passage would help to clarify the development of the large-scale vortices and their effect on the endwall boundary layer. Increased near-wall resolution (below $z^+=30$) would provide important information about how the three-dimensional

boundary layer influences the endwall heat transfer. Also, more detail for the endwall shear stress measurements would be helpful in connecting the flowfield measurements to the state of the endwall boundary layer.

A particular region of interest that should be investigated is the aft portion of the passage, downstream of the inlet boundary layer separation. The new endwall boundary layer downstream of the separation is extremely thin; preliminary measurements indicated a 99% thickness of approximately 1 mm at the 8.6X scale of the low-pressure turbine cascade. Significant changes to the experimental setup would be required to capture the details of this boundary layer. However, the computational results described in the second paper indicate that the predictions of endwall heat transfer begin to significantly deviate from the measurements in the aft portion of the passage, so it seems that some important flow physics are occurring in the very thin boundary layer.

In addition to in-passage measurements, flowfield measurements around the leakage interfaces should be investigated. The upstream cavity appeared to play a significant role in the development of the horseshoe vortex, and future work should examine the flowfield around the cavity in more detail. In particular, the position of the secondary flow vortices off the endwall should be investigated. Also, the platform gap was shown to have a significant impact on loss and heat transfer, and although some of the physics of the gap ejection flow have been presented, no flowfield measurements near the platform gap have been reported in the open literature.

Finally, a topic that has not been adequately addressed is the sensitivity of a contoured endwall design methodology to the choice of optimization parameter, turbulence model, inclusion of leakage features, and so on. It is not clear how much different a non-axisymmetric contoured endwall would be if the optimization were based on endwall heat transfer versus total pressure loss. The second paper in this dissertation clearly indicates that the choice of turbulence model has a significant effect on total pressure loss prediction accuracy. In the open literature, non-axisymmetric endwall contours are generally designed without considering higher-level detail such as leakage gaps. The fifth paper indicates that the intended benefit of the contour may be negated by changes in secondary flows caused by the upstream rim seal cavity and the platform gap.

Appendix A: Velocity Transformations for Laser Doppler Velocimeter Measurements

This appendix documents the non-orthogonal and cascade coordinate transformations applied to the three-component flowfield data obtained with a laser Doppler velocimeter. Schematics of the probe setup relative to the cascade are included, as well as the transformation equations to convert the measured probe velocities to the cascade coordinate system.

Figure A.1 shows the measurement locations in the cascade. Flowfield measurements were obtained in two planes, where Plane A was located $0.2C_{ax}$ downstream of the leading edge plane of the cascade, and Plane B was located $1.03C_{ax}$ downstream of the leading edge plane. A further description of the plane coordinate systems and velocity transformations from the cascade coordinate system (X,Y,Z) to the desired local coordinate system is given in Paper 3. Boundary layer profiles (see Figure A.1b) were obtained at three locations in Plane A, as well as at three locations (denoted S1-S3) along the path of an endwall streakline originating upstream of the cascade.

Each of the setups for Plane A, Plane B, and endwall streakline measurements required unique non-orthogonal configurations of the LDV. In general, transformation from non-orthogonal probe measurements to orthogonal cascade coordinates required a non-orthogonal transformation, a tilt transformation, and a rotation transformation to be successively applied. The transformations were applied to the instantaneous coincident measurements before statistics were calculated. The following provides a schematic of the setup and the transformation equations for each configuration.

Nomenclature

C_{ax}	blade axial chord
P	blade pitch
PS	pressure side
SS	suction side
u'	instantaneous velocity in the x'-direction in the probe coordinate system
v'	instantaneous velocity in the y'-direction in the probe coordinate system
w'	instantaneous velocity in the z'-direction in the probe coordinate system

u"	instantaneous velocity in the x"-direction in the rotated coordinate system
v"	instantaneous velocity in the y"-direction in the rotated coordinate system
w"	instantaneous velocity in the z"-direction in the rotated coordinate system
u_g	instantaneous measured velocity by the green beam pair
u_b	instantaneous measured velocity by the blue beam pair
u_v	instantaneous measured velocity by the violet beam pair
U	instantaneous velocity in the X-direction in the cascade coordinate system
V	instantaneous velocity in the Y-direction in the cascade coordinate system
W	instantaneous velocity in the Z-direction in the cascade coordinate system
x, y, z	local orthogonal coordinate system for presentation of data (see Figure A.1a)
x', y', z'	probe orthogonal coordinate system (rotated and tilted with respect to cascade coordinate system)
x", y", z"	rotated orthogonal coordinate system (rotated with respect to cascade coordinate system)
X, Y, Z	blade cascade orthogonal coordinate system, where X is blade axial direction and Y is pitchwise direction (see Figure A.1a)

Greek

θ_g	angle of the blue-green probe off the z'-axis in the probe coordinate system
θ_v	angle of the violet probe off the z'-axis in the probe coordinate system
θ_{tilt}	tilt angle of the probe z'-axis relative to the cascade Z-axis
θ_{rot}	rotation angle of the rotated coordinate system x"-axis relative to the cascade X-axis

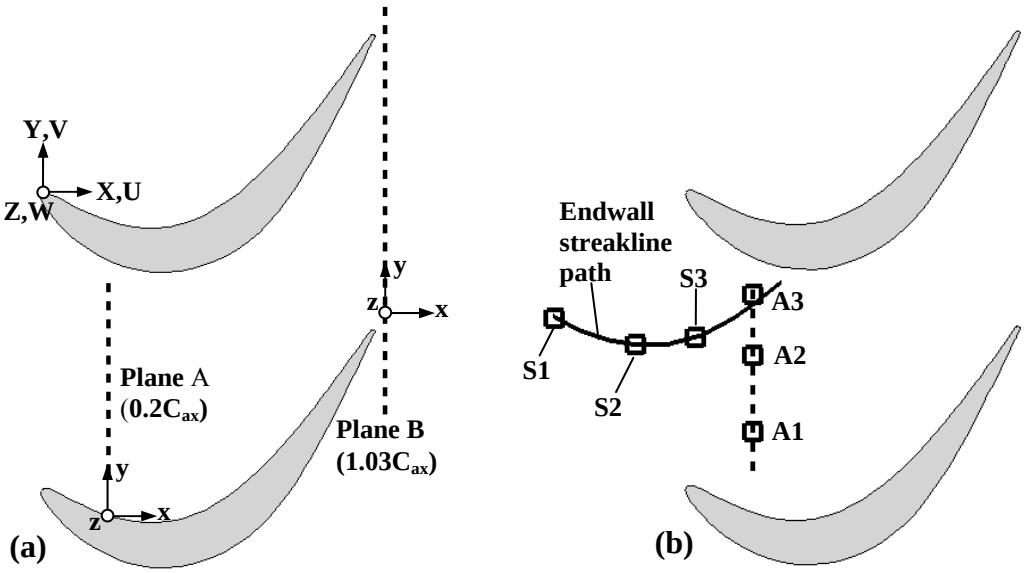

Figure A.1. (a) Locations of flowfield measurement planes; and (b) locations of endwall boundary layer measurements.

Endwall Streakline Measurement Setup and Velocity Transformations

For measurements at stations S1-S3 along the streakline path, the LDV probes were placed on the side of the test section and the beams were transmitted through a glass sidewall, as shown in Figure A.2. Figure A.3 depicts the three coordinate transformations necessary to transform the non-orthogonal measurements to the orthogonal blade cascade coordinate system. Equations (A.1-A.3) document the equations for the coordinate transformations, and Table A.1 documents the system angles in the coordinate transformations.

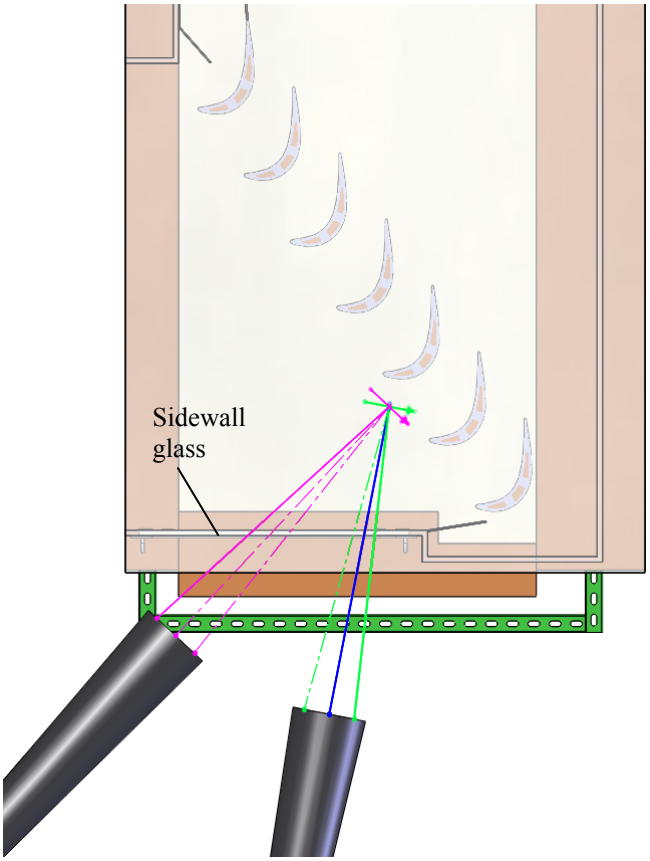

Figure A.2. Depiction of the non-orthogonal setup to measure endwall streakline stations S1-S3.

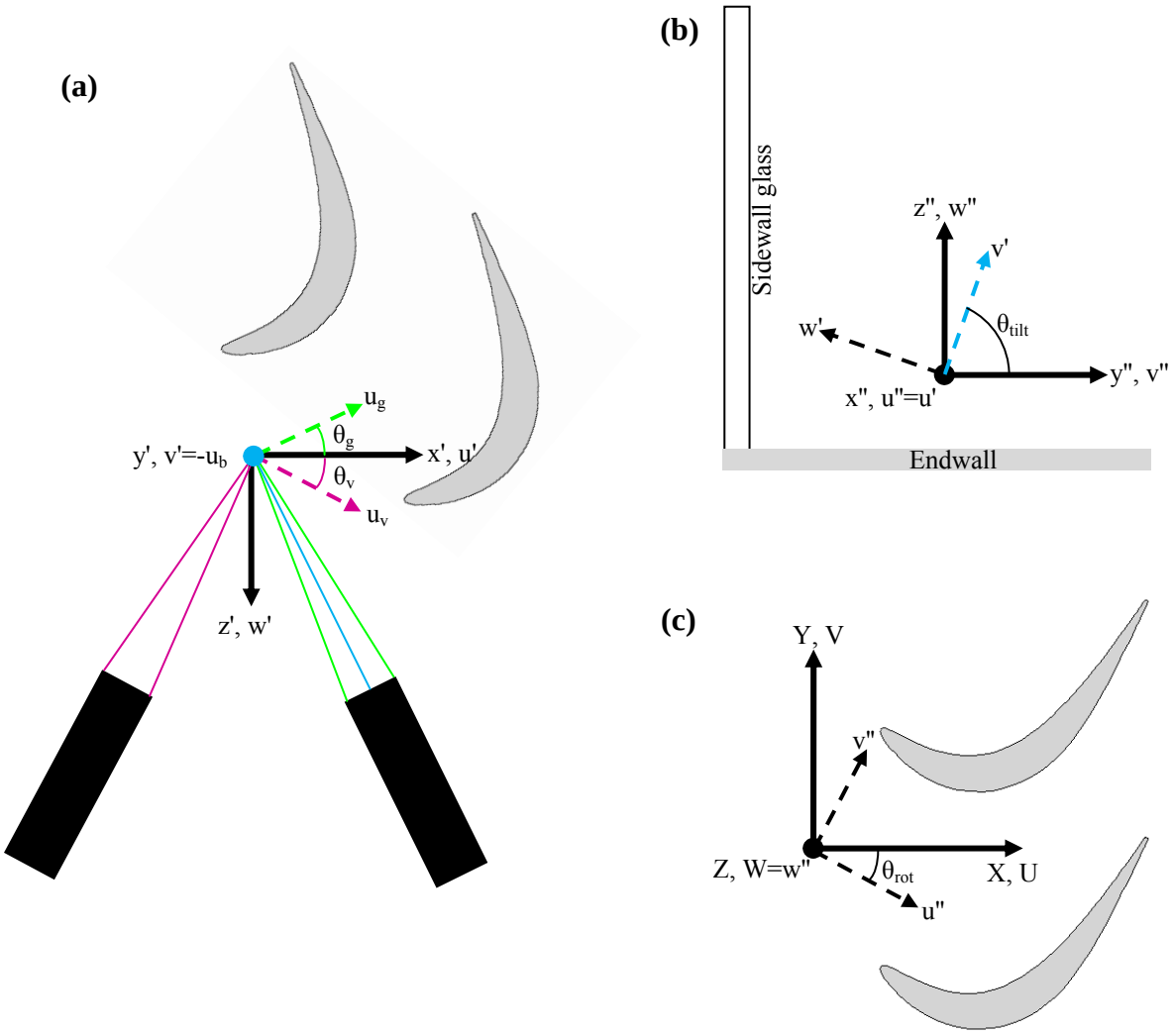

Figure A.3. (a) The non-orthogonal to orthogonal transformation; (b) the tilt transformation; and (c) the rotation transformation for the endwall streakline profiles.

Non-orthogonal to orthogonal transformation:

$$u' = \frac{u_g \sin(\theta_v) + u_v \sin(\theta_g)}{\sin(\theta_g + \theta_v)}$$
$$v' = -u_b \qquad \text{(A.1)}$$
$$w' = \frac{-u_g \cos(\theta_v) + u_v \cos(\theta_g)}{\sin(\theta_g + \theta_v)}$$

Tilt transformation:

$$u'' = u'$$
$$v'' = v' \cos(\theta_{tilt}) - w' \sin(\theta_{tilt}) \qquad \text{(A.2)}$$
$$w'' = v' \sin(\theta_{tilt}) + w' \cos(\theta_{tilt})$$

Rotation transformation:

$$U = u'' \cos(\theta_{rot}) + v'' \sin(\theta_{rot})$$
$$V = -u'' \sin(\theta_{rot}) + v'' \cos(\theta_{rot}) \quad \text{(A.3)}$$
$$W = w''$$

Table A.1 Velocity Transformation Angles for Endwall Streakline Measurements (S1-S3)

	Flat	**Contour**
θ_g	16.0°	16.0°
θ_v	16.0°	16.0°
θ_{tilt}	82.8°	83.0°
θ_{rot}	63.9°	64.0°

Plane A Setup and Velocity Transformations

For Plane A measurements, a steel fence structure was placed around the test section and the probes (with 3-axis traverse) was suspended on the fence above the test section. Beams were transmitted through a glass top endwall for measurements on the bottom endwall, as shown in Figure A.4. Figure A.5 depicts the three coordinate transformations necessary to transform the non-orthogonal measurements to the orthogonal blade cascade coordinate system. Equations (A.4-A.6) document the equations for the coordinate transformations, and Table A.2 documents the system angles in the coordinate transformations.

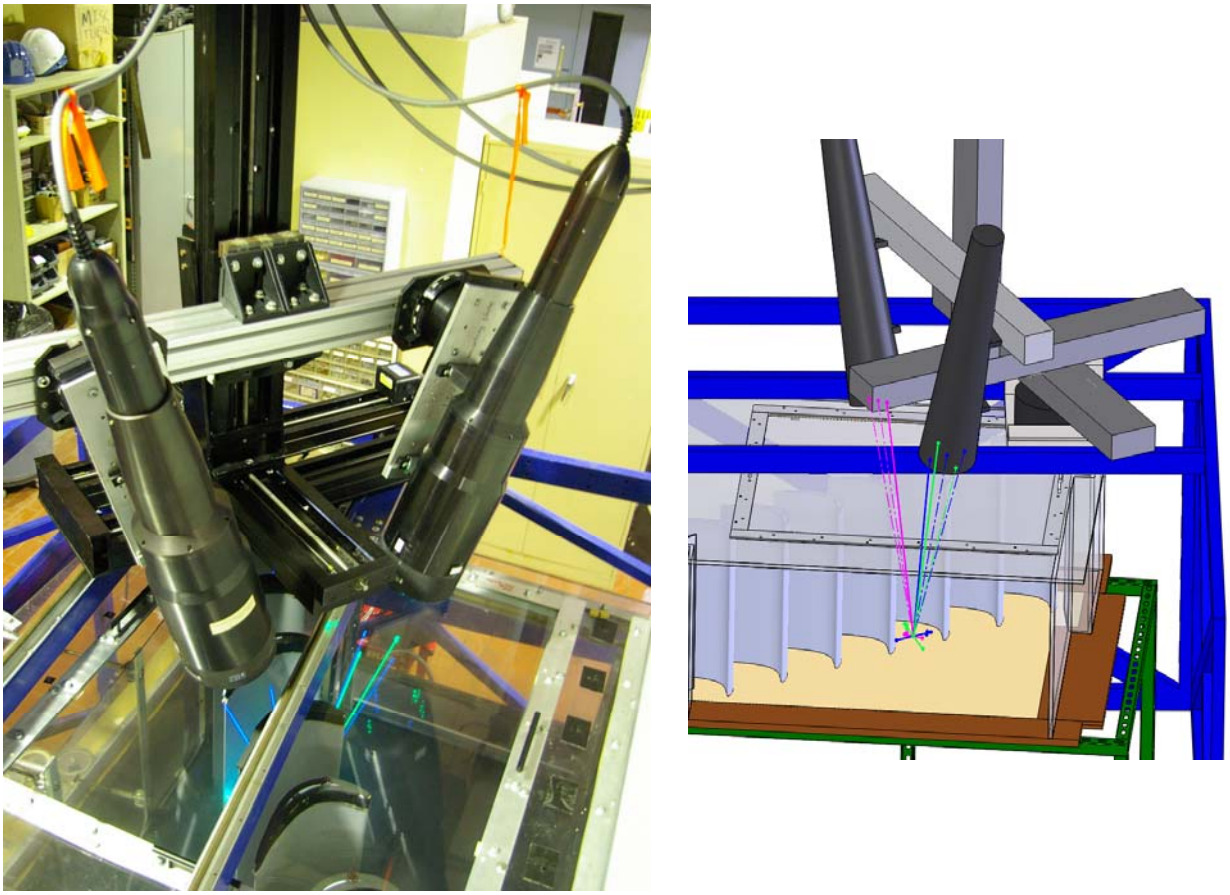

Figure A.4. Non-orthogonal three-component LDV configuration for measurements in Plane A.

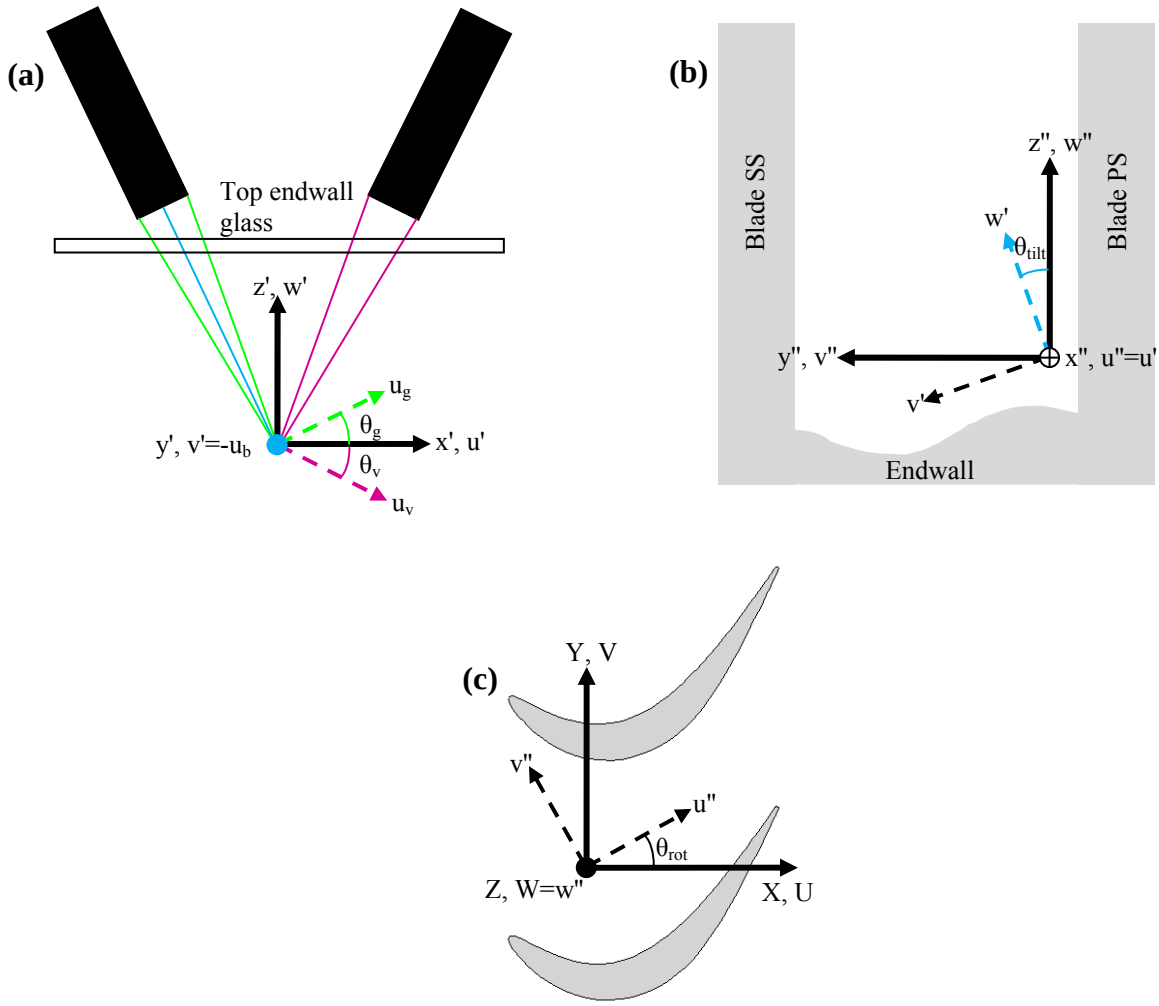

Figure A.5. (a) The non-orthogonal to orthogonal transformation; (b) the tilt transformation; and (c) the rotation transformation for Plane A measurements.

Non-orthogonal to orthogonal transformation:

$$u' = \frac{u_g \sin(\theta_v) + u_v \sin(\theta_g)}{\sin(\theta_g + \theta_v)}$$
$$v' = -u_b \qquad \text{(A.4)}$$
$$w' = \frac{u_g \cos(\theta_v) - u_v \cos(\theta_g)}{\sin(\theta_g + \theta_v)}$$

Tilt transformation:

$$u'' = u'$$
$$v'' = v' \cos(\theta_{tilt}) + w' \sin(\theta_{tilt}) \qquad \text{(A.5)}$$
$$w'' = -v' \sin(\theta_{tilt}) + w' \cos(\theta_{tilt})$$

Rotation transformation:

$$U = u''\cos(\theta_{rot}) - v''\sin(\theta_{rot})$$
$$V = u''\sin(\theta_{rot}) + v''\cos(\theta_{rot}) \quad \text{(A.6)}$$
$$W = w''$$

Table A.2 Velocity Transformation Angles for Plane A Measurements

Location	**0.15<y/P<0.27**		**0.27<y/P<0.66**		**0.66<y/P<0.8**	
	Flat	**Contour**	**Flat**	**Contour**	**Flat**	**Contour**
θ_g	17.5°	17.5°	17.5°	17.5°	17.5°	17.5°
θ_v	17.8°	17.5°	17.8°	17.5°	17.8°	17.5°
θ_{tilt}	6.0°	6.0°	0°	0°	0°	0°
θ_{rot}	15.6°	20.9°	22.6°	23.0°	1.4°	0°

Plane B Setup and Velocity Transformations

The probes were rotated on the steel fence structure for Plane B measurements, such that the beams would not interfere with the blades as shown inFigure A.6. Figure A.7 depicts the three coordinate transformations from non-orthogonal measurements to the orthogonal blade cascade coordinate system. Equations (A.7-A.9) document the equations for the coordinate transformations, and Table A.3 documents the system angles in the coordinate transformations.

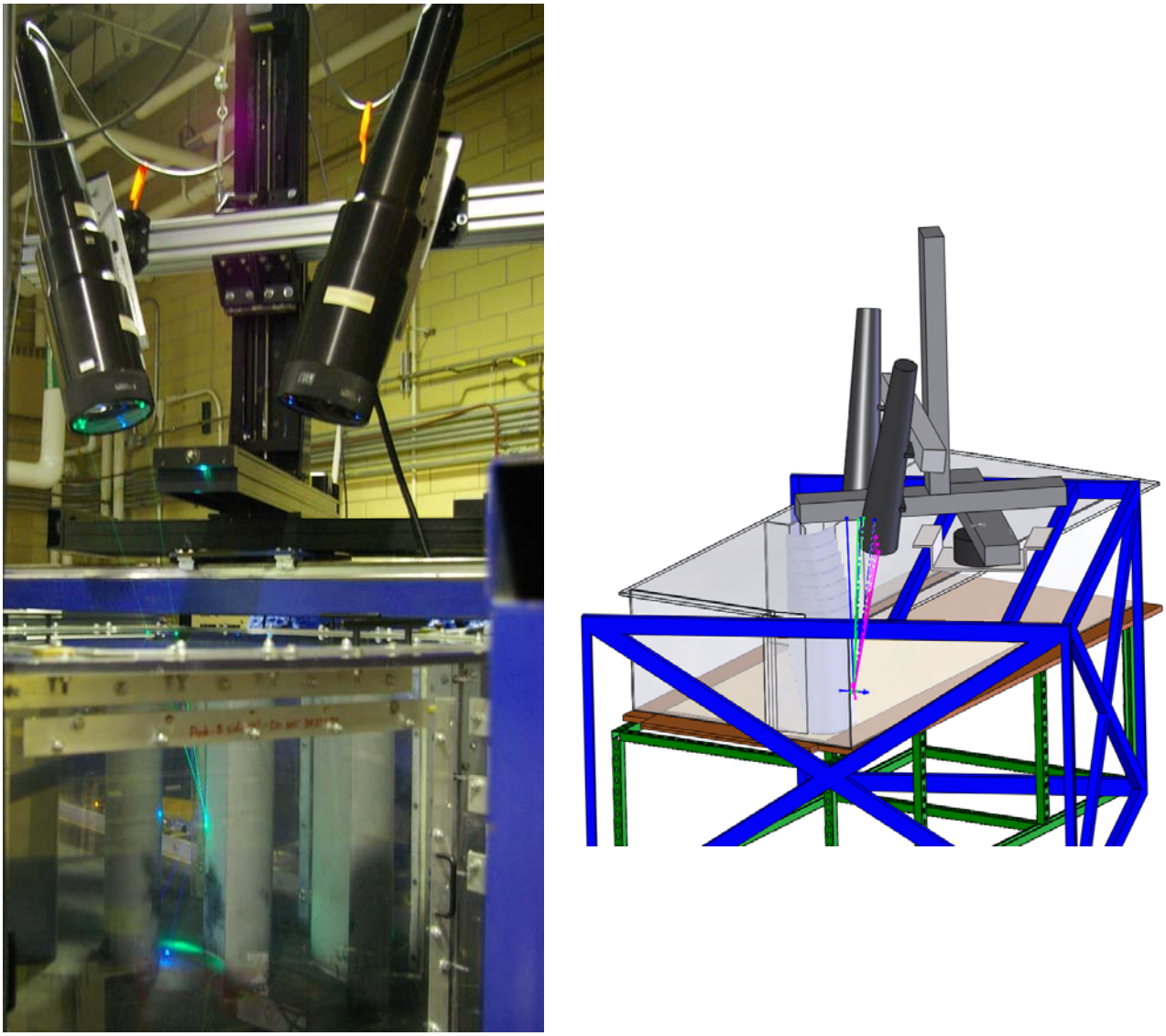

Figure A.6. Non-orthogonal three-component LDV configuration for measurements in Plane B downstream of the cascade.

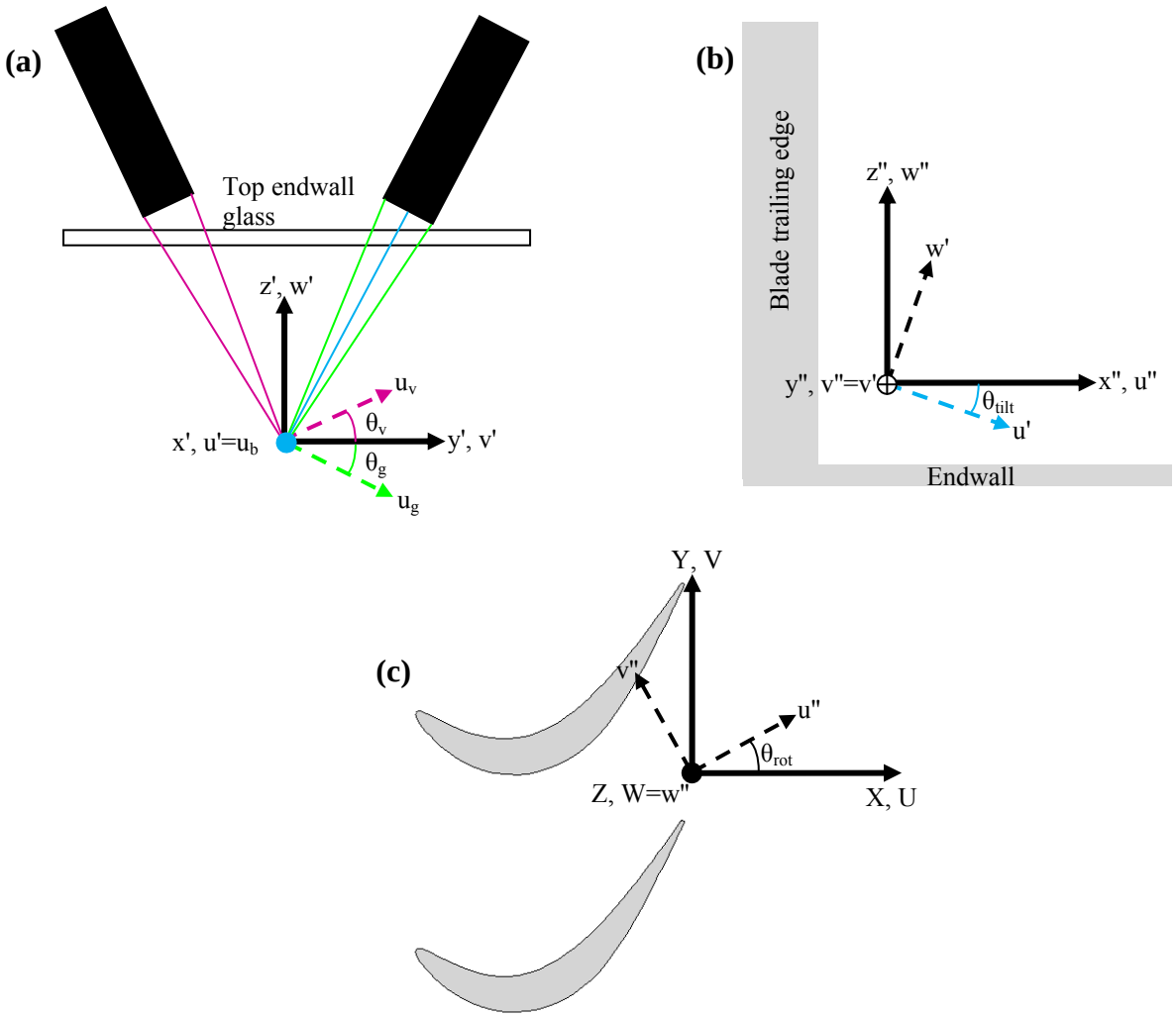

Figure A.7. (a) The non-orthogonal to orthogonal transformation; (b) the tilt transformation; and (c) the rotation transformation for Plane B measurements.

Non-orthogonal to orthogonal transformation:

$$
\begin{aligned}
u' &= u_b \\
v' &= \frac{u_g \sin(\theta_v) + u_v \sin(\theta_g)}{\sin(\theta_g + \theta_v)} \\
w' &= \frac{-u_g \cos(\theta_v) + u_v \cos(\theta_g)}{\sin(\theta_g + \theta_v)}
\end{aligned}
\tag{A.7}
$$

Tilt transformation:

$$
\begin{aligned}
u'' &= u' \cos(\theta_{tilt}) + w' \sin(\theta_{tilt}) \\
v'' &= v' \\
w'' &= -u' \sin(\theta_{tilt}) + w' \cos(\theta_{tilt})
\end{aligned}
\tag{A.8}
$$

Rotation transformation:

$$U = u'' \cos(\theta_{rot}) - v'' \sin(\theta_{rot})$$
$$V = u'' \sin(\theta_{rot}) + v'' \cos(\theta_{rot}) \quad \text{(A.9)}$$
$$W = w''$$

Table A.3 Velocity Transformation Angles for Plane B Measurements

	Flat	**Contour**
θ_g	15.5°	16.5°
θ_v	15.8°	16.0°
θ_{tilt}	5.8°	7.0°
θ_{rot}	0°	1.0°

Appendix B: Uncertainty Estimates for Reported Variables

Estimates of uncertainty in the experimental measurements are documented in this appendix. Both the partial derivative and sequential perturbation methods of Moffat [1] were used. In general, reported variables (Y) were a function of various measured variables (X_i):

$$Y = f(X_1, X_2, ..., X_n) \tag{B.1}$$

The total uncertainty of the reported variable is determined by the the root-sum-square of the contributions (C_i) of the individual measured variables:

$$\delta Y = \sqrt{C_1^2 + C_2^2 + ... + C_n^2} \tag{B.2}$$

The difference between the partial derivative and sequential perturbation methods was the method of determining the contributions (C_i) of the individual measured variables.

In the partial derivative method, the contribution of the i-th measured variable is formed from the partial derivative of the function for Y, multiplied by the total uncertainty of the measured variable (δX_i):

$$C_i = \frac{\partial Y}{\partial X_i} \delta X_i \tag{B.3}$$

For some reported variables (particularly the total pressure loss measurements), the partial derivative method was too complex or difficult to apply due to reliance on computer analysis (for numerical integration, for example). In that case, the sequential perturbation method was applied, whereby the uncertainty in a reported variable is estimated by sequentially perturbing the individual measured variables in the analysis code. The effect of a positive excursion of the i-th measured variable is computed by adding the measured variable uncertainty to its nominal value, and computing a new value for the reported variable. Then, the relative contribution of the positive excursion (C^+) is determined by the absolute value of the difference between the new reported variable value and its nominal value, without any excursions:

$$C_i^+ = \left| Y(X_1, ..., X_i + \delta X_i, ..., X_n) - Y(X_1, ..., X_i, ..., X_n) \right| \tag{B.4}$$

The effect of a negative excursion is determined in a similar way:

$$C_i^- = \left| Y(X_1, ..., X_i - \delta X_i, ..., X_n) - Y(X_1, ..., X_i, ..., X_n) \right| \tag{B.5}$$

The contribution of the i-th measured variable to the reported variable's uncertainty is determined by the average of the positive and negative excursion contributions:

$$C_i = \frac{C_i^+ + C_i^-}{2} \tag{B.6}$$

The individual contributions of the measured variables are combined to determine the total uncertainty in the reported variable as shown in Eq. B.2.

The total uncertainty of a measured variable is determined by the root-sum-square of the bias (B_i) and precision (P_i) uncertainties:

$$\delta X_i = \sqrt{B_i^2 + P_i^2} \tag{B.7}$$

The bias uncertainty generally arises from the measurement tools used to make the measurement, while the precision uncertainty is based on the statistical uncertainty of random measurements. In general, the measurements in this dissertation were obtained from multiple-sample experiments, where the reported variable is the mean of the individual means of repeated series of samples. In this case, the precision uncertainty is determined by multiplying the standard deviation (S) of the repeated series' means by the Student's t value for 95% confidence, and dividing by the square root of the number (N) of repeated series:

$$P_i = \frac{tS_i}{\sqrt{N_i}} \tag{B.8}$$

Nomenclature

A	area of inconel heater
B_i	bias uncertainty of i-th measured variable
C1, C2	constants in oil viscosity correlation
C_{ax}	blade axial chord
$C_{f,Uin}$	friction coefficient based on inlet freestream velocity
$C_{f,Uloc}$	friction coefficient based on local freestream velocity
C_i	contribution of i-th measured variable
C_p	specific heat of air
C_{Ptot}	total pressure loss coefficient
C_{SKE}	secondary kinetic energy coefficient

D	direct-line distance of light source from oil film patch
h	convective heat transfer coefficient
h_{oil}	height of oil film
H	half-distance from camera to light source, parallel to foil patch plane
I	current through inconel heater
k	thermal conductivity or turbulent kinetic energy
L	distance from foil patch to camera-light source intersection line
L_f	average distance between interferogram bands in oil film image
n_{air}	refractive index of air
n_{oil}	refractive index of oil
N_i	number of repeated series of measurements for precision uncertainty analysis
Nu	Nusselt number based on blade axial chord
$P_{1\text{-}5}$	measured pressures on 5-hole probe, where 1 is the total pressure port
P_{atm}	atmospheric (barometric) pressure
P_{dyn}	dynamic pressure
P_i	precision uncertainty of i-th measured variable
P_{ref}	reference pressure (blade stagnation pressure) for 5-hole probe pressures
P_s	static pressure
P_{tot}	total pressure
q''_w	convective heat flux at wall
q''_{tot}	total heat flux of inconel heater
q''_{cond}	conductive heat loss
q''_{rad}	radiative heat loss
$R_{1\Omega}$	resistance of 1Ω precision resistor
R_{air}	gas constant for air
Re_{in}	inlet Reynolds number based on axial chord
S_i	standard deviation of the mean of the multiple-sample set
St	Stanton number based on inlet freestream velocity

Δt	elapsed time during oil film interferometry test
t	Student's t-value
T	temperature
T_s	surface temperature measured with the IR camera
U_{in}	freestream velocity magnitude at cascade inlet
U_{loc}	local freestream velocity magnitude
u, v, w	axial, pitchwise, spanwise velocities in local freestream coordinate system
U, V, W	axial, pitchwise, spanwise velocities in cascade coordinate system
V	voltage across inconel heater
$V_{1\Omega}$	voltage across 1Ω precision resistor
V_s	streamwise velocity component
V_n	pitchwise velocity in a plane orthogonal to midspan streamwise flow direction
V_z	spanwise velocity in a plane orthogonal to midspan streamwise flow direction
X_i	i-th measured variable
δX_i	total uncertainty in i-th measured variable
Y	reported variable calculated from measured variables
δY	total uncertainty in reported variable

Greek

β	yaw angle
β_w	wall shear angle
γ	pitch angle
γ_{oil}	specific gravity of oil
ε	emissivity of surface
η	adiabatic effectiveness
θ	incidence angle of light on foil patch
λ	wavelength of light source
μ_{oil}	dynamic viscosity of oil
ν	kinematic viscosity
ρ	density
σ	Stefan-Boltzmann constant

Superscripts/Subscripts

′	fluctuating component of velocity
–	ensemble average
+	positive excursion (addition of uncertainty to mean)
-	negative excursion (subtraction of uncertainty from mean)
in	inlet freestream conditions
lex	lexan properties
f	foam properties
MDF	medium density fiberboard (MDF) properties
plen	plenum conditions
ref	reference conditions for oil viscosity correlation

Uncertainty in Inlet Conditions

The partial derivative method was used to estimate uncertainties in the inlet conditions to the blade cascades. Table B.1 lists the measured variables and their uncertainties. Note that precision uncertainties were estimated with a 95% confidence interval. The equations for derived quantities and the resulting uncertainties are listed in Table B.2.

Table B.1 Uncertainty in Measured Variables for Cascade Inlet Conditions

X_i	Mean	Bias Uncertainty	Precision Uncertainty	Total Uncertainty (δX_i)	Percent
T_{in}	299.5 K	±0.50 K	±0.07 K	±0.50 K	±0.17%
P_{atm}	97939 Pa	±6.18 Pa	±3.93Pa	±7.32 Pa	±0.01%
P_{dyn}	46.2 Pa	±0.13 Pa	±2.12 Pa	±2.13 Pa	±4.6%
ν	1.51e-5 m^2/s	--	--	--	--
C_{ax}	0.2184 m	--	--	--	--
R_{air}	287 J/kg-K	--	--	--	--

Table B.2 Uncertainty in Calculated Variables for Cascade Inlet Conditions

$Y=f(X_i)$	Mean	Total Uncertainty (δY)	Pct	Partial Derivatives
$\rho = \frac{P_{atm}}{R_{air} T_{in}}$	1.14 kg/m^3	±0.002 kg/m^3	±0.17%	$\frac{\partial \rho}{\partial P_{atm}} = \frac{1}{R_{air} T_{in}}$, $\frac{\partial \rho}{\partial T_{in}} = \frac{-P_{atm}}{R_{air} T_{in}^2}$
$U_{in} = \sqrt{\frac{2}{\rho} P_{dyn}}$	9.00 m/s	±0.21 m/s	±2.3%	$\frac{\partial U_{in}}{\partial \rho} = \frac{-P_{dyn}}{\rho^2}\left(\frac{2}{\rho} P_{dyn}\right)^{-1/2}$, $\frac{\partial U_{in}}{\partial P_{dyn}} = \frac{1}{\rho}\left(\frac{2}{\rho} P_{dyn}\right)^{-1/2}$
$Re_{in} = \frac{U_{in} C_{ax}}{\nu}$	167,750	±3,040	±1.8%	$\frac{\partial Re}{\partial U_{in}} = \frac{C_{ax}}{\nu}$

Uncertainty in Endwall Heat Transfer Coefficients

Heat transfer coefficients were reported in this dissertation in non-dimensional form. One form was as a Nusselt number based on blade axial chord, while the other was Stanton number based on inlet density, specific heat, and velocity. Several measured variables were experimentally obtained in order to calculate the non-dimensional heat transfer coefficient. Their mean values and estimated uncertainties are listed in Table B.3. Note that all precision uncertainties were calculated with a 95% confidence interval. The bias uncertainty for the surface temperature measurement with the IR camera was the root-sum-square of the thermocouple bias and the average deviation of the calibrated IR images from the thermocouple readings. Precision uncertainty for the surface temperatures was determined by taking the standard deviation of the means of six sets of IR images, where each set consisted of five images.

Uncertainty for reported variables was estimated using the partial derivative method. Several intermediate variables were calculated during the data reduction. Table B.4 lists the equations for the calculated quantities and their estimates of uncertainty.

Table B.3 Uncertainty in Measured Variables for Heat Transfer Coefficient Measurements

X_i	Mean	Bias Uncertainty	Precision Uncertainty	Total Uncertainty (δX_i)	Percent
$V_{1\Omega}$	1.891 V	±0.0067 V	±0.00031 V	±0.0068 V	±0.35%
$R_{1\Omega}$	1.0 Ω	±0.01 Ω	--	±0.01 Ω	±1.0%
V	88.2 V	±0.36 V	±0.000 V	±0.36 V	±0.00%
T_s	306.7 K	±0.83 K	±0.14 K	±0.85 K	±0.28%
T_{plen}	294.8 K	±0.50 K	±0.04 K	±0.50 K	±0.17%
T_{in}	286.7 K	±0.50 K	±0.29 K	±0.58 K	±0.18%
A	0.16657 m^2	--	--	--	--
t_{lex}	0.00318 m	--	--	--	--
k_{lex}	0.19 W/m-K	--	--	--	--
t_f	0.0127 m	--	--	--	--
k_f	0.032 W/m-K	--	--	--	--
t_{MDF}	0.0127 m	--	--	--	--
k_{MDF}	0.135 W/m-K	--	--	--	--
h_{plen}	5 W/m^2-K	--	--	--	--
C_p	1000 J/kg-K	--	--	--	--
k_{air}	0.026 W/m-K	--	--	--	--
ε	0.96	--	--	--	--
σ	$5.67x10^{-8}$ W/m^2-K^4	--	--	--	--

Table B.4 Uncertainty in Calculated Variables for Heat Transfer Coefficient Measurements

$Y=f(X_i)$	Mean	Total Uncertainty (δY)	Pct	Partial Derivatives
$I = \frac{V_{1\Omega}}{R_{1\Omega}}$	1.891 A	±0.020 A	±1.1%	$\frac{\partial I}{\partial V_{1\Omega}} = \frac{1}{R_{1\Omega}}, \quad \frac{\partial I}{\partial R_{1\Omega}} = \frac{-V_{1\Omega}}{R_{1\Omega}^2}$
$q''_{tot} = \frac{VI}{A}$	1001 W/m^2	±11.4 W/m^2	±1.1%	$\frac{\partial q''_{tot}}{\partial V} = \frac{I}{A}, \quad \frac{\partial q''_{tot}}{\partial I} = \frac{V}{A}$ $\frac{\partial q''_{tot}}{\partial A} = \frac{-VI}{A^2}$
$q''_{cond} = \frac{T_s - T_{plen}}{\frac{t_{lex}}{k_{lex}} + \frac{t_f}{k_f} + \frac{t_{MDF}}{k_{MDF}} + \frac{1}{h_{plen}}}$	8.0 W/m^2	±0.65 W/m^2	±8.1%	$\frac{\partial q''_{cond}}{\partial T_s} = \frac{1}{\frac{t_{lex}}{k_{lex}} + \frac{t_f}{k_f} + \frac{t_{MDF}}{k_{MDF}} + \frac{1}{h_{plen}}}$ $\frac{\partial q''_{cond}}{\partial T_{plen}} = \frac{-1}{\frac{t_{lex}}{k_{lex}} + \frac{t_f}{k_f} + \frac{t_{MDF}}{k_{MDF}} + \frac{1}{h_{plen}}}$
$q''_{rad} = \varepsilon\sigma\left(T_s^4 - T_{in}^4\right)$	114 W/m^2	±6.08 W/m^2	±5.3%	$\frac{\partial q''_{rad}}{\partial T_s} = 4\varepsilon\sigma T_s^3, \quad \frac{\partial q''_{rad}}{\partial T_{in}} = -4\varepsilon\sigma T_{in}^3$
$q''_w = q''_{tot} - q''_{cond} - q''_{rad}$	879 W/m^2	±12.9 W/m^2	±1.5%	$\frac{\partial q''_w}{\partial q''_{tot}} = 1, \quad \frac{\partial q''_w}{\partial q''_{cond}} = -1$ $\frac{\partial q''_w}{\partial q''_{rad}} = -1$
$h = \frac{q_w''}{T_s - T_{in}}$	43.8 W/m^2*K	±2.43 W/m^2*K	±1.5%	$\frac{\partial h}{\partial q_w''} = \frac{1}{T_s - T_{in}}, \quad \frac{\partial h}{\partial T_s} = \frac{-q_w''}{(T_s - T_{in})^2}$ $\frac{\partial h}{\partial T_{in}} = \frac{q_w''}{(T_s - T_{in})^2}$
$Nu = \frac{hC_{ax}}{k_{air}}$	358.0	±19.9	±5.6%	$\frac{\partial Nu}{\partial h} = \frac{C_{ax}}{k_{air}}$
$St = \frac{h}{\rho C_p U_{in}}$	0.0043	±0.00026	±6.1%	$\frac{\partial St}{\partial h} = \frac{1}{\rho C_p U_{in}}, \quad \frac{\partial St}{\partial \rho} = \frac{h}{C_p U_{in}}\frac{-1}{\rho^2}$ $\frac{\partial St}{\partial U_{in}} = \frac{h}{\rho C_p}\frac{-1}{U_{in}^2}$

Uncertainty in Adiabatic Film Effectiveness

Adiabatic film effectiveness was determined from surface measurements of temperature using the IR camera. Uncertainty in film effectiveness was determined by the partial derivative method. Table B.5 lists the uncertainties for the various measured quantities. The surface temperature bias uncertainty included the average difference between the calibrated endwall images and the wall-embedded thermocouples, and the surface temperature precision uncertainty was obtained from the standard deviation of the means of 8 separate sets of IR acquisitions, where each acquisition was the average of 5 images. Note that the confidence interval of the precision uncertainty is 95%. The overall uncertainty for effectiveness is listed in Table B.6. Although the percent uncertainty seems high, note that the mean value is very small (near zero) in the uncooled region of the endwall, where the uncertainty analysis predicted the highest absolute uncertainty.

Table B.5 Uncertainty in Measured Variables for Adiabatic Film Effectiveness

X_i	Mean	Bias Uncertainty	Precision Uncertainty	Total Uncertainty (δX_i)	Percent
T_{in}	318.0 K	±0.50 K	±0.04 K	±0.50 K	±0.16%
T_{plen}	299.8 K	±0.50 K	±0.02 K	±0.50 K	±0.17%
T_s	317.0 K	±0.57 K	±0.21 K	±0.60 K	±0.19%

Table B.6 Uncertainty in Calculated Variables for Adiabatic Film Effectiveness

$Y=f(X_i)$	Mean	Total Uncertainty (δY)	Pct	Partial Derivatives
$\eta = \frac{T_{in} - T_s}{T_{in} - T_{plen}}$	0.053	±0.042	±79.4%	$\frac{\partial \eta}{\partial T_{in}} = \frac{1}{T_{in} - T_{plen}} - \frac{T_s}{(T_{in} - T_{plen})^2}$, $\frac{\partial \eta}{\partial T_{plen}} = \frac{T_{in} - T_s}{(T_{in} - T_{plen})^2}$, $\frac{\partial \eta}{\partial T_s} = \frac{-1}{T_{in} - T_{plen}}$

Uncertainty in Friction Coefficients

Friction coefficients were measured by the oil film interferometry method described by Naughton and Sheplak [2], Holley, et al. [3], and Lynch and Thole [4]. The uncertainty analysis was based on the partial derivative method, and Table B.7 and Table B.8 contain the measured and calculated uncertainties, respectively. This analysis assumed that the dynamic pressure and temperature of the oil were constants during the run time, which was considered reasonable since: 1) the run times were on the order of 20 minutes and startup/shutdown were achieved within 30 seconds, and 2) the tunnel had a heat exchanger designed to hold the air temperature to within a degree. During the typical analysis, however, the temporal variation in dynamic pressure and tunnel temperature were taken into account by numerically integrating those quantities over the run time. It is expected that the assumption of constant dynamic pressure and temperature is conservative in this error analysis.

The wall shear angle (β_w) was determined by the direction of the limiting streamlines inferred from the oil film flow pattern. The uncertainty in the shear angle was determined from five separate measurements, where the bias uncertainty of the measurements was 1° and the precision uncertainty at a 95% confidence interval was 4°. The total uncertainty in shear angle is listed in Table B.8.

Table B.7 Uncertainty in Measured Variables for Friction Coefficients

X_i	Mean	Bias Uncertainty	Precision Uncertainty	Total Uncertainty (δX_i)	Percent
T_{in}	295.4 K	±0.50 K	±0.82 K	±0.96 K	±0.32%
P_{dyn}	39.1 Pa	±0.13 Pa	±0.35 Pa	±0.37 Pa	±0.95%
H	0.238 m	±0.00635 m	--	±0.00635 m	±2.7%
D	1.09 m	±0.00635 m	--	±0.00635 m	±0.6%
L_f	5.11×10^{-4} m	$\pm 2.55 \times 10^{-5}$ m	$\pm 8.59 \times 10^{-6}$ m	$\pm 2.70 \times 10^{-6}$ m	±5.3%
α_{tilt}	2°	--	--	--	--
λ	5.89×10^{-7} m	--	--	--	--
n_{air}	1.00027	--	--	--	--
n_{oil}	1.403	--	--	--	--
γ_{oil}	0.964	--	--	--	--
ν_{ref}	4.84×10^{-4} m^2/s	--	$\pm 1.70 \times 10^{-6}$ m^2/s	$--\pm 1.70 \times 10^{-6}$ m^2/s	±0.35%
T_{ref}	298.15 K	±0.5 K	--	±0.5 K	±0.17%
C1	774.8622	--	--	--	--
C2	2.6486	--	--	--	--
Δt	2235.6 sec	--	--	--	--
U_{in}	8.2 m/s	--	--	0.16 m/s	2.0%
U_{loc}	12.6 m/s	--	--	0.25 m/s	2.0%

Table B.8 Uncertainty in Calculated Variables for Friction Coefficients

$Y=f(X_i)$	Mean	Total Uncertainty (δY)	Pct	Partial Derivatives
$L = \sqrt{D^2 - H^2}$	1.0659 m	±0.00635 m	±0.6%	$\frac{\partial L}{\partial D} = \frac{D}{\sqrt{D^2 - H^2}}$, $\frac{\partial L}{\partial H} = \frac{H}{\sqrt{D^2 - H^2}}$
$\theta = \tan^{-1}\left(\frac{H}{L}\right)$	14.6°	±0.3°	±2.0%	$\frac{\partial \theta}{\partial H} = \frac{L}{\sqrt{H^2 + L^2}}$, $\frac{\partial \theta}{\partial L} = \frac{-H}{\sqrt{H^2 + L^2}}$
$h_{oil} = \frac{\lambda}{2\sqrt{n_{oil}^2 - n_{air}^2 \sin^2\theta}}$	$2.13\text{x}10^{-7}$ m	$\pm 3.05\text{x}10^{-10}$ m	±0.1%	$\frac{\partial h_{oil}}{\partial \theta} = \frac{\frac{1}{2}\lambda n_{oil}^2 \sin\theta\cos\theta}{\left(n_{oil}^2 - n_{air}^2 \sin^2\theta\right)^{3/2}}$
$\mu_{oil} = 1000\nu_{ref}\gamma_{oil}10^{\left(\frac{Cl}{C2+T_{in}} - \frac{Cl}{C2+T_{ref}}\right)}$	0.493 kg-m/s^2	±0.011 kg-m/s^2	±2.2%	
$C_{f,Uin} = \frac{L_f \mu_{oil}}{h_{oil} P_{dyn} \Delta t}$	0.0135	±0.00078	±5.8%	$\frac{\partial C_{f,Uin}}{\partial L_f} = \frac{\mu_{oil}}{h_{oil} P_{dyn} \Delta t}$, $\frac{\partial C_{f,Uin}}{\partial \mu_{oil}} = \frac{L_f}{h_{oil} P_{dyn} \Delta t}$ $\frac{\partial C_{f,Uin}}{\partial h_{oil}} = \frac{-L_f \mu_{oil}}{h_{oil}^2 P_{dyn} \Delta t}$, $\frac{\partial C_{f,Uin}}{\partial P_{dyn}} = \frac{-L_f \mu_{oil}}{h_{oil} P_{dyn}^2 \Delta t}$
$C_{f,Uloc} = \left(\frac{U_{in}}{U_{loc}}\right)^2 C_{f,Uin}$	0.00284	±0.00023	±8.1%	$\frac{\partial C_{f,Uloc}}{\partial U_{in}} = 2C_{f,Uin}\frac{U_{in}}{U_{loc}^2}$, $\frac{\partial C_{f,Uloc}}{\partial U_{loc}} = -2C_{f,Uin}\frac{U_{in}^2}{U_{loc}^3}$, $\frac{\partial C_{f,Uloc}}{\partial C_{f,Uin}} = \frac{U_{in}^2}{U_{loc}^2}$,
$\beta_w = \tan^{-1}\left(\frac{C_{f,y}}{C_{f,x}}\right)$	75.5°	±4.1°	±5.4%	

Uncertainty in 5-Hole Probe Aerodynamic Loss

The data analysis for the five-hole probe required the use of all five measured pressures with a calibration map to determine velocity, flow angle, total, and static pressure. This was performed with a Matlab routine, and thus it was appropriate to use the method of sequential perturbation to determine uncertainties in reported quantities.

Ten individual realizations were obtained at a highly turbulent location in the flowfield (see Paper 5 for details) where the total pressure loss was high and fluctuations in the readings were largest. The estimated uncertainties are thus expected to be representative of an upper bound for the rest of the flowfield. For each of the five measured pressures from the probe, precision uncertainty at a point location was determined by multiplying the standard deviation of the ten captures by the Student-t factor for 95% confidence interval, and dividing by the square root of the number of captures. Bias uncertainty for each of the five measured probe pressures was the root-sum-square of probe calibration bias uncertainty (0.3% of total velocity), the DAQ digitizing error ($5/2^{12}$ volts/bit) converted to pressure units, and the bias uncertainty of the transducers (0.25% full-scale, with 0-5"WC transducers). Table B.9 lists the uncertainties of the measured pressures. Sequential perturbation was then applied, using the total uncertainties of the five measured pressures propagated through the data analysis procedure, to determine uncertainty in the reported aerodynamic parameters. The results of the sequential perturbation are summarized in Table B.10.

Table B.9 Uncertainty in Measured Variables for Aerodynamic Loss

X_i	Mean	Bias Uncertainty	Precision Uncertainty	Total Uncertainty (δX_i)	Percent
P_{ref}-P_1	54.92 Pa	±1.04 Pa	±2.07 Pa	±2.32 Pa	±4.2%
P_{ref}-P_2	334.10 Pa	±3.55 Pa	±2.58 Pa	±4.39 Pa	±1.3%
P_{ref}-P_3	261.38 Pa	±3.55 Pa	±1.32 Pa	±3.79 Pa	±1.4%
P_{ref}-P_4	279.55 Pa	±1.90 Pa	±0.58 Pa	±1.99 Pa	±0.7%
P_{ref}-P_5	327.25 Pa	±2.22 Pa	±1.98 Pa	±2.97 Pa	±0.9%

Table B.10 Uncertainty in Calculated Variables for Aerodynamic Loss

$Y=f(X_i)$	Mean	Total Uncertainty (δY)	Percent
γ (pitch)	64.8°	±0.7°	±1%
β (yaw)	5.9°	±0.3°	±4.5%
P_{ref}-P_{tot}	45.81 Pa	±2.98 Pa	±6.5%
$P_{dyn} = P_{tot} - P_s$	237.85 Pa	±3.54 Pa	±1.5%
$C_{Ptot} = \frac{P_{tot} - P_{tot,in}}{\frac{1}{2}\rho U_{in}^2}$	1.7	±0.11	±6.4%
$V_n = -U\sin\beta + V\cos\beta$	-2.7 m/s	±0.25 m/s	±9.3%
$V_z = W$	2.1 m/s	±0.10 m/s	±4.4%
$C_{SKE} = \frac{V_n^2 + V_z^2}{U_{in}^2}$	0.245	±0.026	±10.8%

Uncertainty in LDV Flowfield Measurements

Measurements obtained with the laser Doppler velocimeter required a transformation from non-orthogonal coordinates to orthogonal coordinates aligned with the blade cascade (see Appendix A). Because this generally required a Matlab post-processing routine, the sequential perturbation method was chosen to propagate uncertainties through the coordinate transformation. Then, uncertainty in the derived quantities that utilized the orthogonal velocity components was obtained by the partial derivative method.

The transformation from non-orthogonal to orthogonal coordinates aligned with the blade cascade required the measurement of 1) the angle between probes, 2) the tilt of the probes relative to the vertical axis, and 3) the rotation of the probes relative to the cascade axial direction. Each of those angle measurements had a total uncertainty of 0.5°. Each of the three measured velocity components in the non-orthogonal coordinate system had a bias uncertainty of 1%. Those uncertainties were propagated through the coordinate transformation to produce an effective bias precision for the transformed velocities in the orthogonal coordinate system.

Ten individual realizations were obtained at a highly turbulent location in the flowfield (see Paper 3 for details). The estimated precision uncertainties are thus expected to be representative of an upper bound for the rest of the flowfield. Precision uncertainties were estimated for the transformed velocity components by multiplying the standard deviation of the ten realizations by the Student-t factor for 95% confidence interval, and dividing by the square root of the number of realizations. Table B.11 lists the uncertainties of the velocity components in the orthogonal coordinate system.

Uncertainties in derived quantities were obtained by the partial derivative method, and are summarized in Table B.12.

Table B.11 Uncertainty in Orthogonal Velocity Components Measured by the LDV

X_i	Mean	Bias Uncertainty	Precision Uncertainty	Total Uncertainty (δX_i)	Percent
U	3.57 m/s	±0.039 m/s	±0.0124 m/s	±0.041 m/s	±1.2%
V	1.70 m/s	±0.036 m/s	±0.0050 m/s	±0.036 m/s	±2.1%
W	-0.25 m/s	±0.043 m/s	±0.0048 m/s	±0.043 m/s	±17.3%
$\overline{u'}$	1.17 m/s	±0.013 m/s	±0.0050 m/s	±0.013 m/s	±1.2%
$\overline{v'}$	1.06 m/s	±0.012 m/s	±0.0052 m/s	±0.013 m/s	±1.2%
$\overline{w'}$	0.73 m/s	±0.015 m/s	±0.0049 m/s	±0.016 m/s	±2.2%
$\overline{u'v'}$	-0.53 m^2/s^2	±0.0058 m^2/s^2	±0.0062 m^2/s^2	±0.0085 m^2/s^2	±1.6%
$\overline{u'w'}$	-0.13 m^2/s^2	±0.0068 m^2/s^2	±0.0053 m^2/s^2	±0.0086 m^2/s^2	±6.4%
$\overline{v'w'}$	0.10 m^2/s^2	±0.0037 m^2/s^2	±0.0052 m^2/s^2	±0.0063 m^2/s^2	±6.1%

Table B.12 Uncertainty in Calculated Variables from LDV Measurements

$Y=f(X_i)$	Mean	Total Uncertainty (δY)	Percent	Partial Derivatives
u/U_{in}	0.436	±0.011	±2.6%	$\frac{\partial\beta}{\partial u}=\frac{1}{U_{in}}$, $\frac{\partial\beta}{\partial U_{in}}=\frac{-u}{U_{in}^2}$
v/U_{in}	0.207	±0.0065	±3.1%	$\frac{\partial\beta}{\partial v}=\frac{1}{U_{in}}$, $\frac{\partial\beta}{\partial U_{in}}=\frac{-v}{U_{in}^2}$
w/U_{in}	-0.030	±0.0053	±17.5%	$\frac{\partial\beta}{\partial w}=\frac{1}{U_{in}}$, $\frac{\partial\beta}{\partial U_{in}}=\frac{-w}{U_{in}^2}$
$\beta=\tan^{-1}\left(\frac{V}{U}\right)$	25.4°	±0.5°	±2.0%	$\frac{\partial\beta}{\partial U}=\frac{-1}{U^2\left[1+\left(\frac{V}{U}\right)^2\right]}$, $\frac{\partial\beta}{\partial V}=\frac{1}{U\left[1+\left(\frac{V}{U}\right)^2\right]}$
$\frac{V_s}{U_{in}}=\frac{U\cos(\beta_{ms})+V\sin(\beta_{ms})}{U_{in}}$	0.390	±0.041	±1.3%	$\frac{\partial V_s/U_{in}}{\partial U}=\frac{\cos(\beta_{ms})}{U_{in}}$, $\frac{\partial V_s/U_{in}}{\partial V}=\frac{\sin(\beta_{ms})}{U_{in}}$, $\frac{V_s}{U_{in}}=\frac{-(U\cos(\beta_{ms})+V\sin(\beta_{ms}))}{U_{in}^2}$
$\frac{V_n}{U_{in}}=\frac{-U\sin(\beta_{ms})+V\cos(\beta_{ms})}{U_{in}}$	0.283	±0.036	±1.6%	$\frac{\partial V_n/U_{in}}{\partial U}=\frac{-\sin(\beta_{ms})}{U_{in}}$, $\frac{\partial V_s/U_{in}}{\partial V}=\frac{\cos(\beta_{ms})}{U_{in}}$, $\frac{V_s}{U_{in}}=\frac{-(-U\sin(\beta_{ms})+V\cos(\beta_{ms}))}{U_{in}^2}$
$V_z/U_{in}=W/U_{in}$	-0.030	±0.0053	±17.5%	$\frac{\partial V_z/U_{in}}{\partial W}=\frac{1}{U_{in}}$, $\frac{\partial V_z/U_{in}}{\partial U_{in}}=\frac{-W}{U_{in}^2}$
$\frac{k}{U_{in}^2}=\frac{\left(\overline{u'}^2+\overline{v'}^2+\overline{w'}^2\right)}{U_{in}^2}$	0.023	±0.0011	±4.9%	$\frac{\partial k/U_{in}^2}{\partial\overline{u'}^2}=\frac{\overline{u'}}{U_{in}^2}$, $\frac{\partial k/U_{in}^2}{\partial\overline{v'}^2}=\frac{\overline{v'}}{U_{in}^2}$, $\frac{\partial k/U_{in}^2}{\partial\overline{w'}^2}=\frac{\overline{w'}}{U_{in}^2}$, $\frac{\partial k/U_{in}^2}{\partial U_{in}}=\frac{-2\left(\overline{u'}^2+\overline{v'}^2+\overline{w'}^2\right)}{U_{in}^3}$
$\overline{u'}/U_{in}$	0.143	±0.0037	±2.6%	$\frac{\partial\overline{u'}/U_{in}}{\partial\overline{u'}}=\frac{1}{U_{in}}$, $\frac{\partial\overline{u'}/U_{in}}{\partial U_{in}}=\frac{-\overline{u'}}{U_{in}^2}$
$\overline{v'}/U_{in}$	0.130	±0.0034	±2.6%	$\frac{\partial\overline{v'}/U_{in}}{\partial\overline{v'}}=\frac{1}{U_{in}}$, $\frac{\partial\overline{v'}/U_{in}}{\partial U_{in}}=\frac{-\overline{v'}}{U_{in}^2}$
$\overline{w'}/U_{in}$	0.089	±0.0028	±3.2%	$\frac{\partial\overline{w'}/U_{in}}{\partial\overline{w'}}=\frac{1}{U_{in}}$, $\frac{\partial\overline{w'}/U_{in}}{\partial U_{in}}=\frac{-\overline{w'}}{U_{in}^2}$

References

[1] Moffat, R. J., 1988, "Describing the Uncertainties in Experimental Results," *Exp. Therm Fluid Sci.*, **1**, pp. 3-17.

[2] Naughton, J. W., and Sheplak, M., 2002, "Modern Developments in Shear-Stress Measurement," *Prog. Aerosp. Sci.*, **38**(6-7), pp. 515-570.

[3] Holley, B. M., Becz, S., and Langston, L. S., 2006, "Measurement and Calculation of Turbine Cascade Endwall Pressure and Shear Stress," *J. Turbomach.*, **128**(2), pp. 232-239.

[4] Lynch, S. P., and Thole, K. A., 2008, "The Effect of Combustor-Turbine Interface Gap Leakage on the Endwall Heat Transfer for a Nozzle Guide Vane," *J. Turbomach.*, **130**(4), p. 041019.

Appendix C: Design and Construction of Endwalls

Insulated endwalls were desired for the heat transfer and film cooling studies discussed in this dissertation. A process was developed to create endwall contours using two-part expanding polyurethane foam in a mold constructed from stereolithography (SLA) material. This allowed for a rapid and accurate mold design that could be used to construct multiple endwalls. This appendix dscusses some of the design features and construction considerations for the various endwalls.

All foam endwalls were constructed from a two-part polyurethane foam from US Composites (http://shopmaninc.com/foam.html). The foam nominal (free-rise) density was 4 lb/ft^3, which provided a low thermal conductivity of approximately 0.03 W/m-K. The polyurethane foam had a limited shelf life, so more foam was ordered after approximately 6 months of shelf time. For best performance, the two components were mixed for 20 seconds using a dual-propeller mixer in a hand drill, operated at the highest possible speed. Note that the foaming and curing processes are exothermic and generate a significant amount of heat which can damage SLA mold materials if not properly cooled and constrained during the entire molding process.

Initial mold preparation generally required a significant amount of hand sanding on the contoured endwall surface to make it glassy smooth. Coarse (200 grit) to 1200 grit roughnesses were used successively until the surface was extremely smooth. The rest of the mold surfaces exposed to foam were covered with Teflon-covered mold release tape, which had to be replaced regularly during heavy molding use. All surfaces were sprayed with PolyCast 2300 mold release agent immediately before making a part. The release agent was brushed lightly over all surfaces to ensure an even and complete coating before filling the mold with the thoroughly-mixed two-part foam.

The smoothest contoured endwall foam surfaces were obtained when the molds were placed at a 45° angle with the contoured surface on top, facing downward, so that the foam grew upward to meet the contoured surface. The molds were filled with enough foam to completely fill the entire mold cavity uniformly and spill out of approximately five small relief holes (~6.35 mm) for five seconds, which ensured good packing of the foam within the mold.

Pack-B Endwall Contour Molds and Heaters

It was determined early in the endwall contour design phase that a stiff, non-frangible surface would be required to provide a firm adhesion surface for an inconel film heater. SLA was chosen as a logical material since it could be rapidly and accurately constructed in the shape of the non-axisymmetric contour, and had relatively low thermal conductivity. However, it was desirable to minimize conduction losses in the endwall so a low thermal conductivity material like foam was also necessary. The design of the endwall attempted to incorporate both materials into a multi-layer construction shown in Figure C.1. A 1-D conduction analysis was performed to determine the maximum allowable thickness of SLA versus foam, and the resulting expected conduction loss through the endwall. The final design had a 3.18 mm thick SLA top surface over a foam surface with a minimum thickness of 12 mm. The expected conduction loss was less than 2% of the input heat flux, which was deemed acceptable.

The Pack-B foam endwalls were constructed from SLA molds shown in Figure C.2. The mold was designed to disassemble around the formed endwall to minimize de-molding time and eliminate damage to the molded part. A separate top lid made of lexan was constructed and clamped to the assembled mold by eight C-clamps around the perimeter of the lid. The clamping strength during a mold was a compromise between minimizing leakage out from the sides of the mold, and the potential to crack or deform the SLA mold during the vigorous foaming process.

For heat transfer coefficient studies, a constant heat flux surface was designed and manufactured through the help of Electrofilm Manufacturing. Three separate heaters were constructed to cover the entire cascade endwall as shown in Figure C.3. Each heater was multi-layer including an inconel circuit placed between two Kapton sheets that was then covered by a vacuum-deposited, thin copper layer. The Kapton-encapsulated heater was 0.007” (0.18mm) thick, and the copper top layer was 0.0014” (0.04mm) thick. The circuit was designed to ensure a uniform heat flux surface, and the pattern of the traces can be seen in Figure C.3. The center heater (in red) was designed to be removable from the cascade for flat or contoured endwall studies.

It was quite challenging to provide a constant heat flux for the contoured endwall surface since the surface itself was not wrappable. The isoheight contours in Figure C.4 show the varying shape of the endwall, which was complex enough that a simple flat sheet (such as the inconel heater) could not follow the contours. After numerous tries, a heater surface was

designed by putting in relief slits into the heater along with breaking up the heater into two different heater surfaces. See Figure C.4 for a depiction of some of the many iterations on the contoured endwall heater design. The contoured heater itself was the same construction as was the flat endwall heater using the sandwich of inconel and Kapton with a copper layer. The installation of the heater onto the SLA endwall form was completed at Electrofilm by placing pressure-sensitive adhesive on the heater and using a vacuum-bag sealing technique to conform the heater to the SLA. That assembly was then attached to the porous foam and MDF multi-layer endwall structure described earlier.

For adiabatic effectiveness studies, film cooling holes were drilled into the foam endwalls by a mill with a rotating head. The foam parts were held in a fixture on an angle table, which in combination with the rotating mill head allowed for any type of compound angle. Five holes were located near the pressure side, in the region of high heat transfer coefficients seen from the earlier studies. The angle of the holes relative to the surface were limited, in accordance with engine considerations that the holes might be fed from a platform under the blade. Two types of hole directions were considered: aligned with the endwall streakline direction, and 45 degrees counter-clockwise to the endwall streamwise direction. The two types of holes are depicted in Figure C.5 for the flat and contoured endwalls. Figure C.5 also shows a foam contour with film holes, and the smoothness of the contour surface when prepared properly.

Pack-H1 Endwall Contour Molds and Heaters

The Pack-H1 endwall mold and heater design benefitted significantly from the lessons learned in the Pack-B study. A similar composite endwall construction was developed, with a 3.2 mm (1/8”) thick SLA top surface for heater adhesion and foam below. However, for the Pack-H1 endwall, the foam was poured directly onto the bottom sides of the SLA, integrally molding the foam to the SLA and providing a strong stiff surface.

The flat endwall heater design had to fold over the rim seal geometry upstream of the blade, but otherwise was similar in design to the Pack-B endwall. The circuit pattern for the heater was designed for uniform heat flux and the same thickness of copper was adhered to the top surface of the heater. Figure C.6 shows images of the flat endwall heater, the composite SLA-foam endwall, and the heater adhered to the composite endwall by thin (0.81 mm) double-sided tape.

The contoured endwall was constructed using a similar type of mold as for the Pack-B work. The removable mold sidewalls were designed to create a pocket under the platform in the foam to simulate a platform gap plenum below the endwall, as shown in Figure C.7. The other major design feature of the mold was the use of wooden dowels with threaded inserts in them, which were screwed to the top lid of the mold. The expansion and curing of the foam in the mold meant that the dowels were integrally molded into the foam, providing a means of fastening the contoured endwall with screws for the endwall misalignment studies.

For the endwall heat transfer coefficient studies, a thin SLA sheet was integrally molded into the top surface of the foam to provide a firm non-frangible surface for the heater to adhere to. The heater design shown in Figure C.8 incorporated strain-relief slits to allow the heater to conform to the contour surface. The same vacuum-bag procedure developed at Electrofilm was also used for construction of these heaters. The bottom image in Figure C.8 shows two endwall heater assemblies with the copper top surface visible.

The contour molds were used to create foam endwalls for the adiabatic film effectiveness study. The endwalls had the same integrally-molded dowels with threaded inserts for endwall attachment. Twelve film cooling holes were drilled in three grouped locations around the endwall, as seen in Figure C.9. It was desired to keep the surface angles of the holes to less than 35° to minimize jet separation, which meant that some of the holes would not breatk through the thick part properly. To provide cooling to the holes, pockets were milled in the underside of the endwall. The holes were drilled with the angle table and rotating-head mill used for the Pack-B work.

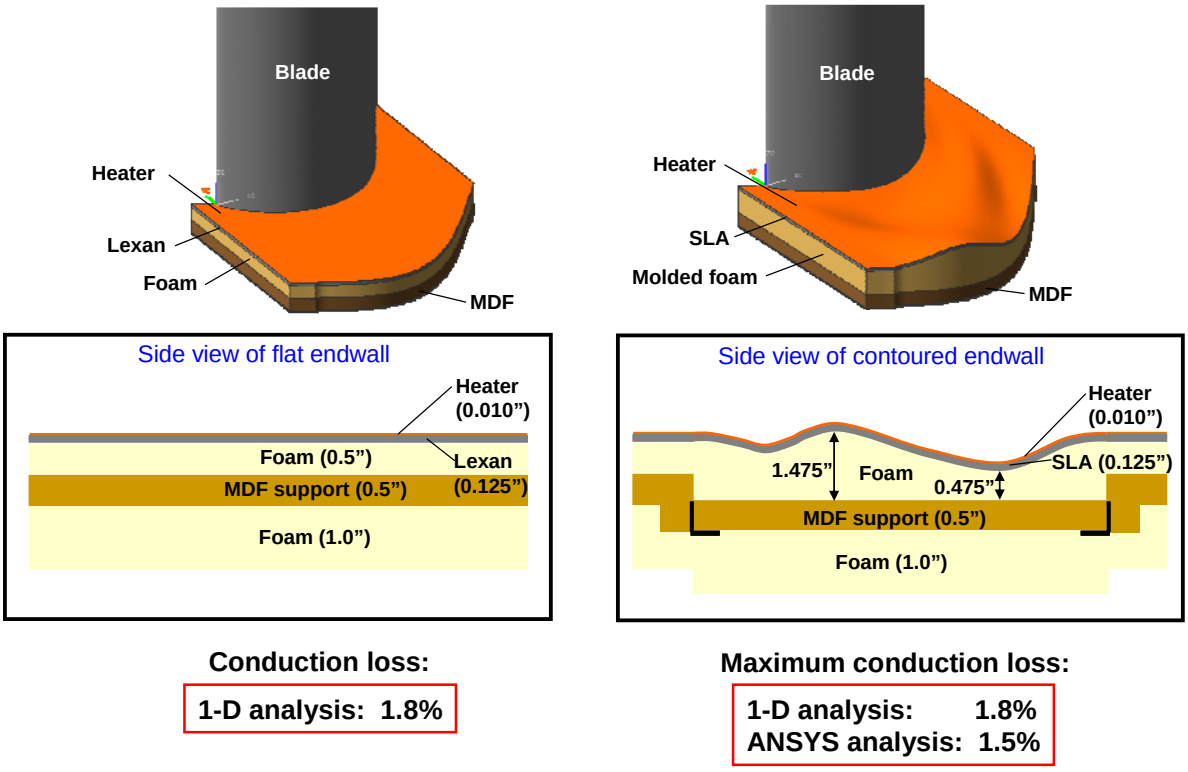

Figure C.1. Pack-B multi-layer endwall designs for heat transfer coefficient studies.

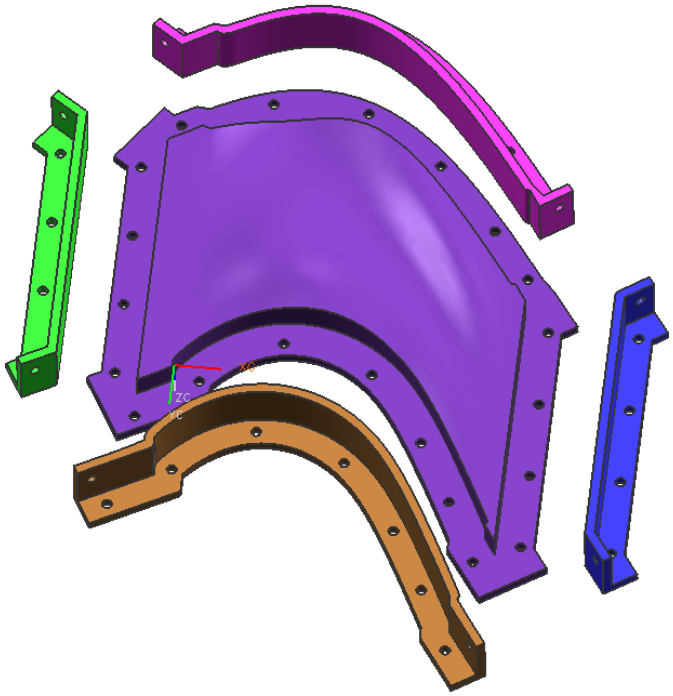

Figure C.2. Contoured endwall foam mold components (exploded assembly).

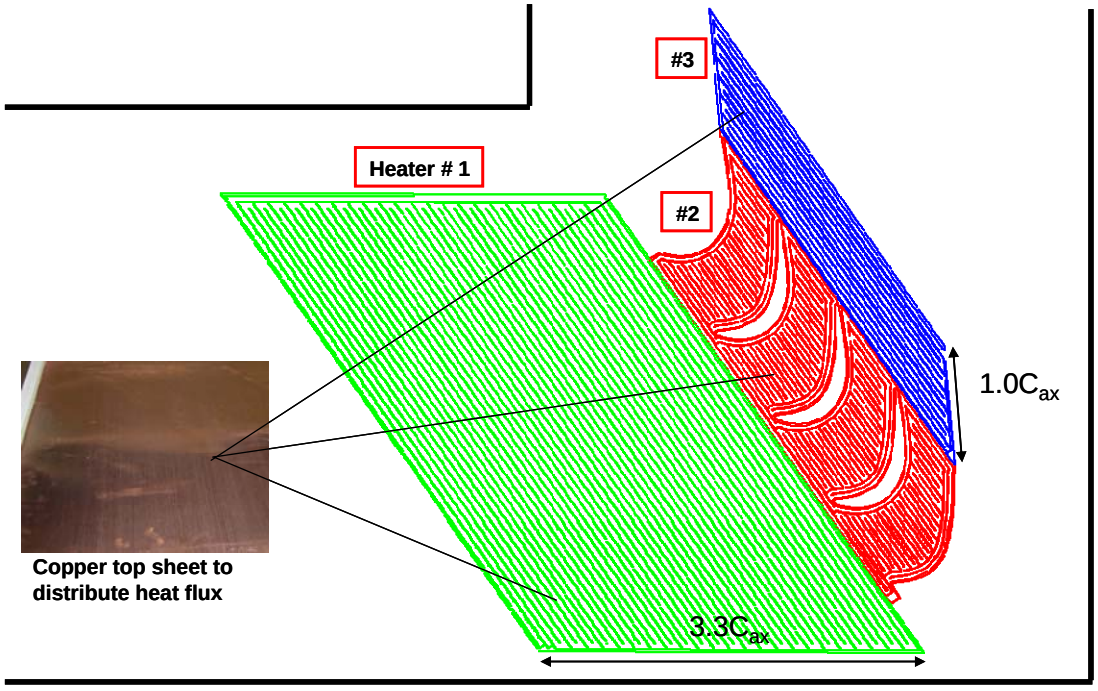

Figure C.3. Three separate heaters were designed to cover the cascade endwall.

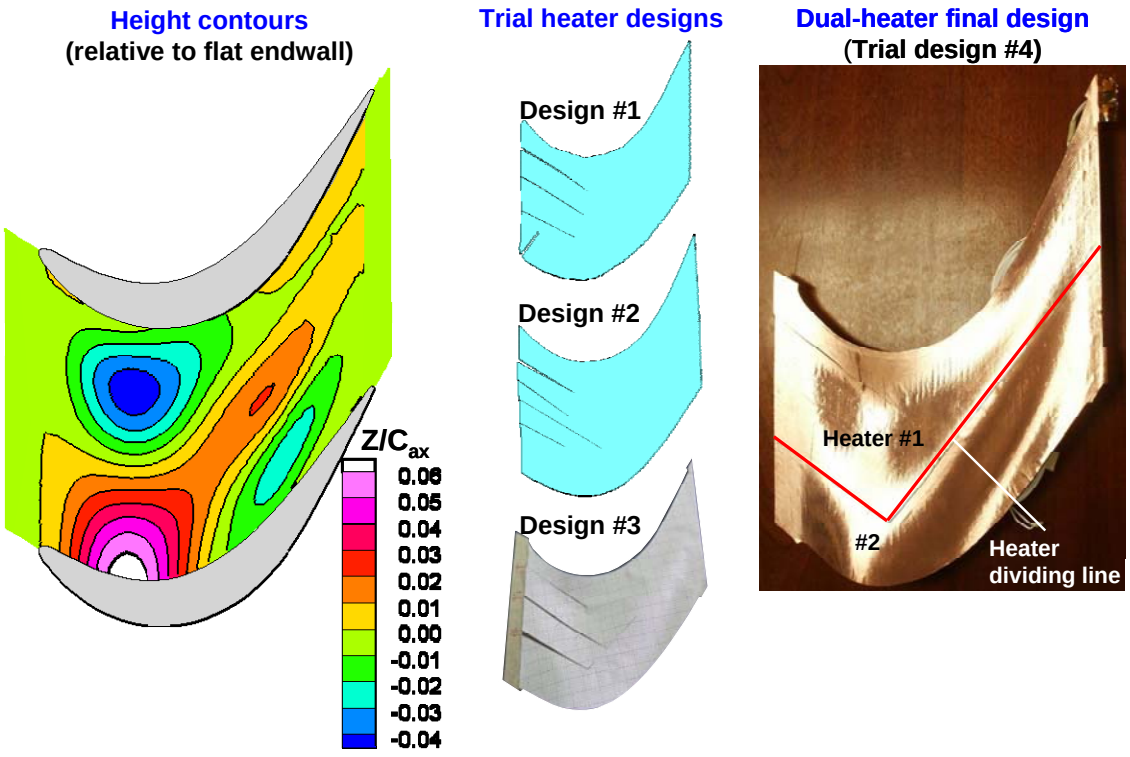

Figure C.4. Pack-B endwall contour isoheight and various trial heater patterns intended to cover the surface.

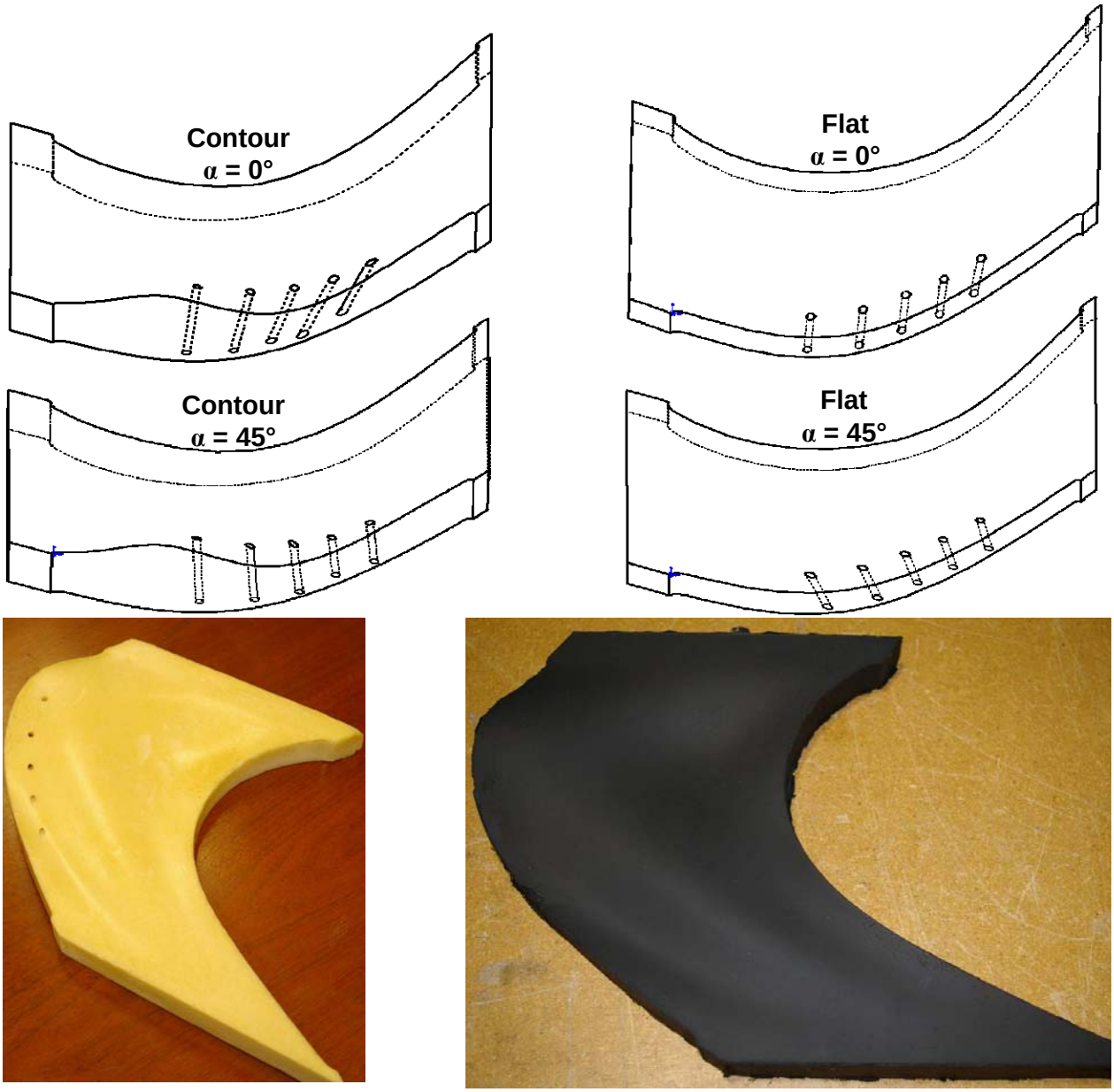

Figure C.5. Flat and contoured endwall film coolling configurations, and images of molded parts.

Bottom side of heater

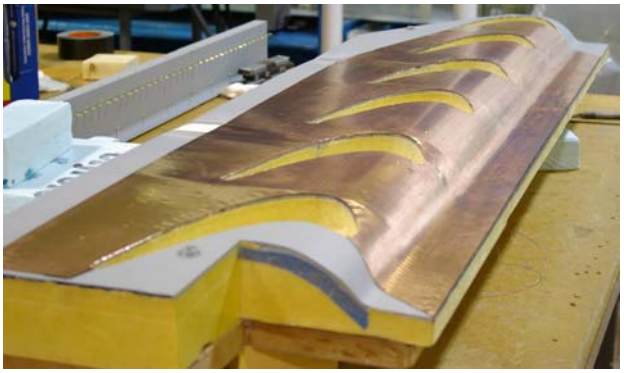

Heater installed on SLA

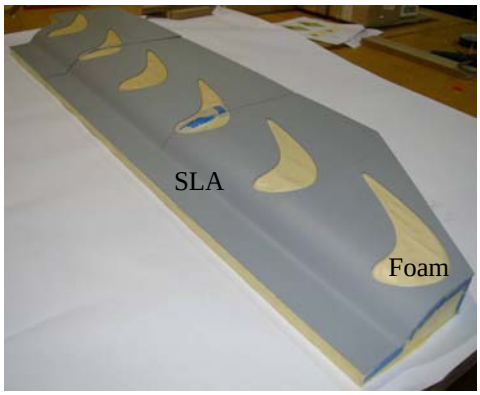

SLA/foam composite endwall

Figure C.6. The flat endwall heater and installation on a SLA-foam composite endwall.

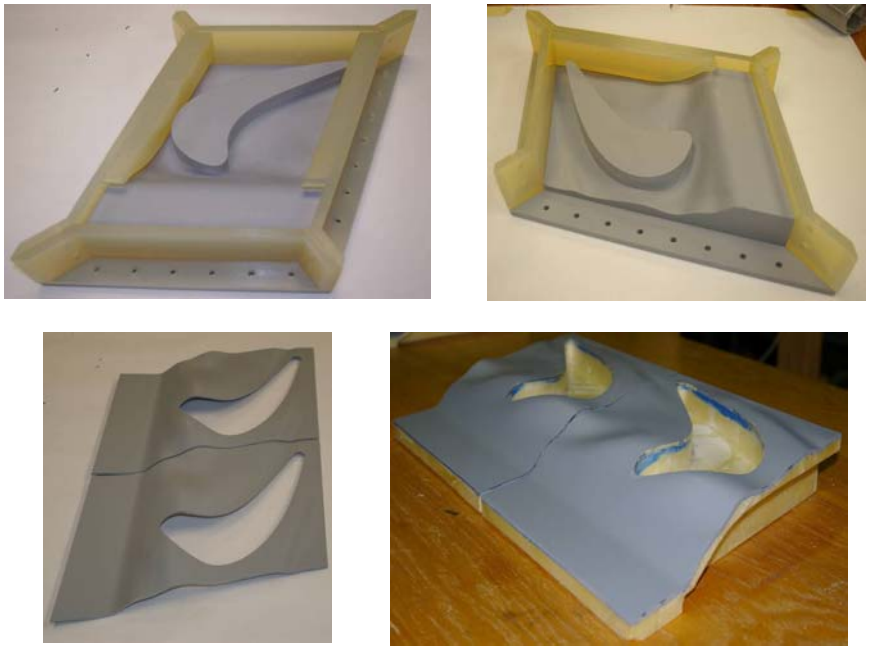

Figure C.7. Pack-H1 contoured endwall mold and SLA/foam composite endwall.

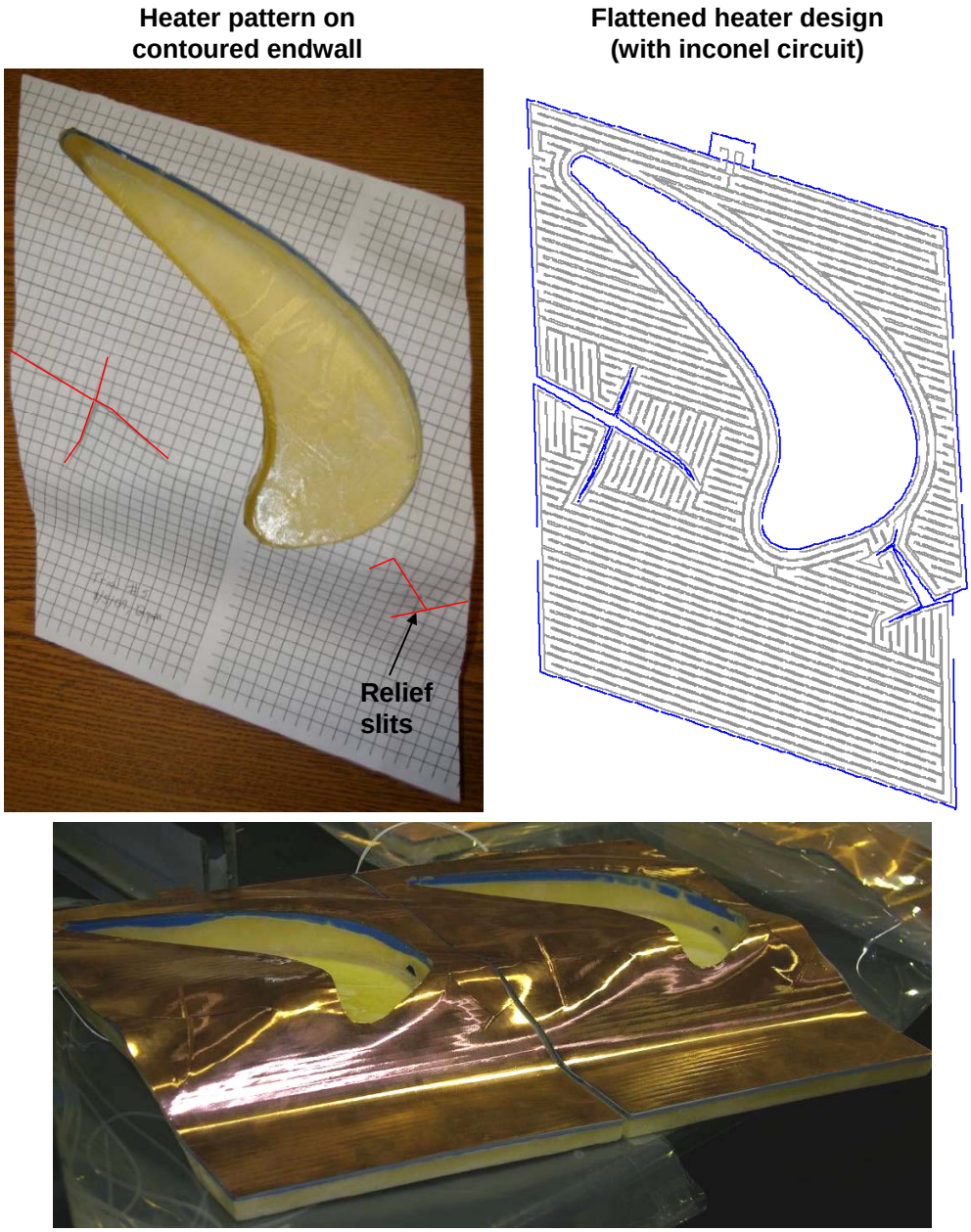

Figure C.8. Pack-H1 contoured endwall heater design, flattened circuit pattern, and installation on SLA-foam composite endwall.

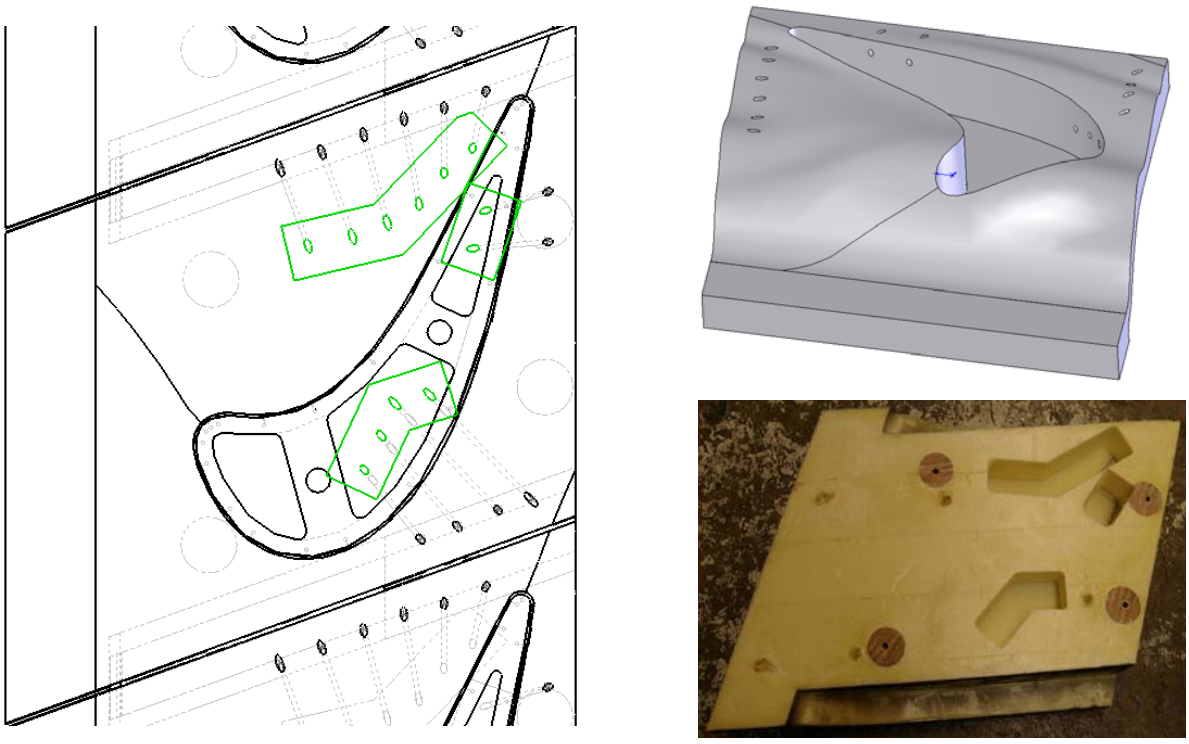

Figure C.9. Pack-H1 contoured endwall film cooling hole design and hole breakout pockets on underside of endwall.

Appendix D: Comparison of CFD to Measurements

This appendix describes some additional comparisons to the computational predictions in Paper 2 of the dissertation, with the intent of determining flow conditions where the CFD agreed well or poorly with experimental measurements described in Paper 3. The flat and contoured endwall simulations without film cooling were used for the comparisons in this appendix. Refer to Paper 2 for more details of the geometry, size, and benchmarking of the grids. Paper 3 describes the flowfield measurement locations, where Plane A is an axial plane located $0.2C_{ax}$ downstream of the leading edge. Boundary layer profiles were obtained at three locations in Plane A, as well as along the path of an inlet streakline determined from the oil flow visualization.

Figure D.1 shows the predictions of endwall static pressure coefficient for the flat and contoured endwalls, as well as the midspan static pressure which is the same for both geometries. Along the inlet streakline path from S1 to S3 in Figure D.1a, the static pressure is decreasing and the three-dimensional turbulent boundary layer is subjected to a favorable pressure gradient. Between S2 and S3, the contour produces a slightly more favorable gradient than the flat endwall. Further along the streakline path near the suction side, however, the contour shows less of a favorable pressure gradient than the flat endwall, as the depression in the contour acts to diffuse the near-wall flow.

Endwall heat transfer predictions are compared to measurements in Figure D.2. Upstream of the cascade, the predictions are slightly higher than the measurements, but the trend of heat transfer decreasing faster than for a 2D boundary layer is captured for both the flat and contoured endwalls. However, toward the end of the streakline path, the predictions do not capture an increase in heat transfer which might be caused by the suction side leg of the horseshoe vortex. Friction coefficients in Figure D.3 also agree well for locations up to station S3, suggesting that the CFD was able to predict the favorable pressure gradient flow with moderate skew (S3 had less than 40 degrees of skew relative to the freestream).

The endwall static pressure across Plane A ranged from high values near station A1 to low values near station A3. It is apparent in Figure D.1 that the contoured endwall results in a decrease in the pressure gradient across the passage, which is consistent with the design intent for non-axisymmetric contouring. Flow approaching the pressure side of the passage experiences

an adverse pressure gradient (which contributes to the horseshoe vortex separation upstream), while flow coming around the suction side (station A3) generally experiences a neutral or slightly favorable pressure gradient.

Mean flowfield comparisons at Plane A are shown in Figure D.4, where the contours are of streamwise velocity and the vectors are secondary flow components as described in Paper 3. In general, the predicted and measured mean streamwise velocities agree well near midspan for both endwall geometries, as expected. However, there are some significant differences in both the streamwise velocity near the pressure side as well as the secondary flow indicated by the vectors. The prediction for the flat endwall in Figure D.4b indicates higher streamwise velocities near the pressure side and a vortex closer to the endwall than is seen in the measurements in Figure D.4a. This could be a contributing factor to the overprediction of endwall heat transfer levels near the pressure side for the flat endwall, as described in Paper 2. While the contoured endwall predictions in Figure D.4d do indicate the elimination of a vortical structure in the secondary flow vectors relative to a flat endwall, the prediction suggests much larger separation velocities near the pressure side, which are a contributing factor to the misprediction of the heat transfer augmentation in Paper 2. In general, the CFD did not do well in capturing the physics of the complex flow developing downstream of the HS vortex separation, where both extremely high levels of skew (>70 degrees) and adverse pressure gradients are present.

Figure D.5 shows mean secondary vectors overlaid on contours of turbulent kinetic energy in Plane A. Although the CFD does predict a slight increase in peak TKE near the endwall for the flat versus contoured endwalls, the magnitudes of the predictions are lower than the measured value, and the peak TKE is more concentrated than in the measurements. It is possible that the measured TKE includes contributions of deterministic unsteadiness due to the bimodal nature of the horseshoe vortex, although histograms of the velocity data did not indicate bimodal behavior. The concentrated TKE in the predictions is likely a contributing factor to the sharp heat transfer gradients seen in the endwall heat transfer predictions in Paper 2.

Measured and predicted skew angles in Figure D.6 show that the boundary layer near the pressure side contains extremely high levels of skew. The trend of higher skew for the flat endwall versus the contoured endwall is captured by the simulations, but the magnitude of skew is not. In particular, the flat endwall prediction overestimates the amount of skew by

approximately 20 degrees at the wall. The simulation has a difficult time capturing the influence of the passage vortex on the endwall boundary layer.

The difficulty in capturing the effect of the passage vortex is more apparent when comparing the predicted to measured endwall heat transfer in Figure D.7, or the predicted to measured friction coefficients in Figure D.8. In Figure D.7 the prediction shows a very steep heat transfer gradient near the pressure side that was not captured in the measurements, although the measurement technique may not have been able to capture that adequately. However, the simulation also overpredicts heat transfer from y/P=0.1 to 0.4, which is associated with the location of the passage vortex in the flowfield measurements. Friction coefficients in Figure D.8 also indicate an overprediction of the effect of separated and reattaching flow near the pressure side, with the measurements showing lower levels of skin friction at station A1 near the pressure side than is indicated by the predictions.

In summary, the steady RANS prediction appears to do well at matching flow and heat transfer measurements in the region of attached flow with a favorable pressure gradient and moderate levels of skew. However, more work is necessary to adequately capture the physics of separated and reattaching flows, particularly in regions with high skew and adverse pressure gradients.

Nomenclature

C_{ax}	axial chord of blade
C_f	friction coefficient, $C_f = \dfrac{\tau_w}{1/2\,\rho U_{edge}^2}$
C_p	static pressure coefficient, $C_{Pstatic} = \dfrac{p_s - p_{s,in}}{1/2\,\rho U_{in}^2}$
h	heat transfer coefficient, $h = q''_w / (T_w - T_{in})$
HS	horseshoe vortex
k	turbulent kinetic energy (TKE), $k = 1/2\left(\overline{u'^2} + \overline{v'^2} + \overline{w'^2}\right)$
P	blade pitch
p	static pressure
Pr	Prandtl number

PS	pressure side
q''_w	wall heat flux
Re_s	streamwise Reynolds number, $Re_s = sU_{edge} / \nu$
s	distance along streamwise direction
S	blade span
SS	suction side
St	Stanton number, $St = h/\rho C_p U_{edge}$
T	temperature
x, y, z	local coordinates
X, Y, Z	blade cascade coordinates, where X is blade axial direction
u, v, w	velocity components in a local coordinate system
V_s, V_n, V_z	secondary velocity components
U_{in}	magnitude of inlet streamwise velocity
U_{edge}	magnitude of local freestream velocity at the boundary layer edge

Greek

β	mean flow angle
δ_{99}	boundary layer thickness (99%)
μ	dynamic viscosity
ν	kinematic viscosity
ρ	density
τ_w	wall shear stress

Subscripts

edge	quantity at boundary layer edge
in	inlet freestream conditions
ms	midspan (inviscid) conditions
w	wall conditions

Superscripts

'	fluctuating quantity
$\overline{(\,)}$	time-averaged quantity

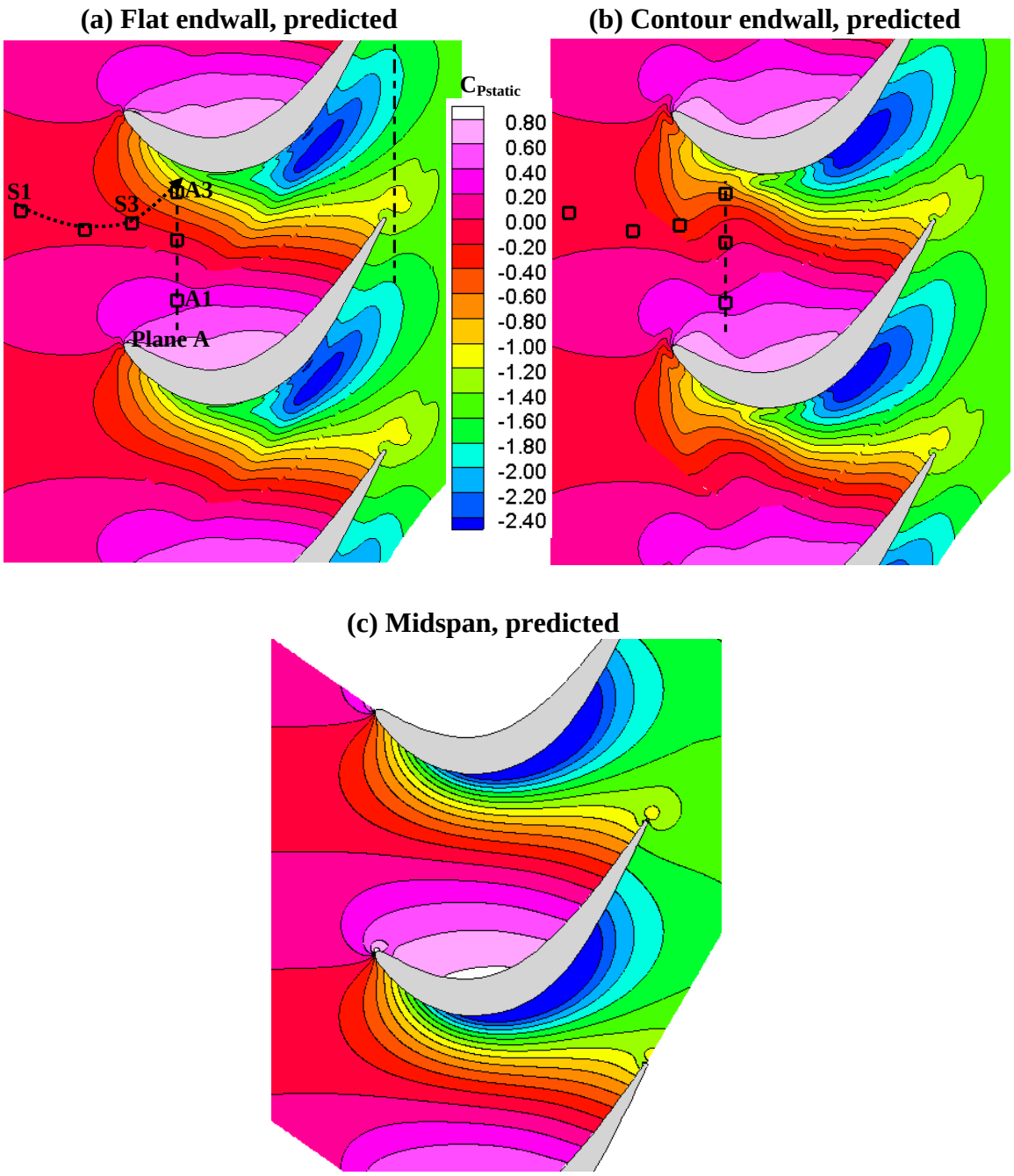

Figure D.1. Predictions of non-dimensional static pressure for the (a) flat endwall, (b) contoured endwall, and (c) at midspan (same for both geometries).

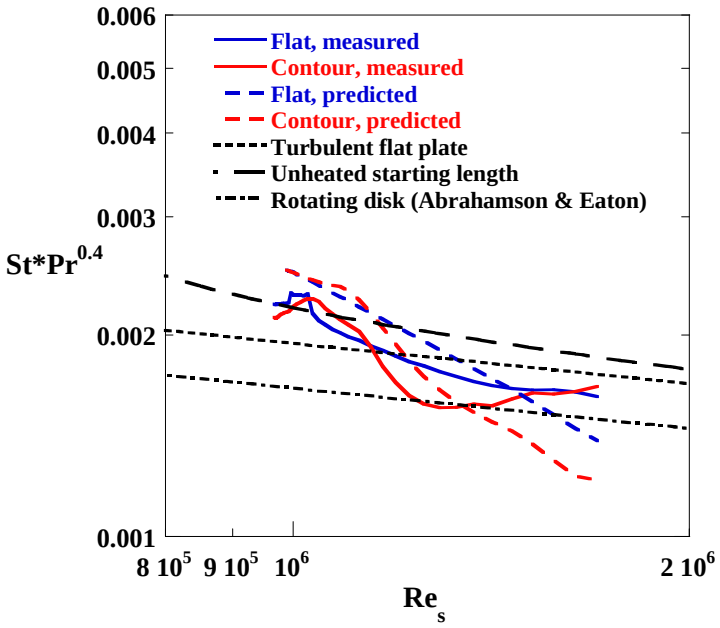

Figure D.2. Comparison of measured and predicted endwall heat transfer along an inlet streakline path.

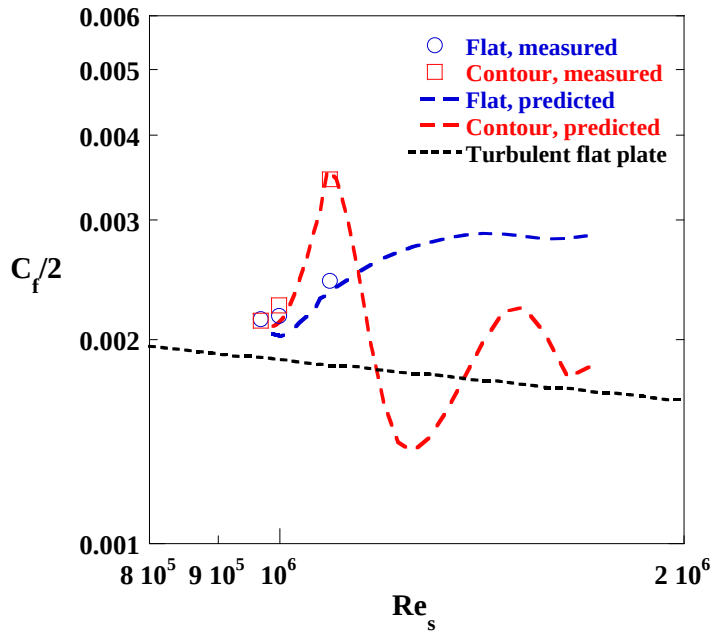

Figure D.3. Comparison of measured and predicted endwall friction coefficients along an inlet streakline path.

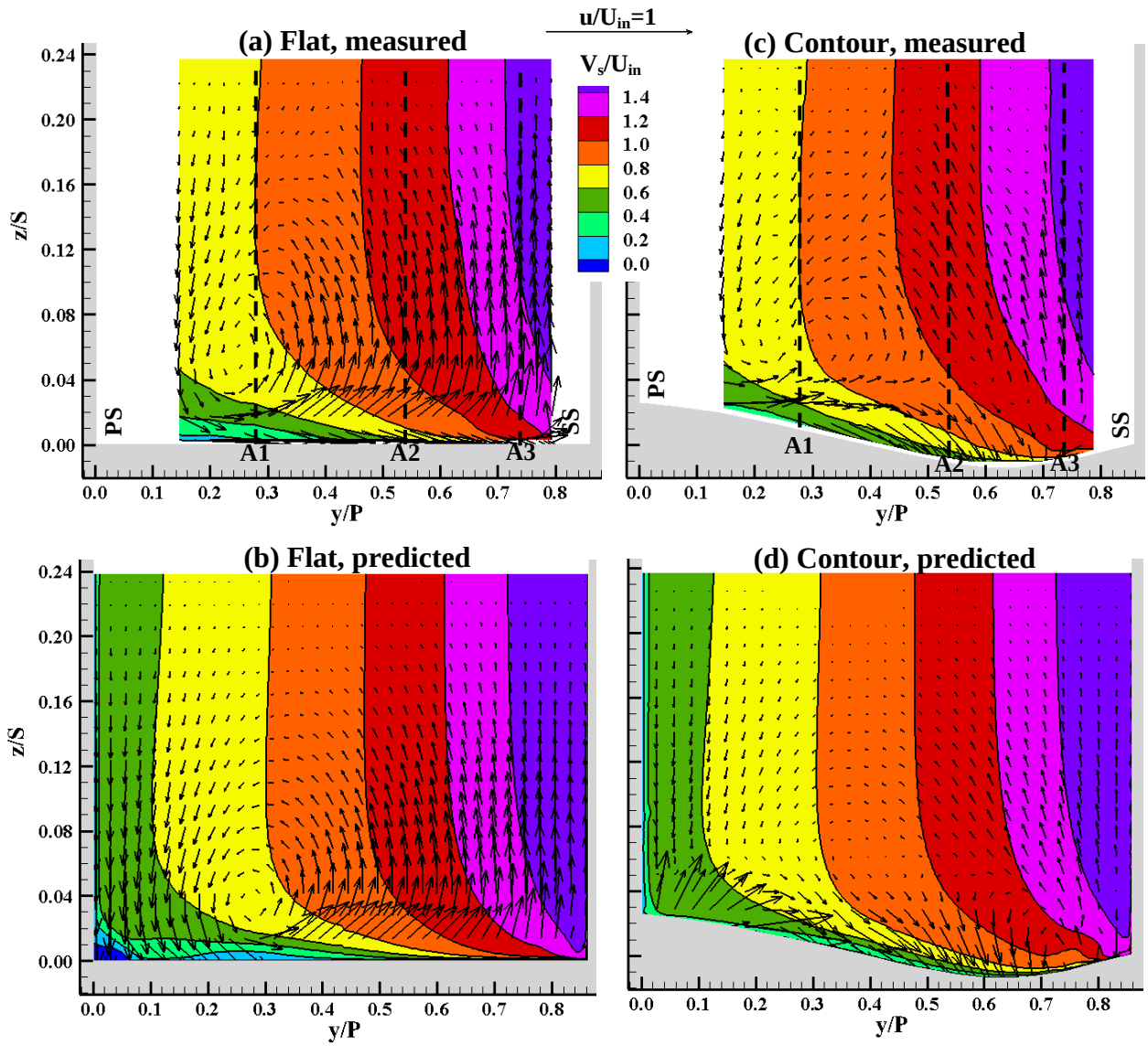

Figure D.4. Mean streamwise velocity and secondary flow vectors at Plane A ($0.2C_{ax}$ from the leading edge) for the: a) flat endwall measurements; b) flat endwall predictions; c) contoured endwall measurements; d) contoured endwall predictions.

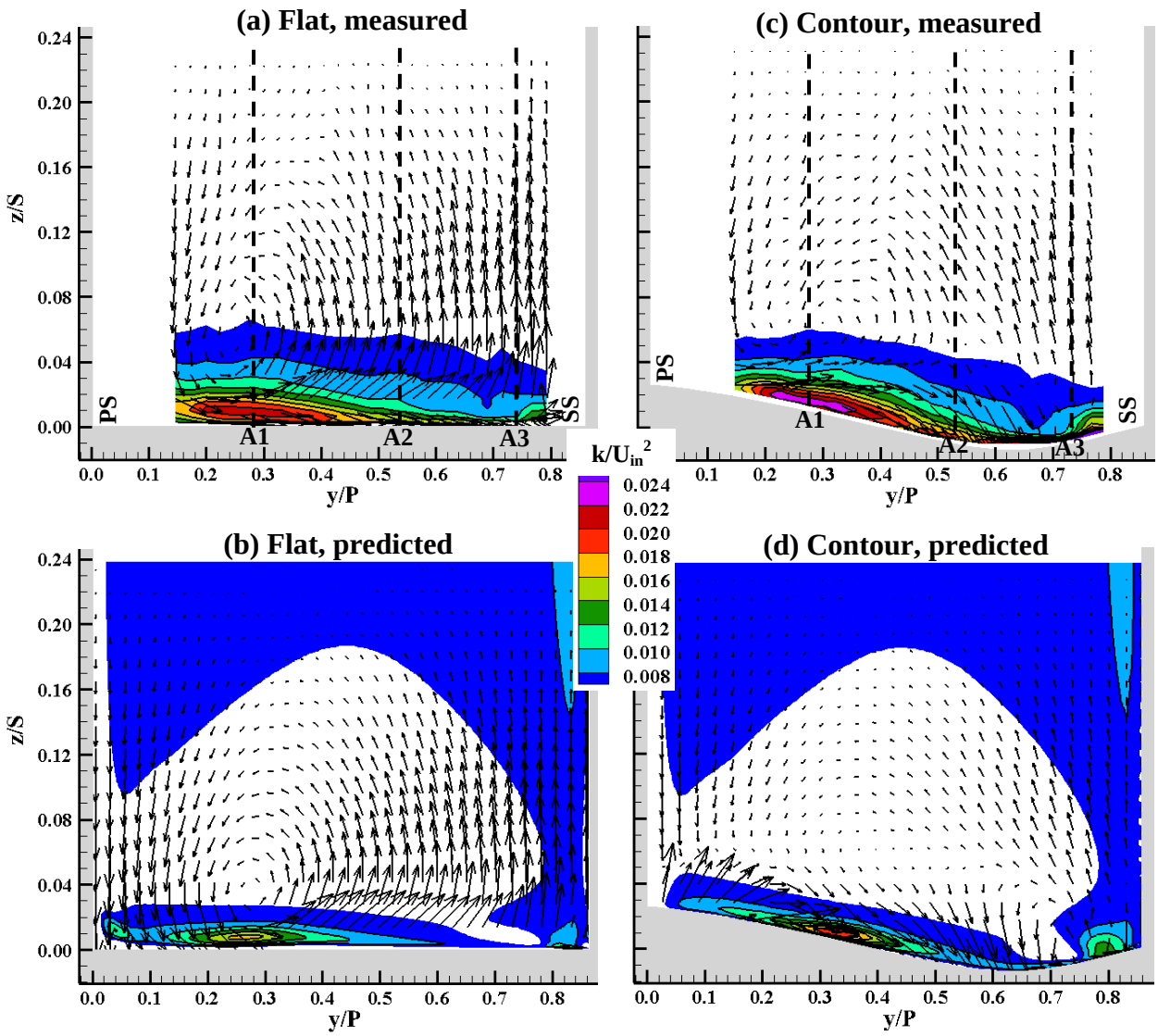

Figure D.5. Mean secondary vectors and turbulent kinetic energy at Plane A ($0.2C_{ax}$ from the leading edge) for the: a) flat endwall measurements; b) flat endwall predictions; c) contoured endwall measurements, and d) contoured endwall predictions.

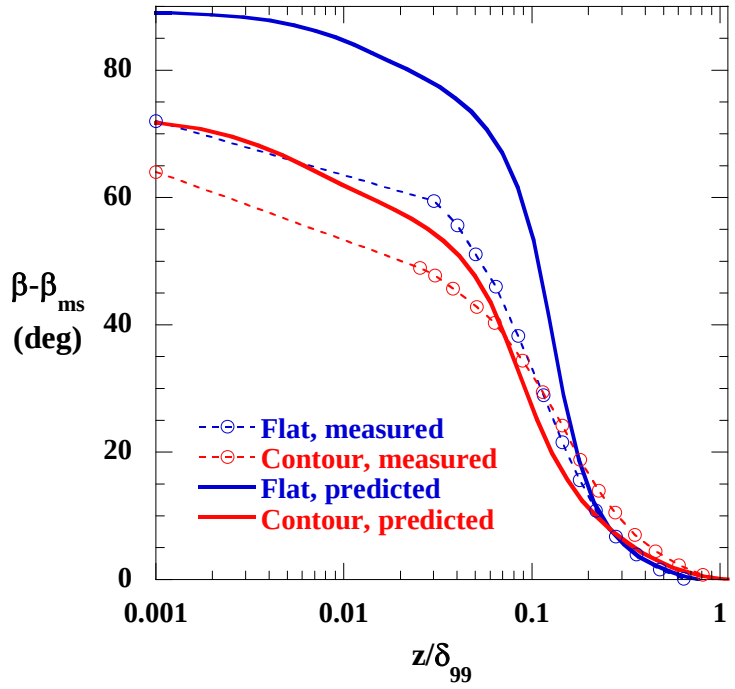

Figure D.6. Profiles of mean flow skew angle relative to the freestream at station A1 near the pressure side.

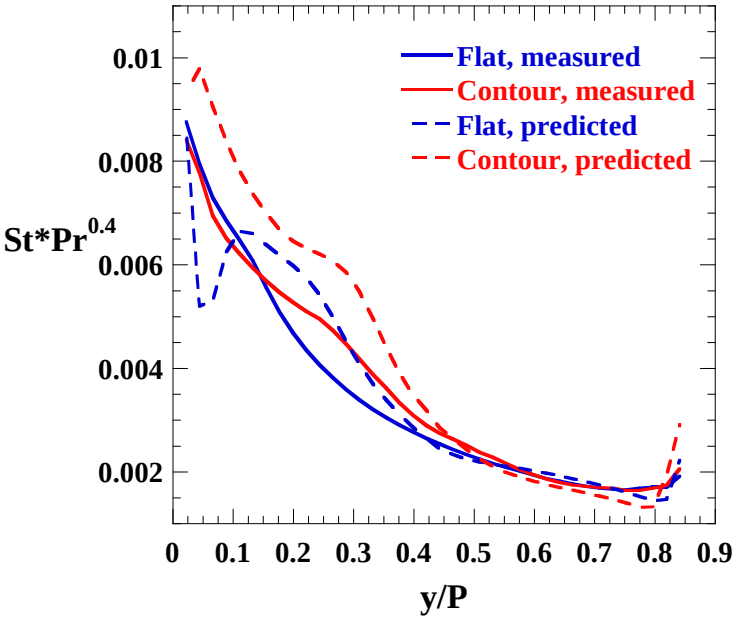

Figure D.7. Measured and predicted endwall heat transfer at Plane A.

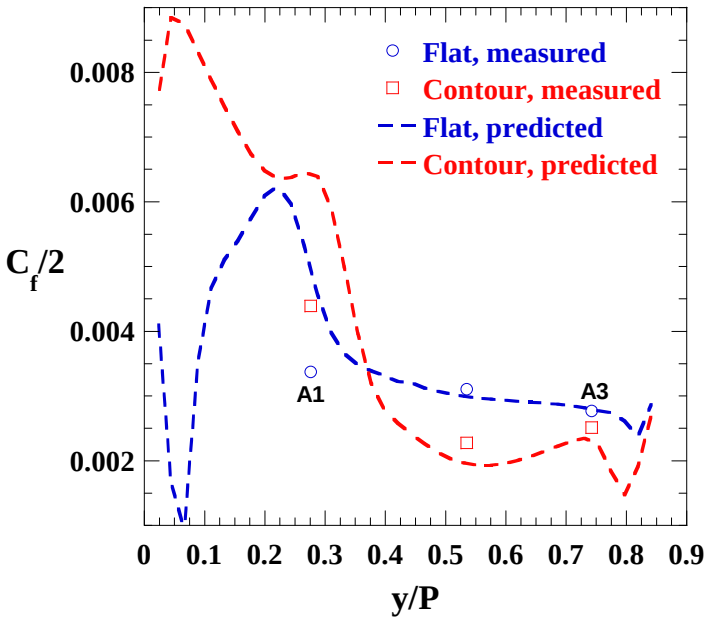

Figure D.8. Measured and predicted endwall friction coefficients at Plane A.